annual report 1975

nuclear physics laboratory
university of washington

LIBRARY COPY
DO NOT REMOVE

Nuclear Physics Laboratory, GL-10
University of Washington
Seattle, Wash. 98195

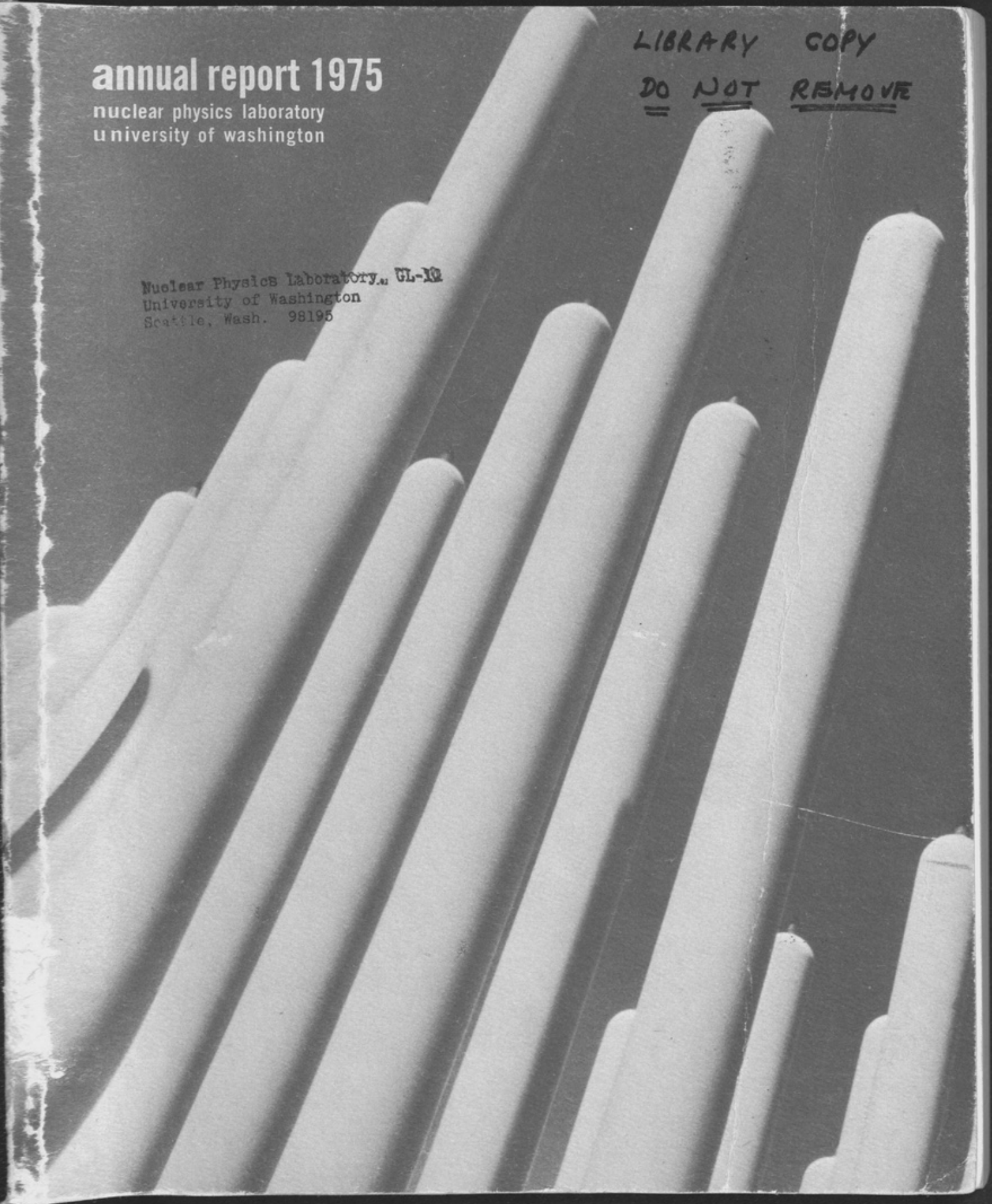

Nuclear Physics Laboratory, GL-10
University of Washington
Seattle, Wash. 98195

ANNUAL REPORT

Nuclear Physics Laboratory
University of Washington
June, 1975

THE COVER DESIGN

For our cover picture we continue the tradition of the past several years and show the photograph of the high pressure gas cylinders which store the nitrogen and carbon dioxide mixture used for insulating the high potential terminals of the two Van de Graaff machines. They form a group of towers which front on the Van de Graaff building and have aroused considerable local interest and curiosity.

INTRODUCTION

The major areas of research interest in the Laboratory remain much the same as they were last year. There have been further studies of light nuclei, some probing their structure, and other studies emphasizing weak interactions. There has been considerable work with polarized particles, including some new examinations of depolarization in elastic scattering. Light heavy-ion reaction studies have stressed the role of surface transparency in elastic and transfer reactions and studies with so-called heavy heavy ions have concerned themselves with energy and angle distributions resulting from encounters between heavier partners. The investigation of the concentrations of higher lying multipole strength in nuclei continues using the radiative capture reaction and work on the same problem has been started using pions. The measurement of pion total cross-sections progresses at LAMPF. Our extensive program on inner-shell ionization of atoms is still going on and so are the many applied researches which are being pursued at the cyclotron.

We must call attention to the exciting prospect of upgrading the tandem facility by the addition of a linear accelerator afterburner of special design. Some features of this afterburner are discussed in this report and we expect to continue to explore the practicability (and cost) of bringing such a machine into operation.

We close this introduction with the standard reminder that the articles in this report describe work in progress and are not to be regarded as publications nor quoted without permission of the investigators. The names of the investigators on each article have been listed alphabetically but where appropriate, the name of the person primarily responsible for the report has been underlined.

As always, we welcome applications from outsiders for the use of our facilities. As handy reference for potential users we list in the table on the following page the vital statistics of our accelerators. For further information please write or phone Dr. W.G. Weitkamp, Technical Director, Nuclear Physics Laboratory, University of Washington, Seattle, WA 98195; (206) 543-4080.

THREE STAGE TANDEM VAN DE GRAAFF ACCELERATOR

(A High Voltage Engineering Corp. Model FN)

Completed: 1967
Funding: Purchased with NSF funds; maintained by AEC(ERDA) funds and some funds from the State of Washington.

Beams currently available: (See also W.G. Weitkamp & F.H. Schmidt "The University of Washington Three Stage Van de Graaff Accelerator" Nucl. Instrum. Methods *122*, 65 (1974).)

Ion	Typical Current (nA)	Maximum Practical Energy (MeV)
p,d(3 stage)	1000	25
p,d(2 stage)	> 2000	18
polarized p,d	15	18
He	800	27
Li	500	36
C	200	63
N	100	72
O	1000	87
Al	20	68
Si	100	90
Cl	200	99

CYCLOTRON

(A 60-inch fixed energy machine)

Completed: 1952
Funding: Constructed primarily with State funds and subsequently supported by AEC funds. Now sustained by funds from outside users.

Beams currently available:

Ion	Typical Current (μA)	Maximum Practical Energy (MeV)
p	75	11
d	150	22
^{4}He	30	42

TABLE OF CONTENTS

1. ACCELERATOR DEVELOPMENT

1.1 Van de Graaff Accelerator Operations and Improvements

J.W. Orth and Staff

This year several new milestones have been passed. The Laboratory is continually developing new capabilities in heavy ion acceleration. This year we have accelerated 81 MeV $^{16}O^{+8}$, 35 MeV $^{15}N^{+6}$, 108 MeV Ag^{+15}, and Si and Pb ions. These new beams have been made possible by the availablilty of the new terminal source and the new sputter source (see Sections 2.2 and 2.3).

We would like to call attention to the long life of our beam tubes. We now have 54,000 hours on our inclined field tubes and are still able to hold 9 MV on the terminal with no observable deterioration in sight. We attribute this long life to our standard procedures for tube conditioning.

Statistics of Van de Graaff operation are given in Table 1.1-1.

The following are improvements and additions which have been made to the machine during this past year:

(1) The most needed improvement made this year was the renewal of the Tandem resistors by a new in-house design (see Sec. 1.4).

(2) Another much needed updating was the changing of the transistors in both the analyzing and switching magnets from germanium to silicon types. We have also replaced the Keithley with modern integrated circuitry to provide improved stability and reliability.

(3) A new sputter ion source was added as an alternate for the direct extraction source to improve heavy ion production (see Sec. 2.3).

(4) The beam line was extended beyond the 90° magnet to produce a fast neutron source for delayed neutron studies (see Sec. 16.5).

(5) The entire neutral source on the injector has been dismanteled and the liquid nitrogen line is now connected through a solenoid valve to the scavenging system. Thus we no longer have to pay for gaseous nitrogen. This represents a considerable saving.

(6) A new roughing line was added to the injector pumping tee to allow the beam tubes to be roughed out without shutting down the direct extraction source or the polarized ion source.

(7) Our tube type quadrupole power supplies have been replaced by Kepco and Sorensen solid state supplies to avoid problems arising from the unavailability (and expense) of replacement vacuum tubes.

(8) The TM diffusion pump on the direct extraction source was replaced with an NRC pump, gate valve and baffle to improve reliability.

(9) Final changes were made in the terminal source (see Sec. 2.2).

Table 1.1-1. Statistics of Van de Graaff Operation from April 16, 1974 to April 15, 1975

1. Division of time among activities	Time (hrs)	Per Cent
Normal operation[a]	7063	81
Scheduled maintenance	324	4
Unscheduled maintenance	486	5
Unrequested time	887	10
Total[b]	8760	100
2. Division of beam-on time among particles		
a. Two stage operation		
protons	1450	21.8
polarized protons	1869	28.1
deuterons	137	2.1
polarized deuterons	155	2.3
^{3}He	691	10.4
^{4}He	256	3.8
^{6}Li	73	1.1
^{12}C	141	2.1
^{14}N	191	2.9
^{15}N	44	0.7
^{16}O	484	7.3
^{18}O	576	8.7
^{27}Al	17	0.3
^{28}Si	70	1.1
^{37}Ag	24	0.4
Subtotal	6178	93
b. Three stage operation		
protons	252	3.8
deuterons	95	1.4
^{12}C	41	0.6
^{14}N	41	0.6
^{16}O	44	0.7
Subtotal	473	7
TOTAL BEAM TIME	6651	100

a) Includes all the time the accelerator was under control of an experimenter.
b) This is the number of hours in a year.

1.2 Cyclotron Operations and Improvements

J. W. Orth and Staff

Most of the running time of the cyclotron has been devoted to Cancer Therapy and to medical research. Many refinements have been made this year in patient handling and treatment techniques (Sec. 16.4). Ten to fifteen patients a day are now being treated on Mondays, Wednesdays, and Fridays. There is also continuing research on fast neutron effects on mice (Sec. 16.2). Due to the appearance of certain side effects in the Austin Texas treatment program, the Texas workers have conducted a study on Rhesus monkeys using our facility when theirs was unavailable.

Atomics International continues to do helium injection into various materials at the cyclotron in order to study structural changes induced by such ions. Workers from Oregon State University have again had a run for a study of ^{235}U fission. A new user on the cyclotron this year is a group from the Electrical Engineering Department. They are studying the shift in optical properties in alkaline halide crystals produced by α particle bombardment. The Department of Pharmacy has had "tagged" isotopes prepared for tracer use in patient diagnostics.

The statistics of cyclotron operation are recorded in Table 1.2-1.

The only machine improvements of importance that have been made during the year are:

(a) A new design scanner plate was installed that uses pivoted "O" ring sealed surfaces in lieu of the rubber hoses previously used. It also has more clearance from the side walls.

(b) A new set of needle valves using 120 volt motors replaces the old 12 volt DC motors previously used.

(c) A system of switches and vacuum solenoids was installed to extend operation of the double gate valve to the control room.

Incidentally, the whole Nuclear Physics Laboratory has undergone a new paint job this year, an enhancement long overdue. There have also been a number of changes in the Machine Shop. Because of deficiencies in the electrical service and obsolete wiring in the shop, the State electrical inspector required that the shop be updated to meet present codes. James Fowler & Associates was hired and has prepared a schedule for enlarging the electrical service and correcting code violations. The Office of Facilities Resources has agreed to fund these renovations to the amount of $67,000. The work is presently out on bid and is to be completed by June. In the meantime the machine-tool layout in the shop has been reorganized and is gradually being brought to OSHA standards for machine shops.

Table 1.2-1. Statistics of Cyclotron Operations from April 16, 1974 to April 15, 1975

		Time (Hrs)	Per Cent
1.	Division of time among activities		
	Normal operation	1451	92
	Scheduled maintenance	56	4
	Unscheduled maintenance	69	4
	Total	1576	100
2.	Division of beam time among particles		
	Alpha particles	92.3	16
	Deuterons	473.1	82
	Protons	10.0	2
	Total	575.4	100
3.	Division of normal operating time among users		
	Atomics International	129	10
	Battelle Northwest	1	< 1
	Cancer Therapy Group		
	a. Therapy	745	56
	b. Physics	151	11
	c. Experimental Oncology	25	2
	d. Biology	7	< 1
	e. M.D. Anderson Hospital (Texas)	52	4
	Oregon State University	6	< 1
	Western Washington State College	13	1
	University of Washington Department of Nuclear Engineering	36	3
	University of Washington Department of Nuclear Medicine	100	8
	University of Washington Department of Nuclear Pharmacy	10	1
	University of Washington Department of Nuclear Physics	12	1
	University of Washington Department of Physics	31	2
	University of Washington Department of Electrical Engineering	4	< 1
	Total	1322	100%

1.3 Design and Construction of Electronic Equipment

H. Fauska and Rod Stowell

Electronic projects completed during the last year include the following:

a. A nano ammeter to monitor the polarized ion source beam was designed and constructed.

b. The analyzing and switching magnet regulators on the Van de Graaff beam line were updated with silicon series passing transistors. A new pre-amplifier and regulator was constructed and installed.

c. A new beam monitoring system was installed which included construction of remote readout meters, remote range indicators, computer readout capability, and a current range expander for the machine operator's position.

d. A five channel pre-scaler of divide-by-ten was designed and constructed.

e. A coincidence data switch was designed and constructed. The unit allows five channels of triple coincidence to be switched during polarization studies.

f. The design and construction was done on a four channel beam current de-randomizer.

g. The power supply on the fine adjustment of the switching magnet was replaced with a newly designed and constructed supply.

h. An emittance monitor was constructed to help with ion source studies.

i. A small 60-130 MHz R.F. generator was designed and constructed for testing of the spiral resonator accelerating cavity prototype (see Sec. 1.6).

1.4 Van de Graaff Resistor Replacement

W.G. Weitkamp and Staff

Because the beam trajectory through a Van de Graaff accelerator equipped with inclined field tubes depends critically on the column voltage gradient, it is important to have a stable resistor string on the column. Furthermore, since resistor failure can be a major maintenance problem as well as a limit on the maximum terminal voltage, it is important that the column resistors be reliable as well. The high cost of suitable commercial resistors designed specifically for Van de Graaff use has led us to look for an alternative design to replace the resistors originally installed in the tandem.

The resistor assembly that resulted is shown in Fig. 1.4-1. Four epoxy coated spiral carbon resistors[1] are held in firm contact inside a PVC tube by a

spring mounted in the lower end. These resistors are rated at 4 watts, 15 kV each. The lower end of the assembly is threaded so the resistors can be removed easily from the PVC tube. The total cost of materials for these resistor assemblies is about $12 each.

It is not yet clear how well the mean life of these resistors will compare with commercial Van de Graaff resistors. The tandem has run for 6651 hours with these resistors with only one resistor failure. The resistance has changed by not more than 2% on the average in that time. Even if the mean life proves to be shorter than that of our old resistors the relatively low cost and ease of replacement of these resistors should make them a satisfactory alternative.

It should be noted that the University of Washington Tandem is not normally pressured with SF_6; it is not expected that this resistor design would be suitable in a Van de Graaff containing a substantial fraction of SF_6.

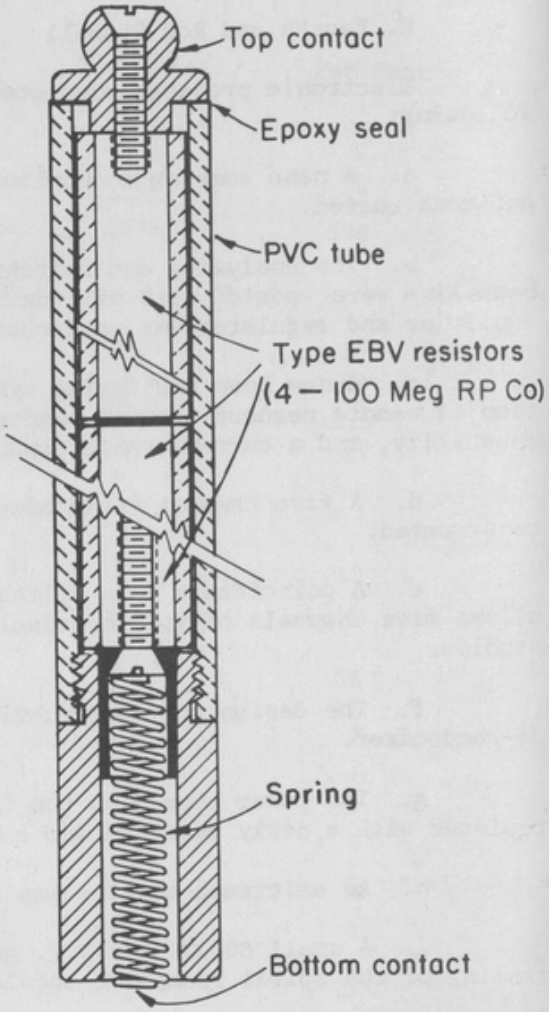

Fig. 1.4-1. Van de Graaff resistor assembly.

---

1. Model EBV 100 meg resistors obtained from Resistor Products Company, 914 South 13th St., Harrisburg, PA 17104,

1.5 Feasibility Study for a Linac Postaccelerator for the Tandem

D. Burch, J.G. Cramer, and T.A. Trainor

The Laboratory has for some time been interested in possible ways of expanding or replacing the existing accelerator facility with a larger facility which would provide access to a broader range of nuclear reactions. Beginning at about the first of the year, we have begun a feasilibity study to achieve this goal by adding a postaccelerator to the existing facility, to be injected by the present tandem in either two or three stage operation. After some study of possible alternatives, we have concluded that cyclotrons either normal or superconducting, are too large, expensive, and technically demanding to be reasonable

for our purposes, and that there is no real advantage of superconducting linacs over normal ones, with the exception of perhaps a factor of 4 less power consumption. The impressive performance obtained by the Los Alamos group in their tests of spiral resonator accelerating cavities, as reported at the Informal Conference on Tandem Postaccelerators held in Pittsburgh in October of 1974 prompted us to begin a detailed study of the possibility of adapting this conventional technology to our own postaccelerator needs.

We have worked closely with Dr. R.H. Stokes of LASL on this project. Since the Los Alamos effort on the investigation of spiral resonator linac technology has been essentially terminated, we were very fortunate in being able to obtain their prototype triple resonator cavity through the generousity of our colleagure there. This cavity was previously used by the Los Alamos group in full power tests at power level in excess of 20 KW, and was used to accelerate alpha particles as a demonstration of the feasibility of this acceleration scheme. We have used the cavity to perform bead-perturbation measurements of the electric field-strength in profiles of the normal modes which will be discussed in Sec. 1.6.

In the course of our feasibility study, two important design concepts have been developed which had not been previously considered for machines of this kind. The first of these concepts is the idea, mentioned previously, of using all three of the resonant normal modes of the cavity to change the effective phase velocity of the cavity and thereby greatly increase the capability of the accelerator to accelerate light as well as heavy ions. This scheme presents one important problem: the cavity must be tunable so that all of the normal modes can be shifted to the frequency of the driver oscillator, or alternatively, the driver oscillator must be capable of tuning over a frequency range which spans the normal modes. The latter alternative appears unfeasible in the context of available RF power amplifiers, so we are concentrating our attention on the tuning of the cavities. One way in which this can be accomplished over about a 15% frequency range is by recessing the ground connections at the ends of the spiral coils in cups. A "spider" is placed in this recess which can be positioned in such a way as to change the effective length of the spiral. In the case of the test resonator unit discussed previously this would suffice to tune two of the modes, but would not tune the other mode unless the helicities of the spirals were changed to a +++ arrangement. Mathematical analysis of the system has shown that the splitting of the resonant frequencies of the three normal modes may be reduced by better balancing of the inductive and capacitive coupling of the system. At any rate, retuning of the triple resonator cavities to the three modes appears to be quite feasible, but may result in complication of the mechanical design of the structures.

A related question is the shunt impedance of the cavity in each mode. Since little information is available on the shunt impedances in the two higher frequency modes, we have made rather conservative estimates of this quantity in the design of the proposed accelerator, and we are now preparing a detailed investigation of this question.

The second concept which has not been previously considered for a machine of this type is the idea of providing RF power which can be applied either continuously, for 100% duty factor operation and high beam intensity, or in a fractional duty factor mode, e.g., with the RF supplied for 20% of the time,

providing 5 times the instantaneous power 1/5 of the time for the same average power. This mode permits exploitation of the characteristic of the spiral resonator cavities mentioned above, that of sustaining very high RF electric fields. Essentially, the fractional duty-factor mode permits the experimenter the option of trading intensity for energy, reducing the beam intensity by up to a factor of 5 but increasing the effective accelerating field by about a factor of 2.2. The loss of intensity in this mode may not actually be as bad as a factor of 5, for ion species which are limited in intensity by ion source arc currents or tandem loading. For such cases, pulsing of the ion source could result in higher instantaneous ion currents while maintaining the same average ion current as in the continuous mode of operation. It should be noted that fractional duty factor operation is not in itself an innovation; for most existing heavy ion and high energy accelerators it is a way of life. The innovation discussed here is incorporating the option of 20% duty factor operation to exploit the high voltage gradients available with spiral resonator cavities.

We have written an extensive design program which chooses optimum cavity parameters for a particular ion and predicts the performance of a particular design for any specified set of operating conditions and ions. Using this program, the information available from LASL, and the two design concepts mentioned above, we found that it is possible to design a very modest machine which is capable of providing ions of any mass with energy that exceeds the Coulomb barrier on any target.

The postaccelerator design under study employs the recently developed technology of spiral resonator RF cavities at room temperature to achieve a very high level of performance at a modest cost. There are a number of significant advantages to this approach:

a. Simple modular construction with many interchangable structural elements
b. Small radial dimensions for small volume vacuum system
c. Relatively large RF field capabilities with no limits imposed by B field
d. High shunt impedance for moderate RF power consumption
e. Independence of resonant properties and electric field shaping
f. No demanding tolerances for mechanical structures or fields
g. Radial focusing by quadrupoles outside the vacuum system, independent of RF phase
h. Good acceptance in position and phase
i. Simple continuous variation of energy from maximum down to injector energy
j. Flexibility of trading intensity for energy in several ways
k. Multiple resonant normal modes for efficient acceleration of all ion species.

These features have been used in a design employing 41 triple spiral resonator accelerating elements to produce a postaccelerator which significantly increases the energy of all particles from protons to uranium and makes possible the study of nuclear reactions with any beam on any target in the periodic table of elements.

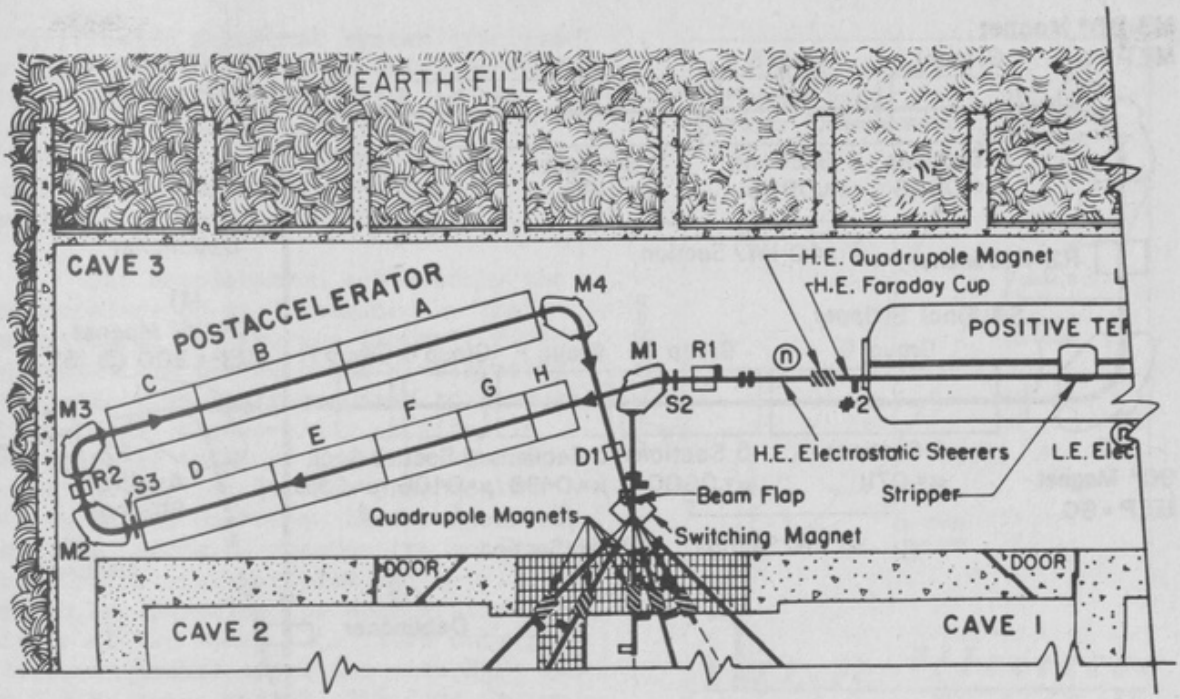

Fig. 1.5-1. Overhead view of positioning of Postaccelerator in Cave 3 area of Accelerator Tunnel.

The postaccelerator is injected with beam from the existing 3-stage tandem accelerator after a 15° analysis by magnet M1, as shown in Fig. 1.5-1. The beam handling system uses three additional 90° magnets, M2, M3 and M4, to bend the beam around a long rectangular path and back into the existing switching magnet M5 at an angle of 15° to the normal entry. In travelling on this path, the beam passes through two 14 meter sections of linear accelerator to be located in the Cave 3 area of the Laboratory. This cave, like the rest of the accelerator tunnel, is very well shielded but is presently used only as a storage area. The arrangement shown in Fig. 1.5-2 permits accomodation of the postaccelerator in the existing building without modification, and will create only minimal interference with the normal operation of the present 3-stage tandem facility during and after construction of the new postaccelerator.

Figure 1.5-3 shows a schematic diagram of the structure of the postaccelerator. It consists of 8 groups of spiral resonator accelerating sections for a total of 41 resonator sections, with all sections within a group being identical in design and having the same phase velocity μ, given here as a fraction of c. The groups of resonators are labeled A through H in Fig. 1.5-3. Group A at the exit of the postaccelerator consists of seven 40 KW (μ = .1186) resonator sections, and group H at the entrance of the postaccelerator consists of three 20 KW (μ = .0333) resonator sections.

Between resonator groups C and D the postaccelerator is "folded" by the

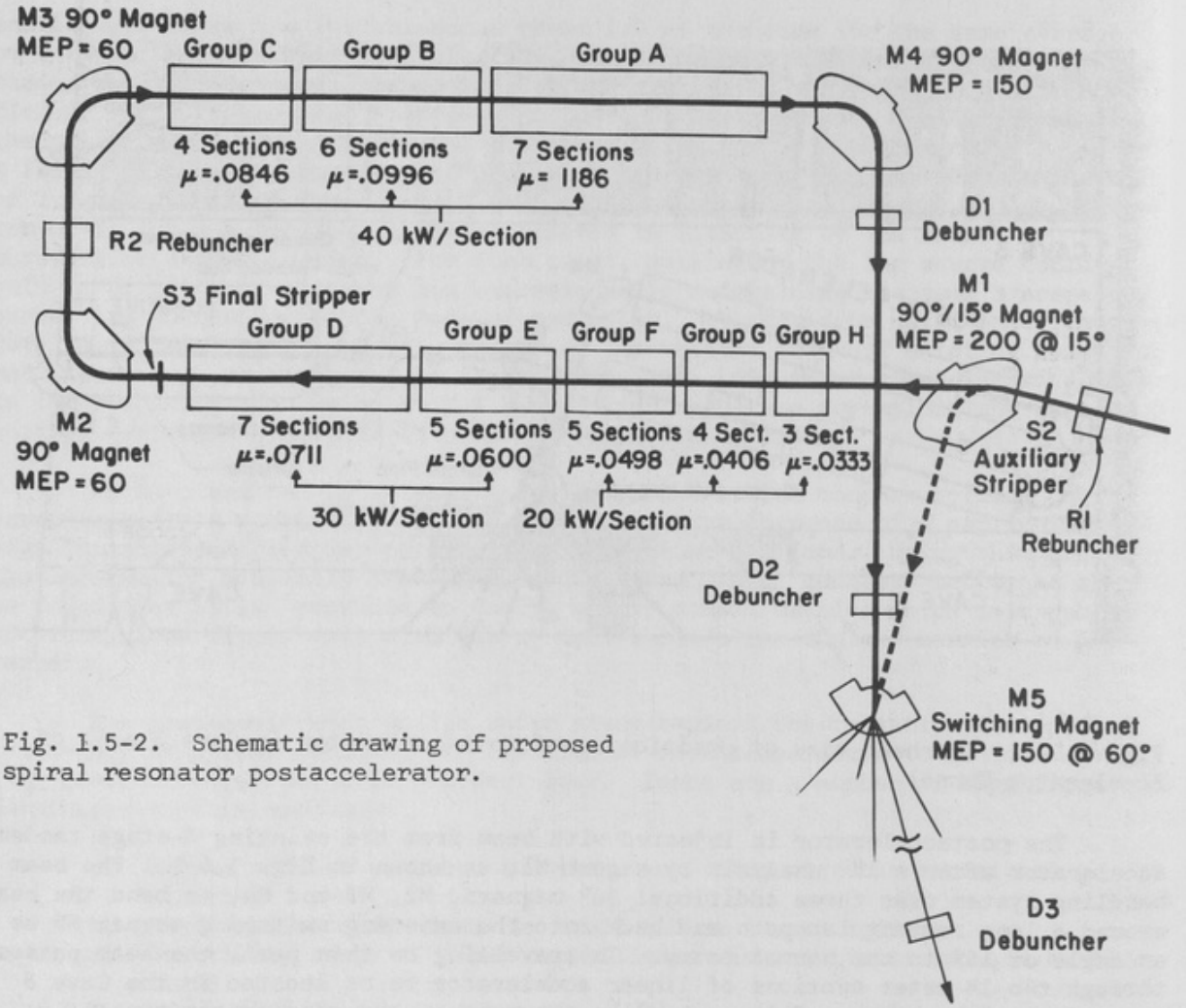

Fig. 1.5-2. Schematic drawing of proposed spiral resonator postaccelerator.

two 90° magnets M2 and M3. This fold not only saves building space but also provides a charge-state selector for the final stripper unit S3. Such charge-state selection is required for an accelerator of this type to obtain good time and energy resolution and to avoid multiple beams. An auxilliary stripper S2 is located just before the first deflection magnet M1 so that this magnet acts as a charge state selector for this stripper. The S2 stripper is used only in the "3-strip" mode of operation to obtain the highest possible energy from the full postaccelerator at reduced intensity.

The beam injected from the 3-stage tandem is chopped at the operating frequency of the postaccelerator (∿ 100 MHz) and bunched to about .5 ns FWHM to match the phase acceptance of the postaccelerator. Between resonator groups D and C there must be a rebunching unit R2 which preserves the time structure of the beam. At some distance beyond the exit of the postaccelerator there will be

a distributed debuncher system comprised of elements D1, D2 and D3 which converts the excellent time resolution of the beam to good energy resolution ($\Delta E/E < 3 \times 10^{-3}$) or alternatively achieves optimum time resolution on target by acting as a rebuncher.

The acceleration achieved by the postaccelerator is determined by the magnitude of the average electric field E_0 present in the resonant accelerating sections. The power required to operate the resonant accelerating sections is proportional to E_0^2. For this reason, power consumption imposes practical limits on the operation of the accelerator long before E_0 reaches its achievable limit. This problem can be alleviated by operating the accelerator in either of two modes: (1) 100% duty factor (continuous) operation with E_0 = 1.1 to 2.1 MV/meter and (2) 20% duty factor operation (macro-pulsed at a frequency of perhaps 1 KHZ) with E_0 = 2.5 to 4.7 MV/meter. The latter fields are rather high, but are considerably less than the highest effective field strengths (5.5 MV/meter) which have been achieved for spiral resonator units of this type. Both the continuous and macro-pulsed modes use the same RF power, but the latter results in considerably higher beam energies. On the other hand, macro-pulsed operation reduces beam intensity by a factor of 2 to 5 and also increases experimental problems such as pileup and instrumental dead-time. It is possible that by operating the ion-source and tandem in the same macro-pulsed way, it may be possible to recover some of the lost intensity in pulsed operation.

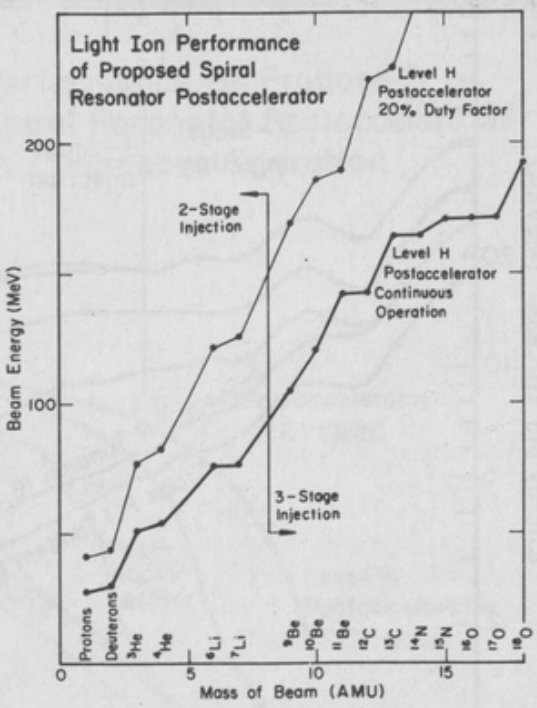

Fig. 1.5-3. Light ion performance of proposed postaccelerator.

An even more serious constraint than power requirements is, of course, available funding. The proposed postaccelerator is uniquely able to adjust to a spectrum of funding levels because of its highly modular construction. It could, in prinicple, be implemented at 41 levels ranging from 1 accelerating section to all 41 accelerating sections. For the purposes of this proposal, we have chosen to examine its operation at three levels of implementation which we will call Level A, Level C, and Level H. Level A consists of the accelerator with only seven resonators in the A group in operation, or about 1/4 of the full accelerator. Level C assumes that resonator groups A, B, and C are in operation, about 1/2 of the full accelerator, and Level H assumes that all resonator groups, A through H, are in operation. As mentioned previously, it is possible to operate the proposed accelerator in either the "2-strip" or "3-strip" mode, depending on how many times the beam passes through a stripper foil during acceleration. The 3-strip mode is only of advantage in Level H operation, and so it will only be considered for that case. Tables 1.5-1 and 1.5-2 summarize the

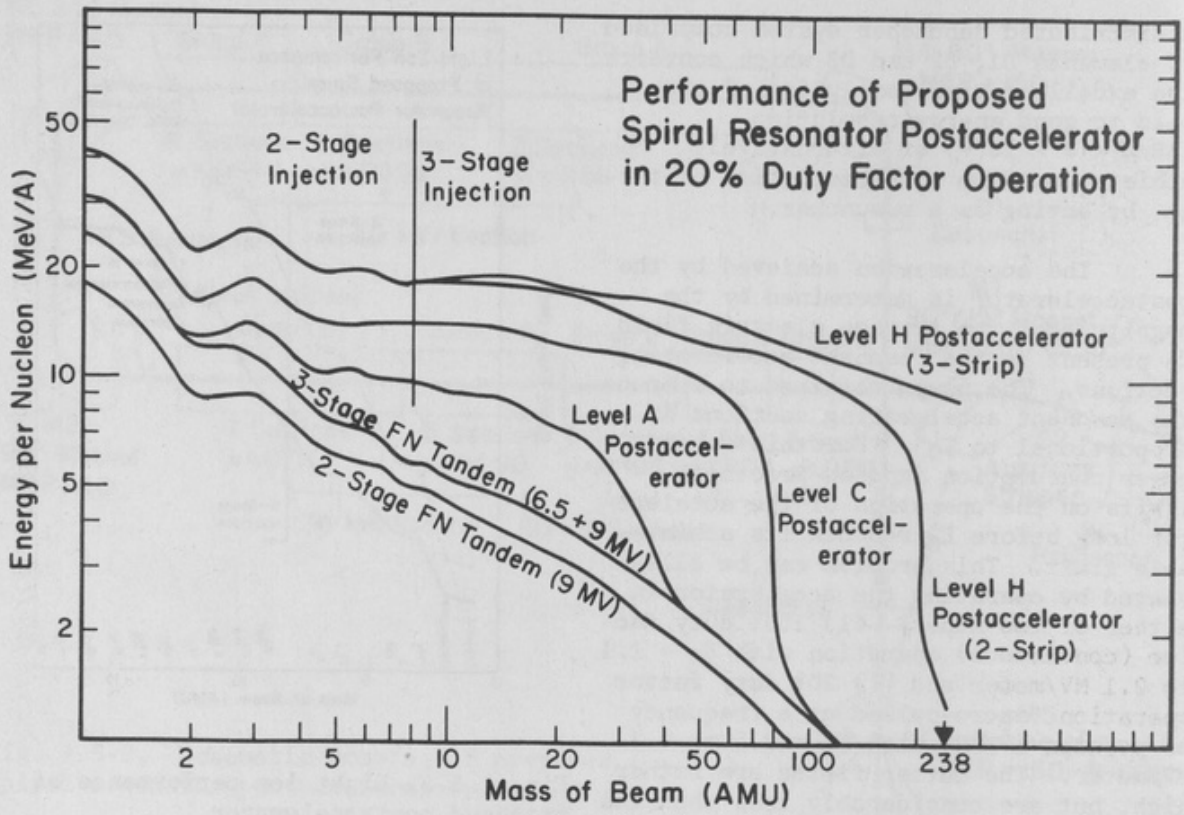

Fig. 1.5-4. Performance of proposed postaccelerator operated in 20% duty factor mode.

operating performance of the proposed postaccelerator in the modes of operation described above. Figures 1.5-3, 1.5-4 and 1.5-5 illustrate this performance for light and heavy ions.

These tables and figures give the energy performance of the proposed postaccelerator, but do not address themselves to the related question of beam intensity. This was done because, while the energy performance can be calculated with some precision, the intensity of the beam is much less accessible to precise analysis. The principal causes of beam loss in the proposed accelerator arise from emittance mismatch between units of the accelerator, charge state fractionation during stripping, bunching losses, and losses due to fractional duty cycle macro-pulsed operation.

We have performed some crude calculations of the losses of beam due to emittance mismatch. The only such loss which bears close scrutiny is the possible mismatch between the beam following stripping at the tandem terminal and the acceptance of the high energy tandem tube.

We have come to some rather different conclusions than other groups on the probability of severe loss of the heavier ions due to multiple scattering at the

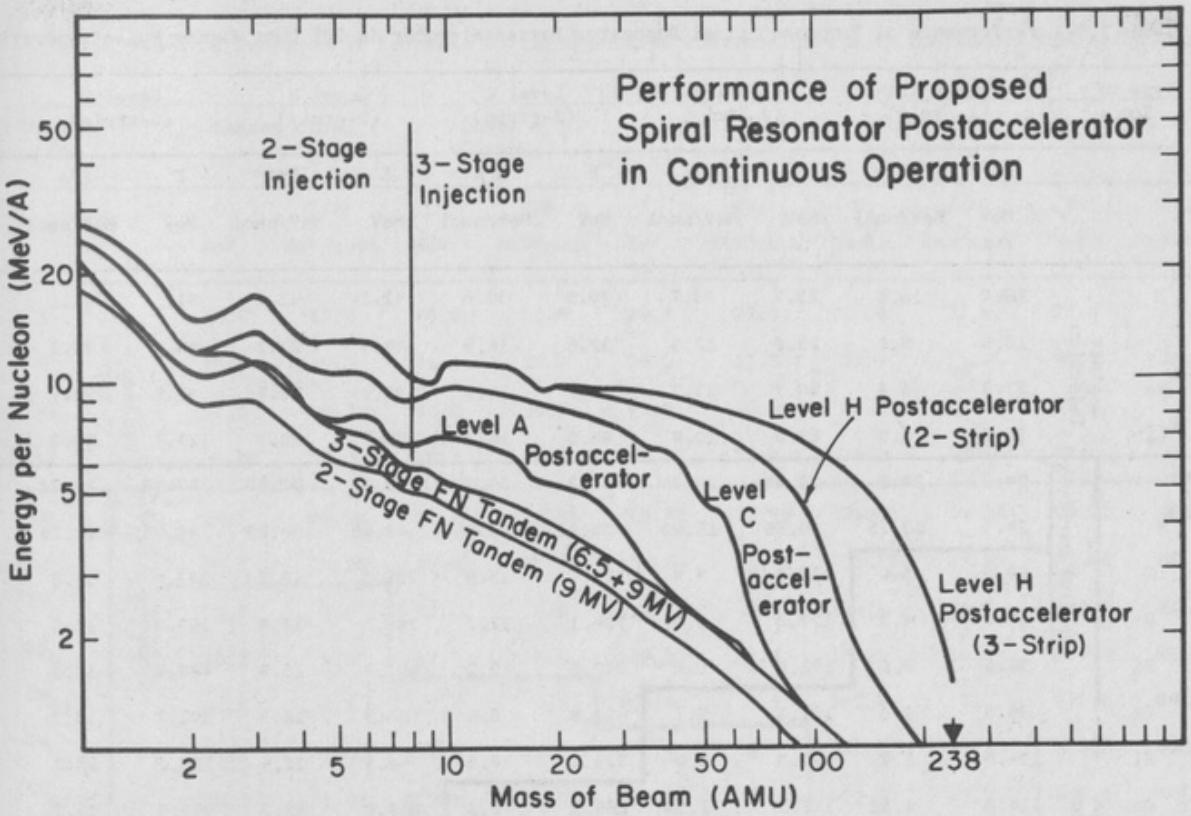

Fig. 1.5-5. Performance of the proposed postaccelerator in the 100% duty factor mode.

stripper. Our calculations indicate that 80% or more of a 15.5 MeV ^{238}U beam should be transmitted through the high energy tube after multiple scattering in a 5 μgm carbon foil stripper. Thus we have not considered multiple scattering as an important source of beam loss.

In the design of the proposed accelerator system, we have always assumed that the most probable charge state will be selected following stripping, and have used the relations of Nikolaev and Dmitriev to estimate this. The fraction of the beam predicted to be present in the most probable charge state, ranges from nearly 100% for ions lighter than mass 10 to about 17% for ^{238}U. From these fractions we have estimated the stripping transmission factors for the two-strip and three strip modes of operation described above.

For operation of the accelerator system with two strippers (S1 and S3) the stripping transmission factors are 17.1% for ^{16}O, 9.4% for ^{48}Ca, 6.6% for ^{76}Ge, 5.3% for ^{100}Mo, 3.4% for ^{186}W, and 2.9% for ^{238}U. For operation with all three strippers (S1, S2, and S3), which gives higher energies for the heavier ions, the stripping transmission factors are 7.2% for ^{16}O, 2.9% for ^{48}Ca, 1.6% for ^{76}Ge, 1.3% for ^{100}Mo, 0.64% for ^{186}W, and 0.49% for ^{238}U.

Table 1.5-1. Performance of Proposed Spiral Resonator Postaccelerator in 20% Duty Factor Pulsed Operation.

Type of Ion		Tandem Alone (1-strip)		Level A (2-strip)		Level C (2-strip)		Level H (2-strip)		Level H (3-strip)	
		E MeV	E/A MeV/nucl	E MeV	E/A MeV/nucl	E MeV	E/A MeV/nucl	E MeV	E/A MeV/nucl	E MeV	E/A MeV/nucl
^{1}H	2-stage Injection	18.0	18.0	23.7	23.7	30.6	30.6	41.1	41.1	41.1	41.1
^{2}H	2-stage Injection	18.0	9.0	25.8	12.9	32.6	16.3	44.2	22.1	44.2	22.1
^{4}He	2-stage Injection	27.0	6.8	44.2	17.2	58.7	14.7	82.9	20.7	82.9	20.7
^{6}Li	2-stage Injection	36.0	6.0	62.3	10.4	86.0	14.3	121.7	20.3	121.7	20.3
^{1}H	(Uranium Barrier)	24.5	24.5	29.84	29.84	35.74	35.74	47.98	47.98	47.98	47.98
^{2}H	(Uranium Barrier)	24.5	12.25	30.86	15.43	38.91	19.45	48.45	24.23	48.45	24.23
^{12}C	(Uranium Barrier)	60.5	5.0	112.8	9.4	166.9	13.9	225.1	18.8	237.0	19.8
^{16}O	(Uranium Barrier)	69.5	4.3	127.3	8.0	204.1	12.7	284.5	17.8	297.7	18.6
^{28}Si	(Uranium Barrier)	96.5	3.5	171.9	6.1	340.5	12.2	443.3	15.9	488.7	17.5
^{48}Ca	(Uranium Barrier)	96.5	2.0	101.1	2.1	411.8	8.6	566.5	11.8	641.7	13.7
^{60}Ni	(Uranium Barrier)	114.5	1.91	120.3	2.0	529.6	8.8	746.5	12.4	790.2	13.2
^{76}Ge	3-stage Injection	114.5	1.51	117.3	1.54	209.9	2.8	850.0	11.2	929.9	12.2
^{90}Zr	3-stage Injection	114.5	1.27	117.3	1.30	130.4	1.45	985.4	11.0	1109.1	12.3
^{124}Sn	3-stage Injection	114.5	.92	127.0	1.02	132.2	1.07	1132.5	9.1	1371.5	11.1
^{154}Sm	3-stage Injection	123.5	.80	134.8	.88	140.8	.91	1143.2	8.2	1633.8	10.6
^{186}W	3-stage Injection	123.5	.66	129.7	.70	139.4	.75	1172.5	6.3	1837.1	9.9
^{208}Pb	3-stage Injection	123.5	.59	133.6	.64	145.0	.70	619.7	3.0	1980.8	9.5
^{238}U	3-stage Injection	123.5	.52	127.1	.53	147.2	.62	290.6	1.2	2090.9	8.8
Power Required				280 KW		680 KW		1280 KW		1280 KW	
Effective Accelerating Potential for Optimum Ion				8.8 MV for ^{9}Be		21.7 MV for ^{46}Ca		44.1 MV for ^{124}Sn		44.8 MV for ^{238}U	

Table 1.5-2. Performance of Proposed Spiral Resonator Postaccelerator in Continuous Operation.

Type of Ion		Tandem Alone (1-strip)		Level A (2-strip)		Level C (2-strip)		Level H (2-strip)		Level H (3-strip)	
		E MeV	E/A MeV/nucl	E MeV	E/A MeV/nucl	E MeV	E/A MeV/nucl	E MeV	E/A MeV/nucl	E MeV	E/A MeV/nucl
^{1}H	2-stage Injector	18.0	18.0	20.6	20.6	23.9	23.9	27.4	27.4	27.4	27.4
^{2}H		18.0	9.0	21.7	10.9	25.0	12.5	30.4	15.2	30.4	15.2
^{4}He		27.0	6.8	35.0	8.8	43.6	10.9	53.2	13.3	53.2	13.3
^{6}Li		36.0	6.0	48.0	8.0	62.3	10.4	76.0	12.7	76.0	12.7
^{1}H	3-stage Injector (Uranium Barrier)	24.5	26.94	26.94	26.94	29.79	29.79	34.33	34.33	34.33	34.33
^{2}H		24.5	12.25	27.53	13.76	30.94	15.47	35.89	17.95	35.89	17.95
^{12}C		60.5	5.0	83.3	6.9	118.1	9.1	128.8	10.7	142.0	11.8
^{16}O		69.5	4.3	92.7	5.8	138.0	8.6	165.1	10.3	170.9	10.7
^{28}Si		96.5	3.5	121.3	4.3	216.3	7.7	265.4	9.5	274.6	9.8
^{48}Ca		96.5	2.0	98.6	2.1	171.9	3.6	360.5	7.5	374.8	7.8
^{60}Ni		114.5	1.91	117.1	2.0	201.4	3.4	422.7	7.1	489.1	8.2
^{76}Ge		114.5	1.51	115.8	1.52	126.7	1.67	431.7	5.7	539.9	7.2
^{90}Zr		114.5	1.27	115.7	1.29	120.3	1.34	435.3	4.8	636.1	7.1
^{124}Sn		114.5	.92	120.4	.97	123.2	.99	255.6	2.1	672.3	5.4
^{154}Sm		123.5	.80	127.8	.83	130.6	.85	228.6	1.48	713.0	4.6
^{186}W		123.5	.66	126.7	.68	132.1	.71	198.2	1.07	608.3	3.3
^{208}Pb		123.5	.59	128.0	.62	134.4	.65	181.5	.87	492.1	2.4
^{238}U		123.5	.52	124.9	.52	130.7	.55	171.3	.72	356.8	1.50
Power Required				280 KW		680 KW		1280 KW		1280 KW	
Effective Accelerating Potential for Optimum Ion				4.0 MV for ^{7}Li		10.0 MV for ^{25}Mg		17.9 MV for ^{48}Ca		19.0 MV for ^{400}Mo	

The efficiency of the chopper/buncher system, as discussed in Sec. 3.4 will be at least 30% and could be as high as the 77% estimated for the Unilac buncher which is similar in design. The efficiency expected when operating in the macro-pulsed 20% duty factor mode will be at least 20% and could become 60% or more by employing ion source pulsing, as discussed in Sec. 2.3. Thus, if we take the lowest estimates of buncher and 20% duty factor efficiencies, then for DC input beam of 10 microamp from the ion source the limits of beam intensity in the highest and lowest intensity modes will be as follows: for ^{16}O the beam intensity should be about 513 particle-nanoamps (p-nA) in the two stripper mode with continuous operation (2-strip; 100%) and 43 p-nA (3-strip; 20%); for the ^{238}U beam the intensities should be 87 p-namp (2-strip; 100%) and 3 p-nA (3-strip; 20%). Other beams and operating modes can be calculated from the numbers given above and will lie between these limits. These intensities, while not as large as those quoted for larger machines, appear quite adequate for a wide variety of experiments. We note also that most of the heavy ion experiments presently performed with tandem accelerators use intensities which are exactly in this range.

The energy resolution of the final beam depends on stripper straggling, broadening in the buncher, variation of the accelerating field, broadening due to phase stabilization, and debunching effectiveness. The dominant effect in limiting energy resolution in the present accelerator design is the control of electric field variations during acceleration. It is assumed that the fields can be regulated to 0.5% which implies a $\Delta E/E$ of 2×10^{-3}. The effectiveness of the debuncher in converting time resolution to energy resolution is estimated to give an "improvement factor" of 3 to 5, which implies an energy resolution after debunching of below 10^{-3}. It is possible that better regulation of the electric field can be achieved, but even if this is the case the other sources of resolution degradation mentioned above will become more important, so that the limiting resolution will still be in the 10^{-3} to 10^{-4} range.

Another important feature of the proposed postaccelerator is its capability of delivering very well bunched beams to a target for time of flight measurements. This mode is an important one for heavy ion experiments when used with a large scattering chamber such as our 60" chamber, for it offers an excellent method of distinguishing between particles of different masses which are produced in a nuclear reaction. The debuncher system may be operated in such a way as to further compress the excellent beam bunch produced by the postaccelerator and deliver it to the target with a time resolution of 20 to 50 picosec. The chopper is capable of "weeding" the beam so that, at the expense of intensity, the beam bunches can be altered in repetition rate in steps of two down to very long separation intervals without degradation of this time resolution.

1.6 Measurements of the Properties of Spiral Resonator Cavities

J.G. Cramer and D. Chamberlin

As mentioned in Sec. 1.5, we have obtained on loan from the Los Alamos group their prototype triple resonator cavity which had been used in their full power tests. We have purchased several items of test equipment and have begun a series of measurements aimed at a more complete determination of the properties

of the properties of the cavities, particularly when they are operated on the normal modes not studied by the Los Alamos group. The properties of interest are the resonant frequencies and Q's of the cavity in its three normal modes, the electric field profile of the cavity in these modes, and the shunt impedances of these modes, as obtained from the latter measurements. Figure 1.6-1 shows preliminary field mappings of the electric field in the three normal modes. The signs attached to the peaks indicate the relative sign of the field peaks, as determined by applying extra side conditions to the cavity by electrically grounding or connecting resonator units. These mappings were produced by the bead perturbation technique. A sapphire bead was suspended from a string passing along the axis of the cavity and pulled slowly through the cavity while it was driven on resonance in one of the three normal modes. A vector voltmeter was used to measure the phase difference between the driving signal and the field in the cavity, as picked up on a small pickup antenna at the cavity wall. The phase shift vs position was plotted by an analog plotter as the bead was pulled along by an electric motor, giving a direct estimate of the relative field strength at various points along the cavity axis.

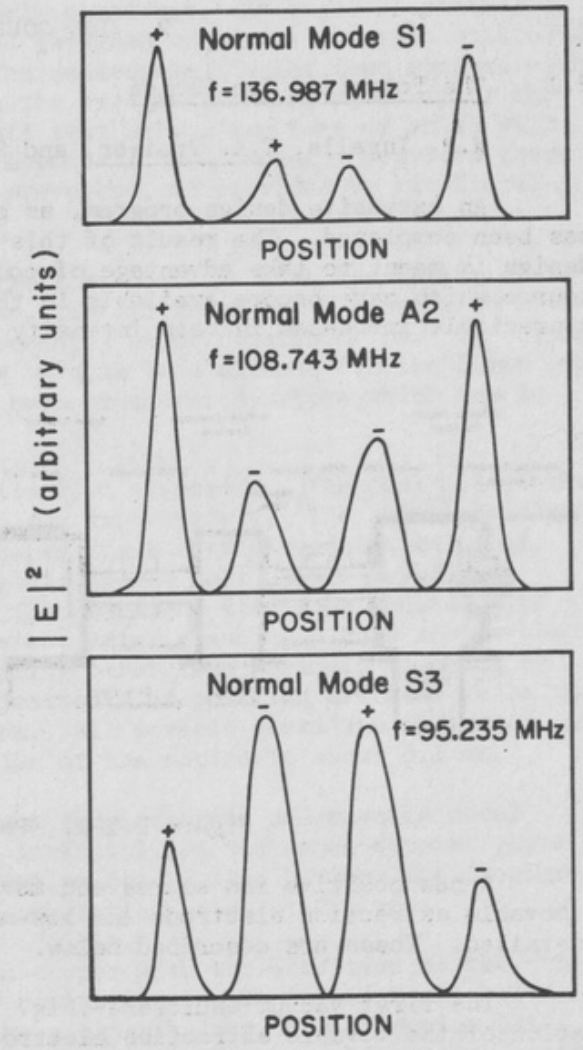

Fig. 1.6-1. Field maps of electric field in triple spiral resonator RF cavity in all normal modes.

We now have under construction a more flexible model cavity which should be electrically identical to the Los Alamos cavity, except that the various elements are attached with screws so that they can be removed, inverted, or modified. We will be able to obtain a full set of data on the cavity with this model, from which a better mathematical model of the system can be deduced.

2. ION SOURCE DEVELOPMENT

2.1 The Polarized Ion Source

W.B. Ingalls, T.A. Trainor, and Staff

An extensive design program, as outlined in the Annual Report last year,[1] has been completed. The result of this work is shown in Fig. 2.1-1. The new design is meant to take advantage of construction principles for a polarized ion source which have become available in the last few years and which have yielded appreciable increases in beam intensity and polarization.

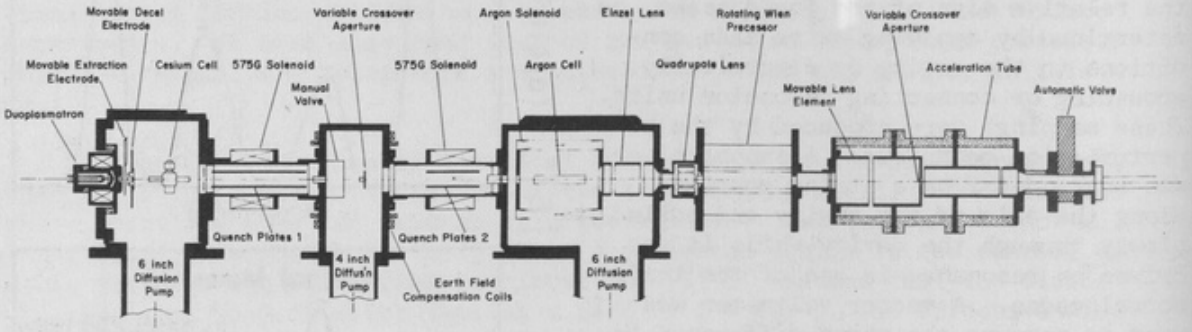

Figure 2.1-1. Polarized Ion Source.

A new positive ion source and movable decel electrode assembly, as well as a movable extraction electrode and low-mass cesium oven have been completed and installed. These are described below.

The first vacuum enclosure (Fig. 2.1-1) has been modified to allow installation of the movable extraction electrode. In addition ports have been enlarged to provide better access to the interior and the support structure has been altered to provide easier and more permanent alignment.

The second vacuum enclosure or crossover box is nearly complete. This provides badly needed pumping in the 150 cm long region between the cesium and argon change exchange cells. A manual valve is included to isolate the duoplasmatron for servicing. Two transverse Helmholtz coil pairs are mounted on the outside to cancel transverse fields at the magnetic field crossover region, and a longitudinal pair allows adjustment of the longitudinal field gradient at the crossover.

The third vacuum enclosure, or argon box, is still in the design stage. However, the general features are as shown in the figure. A large diameter Einzel lens, partially screened to improve argon pumping, immediately follows a 2.54 cm diam × 15.24 cm long argon cell. The argon solenoid has removable flux-return end plates to provide a low-field region for production of tensor polarized deuteron beams and to minimize the magnetic field inside the Einzel lens.

The rotating Wien precessor is nearly completed. It is shown partially assembled in Fig. 2.1-2. The precessor is designed to rotate the spin axis of a 1 kV deuteron beam through about 150°. The quadrupole singlet lens rotates with the precessor and is included to minimize the astigmatic focal property of the precessor. Ion optic calculations indicate that only a few tens of volts will be required on the singlet for maximum precessor field strengths provided there is a beam crossover at the center of the precessor, as provided by the Einzel lens.

Mechanical drawings for the acceleration tube have been completed, with the exception of the last accelerating gap, the design of which depends on modifications to the tandem optical system presently under consideration. The design includes two independent focusing gaps, a movable lens element for the first gap to provide beam steering, and a variable beam crossover aperture which may be used to maximize the beam quality (IP^2).

Figure 2.1-3 shows the movable extraction electrode. The position of the electrode (at left) is adjustable axially and transversely. The axial position is altered by the action of two rollers squeezing a spring-loaded steel cone. The epoxy insulator (shown with its protective cover partially removed) is capable of withstanding at least 25 kV. The electrode itself is mounted with dowel pins to insure reproducible replacement after cleaning. This device has operated for about one year without servicing other than periodic cleaning of deposited cesium from the electrode. Adjustments of position are made while the source is operating by means of nylon rods. All movable parts are supported on teflon pads to reduce friction. Resolution of the motion is about 0.1 mm.

Figures 2.1-4 and 2.1-5 show the new duoplasmatron and movable decel assembly with the low-mass cesium cell. In Fig. 2.1-4 the decel support plate and eccentric mechanisms for transverse motion can be seen between the duoplasmatron and cesium cell. This system has a resolution of about 0.5 mm.

The cesium cell is fabricated from copper with the exception of the stainless steel flare-fitting for addition of cesium and the stainless steel valve stem. The cell weighs about 600 g and has a capacity for 60 g of cesium (although a 15 or 25 g portion is usually used). The low mass combined with a 150 watt heater and freon cooled tab (at rear) allow a response time of about 30 seconds to adjustment of the heater power. This fast response time coupled with purchase of a commercial proportioning temperature controller provide stable operation and easy adjustment of cesium vapor density while the ion source is at high voltage.

Figure 2.1-5 shows the rear of the duoplasmatron with the gear drives for the eccentric mechanisms. Axial position of the decel electrode is determined by a screw, with opposing spring loading, at upper left in the figure. Also shown is the pyrex filament holder which allows inspection of the filament and condition of the arc.

The new duoplasmatron presently uses a 70° cone extraction and decel geometry with a 6.3 mm diameter aperture in the extraction electrode. It produces 15-20 mA proton beams and 20-25 mA deuteron beams with about 10 A arc current. The ion source has operated without a magnetic lens following the decel electrode

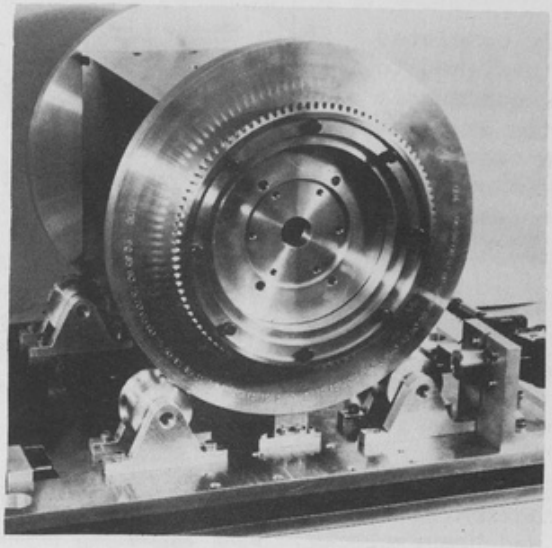

Fig. 2.1-2. Rotating Wien Precessor Partially Assembled.

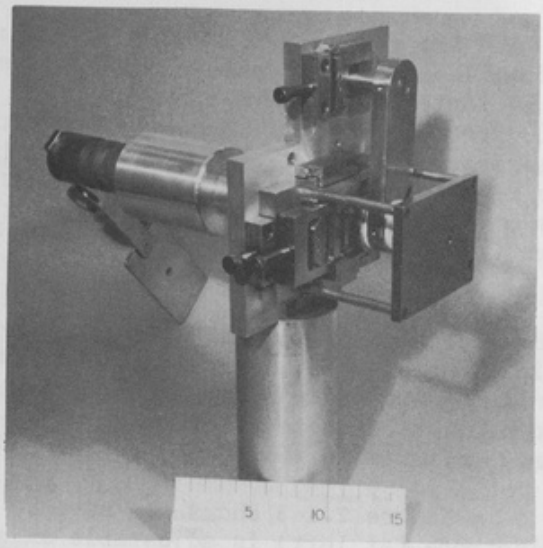

Fig. 2.1-3. Movable Extraction Electrode.

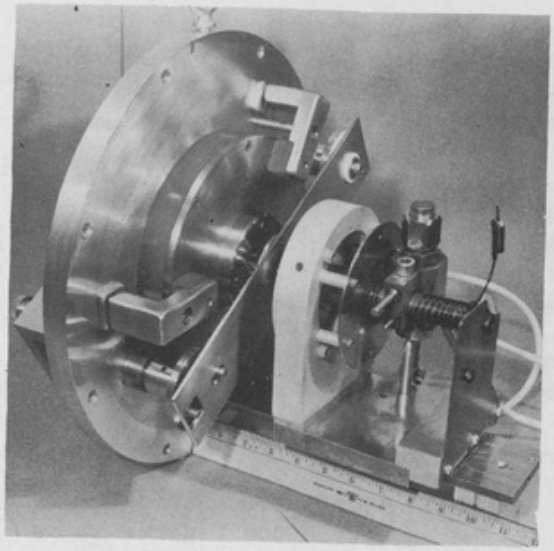

Fig. 2.1-4. Front View of Duoplasmatron and Cesium Cell.

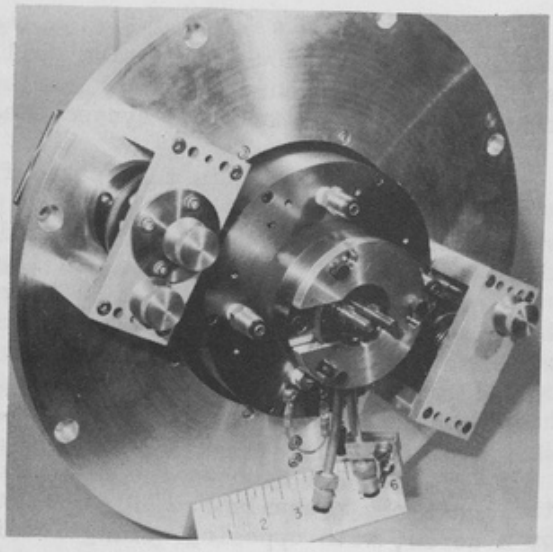

Fig. 2.1-5. Rear View of Duoplasmatron.

for about two years. Experience has shown that it is very difficult to achieve consistent polarized source performance in this mode without movable electrodes and a well regulated cesium cell such as those described here. Slight variations in cesium density affect the space-charge distribution, and therefore the focusin and steering, in the decel region. Further stability has been achieved by placin a freon-cooled copper baffle between the cesium cell and extraction region.

The polarized source presently produces on-target beams of 20-40 nA for protons with 60-70% polarization and 40-60 nA for vector-polarized deuterons with 70-80% of maximum (0.67) beam polarization.

---

1. Nuclear Physics Laboratory Annual Report, University of Washington (1974), p. 13.

2.2 The Terminal Ion Source

G.W. Roth and Staff

The terminal ion source for the injector stage of the three-stage Van de Graaff has been completed and has been used routinely for experiments over the past year.

All design objectives have been achieved with the one exception mentioned below.

(a) The variety of beams from the injector has been greatly increased. Beams used for experiments include protons, deuterons, oxygen, carbon and nitrogen ions. Additional beams common to direct extraction ion sources can be obtained if requested by simply adding appropriate gas bottles in the terminal.

(b) Protons have been observed with a maximum intensity of 8 μa and all of the other ions have intensities of 1-5 μa. The previous injector source produced only protons and deuterons with intensities typically 0.3 to 0.5 μa.

(c) Stripper efficiency for heavy ions as they pass through the tandem terminal has been increased. For example the most probable charge state for oxygen using the injector is about one charge higher than when using the tandem alone.

(d) Reliability has been very good. Terminal sparking has caused no failures to electronic components including the transistors in the terminal. The only spark-related failure was a burned out source aperture due to an extraction supply surge. This supply has now been current-limited.

(e) Ease of operation has been emphasized in the design, making it possible to start the source in a matter of minutes completely from the central console.

(f) The design objective which has not been achieved is an increase in the injector maximum terminal voltage. It was hoped that removal of the four

accelerator tube sections along the low energy column would allow the machine to achieve higher terminal voltage. These tubes were quite badly damaged from radiation and spark tracks and limited the voltage to about 6.5 MV. Voltage now is limited by terminal sparking to less than 7 MV rather than the 8 MV that was hoped for. Dust and moisture in the tank gas appear to cause charge to leak from the terminal. This results in unstable terminal voltage and eventually tank sparks.

The source has operated about 1100 hours since installation in the accelerator. A second duoplasmatron has been constructed so that one source can be cleaned, repaired and checked out on the source test stand while the other is operating in the accelerator. This extra duoplasmatron also serves as a spare source for the tandem.

2.3 The Sputter Ion Source

G.W. Roth and Staff

A sputter ion source has been purchased by the Laboratory this past year to increase the variety of heavy ion beams available from the tandem accelerator. The source was a Mark VII UNIS purchased from Extrion Corporation.[1]

Beams that have been accelerated so far are listed in Table 2.3-1. Also shown there are the source output intensities and the transmissions through the accelerator.

Table 2.3-1. Sputter Source Output and Accelerator Transmission

Particle	Source Output	Accelerator Transmission
P	< 1 μa	20%
Li	1 μa	15%
C	20 μa	15%
O	30 μa	15%
Al	0.2 μa	10%
Si	2-3 μa	10%
Ag	1 μa	2-3%
Pb	0.5 μa	< .1%

---

1. Extrion Corporation, Box 1226, Blackburn Industrial Park, Glouster, Ma 01930.

2.4 Ion Source Test Stand

G.W. Roth

Tight scheduling of beam time and the growing number of ion sources in the Laboratory have made it desirable to acquire an off-line ion source test stand. Various equipment available for several years has been brought together to make a general purpose test facility. The system consists of a pump tee with a 1500 ℓ/s diffusion pump, on which can be mounted any laboratory source except the present helium source. The tee is followed by an analyzing magnet with outputs to left and right at 30°. One output is used for a Faraday cup and the other for an emittance measuring device now under construction. Power supplies salvaged from the old injector neutral ion source are used to operate the sources. These are remotely controllable from outside a wire cage which encloses the power supplies and ion source that operate at high voltage. A freon heat exchanger as well as water are available for source cooling.

A number of uses have been found for this facility. The duoplasmatron sources for both the tandem and injector are routinely checked out after major cleaning or repair and are known to be operating well before being installed on the accelerator. New particle types can be tried in the duoplasmatron and experiments can be planned on the basis of beam intensities achieved on the test stand without taking up accelerator time. The purchase this year of a sputter ion source (see Sec. 2.3) has led to use of the test stand for initial source testing and for development of about a dozen new heavy ion beams.

Finally, new ion sources can be developed on the stand without interfering with the experimental program.

3. INSTRUMENTATION, DETECTORS, RESEARCH TECHNIQUES

3.1 Silicon Detectors

Shirley Kellenbarger

Our method[1] for making surface barrier detectors to use in "sideless" configurations has now been modified by the addition of an HF treatment, a sodium dichromate treatment of the face, and the use of Dow Corning 3140 RTV silicone rubber (DC 3140) instead of p-type epoxy for edge protection of the face. The silicon is etched as before and then is immersed in HF for one minute. After diluting the HF with deionized water and rinsing well with more water, the detector is mounted in the circuit board frame with DC 3140. It is left overnight to allow the DC 3140 to cure, and is then placed under a heat lamp for 10 minutes with the face covered with a 1% aqueous solution of sodium dichromate. The dichromate is rinsed off with plenty of deionized water, and a bead of DC 3140, rather than the p-type epoxy previously used, is immediately applied to the edge of the face. After again leaving overnight to cure, a bead of p-type epoxy is run over the DC 3140 to connect the silicon surface and the copper-covered circuit board. Gold is later evaporated on this bead resulting in a reliable ground.

These modifications were suggested to us by Gigane and Lundgren's recent article.[2] Prior to using the dichromate, some detectors were performing poorly when used for heavy ions, with characteristics indicative of surface multiplication.[3] Since using the dichromate, the problem has disappeared. Not all detector makers have found it advantageous to use the dichromate treatment, but immersion of the detector in the dichromate rather than its application only to the face may account for some of their poor results. This seems reasonable since the theory behind the dichromate treatment involves the provision of a p-type surface. This surface is wanted on the face side only.

Trapping problems exhibited by several detectors were remedied by redrifting for 24 to 48 hours at 80° C with 500 volts bias. Three new detectors needing this treatment represented about one-fourth of the production from one particular ingot. Two others from two other ingots had developed trapping problems after some use.

---

1. Nuclear Physics Laboratory Annual Report, University of Washington (1974), p. 23.
2. J.R. Gigante and R.A. Lundgren, IEEE Trans. Nucl. Sci. *NS-21* (No. 1), 395 (1974).
3. F.J. Walter, IEEE Trans. Nucl. Sci. *NS-11* (No. 3), 232 (1964).

3.2 A Large Solid Angle Gas Cell Detector System

Y-d Chan, J.G. Cramer, K-L Liu, and B.A. Scott

I. Introduction

A gas cell-detector system with a large particle collection efficiency has been constructed for use mainly in Heavy Ion experiments.

The major difference between this and a conventional gas cell design is that the detectors are mounted inside instead of outside of the cell. They are also aligned with their planes close to and parallel to the beam axis. Consequences of this particular configuration are:

1. We get rid of the particle exit foil window that reaction products must otherwise pass through before they reach the detectors. This is desirable for heavy ions since the energy loss in passing through a foil is large.

2. The detector solid angles can be made very large. Hence the design is very suitable for experiments with small cross sections.

3. The detectors have to be operated under target gas pressure.

II. Construction

Major parts of the gas cell are made of brass. The detectors we used are the large area rectanglar sideless surface barrier silicon detectors made in this laboratory.[1]

A schematic drawing of the gas cell and a picture of it are shown in Fig. 3.2-1.

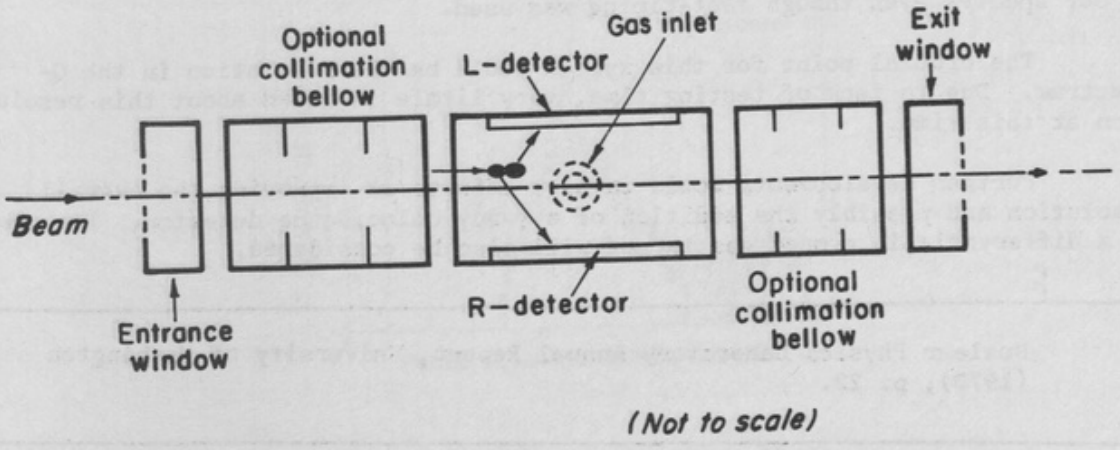

Fig. 3.2-1. Schematic drawing of the gas cell-detector system.

III. Method of Detection and Preliminary Test Results

Two large area, rectangular detectors (left and right) are mounted in symmetric positions facing each other inside the cell. After an event, the energy information of the 2-particle channel products are recorded by these two detectors separately. These two signals are then summed to form a Q-spectrum. The Q-value for any particular event can be obtained from the energy conserva tion relation

$$Q = (E_L + E_R) - E_{inc}$$

where E_{inc} is the energy of the incoming beam.

With appropriate gating on the Q-spectra, one can pick out specific channels of interest, and the following quantity can be measured:

$$\langle\sigma\rangle_{Q,\Delta\theta,\Delta\phi} = \int_{\theta_{min}}^{\theta_{max}} \frac{d\sigma}{d\Omega}(Q,\theta,\phi)d\theta\Delta\phi$$

Here $\Delta\theta \equiv \theta_{max} - \theta_{min}$ and $\Delta\phi$ are the geometrical angles determined by the detector pair.

From kinematic relations, one can also do angular distributions for identical products quite easily.

The gas cell has been tested with an ^{16}O beam and various gas targets, including ^{4}He, ^{14}N, ^{16}O, and Ar.

Preliminary results (Figs.3.2-2, 3.2-3, and 3.2-4) show that contributions from background scattering of the foil and cell are quite significant and, as one would expect, high counting rates caused pile-ups and accidentals in our spectra even though fast-timing was used.

The crucial point for this system would be the resolution in the Q-spectrum. Due to lack of testing time, very little is known about this resolution at this time.

Further developments would involve efforts at improving the overall resolution and possibly the addition of a γ-ray coincidence detector. The use of a differentially pumped gas target will also be considered.

---

1. Nuclear Physics Laboratory Annual Report, University of Washington (1973), p. 22.

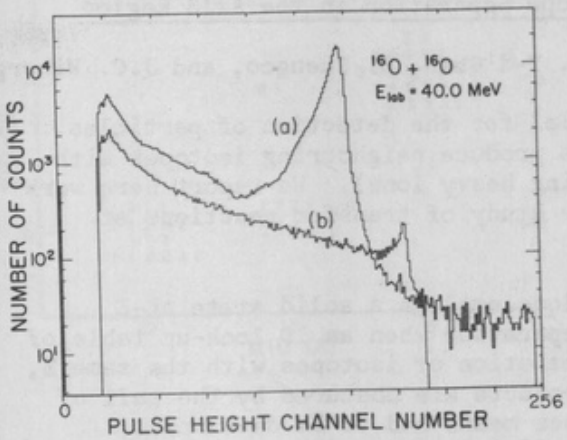

Fig. 3.2-2. Singles spectra without coincidence showing the comparison between (a) pressure of target gas (oxygen) = 7.0 cm Hg and (b) no target gas. (The small peak shown may be due to a small amount of residual gas that was left inside the cell.) The reaction is $^{16}O + ^{16}O$.

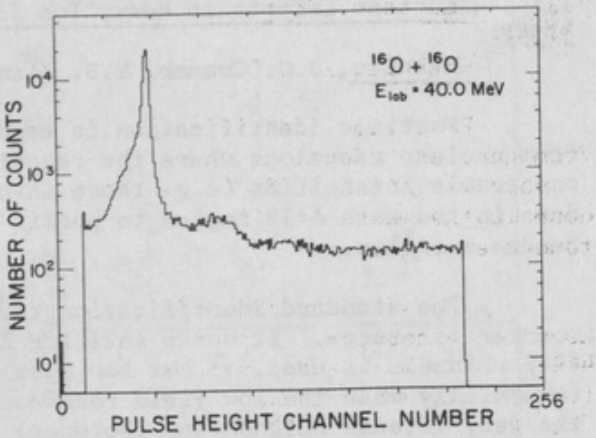

Fig. 3.2-3. TAC spectrum from the left and right detectors ($^{16}O + ^{16}O$).

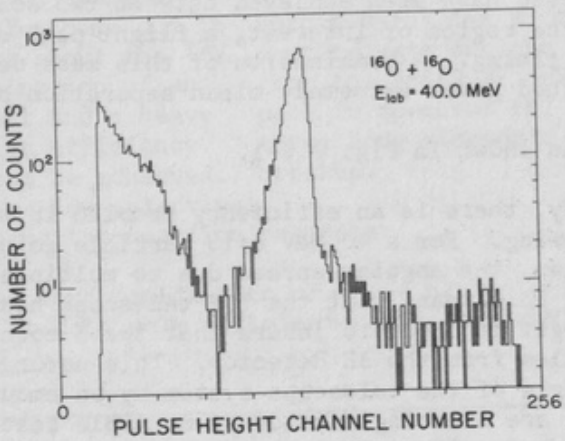

Fig. 3.2-4. The same singles spectrum of fig. 3.2-3(a) but gated by the TAC. (The spectrum was taken by another ADC.)

3.3 Further Efforts in Heavy Ion Isotope Separation in the A=13 Region

K-L Liu, J.G. Cramer, M.S. Zisman, Y-d Chan, B. Cuengco, and J.C. Wiborg

Particle identification is essential for the detection of particles from nuclear reactions where the reactions produce neighboring isotopes with comparable intensities (e.g. those involving heavy ions). We report here work done in the mass A=13 region to permit the study of transfer reactions at tandem energies.

The standard identification technique employs a solid state ΔE-E counter telescope. It works well for Z separation when an ID look-up table of 4096 channels is used,[1,2] but for mass separation of isotopes with the same Z, (expecially when the low yield reaction products are obscured by the tail of the very intense neighboring isotopes) other means had to be developed.

The transmission ΔE detectors available in the laboratory which are useful for our purpose are 10.5 um, 11.2 um and 14.3 um thick. It was found experimentally that none of these has FWHM energy resolution better than 5% for heavy ion detection. Part of this is due to the energy straggling produced in the 'Stochastic Region',[3] and most of the rest can be explained by thickness inhomogeneities of the thin transmission detectors. This 5% energy resolution is poor enough to destroy any mass identification separation in the region of interest. The range formula for the detected particle with energy E, charge Z and mass M is given by $R \sim E^{k} M^{1-k} Z^{-2}$. For heavy ions where $k \sim .67$, better than 5% energy resolution is required to separate isotopes in the A=13 region. Transmission detectors with better homogeneity are not readily available.

The time-of-flight technique was found to be more successful for mass separation than one based on energy loss. With fast timing electronics, time resolutions of 250 psec have been achieved between two solid state detectors. Since $MID \sim ET^2$ in the region of interest, a flight path of 25 cm is adequate to obtain the required timing. A combination of this mass determination with the conventional PID method gives extremely clean separation of both Z and M.

An example is shown in Fig. 3.3-1.

Unfortunately, there is an efficiency problem in this technique arising from multiple scattering. For a 40 MeV A=13 particle going through a 10 um thick silicon detector, the angular spread due to multiple scattering is about 1.5 degrees (FWHM). This means that the TOF telescope has to be situated further from the target in order to insure that the E counter catches most the scattered particles from the ΔE detector. This naturally reduces the solid angle of the telescope system by an amount depending on particle energy. We are starting a study of multiple scattering to find out whether we can correct for it analytically or empirically.

Kinematic coincidence requirements can be used to identify particles in specific reactions but the range where coincidences are effective is very limited. In forward angle reactions the recoil particle does not acquire enough energy to escape the target. Nevertheless, some special reactions can

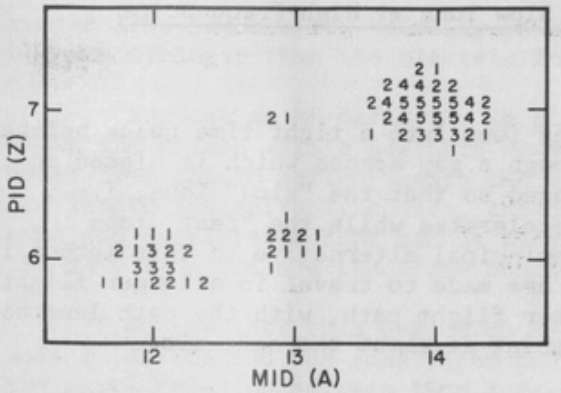

Fig. 3.3-1. PID vs MID spectrum from bombardment of 50 MeV ^{14}N on ^{12}C with the time of flight telescope at 20°. PID was done by table look-up and MID was calculated on line with program MAPID.[2] All the numbers in the spectrum are expressed in powers of 2.

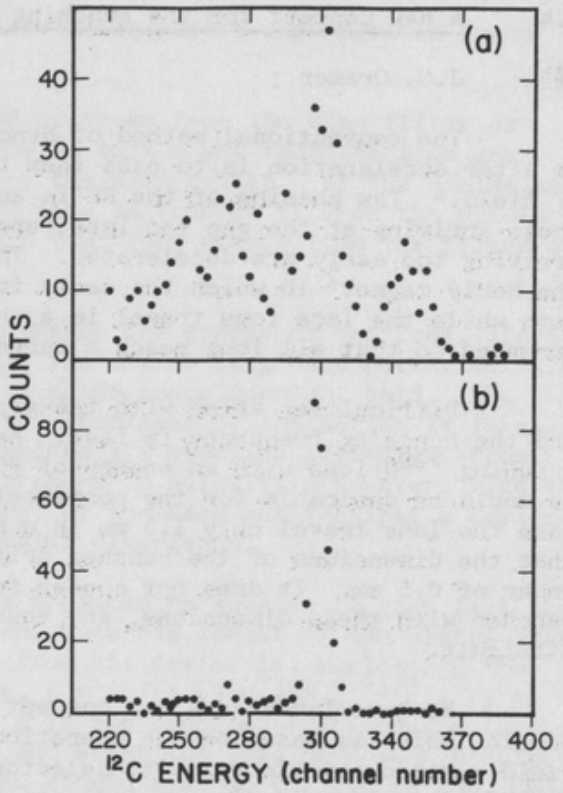

Fig. 3.3-2. Energy spectra for the $^{12}C(^{14}N,^{12}C)$ reaction at 15° for 60 MeV ^{14}N beam. Spectrum (a) is ungated and spectrum (b) has a coincidence requirement to gate out the ^{12}C not coming from the ^{13}N(2.37 MeV) breakup. The peak in spectrum (b) agrees with the three body kinematic energy of this breakup.

be studied if the reaction product is particle unstable, by looking at the break up particles. One of the reactions we studied with this technique is $^{12}C(^{14}N,^{13}N(2.37\ MeV,2s_{1/2})^{13}C$ by looking at the ^{13}N 2.37 MeV excited state which breaks up into a proton and a ^{12}C with 0.4 MeV breakup energy. Here the breakup particles come out in a relatively narrow cone about the ^{13}N direction. With a combination of an annular detector in front and a heavy ion detector behind, high efficiency coincidence detection can be achieved. Figure 3.3-2 demonstrates how selective this method is in choosing the reaction products.

It is hoped that some combination of these particle identification methods will enable us to do highly efficient particle identification in the mass region of interest.

---

1. Nuclear Physics Laboratory Annual Report, University of Washington (1974), p. 24.
2. See Sec. 4.4 of this report.
3. C. Tschlär, Nucl. Instrum. Methods *61*, 141 (1968).

3.4 A New Concept for the Bunching of Slow Ions at High Frequencies

J.G. Cramer

The conventional method of bunching ions into a tight time pulse before or after acceleration is to pass them through a gap across which is placed an RF field.[1] The phasing of the RF is arranged so that the "slow" ions, i.e., those arriving at the gap too late, are accelerated while the "fast" ions arriving too early are decelerated. The principal alternative to this method is the Mobly magnet[2] in which the early ions are made to travel in a longer flight path while the late ions travel in a shorter flight path, with the path lengths arranged so that all ions reach a target point at about the same time.

Difficulties arise with the gap buncher scheme when the ions are slow and the bunching frequency is fast. As an example, consider the problem of bunching ^{238}U ions with an energy of 80 keV at a bunching frequency of 100 MHZ, as would be desirable for the postaccelerator discussed in Sec. 1.5. In this case the ions travel only 1.3 mm in a half cycle of the bunching frequency, so that the dimensions of the buncher drift tubes and gaps would have to be on the order of 0.5 mm. It does not appear feasible to design a conventional gap buncher with these dimensions, and thus the problem of bunching such beams is difficult.

We have invented a new concept (we think) for bunching of beams in this domain, which is based on the operation of the Wien filter, i.e. the crossed-field electromagnetic velocity selector. Figure 3.4-1 shows such a device. The dashed lines in this diagram indicate the equipotential surfaces produced by the electric field plates. Notice that a negatively charged particle entering this device above the center line and travelling parallel to the axis of symmetry will be decelerated by entering a region of negative electric potential. It will also be deflected toward the center line, since, when its velocity is lowered the magnetic force on the particle becomes weaker than the electric force. Similarly, a particle below the center line will be accelerated on entering a region of more positive potential and also deflected toward the

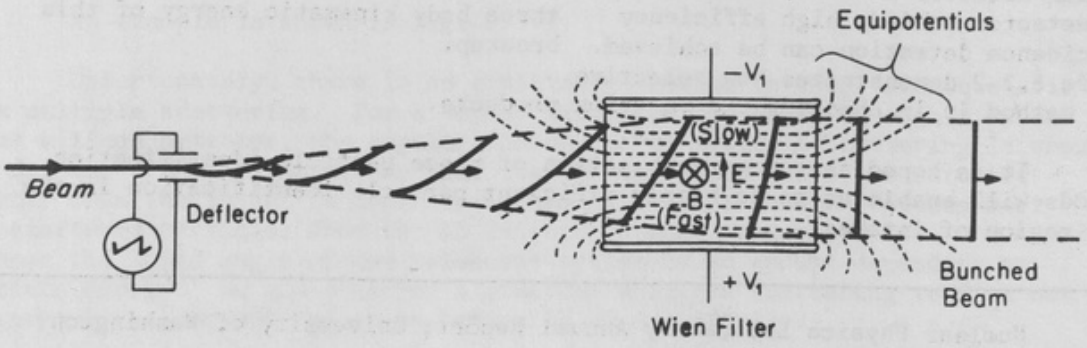

Fig. 3.4-1. Operation of Bunching with a Wien Filter.

center line because its velocity is higher and therefore the magnetic force becomes stronger than the electric force.

Suppose an RF deflector is placed upstream from the Wien filter as shown and driven with a sawtooth wave form in such a way that the ions are swept from top to bottom across the gap of the Wien filter. If the fields and the length are suitably chosen, the difference in transit time of the accelerated and decelerated ions can be made such that they emerge from the filter at the same time and are therefore bunched.

Notice that this device does not change the energy of the ions, since it is a DC device and the ions enter and exit the device at ground potential. Thus the usual relation between time and energy phase space does not hold. The radial phase space of the beam is, however, increased by the action it is analogous to a "linear" Mobly buncher, but derives its bunching action not from differences in path length but from differences in velocity. However, like the Mobly buncher it does not change the energy of the beam but requires a deflector which introduces a time-dependent angular divergence.

If we assume that the defelection produced is such as to just fill the gap of the Wien filter with deflected beam, then the length of the plates such that the beam is bunched when it emerges from the device is, neglecting the cylindrical lens effect referred to above, $L = (c/f)\,(2eV_o/AM_{nuc})^{1/2}V_o/V_1 = \lambda V_o/V_1$ where c is the velocity of light, f is the bunching frequency, e is the electron charge, V_o is the potential through which the ions have been accelerated before reaching the buncher, A is the atomic mass of the ion in AMU, M_{nuc} is the nucleon mass energy in MeV, V_1 is half the potential difference between the plates of the Wien filter, i.e., the potential of either plate with respect to ground and λ is the spatial wavelength of the deflected beam. As an example, with A = 238, V_o = 80 keV, and V_1 = 1 keV, we obtain L = 8.8 cm. Thus the dimensions of this device are quite reasonable, and if one wished to make it somewhat longer, say 20 cm, this could be done by using only the central 44% of the total gap of the Wien instead of filling it.

One obvious limitation of the effectiveness of this device is that the deflection employed must be large compared to the diameter of the beam. Thus the optimum place for such a buncher is at a crossover point, where the beam has a minimum diameter. Since the cylindrical lens effect of the Wien is such as to deflect the beam toward the center as it passes through, the bunching action will be somewhat diminished by this effect. If one wishes the action of the cylindrical lens to correct for the deflection produced by the upstream deflector, then the gap of the Wien filter should be $h = (V_1/2V_o)(LD)^{1/2}$ where D is the distance from the deflector to the Wien filter. If this criterion is used, the beam will emerge from the Wien filter as a parallel beam.

We are considering the use of this device as the low energy buncher for use with the proposed postaccelerator. We have not yet completely evaluated the effect of the vertical (or horizontal if the E field is oriented that way) angular divergence of the beam introduced by this device on the emittance, and transmission of the beam through the tandem.

It should be noted that when this device is operated with polarized beams, it will act to precess the spin of ions in transit unless the spin and the B field are parallel. This effect can be corrected by properly choosing the spin orientation of the beam so as to compensate for this precession, but some depolarization will probably occur due to diferent transit times through the B field.

---

1. H.W. Lefevre, R.C. Borchers, and C.H. Poppe, Rev. Sci. Instrum. *33*, 1231 (1962).
2. R.C. Mobley, Phys. Rev. *88*, 360 (1952).

3.5 A Suggestion for the Design of a Charge-State "Enforcer" for Heavy Ion Accelerators

J.G. Cramer

A common problem among all heavy ion accelerators thus far designed is that of charge changing. This is usually done with a stripping foil or gas, with the result that the incident beam of ions is fractionated into a distribution of charge states, each component of which has different acceleration properties. Since an accelerator must produce a beam with a unique energy, only one of these charge states may be used and the others are lost. The charge state used is chosen not to give the optimum performance from the accelerator but to have a fairly high probability of being formed. Even if the most probable charge state is used however, its fraction is not large for heavy ions, ranging from about 41% for ^{16}O to 17% for uranium. Clearly, this situation is far from ideal, and what one would really like is a device which would strip all of the beam into any desired charge state. Such a device is proposed here, and we christen it a *charge state enforcer*.

Figure 3.5-1 shows the operation of this device. A beam of particles in a very low charge state enters from the right, and enters an intense magnetic field of about 8 Tesla produced by a superconducting solenoid. The beam strikes a thin stripper foil and is fractionated into charge states which are, on the average, of much higher charge than the incident beam. Each of these charge state groups goes into what might be called a microtron orbit,[1] and after traveling in a circular path, returns to its point of impact with the stripper foil and is stripped again. The magnetic field is adjusted so that the charge state which is to be produced is orbited between a pair of C-shaped electric deflection plates which parallel the orbit of the ion for a sizable portion of its path length. The electric field produced by the plates deflects the selected charge state sideways in its orbit, as shown in the top view portion of Fig. 3.5-1. When this charge state comes around to the stripper position, it is displaced in position enough to miss the stripper foil and pass instead into a "super tube", i.e. a tube made of superconducting material so as to act as a perfect shield against magnetic fields. When the selected charge state enters the supertube, it no longer is bent in a circular orbit by the magnetic field, but instead travels in a straight line, and exits from the device. The other

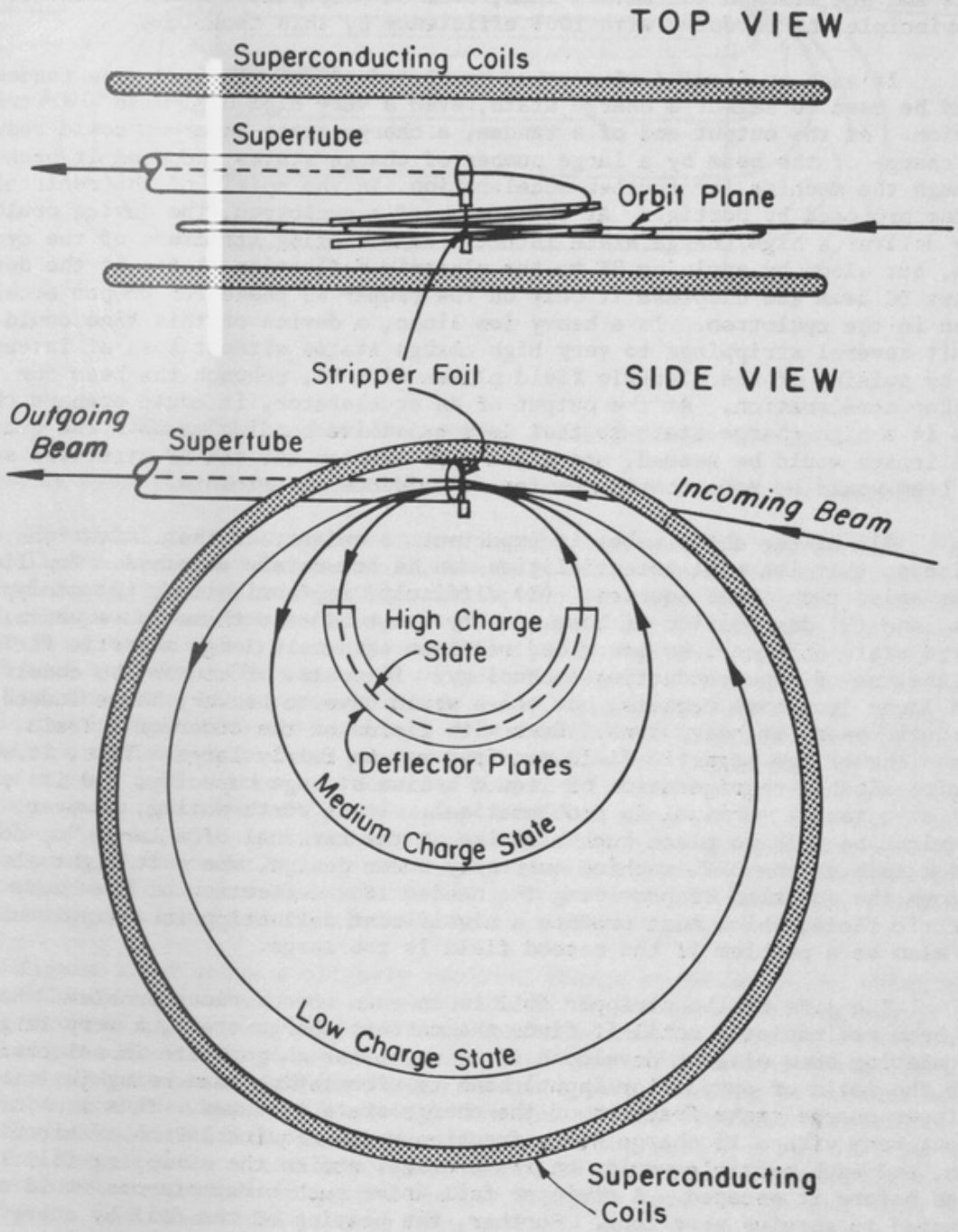

Fig. 3.5-1. Charge State Enforcer

ions are trapped in the field and are not allowed to exit until, after several collisions with the stripper foil, they are stripped into the selected charge state and are allowed to leave. Thus, even an "unpopular" charge state can, in principle, be produced with 100% efficiency by this technique.

If such an ideal device could be placed at the terminal of a tandem, it could be used to select a charge state, even a very high one, with ~100% transmission. At the output end of a tandem, a charge state enforcer could reduce the charge of the beam by a large number of charge states and send it back through the machine for further acceleration, in the spirit of the recirculating tandem proposed by Hortig.[2] At the center of a cyclotron, the device could not only deliver a high charge state into the accelerating structure of the cyclotron, but also, by applying RF to the electric deflection plates of the device, accept DC beam and dispense it only on the proper RF phase for proper acceleration in the cyclotron. In a heavy ion linac, a device of this kind could permit several strippings to very high charge states without loss of intensity, and by pulsing of the electric field plates with RF, rebunch the beam for further acceleration. At the output of an accelerator, it could prepare the beam in a high charge state so that less expensive bending magnets and quadrupole lenses would be needed, and might also average out the RF structure so that the beam would be more continuous for coincidence experiments.

All of the above makes it important to understand the limitations of the device so that its real potentialities can be accurately assessed. Its limitations arise from three sources: (1) difficulty in fabrication, (2) stripper life, and (3) degradation of beam quality. Let us take these in sequence. The charge state enforcer, as described requires extremely large magnetic fields and the use of superconducting technology. It could, of course, be constructed with large iron core magnets, but these would have to be very large indeed for energetic beams of heavy ions. Even with fields on the order of 8 Tesla, the dimensions of the magnetic field required may be fairly large. Thus, it would require sizable refrigeration of liquid helium storage capacity, and its placement at a tandem terminal is problematical. It is worth noting, however, that one might be able to place such a device at the terminal of a large "up-down" tandem such as the ORNL machine currently under design, where it might also perform the function of providing the needed 180° deflection of the beam. The electric field, which must produce a significant deflection in a single orbit, may also be a problem if the needed field is too large.

The life of the stripper foil is an even more serious problem. Because the beam recirculates until it finds the correct charge state, a very large circulating beam will be developed if an unpopular chage state is selected, with the ratio of output (or input) beam to circulating beam being just the stripper charge state fraction of the charge state selected. Thus 1 μA of an output beam with a 1% charge state fraction would require 100 μA of circulating beam, and each particle would, on the average, strike the stripping foil 100 times before it escaped. A stripper foil under such circumstances would not be expected to survive very long. Further, the heating of the foil by energy loss from the beam might cause serious problems, since this foil is placed in close proximity to the supertube. The alternative of a gas stripper does not appear particularly attractive due to the non-localization of the gas and the problems

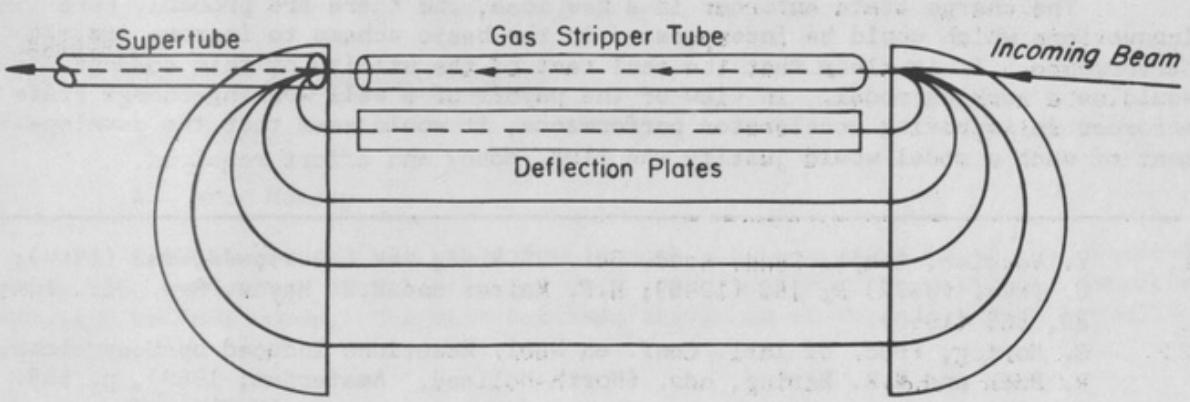

Fig. 3.5-2. Modified Charge State Enforcer Design

incurred by operating superconducting devices in a poor vacuum environment.

The third problem mentioned above is the beam quality degradation. At each collision with the stripper foil, the beam loses a somewhat uncertain amount of energy through straggeling, and at the same time is mutiply scattered through some small but non-zero angle. On repeated collisions with a stripper foil, both of these effects will be magnified, and eventually produce a serious loss of beam quality. The magnitude of this degradation depends on the average number N of times the beam passes through the stripping foil before stripping to the selected charge state. To a rough approximation the degradation of the beam will be equivalent to that produced by a foil with a thickness of Nt, where t is the actual foil thickness. We note that $N \approx [F(Q)]^{-1} - 1$, where F(Q) is the charge state fraction of Q, the charge state of interest. It is clear that when F(Q) is small, the degradation of the beam will be a serious problem. If the emittance of the exit beam or its energy spread becomes large compared to the acceptance of the accelerator into which it is injected, then considerable beam intensity or energy resolution may be lost from the final beam.

Figure 3.5-2 shows a slightly modified charge state enforcer which may provide solutions to some of the above problems. The superconducting magnet is divided into two halves, so that the beam orbits become semicircles connected with straight lines. In this arrangement, both the stripper and the electric deflection plates are outside the fields of the superconducting solenoids, and both can be stretched out. This permits the use of long straight deflection plates for the electrostatic deflector and permits the use of a gas stripper tube. The latter would still have to be pumped so that the pressure in the vicinity of the supertube was good. The gas stripper would be thinner than any useable foil, and thus would produce less multiple scattering and energy straggeling per collision. Further, with a gas stripper, foil life would no longer be a problem.

The charge state enforcer is a new idea, and there are probably more innovations which could be incorporated in the basic scheme to improve its performance. It is clear that the real test of the utility of this concept would be a working model. In view of the payoff of a well working charge state enforcer in improving accelerator performance, it would seem that the development of such a model would justify the time, money and effort required.

---

1. V. Veksler, Compt. Rend. Acad. Sci. USSR *43*, 444 (1944); *44*, 393 (1944); U. Phys. (USSR) *9*, 153 (1945); H.F. Kaiser and W.T. Mayes, Rev. Sci. Inst. *26*, 565 (1955).
2. G. Hortig, Proc. of Intl. Conf. on Nucl. Reactions Induced by Heavy Ions, R. Bock and W.R. Hering, eds. (North-Holland, Amsterdam, 1969), p. 568.

---

4. THE COMPUTER AND COMPUTING

4.1 Computer System Improvements

N.R. Cheney

A. Drum Memory

A 524K word (24 bit word) drum memory has been added to the laboratory's computing hardware. Installation of this unit increases the available drum/disc storage to 786K words. The unit was made available to the laboratory by Valley Computer Inc.

B. CRT Display

A model HP1311A CRT display has been installed on the laboratory's off-line computer. This addition has made a significant improvement in data analysis capability of the off-line computer. The unit was made available to the laboratory by Valley Computer Inc.

4.2 Updated Subroutine Library for On-Line Data Collection Programs

L.D. Knutson, R.S. Kochin, and T.A. Trainor

It was desired to develop compact subroutines for collection, storage, and display of data that could be separately and easily called from Real-Time FORTRAN data-collection programs. Seven updated subroutines written in SDS assembly language SYMBOL and separately callable from Real-Time FORTRAN were thus developed to collect singles data from the ADC's, display data on the CRT and store data on magnetic tape.

DADC is a subroutine for collecting singles data from the ADC's. It was revised from the MULTSING[1] subroutine SSADC to make it independent of other parts of MULTSING. Other changes have been made so that the data from each ADC can be stored in a separate array. DADC must be called with 10 arguments including the number of ADC's to be set-up, arrays containing the ADC numbers and sizes, the count sum array location, and six storage array locations. Like SSADC, up to 6 ADC's may be used. DADC has a second entry point, ONADC, which must be called after DADC to arm the ADC interrupts specified in the arguments for DADC.

OFADC is a short subroutine which turns off all ADC interrupts.

CLEAR is a subroutine which clears a data storage array and its associated count sum. If a data word has its intensification bit set for the CRT display, it remains set.

ONCLP and OFCLP are two short subroutines for turning on and off the CRT display 1/30 second interrupt and the light pen interrupt.

DCRT is a subroutine which displays the spectra on the CRT. It is a revised version of subroutine SHOW.[2] Changes have been made so that the channel number detected by the light pen and appropriate counts for that channel are displayed in decimal. The subroutine is further modified so that many points may be intensified simultaneously on the display for use by peak-summing subroutines.

DTAPE is a subroutine for performing operations on magnetic tape with variable-length records. It uses SDS subroutine MTAPE. Data stored on tape takes up less tape and is recorded more quickly than can be done in FORTRAN. DTAPE can be called with several options in order to read a record, write a recrod, skip records, rewind a tape, skip to End of File and write a record, or read the last record before an End of File.

The subroutines will soon be added to the UWNPL program library.

---

1. Nuclear Physics Laboratory Annual Report, University of Washington (1971), p. 62.
2. J.E. Bussoletti, N.R. Cheney, R.E. Marrs, and D.L. Oberg, private communication.

4.3 Subroutine Package for the Off-Line Display System

L. Baker, J.G. Cramer, and T.A. Trainor

A subroutine set has been prepared for use with the newly installed display hardware for the off-line computer. The set consists of subroutines SETUP and SPLAT.

Subroutine SETUP converts data to a form suitable for the display hardware and is called only when the display is to be modified. Calling arguments include a raw data array, a buffer array, and scale factors and offsets for the x and y axes specified as fractions of the total display area. In addition an extra scale factor for the y axis is included for convenience in displaying data blocks for which the normalization varies widely from block to block.

Subroutine SPLAT displays data from the buffer array prepared by SETUP and is typically called from a display loop. It presents a sequence of 24 bit words to the display hardware. Each word represents one point on a 1024 × 1024 field, and 16 discrete intensity levels are available. Cycle time for the display is about 15 μsec/point. Thus, a raster of 8K points can be displayed without objectionable flicker.

4.4 Further Development of the Particle Identification Program

K-L Liu, T.A. Trainor, and M.S. Zisman

The PID program with an exponential look-up table of 4096 words in the

memory extension was reported last year.[1] It uses the range-energy formula

$$PID = (\Delta E + E + B)^x - (E + B)^x.$$

Many different versions of this program have been developed to handle different particle identification experiments.

Program MAPID (Mass PID) has an additional feature for the mass identification calculation. This version is used with a separated ΔE - E counter telescope system. The program accepts energy signals from the ΔE and the E counters and the time of flight signal (TOF) between them. From this information PID is obtained by table lookup and MID is calculated by

$$MID = A(E - \Delta E)(TOF)^2.$$

Windows can be set in the PID and MID spectra and events sorted into energy spectra according to the value of PID and MID. In addition, the program accepts singles data from a monitor detector so that the beam intensity can be monitored simultaneously.

The PID, MID, and gated energy spectra can all be displayed on the CRT, stored on magnetic tape for later analysis, or plotted on the line printer. To facilitate PID and MID setup, the program also allows the two-dimensional plotting of PID vs $E + \Delta E$, MID vs $E + \Delta E$ and PID vs MID.[2] In addition, event-by-event data recording is possible to allow further data analysis off-line.

Another version, PIDGATE, was written to handle data from a kinematically complete experiment. In an experiment where the channel of interest is overwhelmed by elastic products from a large background, it may be necessary to do a kinematically complete experiment, with particle identification required for both coincident particles detected. This program enables a gate to be set on the first particle ID spectrum to control storage of information from the second telescope.

For the case where four telescopes are used at the same time, there is version, PID4. This program was written for polarized deuteron beam experiments where particle identification is usually required. One pair of telescopes is used for the reaction of interest and another pair for the helium polarimeter to monitor beam polarization. The program employs routing of the energy signals of four counter-telescope systems into two ADCs, i.e., four ΔE signals into one ADC and four E signals into the other.

In this version only light-ion particle identification is required. An ID table of 512 words is used, and has been found to provide sufficient separation. To simplify the parameter input, only one table is used for all four telescopes. An additional feature of the program is on-line peak summing. Peak-sum windows and ID gates are set by light pen on the CRT, which intensifies the corresponding data points for easy resetting and comparison.

All these versions had been successfully used in various experiments and will be condensed into one master program in the future.

---

1. Nuclear Physics Laboratory Annual Report, University of Washington (1974), p. 24.
2. See Sec. 3.3 of this report.

4.5 A Search Code for Heavy-Ion Optical Model Parameters

Y-d Chan

A computer program called SCHOMP (Search Code for Heavy-ion Optical Model Parameters) has been written to run on the NPL 16K SDS 930 computer.

The basic searching control follows the Oak Ridge[1] method. First derivatives of the chi-square:

$$\chi^2 \equiv \frac{1}{N} \sum_{i=i}^{N} \omega_i^2 \left(\frac{\sigma^i_{th}(\underset{\sim}{\lambda}) - \sigma^i_{exp}}{\sigma^i_{exp}} \right)^2$$

where

$N \equiv$ total number of experimental points

$\omega_i \equiv$ weight of the i^{th} point

$\underset{\sim}{\lambda} \equiv \{\lambda_1 \ldots \lambda_M\}$ are the M parameters to be changed

are calculated numerically, and the 2nd partial derivatives are formally approximated by

$$\frac{\partial^2 \chi^2}{\partial \lambda_1 \partial \lambda_2} \rightarrow \left(\frac{\partial \chi^2}{\partial \lambda_1} \right) \left(\frac{\partial \chi^2}{\partial \lambda_2} \right).$$

New parameters are obtained by solving a 1st order linear equation system by matrix inversion, with built in parabolic extrapolation to locate the best point.

A fast integration routine for solving the Schrödinger equation is essential to every practical search code. For the present program, HOP-II[2], which uses the Numerov alogrithm, is being used to do the integration, with minor features trimmed off to trade for speed.

The convergence and speed of the search depends quite sensitively on the input scales and search step sizes. An educated guess of initial parameters and experience with the control of searching scales (changeable via break

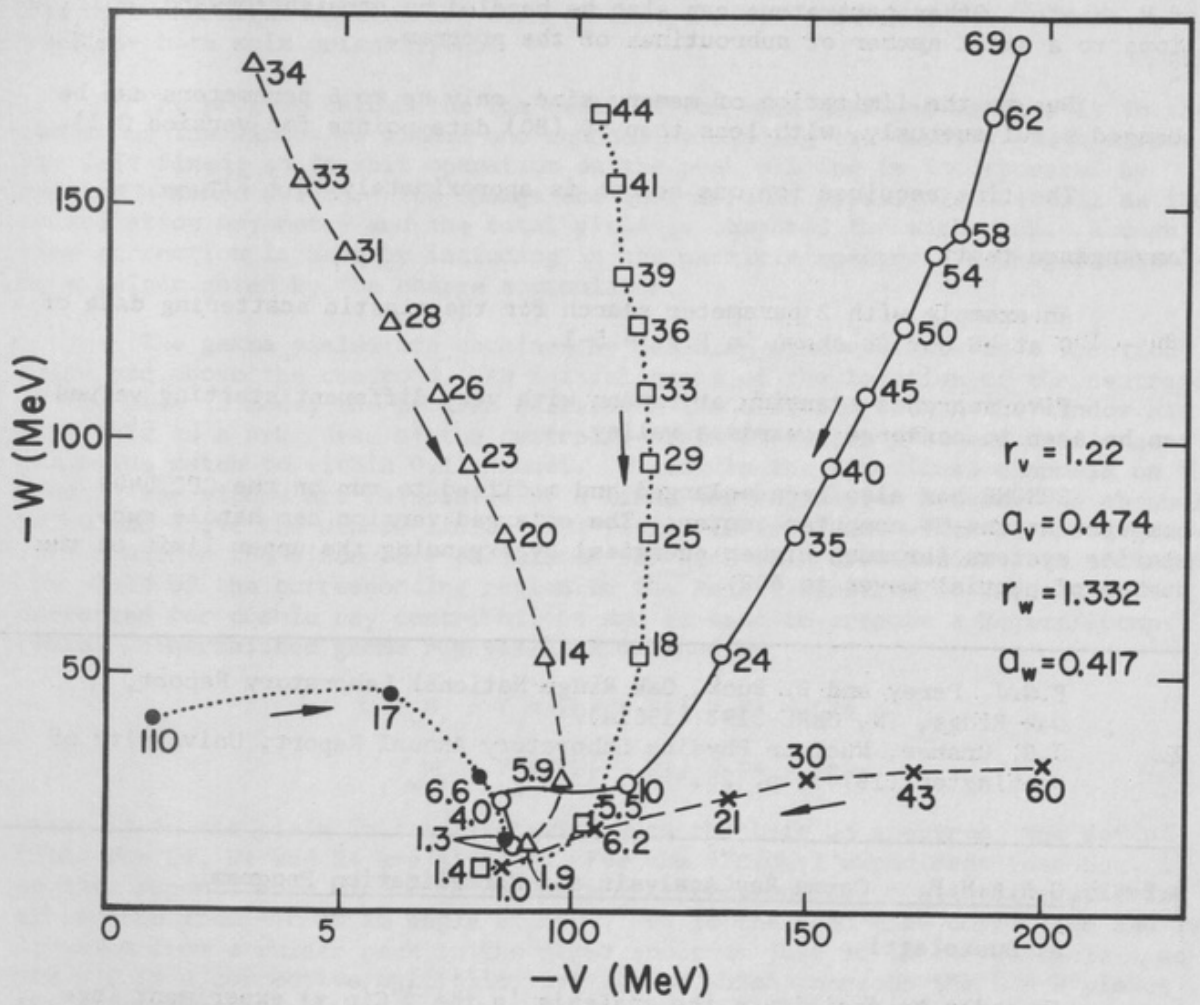

Fig. 4.5-1. Convergence test with 48 MeV ^{58}Ni + ^{16}O data. Only V and W are changed. Numbers on the graph give the χ^2 value for each point. The program uses internal default values for scale and step sizes. All searches are stopped manually after reaching a $\chi^2 \leq 2$.

points) can speed up the search drastically.

Optical model parameters that can be handled directly by the code include:

$$V,\ r_V,\ a_V,\ W,\ r_W,\ a_W,\ L_c,\ \Delta L_c$$

as well as

β (nonlocality range parameter), Linear and quadratic energy dependence

of V, W etc. Other parameters can also be handled by straightforward modifications to a small number of subroutines of the program.

Due to the limitation of memory size, only up to 6 parameters can be changed simultaneously, with less than 50 (80) data points for version G(1).

The time required for one search is approximately $(M + 3)T_{HOP-II}$.

Convergence test:

An example with 2 parameter search for the elastic scattering data of $^{58}N + ^{16}O$ at 48 MeV is shown in Fig. 4.5-1.

Five searches starting at random with very different starting values can be seen to converge towards a valley.

SCHOMP has also been enlarged and modified to run on the CDC 6400 computer at the UW computer center. The enlarged version can handle much heavier systems (or much higher energies) by expanding the upper limit on the number of partial waves to 600.

---

1. F.G.J. Perey and B. Buck, Oak Ridge National Laboratory Report, Oak Ridge, TN, ONRL-3193 (1961a).
2. J.G. Cramer, Nuclear Physics Laboratory Annual Report, University of Washington (1974), p. 26.

4.6 G.R.A.N.P. - Gamma Ray Analysis and Normalization Program

J. Bussoletti

In order to facilitate the analysis in the $^{14}C(\vec{p},\gamma)$ experiment (see Sec. 11 this report) an on-line data reduction program has been written. It features two modes of data collection. The first involves use of the two ND2400 analyzers to accumulate data. The data is then transferred into the computer and is analyzed while the ND2400 analyzers accumulate the next data set. The second data collection mode involves use of the computer itself to accumulate data. The subroutine DADC written by Rochelle Kochin (see Sec. 4.2 this report) is used to read the ADC's.

The data are stored in 2048 word array. The lower 1024 words contain the gamma spectra and the upper 1K contains particle spectra from the polarization monitor. (See Sec. 9 of this report.) The 1K arrays are subdivided into four 256 channel arrays which contain for the particle spectra the arrays Left Up, Right Up, Left Down and Right Down. The gamma spectra are subdivided into accept and reject spectra for both spin orientations.

Up to twenty windows can be defined on the particle spectra. It is assumed in the calculations of the polarization asymmetries that there are ten on the Left arrays and a corresponding ten on the Right arrays. The windows on

the Left and Right spectra are defined independently, but the same window is used for both spin orientations.

The program calculates the centroid for each peak and matches it to the center of the window to within one channel by sliding the window. Backgrounds are left fixed; an inhibit operation on the peak sliding is incorporated by setting a sense switch. The charge and instrumental asymmetrics as well as the polarization asymmetry and the total yield is computed for each peak. A dead time correction is made by including in the particle spectra a peak generated by a pulser gated by the charge accumulator.

The gamma yields are obtained by defining window limits as a fraction below and above the centroid. An initial guess of the location of the centroid of the peak is made; the program calculates the centroid within the window and uses this as a new guess of the centroid. This iteration proceeds until the centroids match to within 0.1 channel. Yields in the fractional channels on the ends of the window are caluclated by a linear extrapolation between the channels below and above the window limit. The yield, centroid and width of the distribution within the window are calculated for each spin orientation. In addition the yield of the corresponding region in the Reject spectrum is calculated, corrected for cosmic ray contributions and is used to compute a Reject/Accept ratio. A normalized gamma ray yield is defined by

$$Y_\gamma N_\uparrow = Y_\gamma\uparrow/(L\uparrow + R\uparrow) \times F\uparrow \times DT\uparrow$$

$$Y_\gamma N_\downarrow = Y_\gamma\downarrow/(L\downarrow + R\downarrow) \times F\downarrow \times DT\downarrow$$

where L↑ is the yield in the first window on the Left up spectrum; the definitions for L↓, R↑ and R↓ are similar. For the $^{14}C(p,\gamma)$ experiment (see Sec. II of this report) this window is on the peak corresponding to elastic scattering at protons from ^{14}C at an angle at 160°. DT is the dead time correction and is computed from a pulser peak in the gamma spectrum just as in the particle spectra. F is a corrective multiplicative factor which corrects the L + R yields for differences in the Left-Right solid angle. F is computed by assuming the analyzing power of the second window is zero. For the $^{14}C(p,\gamma)$ experiment this corresponds to elastic scattering from ^{197}Au at 160° and has A ≃ 0.03. Three normalizations are possible:

$$Y_\gamma N = \frac{\sigma_{o\gamma}\,\Delta\Omega_\gamma}{\sigma_{op}}(1 + PA_\gamma)\,\frac{1}{\Delta\Omega_L}$$

$$Y_\gamma N = \frac{\sigma_{o\gamma}\,\Delta\Omega_\gamma}{\sigma_{op}}(1 + PA_\gamma)\,\frac{1}{\Delta\Omega_R}$$

$$Y_\gamma N = \frac{\sigma_{o\gamma}\,\Delta\Omega_\gamma}{\sigma_{op}}(1 + PA_\gamma)\,\frac{2}{\Delta\Omega_L + \Delta\Omega_R + PA_p(\Delta\Omega_L - \Delta\Omega_R)}$$

All three are computed.

A table of angles may be defined for an angular distribution. Each time a run is ended the program stores the results of that analysis under the appropriate angle in the table. A new entry of the same angle writes over the old one. The table may be printed out on the line printer or punched on cards at any time. The format of the punched cards is compatible with a Legendre - Associated Legendre fitting program LEGALEGFIT.

Data may also be stored on tape. The same on-line program has a subroutine which allows scanning data tapes and performs a variety of operations on the data including both printing the results of the on-line analysis and re-analyzing a sequence of runs.

One addition will soon be made to the program to make it more universally applicable. There will be the option of accumulating gamma ray data only or both particle and gamma data.

4.7 HOP-THREE: An Optical Model Code for Very Heavy Ion Elastic Scattering

R. Vandenbosch

HOP-TWO, an optical model program developed at this laboratory[1] for heavy ion elastic scattering, has been modified to operate on the UW CDC 6400 computer. The number of partial waves has been extended from 200 to 980, enabling calculations for elastic scattering of Kr and Xe projectiles by heavy targets. The program has been checked[2] against the Argonne modification of the code ABACUS for the elastic scattering of 500 MeV ^{84}Kr by ^{208}Pb.

A number of innovations have been introduced to reduce computing time, particularly important when searching for a fit to experimental data. The S-matrix elements for a variable number of the lowest partial waves can be set to zero (complete absorption). It is also possible to calculate for only every other partial wave, interpolating between these values to obtain the values for the partial waves for which computation is skipped. It has been shown that savings of more than a factor of two can be achieved with negligible loss of accuracy.

---

1. J.G. Cramer, Nuclear Physics Laboratory Annual Report, University of Washington (1974), p. 26.
2. I am indebted to A. Friedman for performing this check.

4.8 Extension of the Heavy Ion Optical Model Program HOP-TWO

J.G. Cramer, W.G. Lynch, and J.C. Wiborg

The optical model program HOP-TWO[1] which operates on the XDS 930 computers operated by the laboratory was described in last year's report. During the past year there have been a number of modifications to this program, which is now in version 3.2. These are listed below:

(1) The options for ℓ-dependent absorption have been extensively modified to include two types of energy dependence for the ℓ-cutoff parameter and two forms of ℓ-cutoff diffuseness. (See Sec. 10.3 of this report.)

(2) The plotting program was modified so that the cross section ratio-to-Rutherford could be plotted vs the Coulomb distance of closest approach rather than the scattering angle. Near the Coulomb barrier, this leads to an "invariant" plot of the cross section which is semi-independent of target and projectile mass and of energy.

(3) An option was included for specifying the integration step size in radial units (f) rather than kr units.

(4) An option was included for computing the optical model radius as $R = R_0 A_2^{1/3}$ rather than $R_0[A_1^{1/3} + A_2^{1/3}]$ as is conventional in heavy ion reactions, or to simply specify the radius as $R = R_0$. These options facilitate comparison with calculations performed with other programs in which different conventions are employed.

(5) The identical particle option has been expanded to correctly treat the scattering of identical particles of arbitrary spin, for the case where no spin-orbit or spin-spin forces are present. The effect of the spin is to give an incoherent linear combination of space-symmetric and space-antisymmetric amplitudes with the coefficients of the linear combination depending on the spins involved. This has been used to analyze experimental data on the scattering of ^{27}Al on ^{27}Al, where both particles have $J^\pi = 5/2^+$.

(6) The option has been added to write data and fit curves on magnetic tape after a calculation. Tapes thereby generated can then be used with another program HOP-PLOT to produce Calcomp plots of the data and fits which are of a quality suitable for publication.

(7) A variant of HOP-TWO called RADL has been written which accepts the same input cards but generates computer plots of the radial wave function rather than computing cross sections. For each partial wave, the maximum of the magnitude of the radial wave function is located, and this value is used to find the points which are 1/10 max, 1/100 max, 1/1000 max, etc. The plot then generated thus has contour lines for these points, as well as the region of the nuclear surface and the semi-classical distance of closest approach, all plotted in a radius vs ℓ plot. This program has proved very useful in investigating the variation in the structure of the wave function with ambiguous potentials, and the regions of sensitivity to be expected in elastic scattering and transfer reactions.

(8) In the course of developing the exact non-local optical model program OINK!, which is based on HOP-TWO, many new techniques were devised for saving memory space. These techniques have been incorporated in a special version of HOP-TWO which can handle up to 500 partial waves and up to 600 radial integration steps without interpolation, yet operates on the XDS 930 computer. This makes it possible to investigate the scattering of very heavy ions at high energies with the laboratory off-line computer system. Vandenbosch has developed a similar variant of HOP-TWO for use on the CDC-6400 computer.[2]

---

1. Nuclear Physics Laboratory Annual Report, University of Washington (1974), p. 26.
2. See Sec. 4.7 of this report.

4.9 SIMILAC, A Design Program for Spiral Resonator Linear Accelerators

J.G. Cramer

As discussed in Sec. 1.5, we have comleted a preliminary design of a spiral resonator linac postaccelerator to be injected by the existing tandem.

It became obvious early in this work that the repetitive nature of these design evaluations could be greatly assisted by a computer program. Therefore the spiral resonator accelerator design program SIMILAC was written. It traces the acceleration of an ion through DC accelerating sections, foil or gas strippers, and single, double and triple spiral resonator RF accelerating cavities.

Proper operation of the program requires accurate estimates of the performance of various elements of the postaccelerator. The most probable charge state and charge state fraction following gas or foil stripping are calculated from empirical relations given by Yntema based on the work of Nikolaev and Dmitriev. The program normally takes the charge state which is at the peak of the charge state distribution to be the charge of the beam following stripping, although it can be instructed to use other charge states if desired.

Another important quantity in the accelerator design is the transit time factor, $T_i(\gamma)$, which is defined as the fraction of the average electric field which is actually available for acceleration of the beam. This factor is always less than 1 and becomes quite small if the velocity of the beam differs markedly from the phase velocity of the cavity. We have used the analytical expressions of Stokes and Armstrong to estimate the transit time factor $T_i(\gamma)$, with i=1, 2, or 3 for the S1, A2, and S3 normal modes, respectively (see Sec. 1.5). These expressions are based on idealized segmented sinusoid electric field profiles which are, at best, approximations to the true field profiles in these modes. Better approximations must await electric field mappings of the A2 and S1 normal modes which are now in preparation. We feel that the approximation used should be good to about 5% for the S3 mode and to about 20% for the A2 and S1 modes.

The shunt impedance of the cavity is also estimated empirically, based on the experimental data of Armstrong *et al.*, using a two segment linear fit to the data. In the region of phase velocities larger than .085, where no data

Table 4.9-1.

```
   FINAL POSTACCELERATOR DESIGN  3-STRIP  NORMAL MODE 53    20 PCT OF OPERATION

BEAM MASS=238.00     BEAM Z=92.      FREQUENCY=100.0     DUTY FACTOR= 20.0 PERCENT

          1       RC ACCELERATION SECTION    TIN=    .00,  TOUT=   6.50

          2       RC ACCELERATION SECTION    TIN=   6.50,  TOUT=  15.50

          3       SOLID STRIPPER SECTION     GIN= 1..      GOUT=12.     CHARGE STATE FRACTION=.170

          4       RC ACCELERATION SECTION    TIN=  15.50,  TOUT= 123.50

          5       SOLID STRIPPER SECTION     GIN=12..      GOUT=30.     CHARGE STATE FRACTION=.171

        3 SECTIONS OF TYPE 3
          Q=30.  EO= 4.66  PO=  20.00  PHASE VEL= .0333   Q-LENGTH= 10.0
          LENGTH/SEC= .1994   IMPEDANCE= 43.31   POWER/SEC= 20.00 KW

SEC     GROUP    T(IN)     T(OUT)       DT          BETA       GAMMA      T(GAM)   PHI(GAM)    LENGTH      POWER
  1       6    123.50     144.33     20.4264      .0346      .9815      .7950     76.16        .42       20.00
  2       6    144.33     164.88     20.5565      .0372      .9949      .7847     52.16        .84       40.00
  3       6    164.88     184.59     19.7052      .0396      .9419      .7523     33.04       1.26       60.00
          QUADRUPOLE LENGTH SHOULD BE .GE.  4.41 CM

        4 SECTIONS OF TYPE 3
          Q=30.  EO= 4.35  PO=  20.00  PHASE VEL= .0406   Q-LENGTH= 10.0
          LENGTH/SEC= .2437   IMPEDANCE= 46.19   POWER/SEC= 20.00 KW

SEC     GROUP    T(IN)     T(OUT)       DT          BETA       GAMMA      T(GAM)   PHI(GAM)    LENGTH      POWER
  4       7    184.59     208.34     23.7525      .0419      .9479      .7943     78.44       1.72       40.00
  5       7    208.34     232.00     23.6641      .0444      .9147      .7812     59.14       2.19      100.00
  6       7    232.00     255.68     23.6788      .0447      .8993      .7716     42.95       2.65      120.00
  7       7    255.68     277.32     22.2372      .0488      .8315      .7434     29.34       3.11      140.00
          QUADRUPOLE LENGTH SHOULD BE .GE.  7.22 CM

        5 SECTIONS OF TYPE 3
          Q=30.  EO= 3.80  PO=  20.00  PHASE VEL= .0498   Q-LENGTH= 10.0
          LENGTH/SEC= .2988   IMPEDANCE= 43.21   POWER/SEC= 20.00 KW

SEC     GROUP    T(IN)     T(OUT)       DT          BETA       GAMMA      T(GAM)   PHI(GAM)    LENGTH      POWER
  8       8    277.32     302.71     25.3884      .0510      .9771      .7624     81.77       3.43      160.00
  9       8    302.71     328.19     25.4759      .0532      .9369      .7459     67.28       4.15      180.00
 10       8    328.19     353.41     25.2202      .0552      .9014      .7319     54.50       4.67      200.00
 11       8    353.41     378.14     24.7346      .0572      .8701      .7191     43.23       5.19      220.00
 12       8    378.14     402.26     24.1147      .0591      .8424      .7069     33.27       5.71      240.00
          QUADRUPOLE LENGTH SHOULD BE .GE. 10.48 CM

        5 SECTIONS OF TYPE 3
          Q=30.  EO= 4.08  PO=  20.00  PHASE VEL= .0600   Q-LENGTH= 15.0
          LENGTH/SEC= .3598   IMPEDANCE= 39.94   POWER/SEC= 30.00 KW

SEC     GROUP    T(IN)     T(OUT)       DT          BETA       GAMMA      T(GAM)   PHI(GAM)    LENGTH      POWER
 13       9    402.26     435.03     32.7777      .0612      .9799      .7918     82.75       6.34      270.00
 14       9    435.03     467.97     32.9339      .0636      .9435      .7756     69.67       6.97      300.00
 15       9    467.97     500.68     32.7157      .0659      .9110      .7601     57.96       7.60      330.00
 16       9    500.68     532.92     32.2343      .0680      .8819      .7457     47.49       8.23      360.00
 17       9    532.92     564.50     31.5788      .0701      .8559      .7324     38.19       8.86      390.00
          QUADRUPOLE LENGTH SHOULD BE .GE. 14.70 CM

        7 SECTIONS OF TYPE 3
          Q=30.  EO= 3.58  PO=  20.00  PHASE VEL= .0711   Q-LENGTH= 20.0
          LENGTH/SEC= .4263   IMPEDANCE= 36.37   POWER/SEC= 30.00 KW

SEC     GROUP    T(IN)     T(OUT)       DT          BETA       GAMMA      T(GAM)   PHI(GAM)    LENGTH      POWER
 18      10    564.50     598.46     33.9798      .0727      .9492      .7604     84.88       9.60      420.00
 19      10    598.46     632.67     34.1914      .0743      .9576      .7653     74.72      10.34      450.00
 20      10    632.67     666.83     34.1628      .0763      .9320      .7544     65.53      11.10      480.00
 21      10    666.83     700.78     33.9444      .0783      .9085      .7434     57.07      11.84      510.00
 22      10    700.78     734.36     33.5815      .0802      .8869      .7311     49.28      12.59      540.00
 23      10    734.36     767.47     33.1120      .0820      .8670      .7202     42.11      13.33      570.00
 24      10    767.47     800.04     32.5670      .0838      .8486      .7078     35.50      14.07      600.00
          QUADRUPOLE LENGTH SHOULD BE .GE. 20.84 CM

          11      SOLID STRIPPER SECTION     GIN=30..      GOUT=56.     CHARGE STATE FRACTION=.171

        4 SECTIONS OF TYPE 3
          Q=56.  EO= 3.55  PO=  20.00  PHASE VEL= .0946   Q-LENGTH= 10.0
          LENGTH/SEC= .5075   IMPEDANCE= 32.02   POWER/SEC= 40.00 KW

SEC     GROUP    T(IN)     T(OUT)       DT          BETA       GAMMA      T(GAM)   PHI(GAM)    LENGTH      POWER
 25      12    800.04     877.93     77.8905      .0867      .9760      .7927     81.34      14.81      640.00
 26      12    877.93     956.03     78.1003      .0906      .9339      .7748     66.07      15.54      680.00
 27      12    956.03    1033.19     77.1903      .0944      .8984      .7593     52.69      16.26      720.00
 28      12   1033.19    1108.67     75.4744      .0979      .8638      .7449     40.96      16.99      760.00
          QUADRUPOLE LENGTH SHOULD BE .GE.  7.73 CM

        6 SECTIONS OF TYPE 3
          Q=56.  EO= 3.02  PO=  20.00  PHASE VEL= .0996   Q-LENGTH= 10.0
          LENGTH/SEC= .5974   IMPEDANCE= 27.19   POWER/SEC= 40.00 KW

SEC     GROUP    T(IN)     T(OUT)       DT          BETA       GAMMA      T(GAM)   PHI(GAM)    LENGTH      POWER
 29      13   1108.67    1186.40     77.7248      .1014      .9825      .7911     83.68      17.81      800.00
 30      13   1186.40    1264.56     78.1655      .1048      .9507      .7765     72.24      18.63      840.00
 31      13   1264.56    1342.47     77.9032      .1080      .9218      .7630     61.85      19.44      880.00
 32      13   1342.47    1419.58     77.1148      .1112      .8956      .7499     52.40      20.26      920.00
 33      13   1419.58    1495.53     75.9500      .1143      .8717      .7371     43.82      21.08      960.00
 34      13   1495.53    1570.06     74.5286      .1172      .8501      .7248     36.02      21.89     1000.00
          QUADRUPOLE LENGTH SHOULD BE .GE. 10.94 CM

        7 SECTIONS OF TYPE 3
          Q=56.  EO= 2.44  PO=  20.00  PHASE VEL= .1188   Q-LENGTH= 10.0
          LENGTH/SEC= .7109   IMPEDANCE= 21.04   POWER/SEC= 40.00 KW

SEC     GROUP    T(IN)     T(OUT)       DT          BETA       GAMMA      T(GAM)   PHI(GAM)    LENGTH      POWER
 35      14   1570.06    1644.54     74.4837      .1200      .9884      .7984     85.86      22.83     1040.00
 36      14   1644.54    1719.49     74.9521      .1227      .9663      .7884     77.86      23.78     1080.00
 37      14   1719.49    1794.56     75.0685      .1254      .9454      .7786     70.36      24.69     1120.00
 38      14   1794.56    1869.45     74.8897      .1281      .9259      .7697     63.32      25.62     1160.00
 39      14   1869.45    1943.92     74.4667      .1307      .9076      .7613     56.73      26.55     1200.00
 40      14   1943.99    2017.77     73.8531      .1332      .8904      .7527     50.55      27.48     1240.00
 41      14   2017.77    2090.86     73.0941      .1356      .8744      .7446     44.77      28.41     1280.00
          QUADRUPOLE LENGTH SHOULD BE .GE. 14.57 CM

ENERGY INCREASE=1967.36     ENERGY/NUCLEON= 8.79     EFF VOLTAGE= 33.92
AVERAGE FIELD= 1.44     MASS-ENERGY PROD= 147.93     TRANSMISSION= .00497
```

Table 4.9-2.

FINAL POSTACCELERATOR DESIGN 3-STRIP NORMAL MODE A2 100 PCT OF OPERATION

FREQUENCY=100.0 DUTY FACTOR=100.

MASS	Z	Q	E(IN)	E(OUT)	DE	EN/NUC	FFF V	AV FIELD	M-E PROD	TRANSMIS
1.	1.	1.	24.50	32.57	8.07	32.57	8.07	.44	32.57	1.00000
2.	1.	1.	24.50	35.89	11.39	17.95	11.39	.62	71.79	1.00000
3.	2.	2.	33.50	56.61	23.11	18.87	11.56	.63	42.46	.49967
4.	2.	2.	33.50	58.71	25.21	14.68	12.61	.68	58.71	.49734
6.	3.	3.	42.50	81.53	39.03	13.59	13.01	.71	54.36	.29116
7.	3.	3.	42.50	82.25	39.75	11.75	13.25	.72	63.97	.28645
9.	4.	4.	51.50	104.89	53.39	11.65	13.35	.72	59.00	.17571
10.	5.	5.	51.50	119.28	67.78	11.93	13.54	.74	47.71	.13353
11.	5.	5.	51.50	119.33	67.83	10.45	13.57	.74	52.50	.13570
12.	6.	6.	60.50	141.99	81.49	11.63	13.58	.74	47.33	.11544
13.	6.	6.	60.50	142.03	81.53	10.93	13.59	.74	51.29	.11475
14.	7.	7.	69.50	164.70	95.20	11.76	13.60	.74	47.06	.08368
15.	7.	7.	69.50	164.72	95.22	10.98	13.60	.74	50.43	.07937
16.	8.	8.	69.50	170.87	101.37	10.68	12.67	.69	42.72	.07555
17.	8.	8.	69.50	170.05	100.55	10.00	12.57	.68	45.17	.07719
18.	8.	8.	69.50	168.91	99.41	9.38	12.43	.67	47.51	.07827
19.	9.	9.	78.50	192.89	114.39	10.15	12.71	.69	45.25	.06474
23.	11.	10.	87.50	223.12	135.62	9.70	13.56	.74	51.32	.05495
24.	12.	11.	87.50	237.87	150.37	9.91	13.67	.74	47.18	.05357
25.	12.	11.	87.50	236.81	149.31	9.47	13.57	.74	48.93	.05257
26.	12.	11.	87.50	235.53	148.03	9.06	13.46	.73	50.61	.05121
27.	13.	12.	87.50	240.06	152.56	8.89	12.71	.69	45.01	.05054
28.	14.	13.	96.50	284.77	188.27	9.46	12.94	.70	43.87	.04513
29.	14.	13.	96.50	283.26	186.76	9.08	12.83	.70	45.17	.04379
30.	14.	13.	87.50	251.02	163.52	8.37	12.58	.68	44.56	.04367
31.	15.	14.	96.50	276.43	179.93	8.99	12.85	.70	43.72	.04129
32.	16.	15.	96.50	280.55	184.05	8.77	12.27	.67	39.90	.03465
33.	16.	15.	96.50	278.30	181.80	8.43	12.12	.66	40.82	.03500
34.	16.	15.	96.50	275.87	179.37	8.11	11.96	.65	41.69	.03506
35.	17.	15.	96.50	285.08	188.58	8.15	12.57	.68	44.35	.03648
36.	16.	14.	96.50	285.16	188.66	7.77	12.09	.65	48.70	.03820
37.	17.	15.	96.50	280.01	183.51	7.57	12.23	.66	46.05	.03773
39.	19.	17.	105.50	309.66	204.16	7.94	12.01	.65	41.79	.03092
40.	20.	18.	105.50	324.73	219.23	8.12	12.18	.66	40.09	.03095
41.	19.	17.	105.50	304.05	198.55	7.42	11.68	.63	43.13	.03023
42.	20.	18.	105.50	319.06	213.56	7.60	11.86	.64	41.36	.03003
43.	20.	18.	105.50	316.02	210.52	7.35	11.70	.63	41.94	.02925
44.	20.	18.	105.50	312.86	207.36	7.11	11.52	.62	42.49	.02831
45.	21.	18.	105.50	309.58	204.08	6.88	11.34	.61	43.00	.02753
46.	20.	17.	96.50	273.36	176.86	8.84	10.40	.56	43.51	.02673
46.	22.	19.	105.50	324.56	219.06	7.06	11.53	.63	41.36	.02809
47.	22.	19.	105.50	321.12	215.62	6.83	11.35	.62	41.81	.02825
48.	20.	17.	96.50	265.76	169.26	5.54	9.96	.54	44.14	.02903
48.	22.	19.	105.50	317.57	212.07	6.62	11.16	.61	42.23	.02820
49.	22.	19.	105.50	313.94	208.44	6.41	10.97	.59	42.61	.02797
50.	22.	19.	105.50	310.23	204.73	6.20	10.78	.58	42.97	.02755
50.	24.	21.	105.50	333.60	228.10	6.67	10.86	.59	37.82	.02326
51.	23.	20.	105.50	310.64	205.14	6.09	10.26	.56	39.61	.02528
52.	24.	21.	105.50	325.53	220.03	6.26	10.48	.57	38.38	.02318
53.	24.	21.	105.50	321.39	215.89	6.06	10.28	.56	38.62	.02288
54.	24.	20.	105.50	313.22	207.72	5.80	10.39	.56	42.28	.02413
54.	26.	22.	114.50	351.72	237.22	6.51	10.78	.58	39.24	.02203
55.	25.	21.	105.50	312.93	207.43	5.80	9.88	.54	39.03	.02322
56.	26.	22.	105.50	327.65	222.15	6.05	10.10	.55	37.91	.02148
57.	26.	22.	105.50	323.23	217.73	5.87	9.91	.54	38.07	.02156
58.	26.	22.	105.50	318.79	213.29	5.50	9.70	.53	38.20	.02149
58.	28.	24.	114.50	358.89	244.39	6.19	10.18	.55	36.14	.01962
59.	27.	23.	114.50	350.36	235.86	5.94	10.25	.56	39.08	.01917
60.	28.	23.	114.50	346.12	231.62	5.77	10.07	.55	39.26	.02030
61.	28.	23.	114.50	341.83	227.33	5.60	9.88	.54	39.42	.02024
62.	28.	23.	114.50	337.53	223.03	5.44	9.70	.53	39.56	.02005
63.	29.	24.	114.50	336.57	222.07	5.34	9.25	.50	36.81	.01927
64.	28.	23.	105.50	294.65	189.15	4.60	8.29	.45	35.65	.01937
64.	30.	25.	114.50	351.11	236.61	5.49	9.46	.51	35.95	.01881
66.	30.	25.	114.50	341.78	227.28	5.18	9.09	.49	36.09	.01780
67.	30.	25.	114.50	337.12	222.62	5.03	8.90	.48	36.14	.01727
68.	30.	24.	114.50	329.74	215.24	4.85	8.97	.49	38.93	.01767
69.	31.	25.	114.50	327.91	213.41	4.75	8.54	.46	36.20	.01860
70.	30.	24.	114.50	305.73	191.23	4.37	7.97	.43	37.16	.01768
71.	31.	25.	114.50	318.89	204.39	4.49	8.18	.44	36.23	.01818
75.	33.	26.	114.50	318.62	204.12	4.25	7.85	.43	35.35	.01687
76.	32.	25.	114.50	297.68	183.18	3.92	7.33	.40	36.20	.01730
79.	35.	27.	114.50	302.88	188.38	3.83	6.98	.38	32.82	.01585
82.	34.	26.	114.50	289.80	175.30	3.53	6.74	.37	35.15	.01588
88.	38.	28.	114.50	282.91	168.41	3.21	6.01	.33	31.75	.01456
90.	40.	30.	114.50	290.09	175.59	3.22	5.85	.32	29.01	.01260
91.	40.	29.	114.50	285.75	171.25	3.14	5.91	.32	30.92	.01333
92.	40.	29.	114.50	282.20	167.70	3.07	5.75	.31	30.47	.01342
94.	40.	29.	114.50	275.39	160.89	2.93	5.55	.30	30.74	.01328
96.	40.	29.	114.50	257.76	143.26	2.69	4.94	.27	29.42	.01278
100.	42.	29.	114.50	256.85	142.35	2.57	4.91	.27	30.54	.01278
103.	45.	31.	114.50	259.20	144.70	2.52	4.67	.25	27.78	.01164
106.	46.	31.	114.50	250.43	135.93	2.36	4.38	.24	27.62	.01137
110.	46.	30.	114.50	238.92	124.42	2.17	4.15	.22	29.30	.01140
116.	48.	30.	114.50	222.87	108.37	1.92	3.81	.20	28.73	.01045
124.	50.	30.	114.50	203.57	89.07	1.64	3.97	.16	28.05	.01042
138.	56.	31.	114.50	189.65	75.15	1.37	3.42	.13	27.23	.00875
140.	58.	31.	114.50	191.07	76.57	1.36	3.47	.13	27.84	.00844
154.	62.	31.	114.50	172.91	58.41	1.12	1.88	.10	27.71	.00798
160.	64.	31.	114.50	166.13	53.63	1.05	1.73	.09	27.98	.00762
164.	66.	31.	114.50	167.42	52.92	1.02	1.71	.09	28.57	.00713
186.	74.	33.	123.50	170.78	47.28	.92	1.43	.08	29.17	.00634
197.	79.	33.	123.50	165.89	42.39	.84	1.28	.07	30.01	.00597
204.	80.	33.	123.50	162.03	38.53	.79	1.17	.06	30.35	.00560
208.	82.	33.	123.50	161.91	38.41	.78	1.16	.06	30.92	.00566
209.	83.	33.	123.50	161.51	38.01	.77	1.15	.06	31.00	.00568
238.	92.	32.	123.50	146.85	23.15	.62	.72	.04	34.09	.00499

TOTAL LENGTH= 29.41 RESONATOR LENGTH= 18.44 TOTAL POWER=1280.00 KW

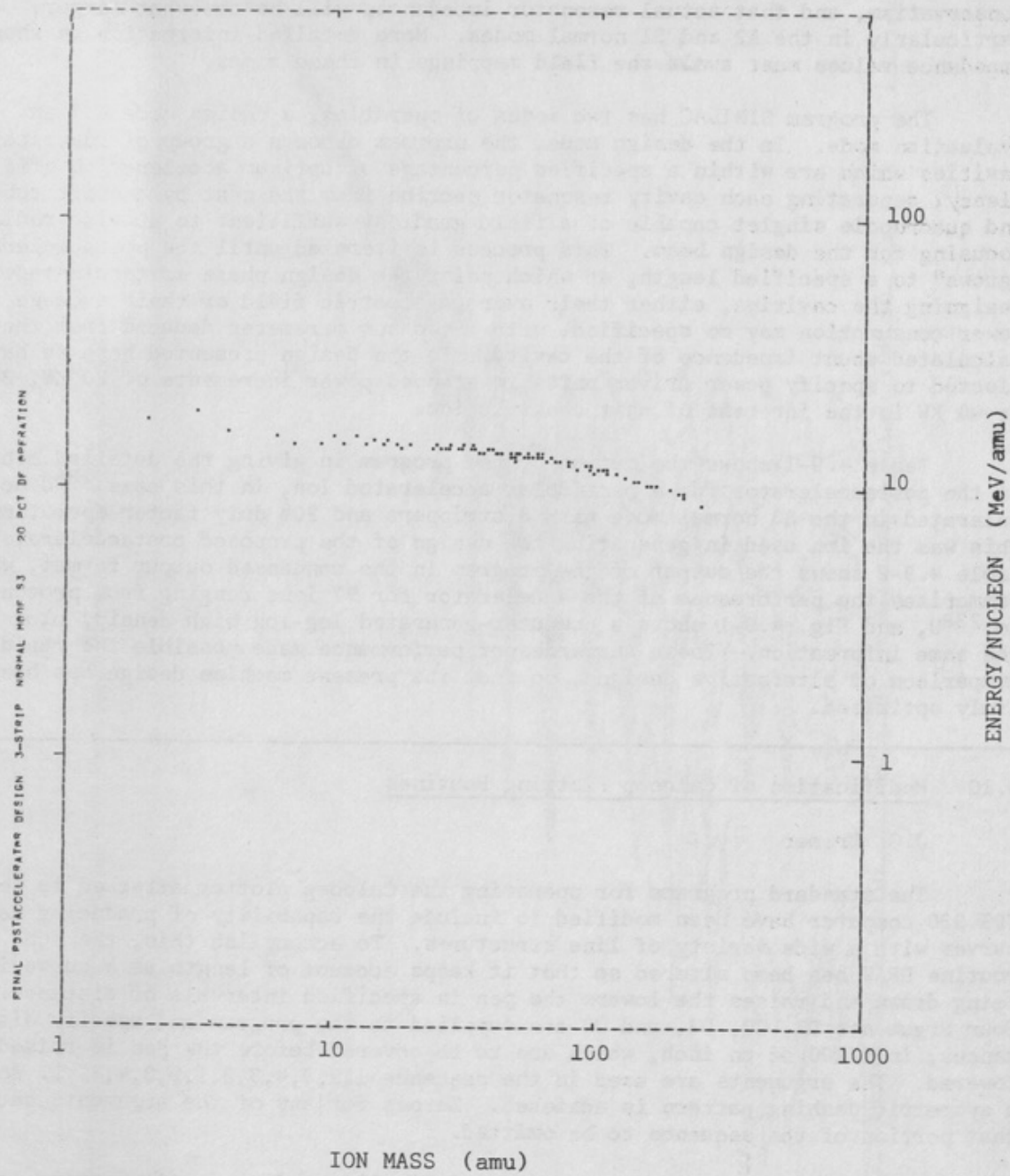

Fig. 4.9-1. Computer generated log-log plot of Final Beam Energy vs Ion Mass.

presently exist, we have extrapolated the linear relation to a minimum Z_s of 8.5 megohms/meter, which is half of the smallest shunt impedance ever measured for a spiral resonator cavity. We feel that this procedure errs on the side of conservatism, and that actual resonator impedances will be comewhat larger, particularly in the A2 and S1 normal modes. More detailed information on shunt impedance values must await the field mappings in these modes.

The program SIMILAC has two modes of operation, a design mode and an evaluation mode. In the design mode, the program chooses a group of identical cavities which are within a specified percentage of optimum acceleration efficiency, separating each cavity resonator section from the next by a drift tube and quadrupole singlet capable of a field gradient sufficient to provide radial focusing for the design beam. This process is iterated until the postaccelerator "grows" to a specified length, at which point the design phase is terminated. In designing the cavities, either their average electric field or their average power consumption may be specified, with the other parameter deduced from the calculated shunt impedance of the cavity. In the design presented here we have elected to specify power driver units in stepped power increments of 20 KW, 30 KW or 40 KW in the interest of unit construction.

Table 4.9-1 shows the output of the program in giving the detailed behavior of the postaccelerator for a particular accelerated ion, in this case ^{238}U accelerated in the S3 normal mode with 3 strippers and 20% duty factor operation. This was the ion used in generating the design of the proposed postaccelerator. Table 4.9-2 shows the output of the program in the condensed output format, which summarizes the performance of the accelerator for 97 ions ranging from protons to ^{238}U, and Fig. 4.9-1 shows a computer-generated log-log high density plot of the same information. These summaries of performance made possible the rapid comparison of alternative designs, so that the present machine design has been truly optimized.

4.10 Modification of Calcomp Plotting Routines

J.G. Cramer

The standard programs for operating the Calcomp plotter attached to the XDS 930 computer have been modified to include the capability of producing dashed curves with a wide variety of line structures. To accomplish this, the subroutine DRAW has been altered so that it keeps account of length as a curve is being drawn and raises the lowers the pen in specified intervals of distance. Four arguments D1, U2, D3, and U4 are supplied to the program and specify distances, in 1/100 of an inch, which are to be covered before the pen is raised or lowered. The arguments are used in the sequence 1,2,3,4,3,2,1,2,3,4,3,... so that a symmetric dashing pattern is achieved. Zeroes for any of the arguments cause that portion of the sequence to be omitted.

As an example, the arguments (20,5,5,5) will produce an alternating long dash .20 inches long and two short dashed .05 inches long which are separated by blank spaces .05 inches long. The arguments (10,0,0,3) will produce a dashed line with .10 inch segments separated by .03 inch spaces. Figure 4.10-1 shows a

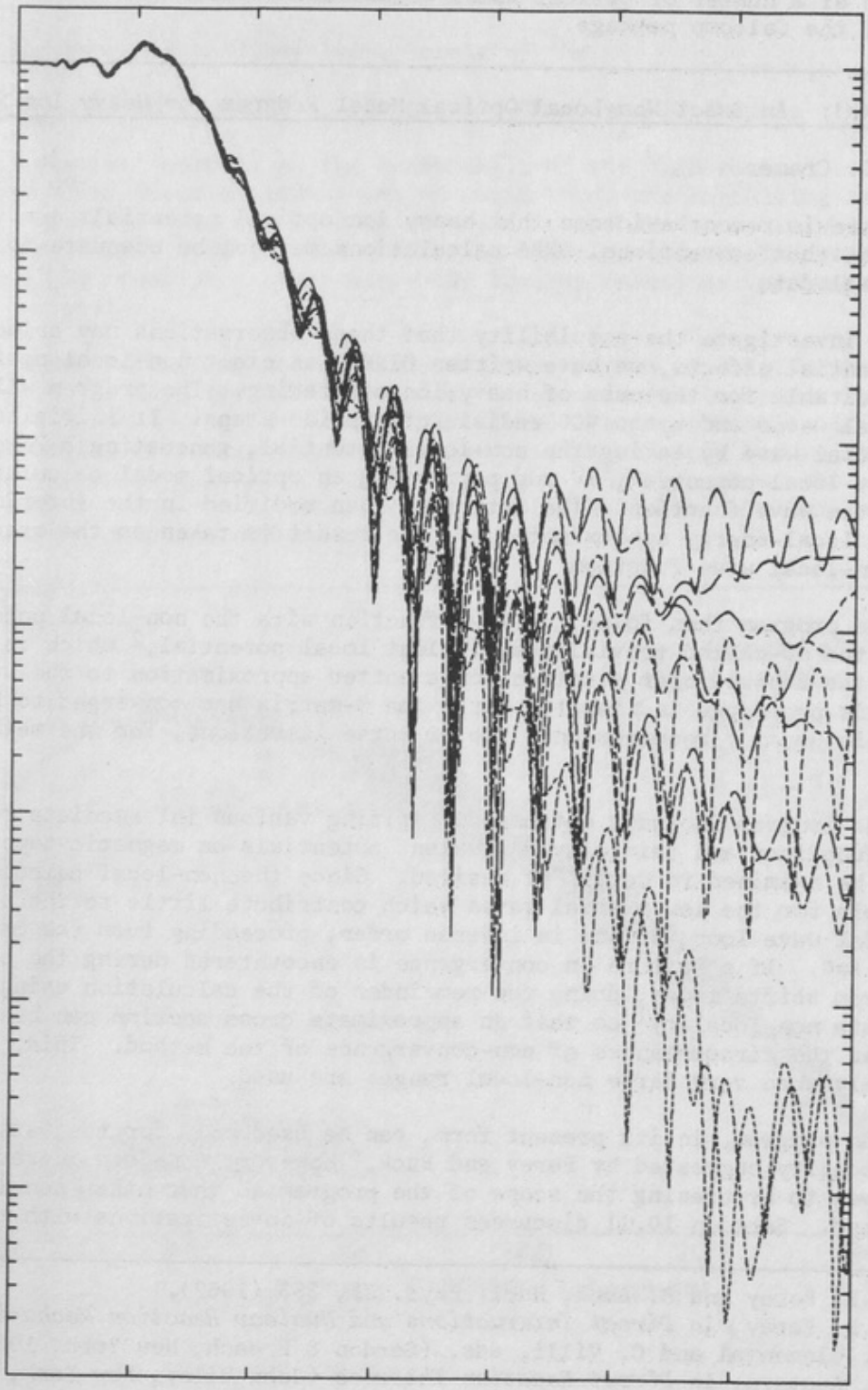

Fig. 4.10-1. An example of dashed curves generated with the modified Calcomp subroutines.

comparison of a number of optical model calculations which was made using this feature of the Calcomp package.

4.11 OINK!: An Exact Non-Local Optical Model Program for Heavy Ion Scattering

J.G. Cramer

There is recent evidence that heavy ion optical potentials are very shallow and that conventional DWBA calculations may not be adequate to explain experimental data.

To investigate the possibility that these observations may arise from non-local potential effects, we have written OINK!, an exact non-local optical model program suitable for the case of heavy ion scattering. The program will handle 120 partial waves and up to 400 radial integration steps. It initializes for a given partial wave by taking the non-local potential, generating a Perey-Buck equivalent local potential,[1,2] and performing an optical model calculation to generate the wave function. The latter is then modified in the interior region using the local-energy approximation.[3] The result is taken as the starting value of the non-local wave function.

The program then folds the wave function with the non-local potential to generate the so-called trivially-equivalent local potential,[2] which is then used to solve the Schroedinger equation for a better approximation to the wave function. This procedure is iterated until the S-matrix has converged to better than 0.1%. This usually requires only two or three iterations, for the method is very stable.

The program includes options for writing various intermediate results such as wave functions and trivially-equivalent potentials on magnetic tape so that they can be examined in detail if desired. Since the non-local calculations may be unstable for the low partial waves which contribute little to the scattering, the partial wave loop is done in inverse order, proceeding from the maximum ℓ-value to ℓ=0. If a failure in convergence is encountered during the calculation, the program shifts modes, doing the remainder of the calculation using Perey-Buck approximate non-locality[1] so that an approximate cross section can be obtained even under the circumstances of non-convergence of the method. This, however, occurs only when very large non-local ranges are used.

The program, in its present form, can be used only for the Gaussian form of non-locality suggested by Perey and Buck. However, some consideration is being given to broadening the scope of the program so that other non-local forms can be used. Section 10.11 discusses results of investigations with this code.

---

1. F.B. Perey and B. Buck, Nucl. Phys. *32*, 353 (1962).
2. F.B. Perey, in *Direct Interactions and Nuclear Reaction Mechanisms*, E. Clemental and C. Villi, eds. (Gordon & Breach, New York, 1963).
3. N. Austern, in *Direct Reaction Theories* (John Wiley, New York, 1970).

---

5. LEVELS IN LIGHT NUCLEI

5.1 On the Search for Higher Lying Levels of ^{5}He

K-L Liu, J.G. Cramer, M.S. Zisman, Y-d Chan, and B. Cuengco

Last year we reported on the measurement of the differential cross section of the ^{7}Li(d,α)^{5}He reaction from which we could study the high-lying levels of ^{5}He.[1] A 28 MeV state was reported in addition to the 24 MeV state which had been observed previously. However, the asymmetric shape of this 28 MeV state indicated that it possibly arose from other many-body breakup reactions, perhaps involving more than one state.

A kinematically complete experiment was performed to clarify these results. The experiment employed two ΔE-E telescopes in coincidence to detect the outgoing α particle plus one of the ^{5}He breakup particles. Target contamination was minimized by preparing the self-supporting ^{7}Li target immediately before the experiment and by surrounding it with a liquid nitrogen trap throughout the experiment. Data were handled with the PIDGATE program[2] and coincidence data were recorded on tape and were analyzed off-line.

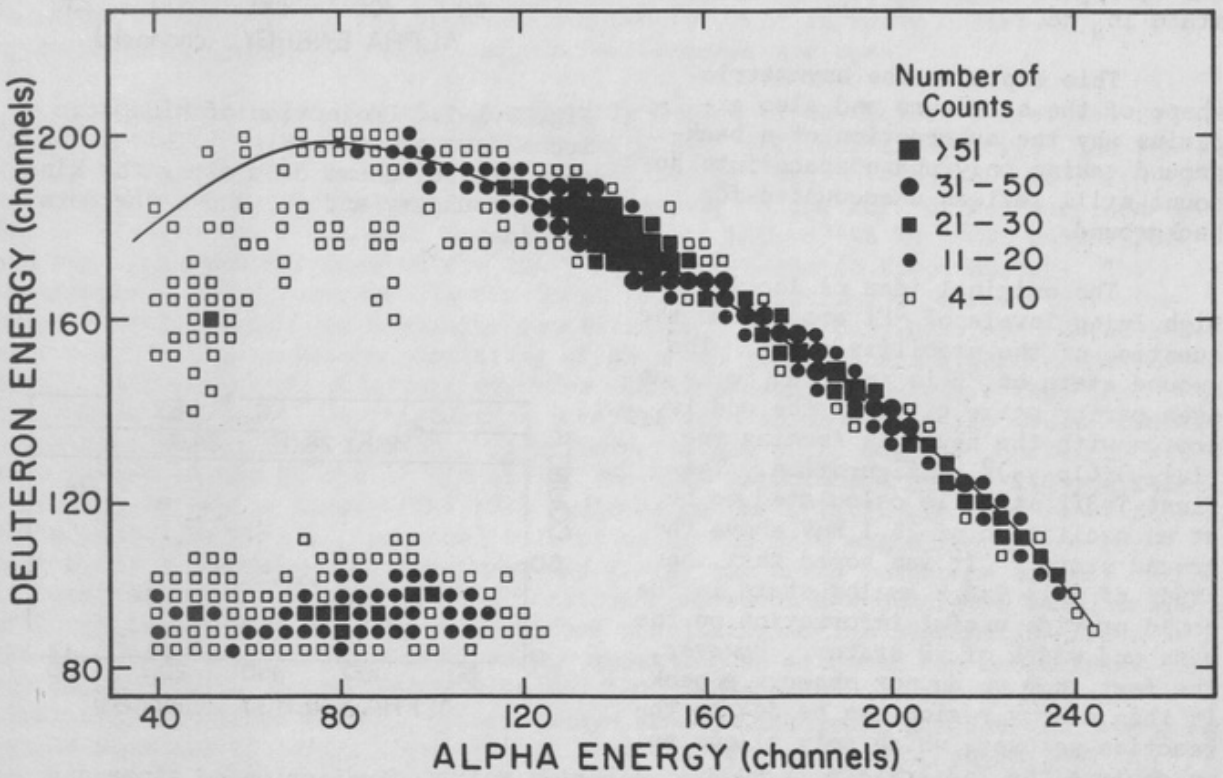

Fig. 5.1-1. Kinematic locus data from detection of alphas and deuterons at 20 deg. and 90 deg. respectively. The reaction is ^{7}Li(d,(α,d)) with a 24 MeV deuteron beam.

Figure 5.1-1 shows the observed alpha-deuteron coincidence spectrum in the bombardment of ^{7}Li by deuterons. The solid line indicates the kinematic boundary. The projections of this coincidence spectrum along and outside the 3 body kinematic boundary onto the E_{α} axis are shown in Fig. 5.1-2. The former is dominated by the state from the $^{7}Li(d,d')^{7}Li(4.6\ MeV)$ reaction with the excited state of ^{7}Li breaking up into α and t. The absence of the 28 MeV structure in the coincidence α spectrum outside the kinematic boundary and in the α spectrum in coincidence with t (Fig. 5.1-3), together with the strong ^{7}Li (4.6 MeV) breakup state, probably mean that the 28 MeV state we saw in the singles spectra came from the $^{7}Li(4.6\ MeV)$ state, rather than from a high-lying state in ^{5}He.

This explains the asymmetric shape of the structure and also explains why the subtraction of a background taking only phase space into account still left an unaccounted-for background.

The original idea of looking for high lying levels of ^{5}He arose from the question of the stability of ^{5}H. The ground state of ^{5}H is expected to be an even parity state given by the odd $1s_{1/2}$ proton with the neutrons forming the $(1s_{1/2})^{2}(1p_{3/2})^{2}$ configuration. The first T=3/2 state is calculated to be at an excitation of 26.1 MeV above the ground state.[3] It was hoped that the study of this T=3/2 analog state in ^{5}He could provide useful information on the mass and width of ^{5}H states. However, the fact that we do not observe a peak in this energy region can be due to the reaction we used, which only allows us to observe the T=3/2 state if such states have a sizable T=1/2 admixture.

There are a variety of theoretical predictions of high excited states of ^{5}He above 24 MeV.[3,4] So far we have

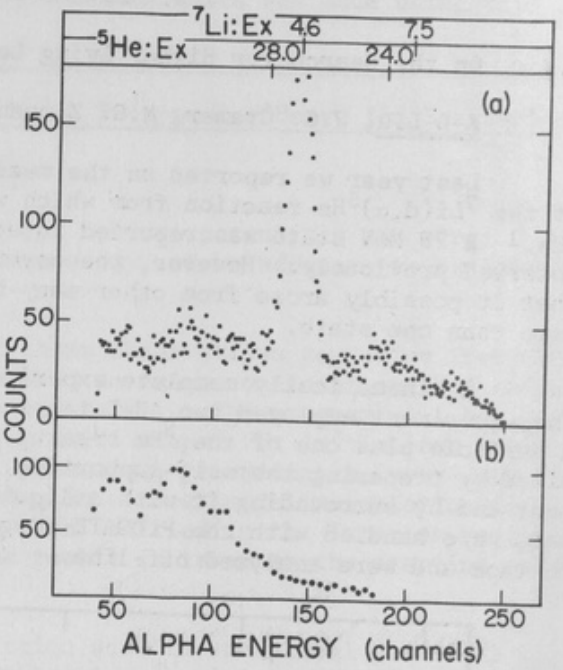

Fig. 5.1-2. Projection of kinematic α locus data shown in Fig. 5.1-1 on the α channels (a) Shows data along the kinematic boundary and (b) shows the data outside.

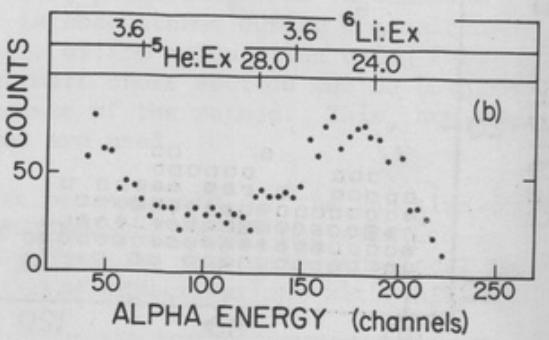

Fig. 5.1-3. Projection of alpha and triton coincidence data onto the alpha axis. The alpha and triton are detected at 20° and 90° respectively. The reaction is the same as in Fig. 5.1-1.

not been able to find experimental evidence for any of them. The fact that at such high excitation ^{5}He is very particle unstable makes for wide levels. Measurement and interpretation of possible states therefore becomes very difficult.

---

1. Nuclear Physics Laboratory Annual Report, University of Washington (1974), p. 37.
2. See Sec. 4.4 of this report.
3. P.F. Fraser and B.M. Spicer, Aust. J. Physics *19*, 893 (1966).
4. R.F. Wagner and C. Werntz, Phys. Rev. C *4*, 1 (1971).

5.2 Isospin Forbidden Charged Particle Decays of the Lowest T=2 States in ^{8}Be, ^{8}Li and ^{12}C*

E.G. Adelberger, S. Freedman†, D.R. Goosman††, A.B. McDonald‡, A.V. Nero†, and R.G.H. Robertson§

Light nuclei form the most interesting systems in which to study isospin forbidden decays because the large variety of open channels provides a rich "window" on the isospin impurity which is not present in heavy nuclei (e.g., the upper sd shell) where in effect only a few channels are open.

We have studied the charged particle decays of the lowest T=2 states in ^{8}Be, ^{8}Li and ^{12}C at the Princeton University AVF cyclotron laboratory. The T=2 levels were populated using the reactions ^{10}Be(p,t)^{8}Be, ^{10}Be(p,^{3}He) and ^{14}C(p,t)^{12}C induced by 46.1 MeV protons. The ^{10}Be target was in the form of BeO enriched to 94% in ^{10}Be.[1] The ^{14}C target was nominally enriched to 94% in ^{14}C. Outgoing t and ^{3}He ions were detected at $\theta = 26.7°$ in a QDDD magnetic spectrometer. The spectrograph had a telescope in the focal plane consisting of a resistive wire proportional counter and a plastic scintillator. Decay particles were detected at $\theta = 120°$ in a telescope consisting of 35 μ and 1000 μ surface barrier detectors. Four parameter data were recorded event-by-event on magnetic tape for subsequent playback. The parameters recorded were ΔE and E' in the decay counter, a position signal from the focal plane detector and a TAC signal. Hardwired gates were placed on the ΔE and E' signals of the QDDD detectors. Ordinarily the large variation in orbits through the QDDD would cause the coincidence time resolution to be poor. We have circumvented this by using the QDDD signal to select the beam burst associated with the event and timing the decay telescope against the RF beam structure. A singles QDDD position spectrum was accumulated simultaneously with the coincidence data so as to reduce possibilities for systematic errors in the branching ratios. As a test of our apparatus we measured the branching ratios for proton decays of the 8.90 MeV $1/2^{-}$ level of ^{13}N to the ground and first excited states of ^{12}C. These decays must be isotropic and the two branching ratios must sum to unity. Preliminary analysis of the ^{8}Be data shows that the decays are in excellent qualitative agreement with the calculations of Barker and Kumar[2] with the dominant decay being to ^{6}Li(0.0) + d. This must be considered an outstanding success for the theory. A preliminary analysis of the ^{8}Li decays reveals sizable branches to t+α+n continuum. The decays of ^{8}Li (T=2) are interesting because the Coulomb force cannot mix states in ^{8}Li with the configuration

$(1p)^4$ based on an inert ^{4}He core because there is only one charged particle. The ^{12}C data has not yet been analyzed.

---

* This work supported in part by the National Science Foundation.

† Permanent address: Princeton University, Princeton, New Jersey.
†† Permanent address: Lawrence Livermore Laboratory, Livermore, California.
‡ Permanent address: Chalk River Nuclear Laboratories, Chalk River, Canada.
§ Permanent address: Michigan State University, East Lansing, Michigan.

1. D.R. Goosman, Nucl. Instrum. Meth. *116*, 445 (1974).
2. F.C. Barker and N. Kumar, Phys. Lett. *30B*, 103 (1969).

5.3 Gamma Decays of the Lowest T = 3/2 Levels in ^{9}Be and ^{9}B

P.A. Dickey, P. Dyer, and K.A. Snover

The charge symmetry concept, which implies that corresponding $\Delta T = \pm 1$ gamma ray transitions in isospin conjugate nuclei should be identical, derives from the decomposition of the electromagnetic current into isoscalar and isovector but not isotensor terms, and from the vanishing of the isoscalar interaction for $\Delta T = \pm 1$. Measurement of the isospin forbidden particle decays[1] of the lowest T = 3/2 levels in the mass 9 mirror nuclei ^{9}Be and ^{9}B has shown that the T = 1/2 admixtures in these levels are probably on the order of 0.5% or less in amplitude. Thus if a comparison of the M1 gamama decays of the T = 3/2 levels to the ground and second excited states in these nuclei (see Fig. 5.3-1) should reveal differences inconsistent with these isospin admistures, one could attribute them to isotensor currents or failure of charge symmetry in the nuclear wave functions. In addition to the M1 decays mentioned there are a number of E1 decays to other low lying excited states and these branches have not been measured before.

The gamma ray decays of the lowest T = 3/2 levels in ^{13}C and ^{13}N have been investigated by Cocke *et al.*[2] and more recently at this Laboratory by Marrs *et al.*[3] The latter experiment benefitted from superior gamma ray energy resolution which permitted clean separation of the γ_0 and γ_2 decay components, although γ_2 and γ_3 were not resolved. The most precisely measured quantity in that experiment was the ratio

$$R = (B_{\gamma_2} + B_{\gamma_3})/B_{\gamma_0},$$

where the quantities B_γ are the reduced transition-strengths. It was found that $R = 1.77 \pm 0.11$ for ^{13}C and 1.83 ± 0.14 for ^{13}N. This result implies a one standard error limit of 2.1% for the ratio of isotensor to isovector amplitudes A_2/A_1 for the favorable case in

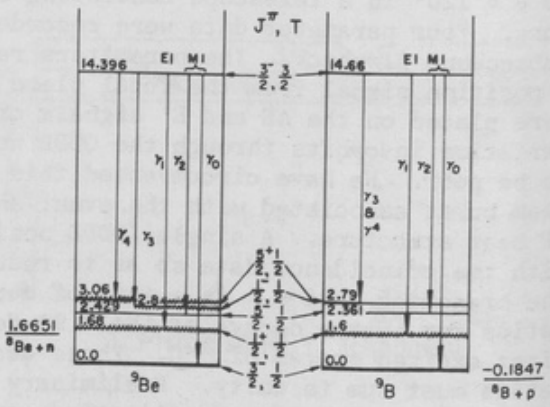

Fig. 5.3-1. Partial level schemes of mass 9 mirror nuclei.

which A_2/A_1 has one sign for the ground state transition and the opposite sign for the excited state transition. Any other combination of phases would suppress the effect of the A_2 term. A factor of two asymmetry was seen in the $\Delta T = 1$, E1 transitions to the first excited states in mass 13. Since a similar asymmetry exists for the first excited state to ground state $\Delta T = 0$ transitions for which the isotensor interaction vanishes, and since the magnitude of the effect seems too large to be accounted for by binding effects, the asymmetry was attributed to failure of charge symmetry in the nuclear wave functions.

The mass 9 gamma decays have also been investigated by Cocke *et al.*[4] No isospin violating effects were seen; however, the energy resolution of their gamma ray spectrometer precluded a clean separation of γ_0 and γ_2 and obscured entirely the E1 decays. In addition, the ratio $\Gamma_{\gamma_0}/\Gamma_{\gamma_2}$ was measured with a different detector in different geometry from the rest of the measurements. For these reasons we have undertaken a measurement of the mass 9 T = 3/2 γ decay rates. The experiment is in progress at this time and the results here are very preliminary.

The experimental method is essentially the same as that used in the mass 13 experiment.[3] The reactions ^{7}Li(^{3}He,p)^{9}Be and ^{7}Li(^{3}He,n)^{9}B were used to populate the T = 3/2 levels and gamma rays were detected in coincidence with protons or neutrons. Particles were detected at 0° and gamma rays at 125°. The targets consisted of 200 $\mu g/cm^2$ of ^{7}Li evaporated onto 200 $\mu g/cm^2$ Ni backings and were transferred to the scattering chamber in vacuum. The Ni backing was a compromise between immunity to attack by the Li and low hydrogen contamination. For the ^{9}Be measurement a 100 namp beam of 8 MeV ^{3}He was ranged out in a 40 mg/cm^2 Au foil. Protons corresponding to the T = 3/2 level in ^{9}Be emerged with about 1.7 MeV of energy and were detected in a ΔE-E telescope. The ^{9}B measurement used a 9 MeV beam; neutrons were detected with a 1" thick NE 102 plastic scintillator. The gamma ray detection system was the same for the two measurements.

A typical gamma ray spectrum from ^{9}Be resulting from the sorting of the event by event data with software windows in the T = 3/2 proton group and the appropriate channels in the time of flight spectrum is shown in Fig. 5.3-2. The data were collected in about 10 hours. The background due to random coincidences is negligible. The solid curve represents a least squares fit to the data in which four transitions have been included. The lineshapes were obtained from a previous measurement[3] of the NaI response to 15.11 MeV gamma rays. In the fit, the lineshapes and gamma ray energies were fixed and only the amplitudes varied to fit the data.

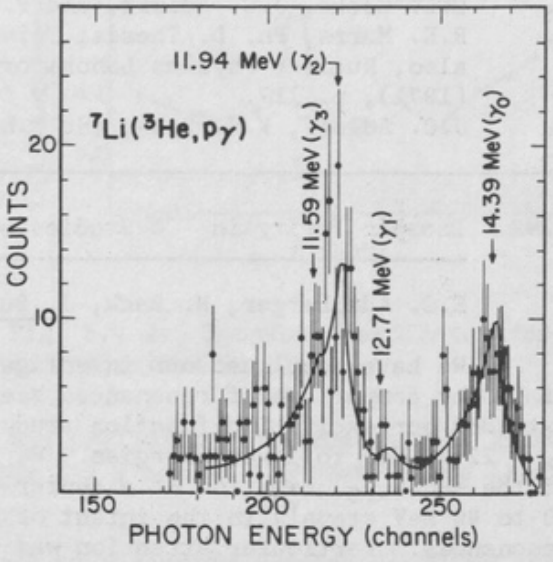

Fig. 5.3-2. Gamma ray spectrum.

After initial runs of about 10 hours for each of the reactions, the data in Table 5.3-1 were obtained. The real to random ratio produced by 100 namps of beam indicates that at least a factor of 3 in beam current is feasible. Running at that current for 40 hours per reaction would yield statistical uncertainties in the ratio R on the same order as those in the mass 13 experiment. The E1 decay branching ratio $\Gamma_{\gamma_1}/\Gamma_{\gamma_0}$ will be much better determined than previously because the necessary gamma rays can be resolved.

Table 5.3-1. Mass 9 Gamma Branching Ratios

	^{9}Be		^{9}B	
Γ_{γ_0}/Γ	.012±.006	(.021±.004*)		
$\Gamma_{\gamma_2}/\Gamma_{\gamma_0}$	1.19±.2	(1.19±.16*)	1.12±.2	(1.39±.2)
$\Gamma_{\gamma_1}/\Gamma_{\gamma_0}$	0.15±.07			
$(\Gamma_{\gamma_3} + \Gamma_{\gamma_4})/\Gamma$	0.16±.1			

* Ref. 4.

1. J.C. Adloff, W.K. Lin, K.H. Souw, and P. Chevallier, Phys. Rev. C *5*, 664 (1972).
2. C.L. Cocke, J.C. Adloff, and P. Chevallier, Phys. Rev. *176*, 1120 (1968).
3. R.E. Marrs, Ph. D. Thesis, University of Washington (1975)(unpublished); also, Nuclear Physics Laboratory Annual Report, University of Washington (1971), p. 117.
4. J.C. Adloff, K.H. Souw, and C.L. Cocke, Phys. Rev. C *3*, 1808 (1971).

5.4 Isospin Purity in ^{16}O Studies by ^{12}C(α,p_0) and ^{12}C(α,n_0)

E.G. Adelberger, N. Back, J. Bussoletti, and K.A. Snover

We have continued our investigation of isospin mixing in continuum states of ^{16}O by comparison of resonances seen in ^{12}C(α,p_0) and ^{12}C(α,n_0).[1] We have extended our excitation function study of the region about the T=2 resonance of E_x = 22.72 MeV to lower energies. We have now measured the excitation function of the ^{12}C(α,p_0) reaction at a center of mass angle of 90° from E_α = 20.3 MeV in 20 to 40 MeV steps with the intent of seeking candidates for isospin mixed resonances. Particular attention was paid to resonances which might be correlated with structure observed in the ^{12}C(α,γ_0) reaction[2] and the ^{15}N(p,γ_0) reaction.[3] Several candidates for both conditions were found. Most of the excitation function seems to be characterized by several broad overlapping resonance.

There are however some regions which seem simpler.

In Fig. 5.4-1 we show the excitation function for the reactions $^{12}C(\alpha,p_0)$ at $\theta_p = 80°$, $^{12}C(\alpha,p_0)$ at $\theta_p = 50°$, and $^{12}C(\alpha,\alpha_0)$ at $\theta_\alpha = 80°$ in the 16 MeV excitation energy region. In the proton channel two resonances appear, one at ∿16.38 MeV with a width of about 80 keV and one at ∿16.44 MeV with a width of about 40 keV. This second state seems to correspond with the 16.407 MeV state listed in the Ajzenberg-Selove[4] compilation on mass 16. The state is described there as having $J^\pi = 2^+$; moreover a peak in the E2 cross section has been observed at this energy in the $^{12}C(\alpha,\gamma_0)$ reaction.[2]

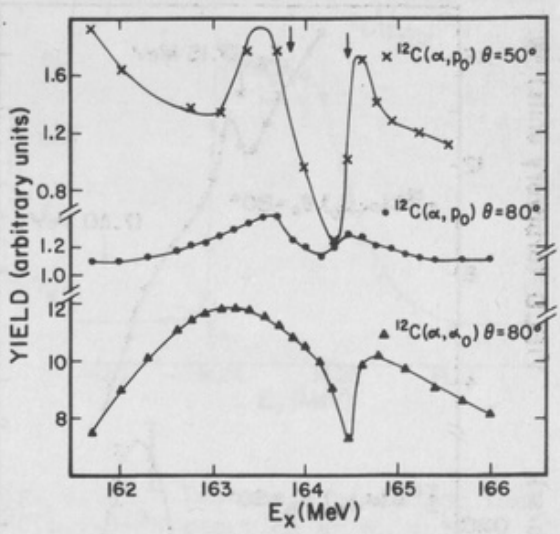

Fig. 5.4-1. Resonances seen in $^{12}C + \alpha$. The upper resonance seems to correspond with a previously reported state at 16.40 MeV with Γ = 45 MeV and $J^\pi = 2^+$.[4] The arrows indicate suggested locations of the resonances.

Figure 5.4-2 shows another interesting region at excitation in mass 16. The two isolated resonances indicated might well form an isospin mixed doublet. A definite conclusion will have to await the comparison with $^{12}C(\alpha,n_0)$ reaction.

Figure 5.4-3 shows a resonance which correlates well in position and width with the 17.142 MeV resonance seen in $^{15}N(p,\gamma_0)$[3] and also observed in $^{12}C(\alpha,\gamma_0)$.[2] We also note the absence of any structure to correspond with the structure seen in both the (α,γ) and (p,γ) work at E_α = 17.30 MeV.

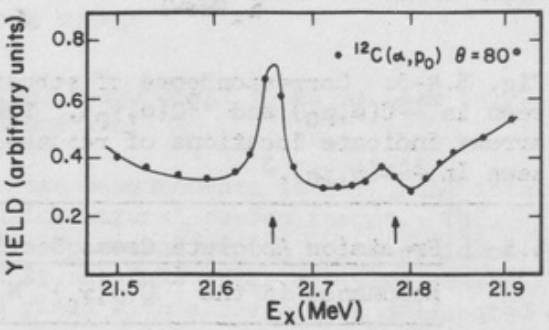

Fig. 5.4-2. Possible candidates for an isospin mixed doublet.

Finally, Fig. 5.4-4 illustrates a region of great interest to us as an understanding of the structure observed here is necessary to enable a determination of the nature of the isospin impurity of the T=2 state.[1] A medium width resonance ($\Gamma \sim 120$ MeV) at E_x = 22.25 MeV appears to be lying on a broad (∿1 MeV) resonance at $E_x \simeq 22.4$ MeV. From the preliminary neutron data it appears that the predominant isospin impurity in the T=2 state is the same as the isospin of the intermediate width resonance.

We intend to complete the proton work by measuring angular distributions on and around these resonances and then proceed with the neutron measurements. Confirmation of our intriguing preliminary indications must await these further measurements.

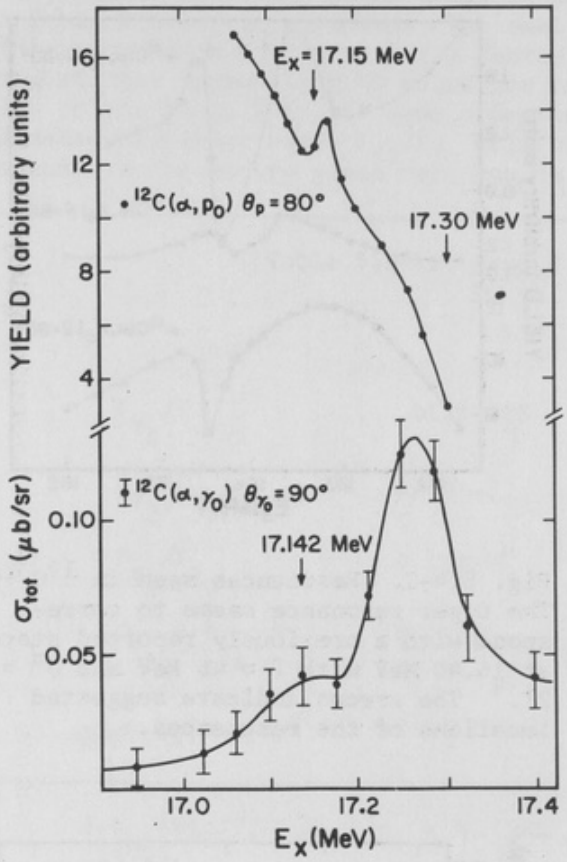

Fig. 5.4-3. Correspondence of structure seen in $^{12}C(\alpha,p_0)$ and $^{12}C(\alpha,\gamma_0)$. The arrows indicate locations of resonances seen in $^{15}N(p,\gamma_0)$.[3]

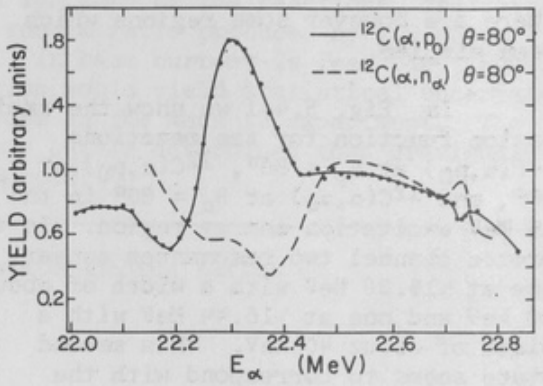

Fig. 5.4-4. Resonant structure near the 0^+ T=2 state in ^{16}O.

1. Nuclear Physics Laboratory Annual Report, University of Washington (1973), p. 32.
2. Nuclear Physics Laboratory Annual Report, University of Washington (1974), p. 141.
3. E.D. Earle and N.W. Tanner, Nucl. Phys. *A95*, 241 (1967).
4. F. Ajzenberg-Selove, Nucl. Phys. *A166*, 1 (1971).

5.5 Precision Absolute Cross Section Measurement for the Lowest T=3/2 Resonance in the $^{12}C(p,\gamma_0)^{13}N$ Reaction

E.G. Adelberger, R.E. Marrs, and K.A. Snover

We have remeasured the absolute yield from the lowest T=3/2 resonance in the $^{12}C(p,\gamma_0)^{13}N$ reaction near E_p = 14.2 MeV, with the purpose of increasing the accuracy of comparison of mirror ΔT=1 γ-decay strengths in mass-13, and providing a precision absolute calibration standard for high-energy γ-rays.

The $^{12}C(p,\gamma_0)^{13}N$ resonance-yield data shown in Fig. 5.5-1 were obtained by bombarding a 1.7 mg/cm^2 natural carbon target with protons from the University of Washington FN Tandem Accelerator. Gamma rays were detected at θ_γ = 125° in the large NaI spectrometer. The data show a ∿12% overshoot on the low-energy edge of the yield curve due to the discontinuous (atomic) energy loss of protons

in the target foil.[1] The solid curve shown in Fig. 5.5-1 is the result of a Monte Carlo calculation, following Costello *et al.*,[2] of the resonance yield including the effects of the discontinuous proton energy loss.

Since the angular distribution of the decay γ rays from an isolated J=3/2 level must have the form $a_0P_0(\cos\theta) + a_2P_2(\cos\theta)$, the step in the total thick-target resonance yield can be obtained from data taken at $\theta_\gamma = 125°$, where $P_2(\cos\theta)$ vanishes. The absolute photopeak efficiency of the detector was determined for 15.1-MeV γ rays using coincidence observation of (tagged) γ-rays from the decay of the 15.1-MeV level in ^{12}C, which was assumed to have $\Gamma_{\gamma_0}/\Gamma = (88.2 \pm 2.1)\%$.[3,4] This J=1 level was populated in the $^{10}B(^3He,p\gamma)^{12}C$ reaction with protons detected at 0° so that the γ-ray angular distribution was also of the form $a_0'P_0(\cos\theta) + a_2'P_2(\cos\theta)$. The $^{12}C(p,\gamma_0)^{13}N$ resonance-yield measurement and the calibration were done consecutively using the same experimental arrangement. Only the target and beam were changed. The resulting absolute calibration (vertical scale in Fig. 5.5-1) is determined to ±3.2%, including ±1% from possible systematic errors in the $^{12}C(p,\gamma_0)$ measurement (such as beam integration), and ±3% from the ^{12}C efficiency calibration.

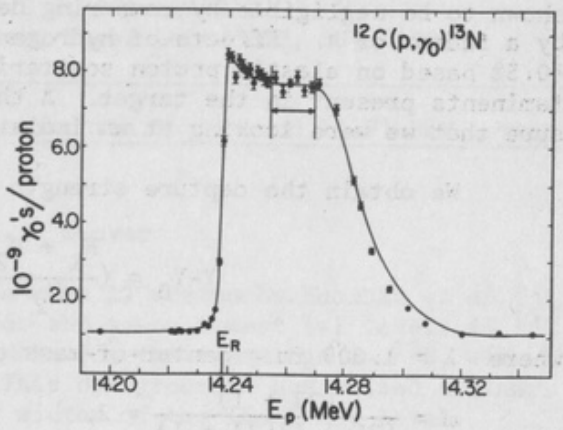

Fig. 5.5-1. Resonance yield for the $^{12}C(p,\gamma_0)^{13}N$ reaction at $\theta_\gamma = 125°$. In addition to the statistical errors shown, there is an overall systematic error of ±3% due to the NaI efficiency calibration. The solid curve results from a Monte Carlo calculation (see text). The plateau region used to obtain the thick-target yield is delineated by the vertical lines. The energy scale was determined from the nominal accelerator calibration rather than the known resonance energy.

The important quantity determined by these measurements is $Y\text{-}Y_0$, the total resonance yield (into 4π) for an infinitely thick natural carbon target. This quantity is the expected resonance yield in the "plateau" region which would be observed with an infinitely thick target, and is obtained after applying small corrections to the difference in the measured yield within the region delineated by vertical bars in Fig. 5.5-1 and the off resonance yield. The result is

$$Y\text{-}Y_0 = (6.83 \pm 0.22) \times 10^{-9}\ \gamma_0\text{'s per incident proton.}$$

This includes the following corrections: (1) +0.7% due essentially to a correction for finite target thickness (determined by the Monte Carlo calculation), (2) +1.1% to account for the fact that $\theta_\gamma = 125.3°$(lab) does not correspond exactly to a zero of $P_2(\cos\theta_{c.m.})$(here we used our measured $a_2 = -0.681 \pm 0.030$) and (3) +1.5% due to the solid angle transformation from laboratory to center-of-mass.

Numerous checks were made to insure that the above result is free from significant systematic errors. For example, errors in dead-time corrections were

shown to be negligible by comparing data taken with counting rates differing by a factor of 4. Effects of hydrogen and oxygen contamination was found to be <0.5% based on elastic proton scattering estimates of the amounts of these contaminents present in the target. A thin-target yield curve was measured to make sure that we were looking at an isolated resonance on top of a flat background.

We obtain the capture strength factor $\Gamma_p\Gamma_{\gamma_0}/\Gamma$ from the following relation

$$Y\text{-}Y_0 = \left(\frac{M_1 + M_2}{M_2}\right) \frac{2\pi^2\lambda^2}{\varepsilon}\, \omega f\, \frac{\Gamma_p\Gamma_{\gamma_0}}{\Gamma}$$

where λ = 1.308 fm = center-of-mass proton wave length

$\omega = \frac{(2J + 1)}{(2S + 1)(2J + 1)} = 2.$

f = 0.989 = fraction of ^{12}C in natural carbon

$\varepsilon = dE_L/dn$ = laboratory stopping power for carbon at E_p = 14.23 MeV (calculated from dE/dK = 30.75 ± 0.31 keV/mg/cm^2)[5]

and the factor $(M_1 + M_2)/M_2$ converts ε to the center-of-mass system.[6] The result is

$$\Gamma_p\Gamma_{\gamma_0}/\Gamma = 5.79 \pm 0.20 \text{ eV}.$$

This value is in good agreement with, and a factor of 4 more accurate than a previous measurement.[7]

The above result should not be significantly affected by interference between the resonance and the background since $\sigma_{res}/\sigma_{back} \approx 230$ and E1 or E2 backgrounds cannot produce interference in a_0. Our data at 125° measure a_0 since the resonance angular distribution was found to have a negligible a_1 coefficient (a_1 = -0.008 ± 0.014).[8]

We may combine this result with a previous measurement of Γ_{p_0}/Γ = 0.236 ± 0.012[9] to obtain Γ_{γ_0} = 24.5 ± 1.5 eV, in agreement with the value measured for the ^{13}C mirror decay of $\Gamma_{\gamma_0}(^{13}C)$ = 23.3 ± 2.7 eV.[10] For a more detailed discussion of the comparison of mirror γ-decays in mass-13, see Sec. 11.2 of the 1974 Annual Report.

---

1. H.W. Lewis, Phys. Rev. *125*, 937 (1962).
2. D.G. Costello *et al.*, Phys. Rev. *51*, 113 (1964).
3. D.E. Alburger and D.H. Wilkinson, Phys. Rev. C *5*, 384 (1972).
4. D.P. Balamuth, R.W. Zurmuhle, and S.L. Tabor, Phys. Rev. C *10*, 975 (1974).
5. H. Bichsel in *American Institute of Physics Handbook*, 3rd Edition (McGraw-Hill, 1972), p. 8142 and private communication.
6. K.A. Snover, Ph.D. Thesis, Stanford University (1969), unpublished.
7. F.S. Dietrich, M. Suffert, A.V. Nero, and S.S. Hanna, Phys. Rev. *168*, 1169 (1968).
8. The Legendre coefficients were determined in the center of mass system.

9. E.G. Adelberger *et al.*, Phys. Rev. C *7*, 889 (1973).
10. G. Wittwer, H.G. Clerc and G.A. Beer, Phys. Lett. *30B*, 634 (1969).

5.6 Measurement of the γ-Decay Branches for the 16.11- and 12.71-MeV Levels in ^{12}C

E.G. Adelberger, R.E. Marrs, and K.A. Snover

In a study of the T=1 states in the mass 12 system by Monahan *et al.*[1] it was pointed out that the nucleon widths for the seven lowest T=1 levels in ^{12}C are in satisfactory agreement with the widths for their analogs in ^{12}B, with the exception of the 2^+ level at 16.11 MeV. This disagreement has raised a minor controversy concerning the particle and γ widths of the 16.11-MeV level.

A recent measurement of the proton width for the 16.11-MeV level by Anderson *et al.*[2] showed the previous value of Γ_p to be a factor of three too large. Because the $^{11}B(p,\gamma)$ resonant cross section, which directly connects Γ_p and Γ_γ, was found to be correct the new value of Γ_p implies that the previous value of Γ_γ is a factor of three too small. Anderson *et al.* attempted to directly measure the γ-ray branching ratio for the 16.1 MeV state but were not successful.[2] Instead they derived a value of $(3.23 \pm 0.50) \times 10^{-3}$ for Γ_γ/Γ from their measurements of the $^{11}B(p,\alpha)$ and $^{11}B(p,\gamma)$ cross sections.[2]

Figure 5.6-1 shows our γ-ray spectrum corresponding to the decay of the 16.11-MeV level in ^{12}C. The spectrum was obtained from $^{10}B(^3He,p\gamma)$ coincidences data taken at $E_{^3He}$ = 4.1 MeV using a 150 μg/cm^2 enriched ^{10}B target. Protons were detected at 0° in a counter consisting of ΔE and E' detectors covered with a thin foil sufficient to stop the ^3He ions while allowing the protons of interest to pass through. Gamma rays were detected at 125° in the 10"×10" NaI spectrometer. Data was event-mode recorded on magnetic tape and sorted on subsequent playback. Most of the γ-decay strength goes to the 4.44-MeV level, producing a γ ray of 11.67 MeV. Spectra obtained separately at γ-ray angles of 30°, 90°, and 125° have been summed to generate the spectrum shown in Fig. 5.6-2.

The apparent weak γ-ray yield at 15.11 MeV is actually in coincidence with background under the $^{12}C(16.11)$ proton group as can be seen by looking at part (b) of the figure. A 4% background correction was made to the final $^{12}C(16.11)$ γ-ray yield on the basis of Fig. 5.6-1b. The solid curve in Fig. 5.6-1a results from a least-squares fit to the data using the measured NaI lineshape. However, since the number of counts is small, the yield of 11.67-MeV γ rays was obtained by summing counts in the region of the full-energy peak rather than from the lineshape fit.

Since the $^{12}C(16.11)$ proton group appears as a well isolated peak in the singles particle spectrum at 0°, it is possible to extract a reliable γ-decay branching ratio for the 16.11-MeV level from the yield of 11.67-MeV γ rays. The 11.67-MeV $(2^+,T=1)\rightarrow(2^+,T=0)$ transition, since it is purely isovector, is expected to be primarily of M1 multipolarity with a small E2 admixture. The γ branching ratio was determined by fitting the data obtained at θ_γ = 30, 90, and 125° to the expression $a_0P_0(\cos\theta) + a_2P_2(\cos\theta) + a_4P_4(\cos\theta)$.

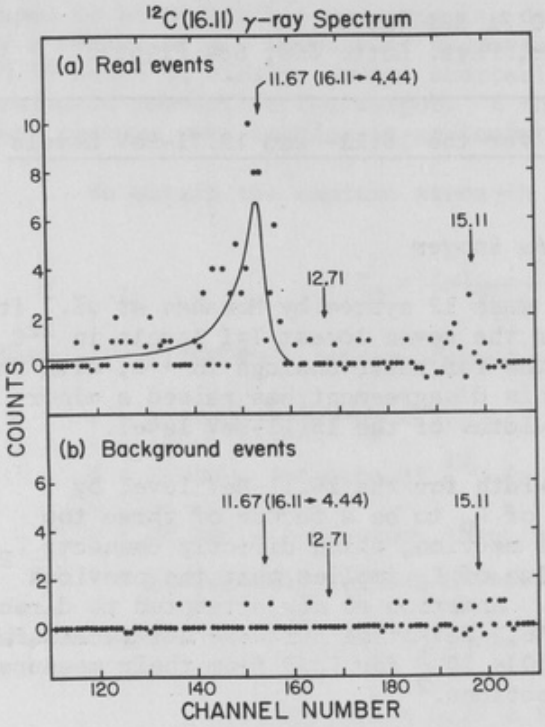

Fig. 5.6-1. (a) Gamma-ray spectrum corresponding to decay of the 16.11-MeV level ion ^{12}C. The solid curve is the result of a least-squares fit using the lineshape measured at 15.11 MeV. (b) Gamma-ray spectrum in coincidence with a region of the particle spectrum adjacent to the ^{12}C(16.11) proton group. The non-integral counts result from the procedure used to subtract the randoms contribution from both spectra. Gamma-ray energies are identified by the vertical arrows.

The resulting value for the γ branch of the ^{12}C(16.11) level is $\Gamma_\gamma/\Gamma = (2.49 \pm 0.30) \times 10^{-3}$, which is in acceptable agreement with but more precise than the value determined indirectly by Anderson *et al.*[2] This value for the total γ branching-ratio was determined from the γ_1 branch using a value of 97% for the fraction of the total ^{12}C(16.11) γ-decay branch which goes to the 4.44-MeV level.

Using the value of 6.7 ± 0.5 keV known for the total width of the 16.11-MeV level[4] our value for Γ_γ/Γ implies a value of Γ_{γ_1} = 16.1 ± 2.3 eV for the (16.11→4.44) transition. This result may be compared with the (8-16)2BME calculations of Cohen and Kurath,[5] which predict a value of 10.7 eV for this transition.

A value for the γ branch of the 12.71-MeV level in ^{12}C has been obtained in a similar manner. A spectrum of γ rays from the decay of the 12.71 MeV state is shown in Fig. 5.6-2. Since the yield of γ rays was larger than that for the 16.11-MeV level, a least-squares lineshape fitting procedure was used in analyzing the ^{12}C(12.71) data. The resulting value for the ground-state branching ratio is Γ_{γ_0}/Γ = (1.93±0.12)%. The data obtained at 30, 90, and 125° was fitted to an angular distribution of the

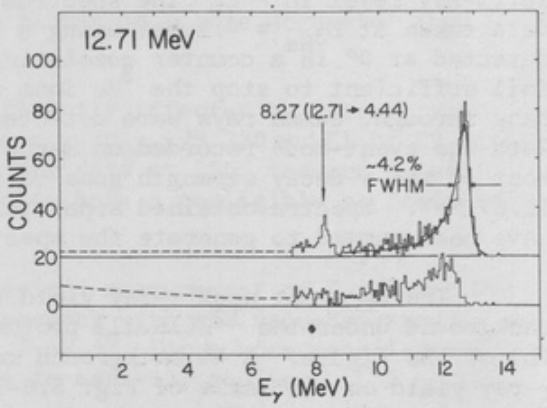

Fig. 5.6-2. Spectrum of gamma rays in coincidences with deuterons populating the 12.71 MeV level of ^{12}C. The figure contains the spectra accepted and rejected by the anticoincidence shield. The accepted spectrum has been shifted up by 20 counts/channel. The spectrum is not shown below 7 MeV due to the presence of background gamma rays.

form $a_0P_0(\cos\theta) + a_2P_2(\cos\theta)$ in order to derive this result. The most precise previous measurement of this branching ratio[6] is $\Gamma_{\gamma_0}/\Gamma = (2.4 \pm 0.3)\%$.

The importance of the $^{12}C(12.71)$ branching ratio comes from its role in understanding the mixing between the T=1 and T=0 1^+ levels in ^{12}C at 15.11 and 12.71 MeV, respectively. This problem has been discussed recently by Balamuth *et al.*[7] who review the different experimental approaches to a determination of the charge-dependent matrix element between the T=0 and T=1 levels.

It is also possible to obtain the relative γ-ray branches for decay of the 12.71-MeV level to the ground and 4.44-MeV levels of ^{12}C. The spectrum shown in Fig. 5.6-2 yields a branching ratio of $\Gamma_{\gamma_1}/\Gamma_{\gamma_0} = 0.150 \pm 0.018$ for these transitions. Because the data are not representative of decays from the 12.71-MeV level below approximately 7 MeV due to the presence of background γ-rays, it is not possible to see γ-ray branches to the levels at 7.65 MeV and above in ^{12}C. If one assumes that these other transitions have zero strength, relative γ-ray branches of (13.0 ± 1.4) and (87.0 ± 1.4)% are obtained for the transitions to the 4.44-MeV and ground states, respectively. These numbers may be compared with values of (15 ± 4) and (85 ± 4)% obtained for the same branches by Alburger and Wilkinson,[8] and with values of (17 ± 3) and (83 ± 3)% obtained by Reisman *et al.*[6] who also obtained an upper limit of 10% for the branch to the 7.65-MeV level.

1. J.E. Monahan, H.T. Fortune, C.M. Vincent, and R.E. Segal, Phys. Rev. C *3*, 2192 (1971).
2. B.D. Anderson, M.R. Dwarkanath, J.S. Schweitzer, and A.V. Nero, Nucl. Phys. *A233*, 286 (1974).
3. F. Ajzenberg-Selove and T. Lauritsen, Nucl. Phys. *A114*, 1 (1968).
4. R.E. Segal and M.J. Bina, Phys. Rev. *124*, 814 (1961).
5. S. Cohen and D. Kurath, Nucl. Phys. *73*, 1 (1965).
6. F.D. Reisman, P.I. Connors, and J.B. Marion, Nucl. Phys. *A153*, 244 (1970).
7. D.P. Balamuth, R.W. Zurmühle, and S.L. Tabor, Phys. Rev. C *10*, 975 (1974).
8. D.E. Alburger and D.H. Wilkinson, Phys. Rev. C *5*, 384 (1972).

5.7 The $^{13}C(p,p')^{13}C^*$(15.1 MeV,T=3/2) Reaction from E_p = 18.7 to 20.0 MeV

E.G. Adelberger, P. Paul, and K.A. Snover

A distinct ($\Gamma \approx 500$ keV) resonance was apparent at E_p = 18.8 MeV in preliminary data[1] on the $^{13}C(p,\gamma_1)^{14}N^*(0^+,T=1)$ reaction at $\theta_\gamma = 90°$. No resonance was apparent in the $^{13}C(p,\gamma_0)^{14}N$ reaction at this energy, prompting speculation that this resonance may have isospin T=2. If the resonance is T=2 it should show up strongly in the $^{13}C(p,p')^{13}C^*$(15.1 MeV,T=3/2) reaction, since the outgoing channel in this reaction is isospin allowed.

Measurements were made with a thin carbon-13 target. The proton beam was obtained using the FN injector and the inelastic protons were detected at scatter-ingle angles between 90° and 130° in a telescope of 2 silicon surface-barrier transmission detectors of thicknesses 30μ and 176μ, followed by a thick reject

detector. A coincidence was required between the first 2 detectors, which eliminated a substantial background from noise and from neutron and γ interactions. Peaks were apparent in the particle spectra from $^{13}C(p,p')^{13}C(15.1)$ and, at a lower energy, from $^{12}C(p,p')^{12}C(15.1)$, the latter from ^{12}C contaminations in the target.

Excitation curves for $^{13}C(p,p')^{13}C(15.1)$ measured at two different angles are shown in Fig. 5.7-1. Data were obtained down to E_p = 18.6 MeV for the θ = 102° angle (the points at 18.6 MeV have a large uncertainty because of distortions in the particle spectra due to the energy cutoff caused by the coincidence condition). No resonance is apparent at 18.8 MeV.[2]

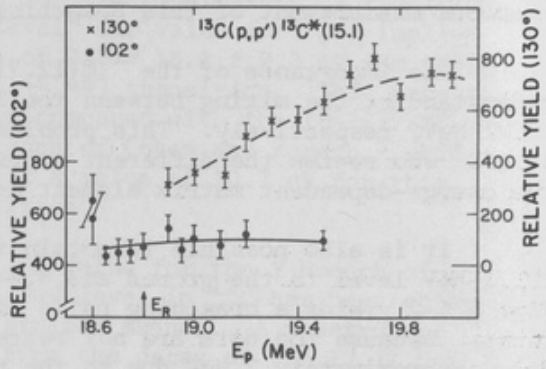

Fig. 5.7-1. Yield curves for the $^{13}C(p,p')^{13}C^*(T=3/2)$ reaction. The arrow indicates the proposed position of the $^{13}C(p,\gamma_1)^{14}N^*(0^+,T=1)$ resonance.

1. P. Paul, H. M. Kuan, and E.K. Warburton, private communication.
2. A re-investigation of the $^{13}C(p,\gamma_1)^{14}N$ reaction[1] has since shown the original data to be in error.

5.8 Gamma Ray and Alpha Particle Decays of Some T=0, T=1 and T=2 Levels of ^{20}Ne

E.G. Adelberger, R.E. Marrs, and K.A. Snover

Introduction:

The study of γ decays in ^{20}Ne reported last year[1] has been completed. Our attention was drawn to this problem by some puzzling features in the γ decay of the 18.43 MeV $J^\pi,T=2^+,2$ state in ^{20}Ne reported by a Stanford group.[2] They found that the decays cascaded via a $J^\pi,T=2^+,1$ state at 12.25 MeV, and that the 12.25 MeV state deexcited by gamma ray emission even though it is unbound to particle emission by 7.52 MeV. The M1 strength of the $(J^\pi,T=2^+,2)$ $(J^\pi,T=2^+,1)$ transition was found to be relatively weak (0.06 W.u.). This is a sharp exception to all of the other known isovector M1 transitions involving low lying T=2 states which are notably faster. The Stanford value for the M1 width of the 18.43 MeV state was obtained by assuming that the 12.25 MeV T=1 state decays 100% by γ emission to the 1.63 MeV state of ^{20}Ne. If the branching ratio were less than unity it would of course necessitate an increase in the value for Γ_γ of the 18.43 MeV states. On the other hand if the 12.25 MeV state does have $\Gamma_\alpha \lesssim \Gamma_\gamma$ and in fact has $J^\pi = 2^+$ the remarkably inhibited α decay would correspond to a spectacularly pure isospin for the 12.25 MeV level. We have made a coincidence study of the $^{19}F(^3He,d\gamma)^{20}Ne$ reaction in order to determine the γ-ray branching ratios of 4 levels in the excitation energy region from 9.5 to 12.5 MeV.

Experiment:

Figure 5.8-1 shows singles and coincident particle spectra obtained at $\theta_d = 0°$ with $E(^3He) = 15.0$ MeV and $\theta_\gamma = 125°$. The singles and coincident spectra were accumulated simultaneously with the same detector, and the coincidence data were recorded on magnetic tape event-by-event for later analysis as described elsewhere.[1,3] All of the levels indicated by arrows in Fig. 5.8-1 were observed to have substantial γ-decay branches except for the 11.23-MeV level, which is very weakly populated in the $^{19}F(^3He,d)$ reaction.

The $^{20}Ne(12.25)$ deuteron group is incompletely resolved from a group corresponding to a level at approximately 12.40 MeV which α decays to the 6.13-MeV level in ^{16}O, as shown by sorting the event data with a window on γ rays of that energy. Hence the ratio of the coincidence and singles yields for ^{20}Ne (12.25) was determined from only the rightmost portion of the deuteron group, as illustrated in Fig. 5.8-1.

Figures 5.8-2-5 shows the coincident γ-ray spectra associated with each of the four prominent deuteron groups identified in Fig. 5.8-1. Only the spectra obtained at $\theta_\gamma = 125°$ are shown, but similar spectra were obtained at $\theta_\gamma = 45$, 70, and 90° in order to measure the γ-ray angular distributions. The solid curves are least-squares fits to the γ-ray data using the known NaI lineshape (measured at $E_\gamma = 15.1$ MeV with the $^{10}B(^3He,p\gamma)^{12}C$ reaction).[3,4] The γ-decay schemes for each of the levels are also diagrammed in Figs. 5.8-2-5.

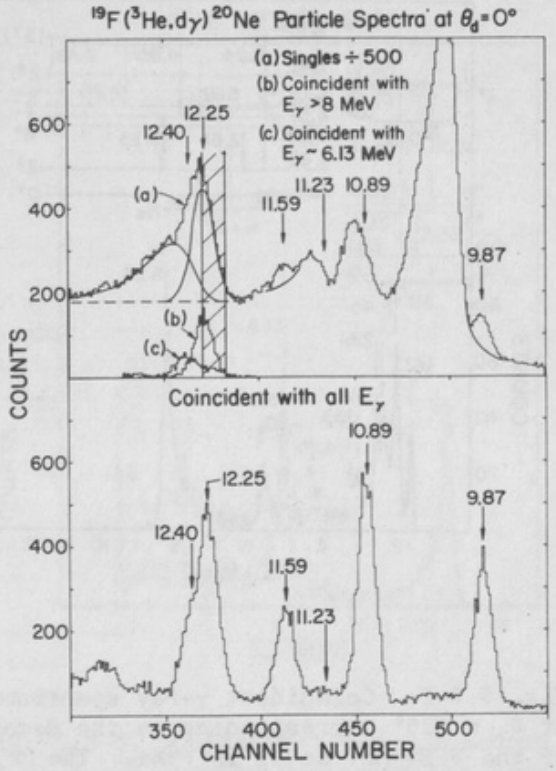

Fig. 5.8-1. Singles and coincident particle spectra obtained with the $^{19}F(^3He,d\gamma)^{20}Ne$ reaction at $E(^3He) = 15.0$ MeV, $\theta_d = 0°$ and $\theta_\gamma = 125°$. The vertical arrows correspond to levels in ^{20}Ne. The solid curves indicate the background underlying the 9.87- and 11.59-MeV peaks, and the separation of the 12.25-MeV contribution from the unresolved group of peaks at the left of the figure. The cross-hatched region was used in computing Γ_γ/Γ for the $^{20}Ne(12.25,T=1)$ level. The large peak at approximately channel 500 in the singles spectrum is due to the $H(^3He,p)$ reaction. (Hydrogen is a target contaminant.)

Discussion:

Our measured absolute and relative γ-ray branching ratios are presented in Table 5.8-1. The γ-ray branching ratio of the 12.25 MeV level is listed only as a lower limit. This is done because a deuteron group from $^{16}O(^3He,d)$ reaction lies near the 12.25 MeV group in the singles spectrum. By comparing our coinci dence spectrum with the good resolution spectrum of Betts, Fortune and Middleton[5]

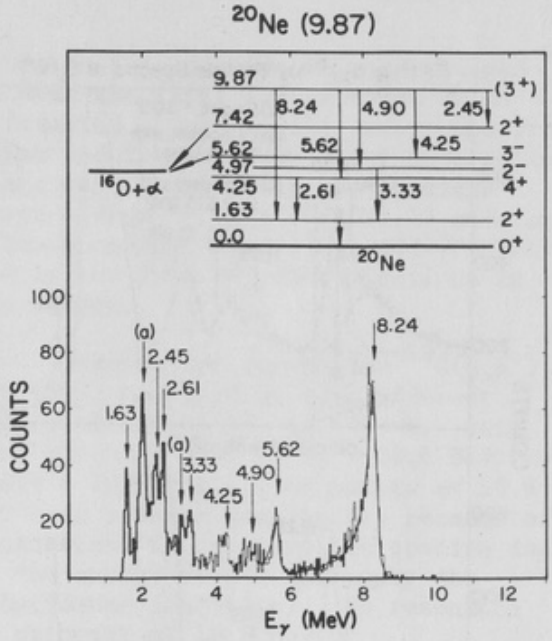

Fig. 5.8-2. Coincident γ-ray spectrum at θ_γ = 125° corresponding to the decay of the 9.87-MeV level in ^{20}Ne. The solid curve is a least-squares fit used to obtain both the energies and intensities of the two strongest transitions. The γ rays labeled (a) at approximately 2.0 and 3.0 MeV are attributed to a level in ^{21}Ne produced via ^{19}F(^{3}He,p) which proton decays to low-lying levels of ^{20}F. The 2.0-MeV γ ray is also produced in the ^{19}F(^{3}He,2p)^{20}F reaction and appears in all the γ-ray spectra.

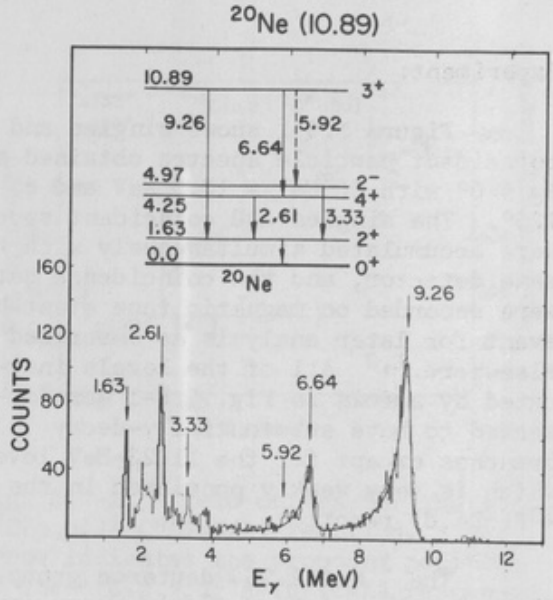

Fig. 5.8-3. Coincident γ-ray spectrum at θ_γ = 125° corresponding to the decay of the 10.89-MeV level in ^{20}Ne. The solid curve is a least-squares fit.

Table 5.8-1. Gamma-ray branching ratios for levels in ^{20}Ne populated with the ^{19}F(^{3}He,dγ)^{20}Ne reaction. The excitation energies are accurate to within ±40 keV. The absolute γ branching ratios (Γ_γ/Γ) include all the observed transitions. The last three columns list the indicated relative γ branching ratios.

J^π,T	E_x(MeV)	Γ_γ/Γ	BR($\frac{0.0,\ 0^+}{1.63,2^+}$)	BR($\frac{4.25,4^+}{1.63,2^+}$)	BR($\frac{4.97,2^-}{1.63,2^+}$)
(3^+),0	9.87[a]	0.82±0.27	<0.007	0.16±0.03	≤0.06
3^+, 1	10.89	large	<0.025	0.30±0.02	≤0.05
$(3^+,0)$	11.59	1.1 ±0.4	<0.01	0.60±0.06	<0.10
(2^+),1	12.25	≥0.23±0.10	≤0.015	<0.03	≤0.04

a) In addition, for ^{20}Ne(9.87)

$$BR(\frac{5.62,3^-}{1.63,2^+}) \sim 0.09,\quad BR(\frac{7.42,2^+}{1.63,2^+}) \sim 0.04$$

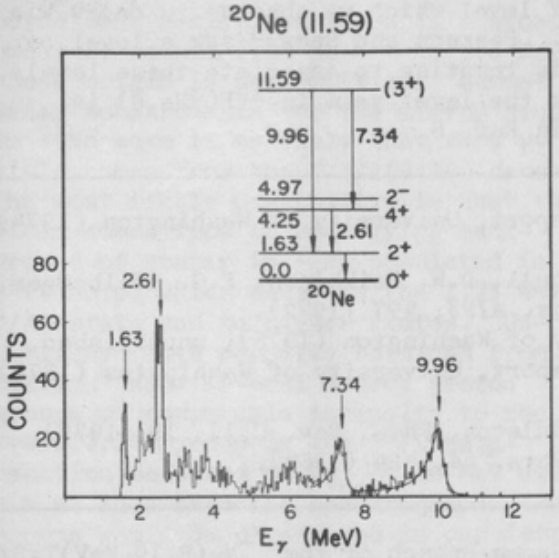

Fig. 5.8-4. Coincident γ-ray spectrum at θ_γ = 125° corresponding to the decay of the 11.59-MeV level in ^{20}Ne. The solid curve is a least-squares fit.

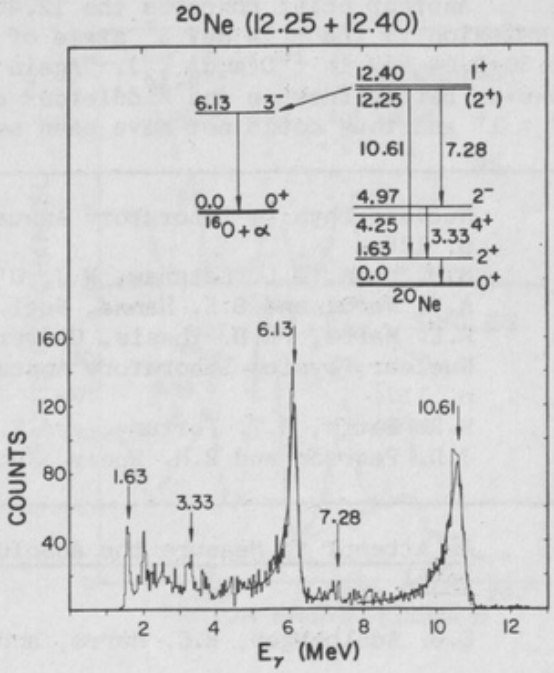

Fig. 5.8-5. Coincident γ-ray spectrum at θ_γ = 125° corresponding to the decay of the 12.25- and 12.40-MeV levels in ^{20}Ne. The 6.13- and 10.61-MeV γ rays were fitted separately over the regions shown by the curves.

also taken at $E_{^3He}$ = 15 MeV but at θ = 7.5°, we estimate that the branching ratio is consistent with unity. The spin and parity assignments listed in the table are taken primarily from Ref. 5, but they are supported by the decay schemes and γ-ray angular distributions observed in the present measurement. The excitation energies listed in the table are accurate to ∿40 keV and were determined from an energy calibration of the γ-ray detector.

However, there are some unexplained puzzles in our results. If the 12.25 MeV level is really a 2$^+$,T=1 state as argued fairly persuasively in Ref. 5, we are faced with an enormously hindered α particle width (Γ_α on the order of eV). To place this in perspective a "single particle" estimate for an α width at this energy in ^{20}Ne is ∿6 MeV. One explanation for this of course is that the level does not in fact have natural spin and parity. However a level at E_x = 12.25 ± 0.04 MeV has been seen in the ^{16}O(α,γ) reaction by Pearson and Spear.[6] It is tempting to associate the state they see with the 12.25 MeV "2$^+$" state seen in ^{19}F(^{3}He,d) since both levels decay exclusively to the 1.63 MeV state of ^{20}Ne. The width Γ = 40±16 keV quoted for the 12.25 MeV level in Ref. 6 is inconsistent with the large γ branch observed in our work. However the data in Ref. 6 were taken in 40 keV steps so the width may not be reliable. In an attempt to resolve this point we intend to reexamine the ^{16}O(α,γ_1) reaction and discover if the true width of the resonance seen in this reaction is much less than the accepted value.

Another point concerns the 12.40 MeV level which we observe to decay via α-emission to the 6.13 MeV 3^- state of ^{16}O. Pearson and Spear[6] saw a level of 12.39±0.04 MeV in $^{16}O(\alpha,\alpha'_{6.13})$. Again it is tempting to associate these levels. However Betts, Fortune and Middleton[5] claim the level seen in $^{19}F(^3He,d)$ is $J^\pi = 1^+$ and thus could not have been seen in Ref. 6.

---

1. Nuclear Physics Laboratory Annual Report, University of Washington (1974), p. 128.
2. H.M. Kuan, G.L. Latshaw, W.J. O'Connell, D.W. Heikkinen, E.G. Adelberger, A.V. Nero, and S.S. Hanna, Nucl. Phys. *A193*, 497 (1972).
3. R.E. Marrs, Ph.D. Thesis, University of Washington (1975), unpublished.
4. Nuclear Physics Laboratory Annual Report, University of Washington (1974), p. 117.
5. R.R. Betts, H.T. Fortune, and R. Middleton, Phys. Rev. C *11*, 19 (1975).
6. J.D. Pearson and R.H. Spear, Nucl. Phys. *54*, 434 (1964).

5.9 An Attempt to Measure the Absolute Gamma-Branch of the ^{21}Ne(9.14 MeV)T=3/2 Level

E.G. Adelberger, R.E. Marrs, and K.A. Snover

Existing data on isospin-forbidden particle decays of T=3/2 mirror levels in light nuclei suggest that ground-state proton decay of proton-rich T=3/2 levels is intrinsically ∿10 times weaker than the ground-state neutron decay of the corresponding mirror T=3/2 levels.[1] However, the systematics for the neutron decays are not nearly as well established as for the mirror proton decays. It was the purpose of this experiment to measure the γ-decay branching ratio Γ_{γ_0}/Γ for the 9.14 MeV ^2Ne T=3/2 level. Since the ground state neutron branching ratio Γ_{n_0}/Γ is known for this level, and Γ_{γ_0} is known for the mirror decay, such a measurement would permit determination of Γ and hence Γ_{n_0} (assuming mirror symmetry for the γ-decay). This would be an important step in a better determination of the neutron-decay systematics.

Particle-gamma coincidence measurements were made for the $^{19}F(^3He,p)^{21}Ne$ reaction, with the particles detected in a solid-state detector at 0° and the γ-rays at 125° in the large NaI spectrometer. Details are similar to those discussed before.[2] Measurements were made at $E_{^3He}$ = 6 MeV with both a LiF^6 and a BaF_2 target, with a combination of Ni and Al foils covering the particle detector to range out the ^3He particles.

Singles and coincidence spectra are shown in Fig. 5.9-1. The spectrum of particles in coincidence with high-energy γ-rays shown in Fig. 5.9-1 is consistent with the population of the known T=3/2 levels except perhaps in the region of the 9.96 MeV level. However, a spectrum of coincident γ-rays corresponding to a particle window on the 9.14 MeV group shows rather complicated structure below 4 MeV, with evidence for contributions from $^{19}F(^3He,d)^{20}Ne$(4.21 MeV) and also $^{19}F(^3He,\alpha)^{18}F^*$. The presence of these deuteron and alpha groups which are unresolved from the 9.14 T=3/2 group in the particle singles spectrum makes the singles normalization of the γ-decay rate difficult. In addition, in the

coincident γ-spectrum there is a broad smear of counts from E_γ = 4 to 7.5 MeV whose origin is unidentified. Gamma-decay measurements[3] of the mirror decays in ^{21}Na make it unlikely that this γ-yield comes from the T=3/2(9.14) decay. The most likely possibility is that this yield comes from an underlying background of states in ^{21}Ne populated in ^{19}F(^{3}He,p) which decay to the 1.75 MeV $7/2^+$ state and to higher states. Unpublished data recently obtained from CalTech[4] show several nearby proton groups of comparable intensity to the T=3/2(9.14) group in the ^{19}F(^{3}He,p) reaction measured at $E_{^3He}$ = 10 MeV and θ = 0° in a magnetic spectrograph. These groups would be unresolved in our data.

If we assume that ground-state γ-decays come only from the T=3/2 levels (as suggested by Fig. 5.9-1), we can deduce a lower limit of $\Gamma_{\gamma_0}/\Gamma \geq 5.3\times10^{-4}$, which yields $\Gamma \leq 20$ keV, a limit which is not particularly significant.

Future efforts may involve a coincidence measurement with a proton detector telescope away from 0°, with the idea of trying to resolve the T=3/2 proton group cleanly in singles (the J=1/2 spin of the 9.14 level would permit such a measurement without complicating the angular correlation).

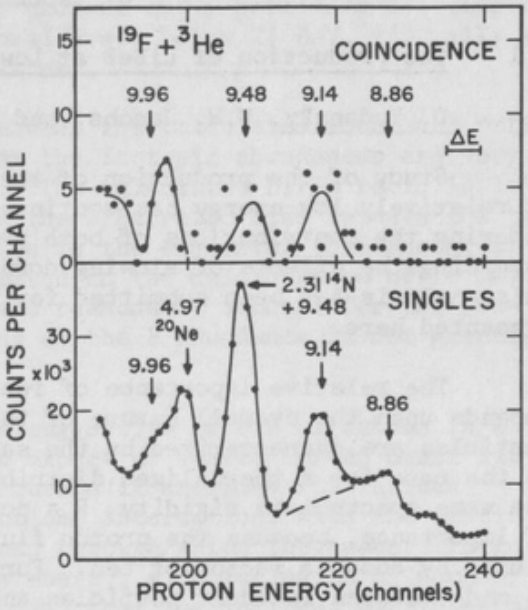

Fig. 5.9-1. Lower half: Singles particle at 0° in the region of the 9.14 T=3/2 group. Numbers with arrows indicate the energies and expected peak locations for protons from (^{3}He,p) populating T=3/2 levels in ^{21}Ne. The other symbols indicated groups from ^{19}F(^{3}He,d)^{20}Ne(4.97) and ^{12}C(^{3}He,p)^{14}N(2.31). Upper half: Particles in coincidence with high energy γ-rays (window from E_α = 8.6 to 9.9 MeV). The particle energy resolution (FWHM) of 130 keV is also shown.

1. E.G. Adelberger, contribution to the Amsterdam Nuclear Physics Conference, September 1974.
2. Nuclear Physics Laboratory Annual Report, University of Washington (1974) p. 117.
3. R.C. Bearse *et al.*, Phys. Rev. C *1*, 608 (1970).
4. D. Hensley, Ph.D. Thesis, CalTech, unpublished.

6. NUCLEAR ASTROPHYSICS

6.1 The Production of LiBeB at Low Energies

D. Bodansky, W.W. Jacobs, and D.L. Oberg

Study of the production of the elements Li, Be, and B in nuclear reactions at relatively low energy has continued, extending previous analyses[1,2] by considering the contributions of both proton and α-particle induced reactions and examining the effects of slowing down of incident particles. A fuller report of this analysis has been submitted for publication,[3] and only a summary will be presented here.

The relative importance of reactions involving protons and α particles depends upon the overall nature of the energy spectra. If spectra for different particles are characterized by the same dependence on total kinetic energy, as is the case for a thermalized distribution, or for protons and α particles with the same spectrum in rigidity, R = pc/z, then only proton induced reactions are of importance, because the proton fluxes can be expected to exceed the α-particle fluxes by about a factor of ten. Further, to the extent that a distinction can be made between incident particles and targets, the reactions of interest would be of protons incident upon heavier nuclei (C, N, and O), because for CNO incident upon hydrogen the energy in the center-of-mass system is a small fraction of the incident (laboratory) energy. If, on the other hand, the spectra are characterized by a similar dependence on energy per nucleon, with the α-particle flux again 1/10 that of the proton flux, then α-particle induced reactions are the ones of primary importance at low energies, because of their lower thresholds.

Both of these possible extreme cases are considered here. For simplicity, terminology is used in which the CNO nuclei are treated as the targets, rather than as projectiles. However, for spectra in energy per nucleon it is immaterial which they are, unless the relative abundances differ appreciably for the two possibilities. Observed abundances for stellar spectra, meteorites, and cosmic rays are sufficiently concordant that the expedient is followed here of using one overall set of relative abundances: the ^{12}C, ^{14}N and ^{16}O are taken to be in the ratios C:N:O of 3.5:1:5 and the $^{13}C/^{12}C$ ratio is taken to be 1/100.

A comparison is made between the calculated product abundance ratios and their solar system ratios, derived primarily from the tabulation of Cameron[4]: 7/6 = 12.5, 11/10 = 4.1, Li/Be = 61, and B/Be = 430. These abundances are found from analyses of meteoritic studies. However, there is substantial evidence that the B meteoritic abundance may not reflect the prevailing cosmic or solar system abundances, and a comparison is also made here to a lower ratio, B/Be = 50 which follows from the estimates given by Reeves[5] for the B and Be abundances: $B/H = 10^{-9\pm1}$ and $Be/H = 2 \times 10^{-11}$. It should be emphasized, however, that even this value for the B abundance is considerably higher than the present interstellar and solar upper limits, and therefore the relevant B/Be ratio may turn out to be substantially below 50.

Yields for the production of LiBeB as a function of kinetic energy were calculated using the relative abundances given above.[6] Ratios of these yields

are plotted in Fig. 6.1-1 for the case where protons and α particles are compared at the same energy. At the energies here considered, below 25 MeV, virtually the entire yield comes from proton induced reactions.

A comparison is made in Fig. 6.1-1 between the calculated abundance ratios and the solar system values. It is seen that the isotopic abundances are very well matched at a proton energy near 16 MeV. The calculated Li/Be ratio is low by about a factor of two at this energy, and the B/Be ratio lies between the two reference lines. In view of the uncertainties in the elemental abundances, it is concluded that a proton spectrum concentrated in the neighborhood of 16 MeV, or with an effective energy near 16 MeV, could reasonably account for the production of the stable LiBeB isotopes, as long as the B abundance is not greatly below the meteoritic value.

While a fit at a single energy can be suggestive of the situation in a general energy region, it is unreasonable to expect or search for an exact fit at one energy. One contribution to a distribution in energies for incident particles is their loss of energy through Coulomb interactions with the electrons, ions and atoms of the medium (mostly hydrogen) through which they pass. Yield ratios as a function of monoenergetic source energy, with inclusion of such losses, are also plotted in Fig. 6.1-1, assuming that the incident particles come to rest in the medium. The regions of best fit are shifted upward in initial energy, but there is little effect on the qualitative shape of the curves.

An alternative set of yield ratios is plotted in Fig. 6.1-2 corresponding to the case where the α-particle flux is 1/10 the proton flux at the same energy per nucleon. Again, yield ratios are also presented for the case where the slowing down of the particles is considered. In both cases, seemingly reasonable fits to the meteoritic abundances are obtained in the neighborhood of 9 MeV per nucleon, but the discrepancies which do exist can only be corrected by assuming selective destruction of Li, or by making arbitrary changes in the assumed relative abundances of the interacting particles.

While the present description, particularly for spectra dependent on total kinetic energy, most naturally leads to a relatively high B/Be ratio, not very much below the meteoritic value, it is of interest to examine the extent to which this is an unavoidable characteristic of LiBeB production at low energies. It is to be noted that the B/Be ratio can be reduced by increasing the $^{13}C/^{14}N$ abundance ratio of 1/5 (about 6 times the value hitherto adopted, the 11/10 ratio is 4.1 and the B/Be ratio is 31. A much lower B/Be ratio would be harder to explain, but could be attained in an environment with little or no ^{14}N. Of course, when the energy spectrum and the relative abundances of the interacting nuclei are treated as free parameters, it is not surprising that a broad variety of results can be reached. While it is of interest to note possible implied connections, for example the possible association of low B and low N abundances, the chief significance of such analyses is in the range of alternatives they suggest should be kept open.

Possible sites for the low energy processes considered above include:

(1) Low energy galactic cosmic rays. Solar modulation obscures the

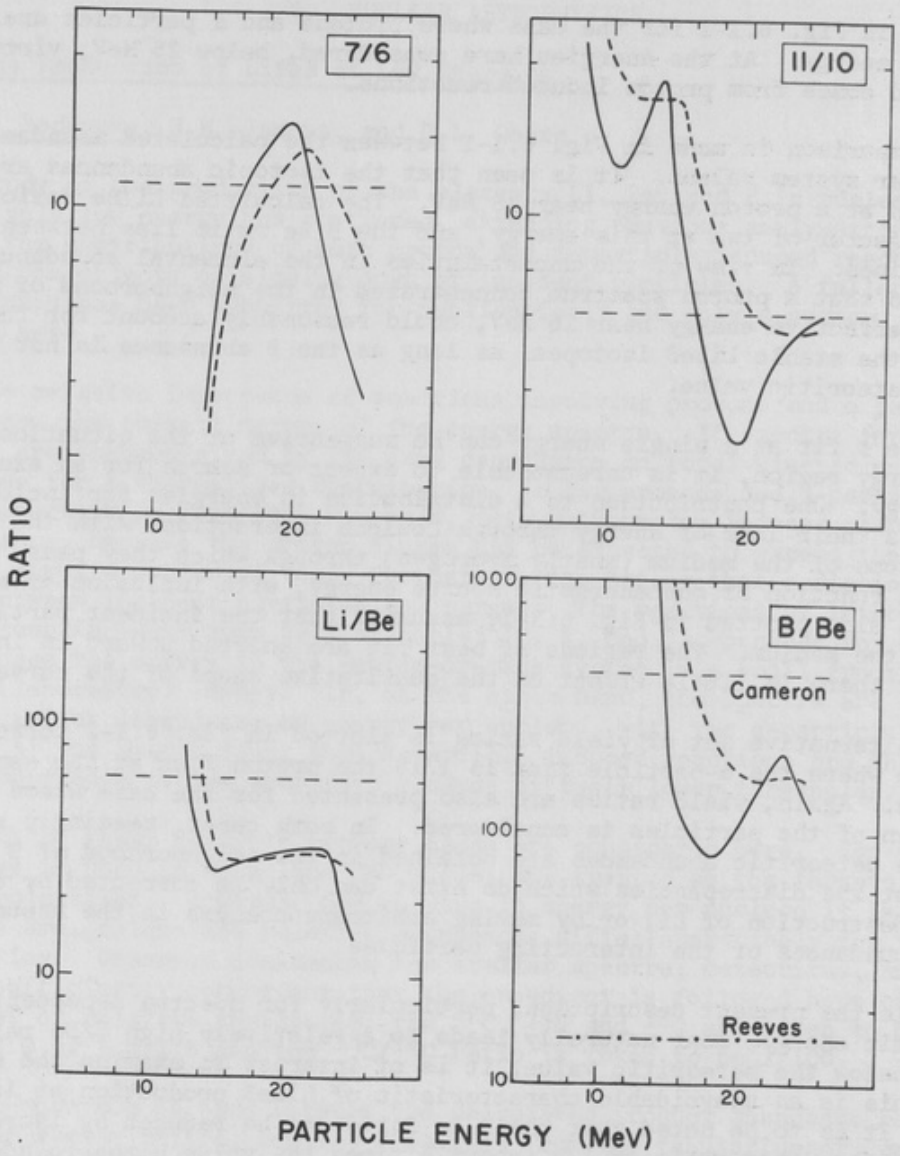

Fig. 6.1-1. Calculated ratios of elemental and isotopic abundances for proton and α-particle interactions. The α-particle flux is taken to be 1/10 of the proton flux (at the same energy) and standard abundances are assumed for other nuclei (see text). The dashed curve includes effects of slowing down of the particles in the medium, starting from the indicated particle energy. The horizontal lines correspond to observed solar system abundances (Ref. 4); for B/Be an alternative value for the observed ratio is also given (Ref. 5).

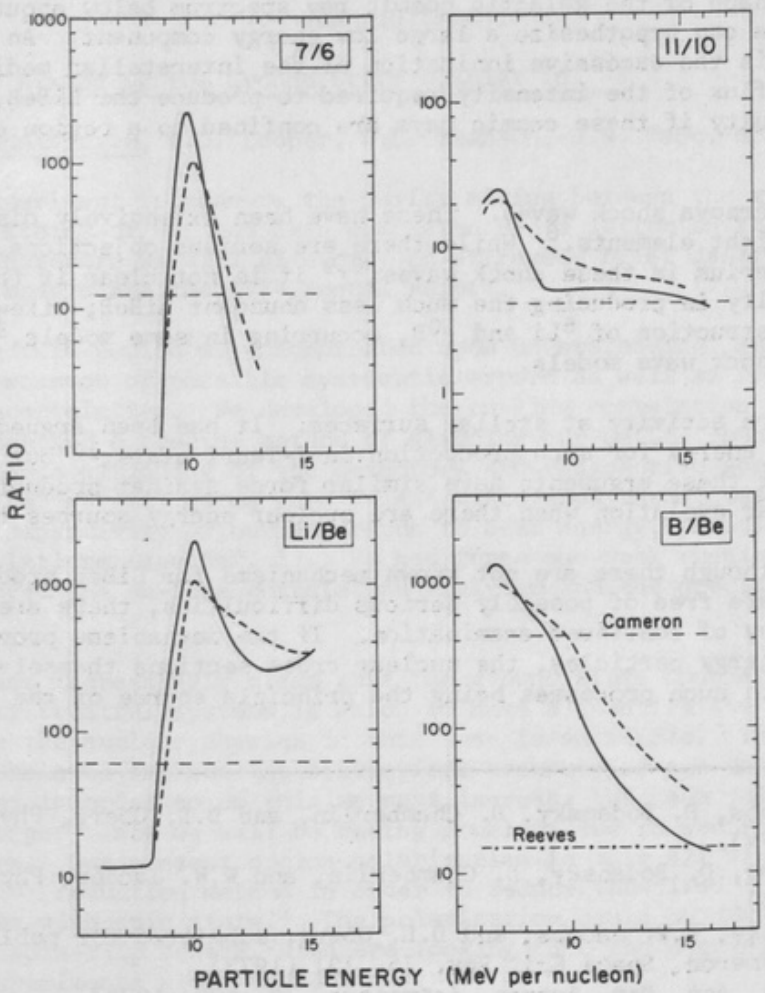

Fig. 6.1-2. Calculated ratios of elemental and isotopic abundances for proton and α-particle interactions. The α-particle flux is taken to be 1/10 the proton flux (at the same energy per nucleon) and standard abundances are assumed for the other nuclei (see text). The curves are only of qualitative significance, in view of large uncertainties in the α-particle cross sections. Between 9 and 12 MeV per nucleon, where the α+α cross sections are varying very rapidly, average cross sections are used, giving somewhat smoother ratios than would be obtained were the actual cross sections employed. The dashed curves include effects of slowing down of particles in the medium, starting from the indicated particle energy. The horizontal lines correspond to the observed solar system abundances (Ref. 4); for B/Be an alternative value for the observed ratio is also given (Ref. 5).

magnitude and shape of the galactic cosmic ray spectrum below about 100 MeV per nucleon, and one can hypothesize a large low energy component. An objection to this mechanism is the excessive ionization of the interstellar medium which might result from a flux of the intensity required to produce the LiBeB, but this may not be a difficulty if these cosmic rays are confined to a region close to the source.[7]

(2) Supernova shock waves. These have been extensively discussed as a source of the light elements.[8] While there are serious objections to the production of deuterium in these shock waves,[8,9] it is not clear if there is comparable difficulty in producing the much less abundant LiBeB; likewise it is not clear if the destruction of ^{6}Li and ^{10}B, occurring in some models,[8] is always inevitable in shock wave models.

(3) Flare activity at stellar surfaces. It has been argued that there is insufficient energy for such production in T-Tauri stars,[10] but it is not established that these arguments have similar force against production in later stages of stellar evolution when there are nuclear energy sources to draw upon.

Thus, although there are not known mechanisms for LiBeB production at low energies which are free of possibly serious difficulties, there are several mechanisms worthy of continued examination. If the mechanisms prove viable as a source of low energy particles, the nuclear cross sections themselves are not inconsistent with such processes being the principle source of the observed LiBeB isotopes.

---

1. W.W. Jacobs, D. Bodansky, D. Chamberlin, and D.L. Oberg, Phys. Rev. C *9*, 2134 (1974).
2. D.L. Oberg, D. Bodansky, D. Chamberlin, and W.W. Jacobs, Phys. Rev. C *11*, 410 (1975).
3. D. Bodansky, W.W. Jacobs, and D.L. Oberg, submitted for publication.
4. A.G.W. Cameron, Space Sci. Rev. *15*, 121 (1973).
5. H. Reeves, Ann. Rev. Astron. Astrophys. *12*, 437 (1974).
6. Cross sections for proton induced reactions are from Refs. 1 and 2, and further references cited therein.Cross sections for α-particle induced reactions, including the α-α reactions, are based on Ref. 1, a literature survey, and rough estimates of unmeasured cross sections.
7. M. Meneguzzi, J. Audouze, and H. Reeves, Astron. Astrophys. *15*, 337 (1971).
8. R.I. Epstein, W.D. Arnett, and D.N. Schramm, Astrophys. J. Lett. *190*, L13 (1974), and references therein.
9. T.A. Weaver and G.F. Chapline, Astrophys. J. Lett. *192*, L57 (1974).
10. C. Ryter, H. Reeves, E. Gradsztajn, and J. Audouze, Astron. Astrophys. *8*, 389 (1970).

---

7. WEAK INTERACTIONS

7.1. Parity Mixing of the Ground State Doublet in ^{19}F

E.G. Adelberger, M.D. Cooper, H.E. Swanson, J.W. Tape, and T.A. Trainor

The experiment to measure the parity mixing between the ground ($1/2^+$) and 110 keV($1/2^-$) states of ^{19}F has been completed and a letter on this work has been published.[1] Therefore we will give only an extremely brief description of the main advances made since the 1974 Annual Report.

During this period we concentrated upon understanding, reducing and measuring all sources of possible systematic errors as well as reducing our statistical uncertainties. We developed the on-line correlation analyzer (see Ref. 1) -- perfected a precise method of aligning our Ge(Li) counters to 0.1° using micrometer positioning of the detectors and radioactive sources of 122 keV (^{57}Co) and 70 keV (^{201}Tl) gamma rays -- and discovered techniques for directly measuring the sensitivity of our apparatus to beam energy, position, angle and intensity modulations (see Ref. 1). We had three one-week running periods during which we employed the on-line correlation analyzer and the precise counter alignment.

It seems increasingly clear that the ground state doublet of ^{19}F forms one of the most fruitful systems in which to make a quantitative study of parity mixing because the nuclear physics in this case is so simple. Thus it would be extremely valuable to improve the statistical accuracy of our data. However it is obvious that in order to do this we must increase the beam polarization as well as run longer since we will be facing problems due to neutron damage to the Ge(Li) counters. Our present proton polarization is only 42% since we use the adiabatic field reduction method in order to reduce undesired correlations of beam properties with spin state.[2] The polarization could be doubled with a more sophisticated spin-flip scheme.[3] We are looking into the possibilities for improving our experiments along these lines.

---

1. E.G. Adelberger, H.E. Swanson, M.D. Cooper, J.W. Tape, and T.A. Trainor, Phys. Rev. Lett. *34*, 402 (1975).
2. Nuclear Physics Laboratory Annual Report, University of Washington (1974), p. 73.
3. J.M. Potter, J.D. Bowman, C.F. Hwang, J.L. McKibben, R.E. Mischke, D.E. Nagle, P.A. Debrunner, H. Fraunfelder, and L.B. Sorensen, Phys. Rev. Lett. *33*, 1307 (1974).

7.2. Parity-Mixing in ^{18}F -- Are There Neutral Weak Currents which Violate Parity?*

E.G. Adelberger, C.A. Barnes†, P.D. Ingalls†, R.E. Marrs, and H. Winkler‡

Not one measurement of the $\Delta T=1$ parity violating (PV) weak nucleon-nucleon force has been successful. Yet this force is extraordinarily interesting because

it is very sensitive to possible PV neutral weak currents. In the Cabibbo (charged currents only) model of the weak interaction, the T=1 PV force arises from the interaction of two $\Delta T = 1/2, \Delta\delta = \pm 1$ currents and is therefore suppressed by a factor of $\sin^2\theta_c \sim 1/20$.[1] The Weinberg-Salam gauge model has, in addition to the usual charged currents, a $\Delta\delta = 0$, $\Delta T = 0,1$ neutral current with V,A character. The interaction of the neutral currents will give a $\Delta T = 1$ PV force which is not suppressed by the factor $\sin^2\theta_c$ and is thus about an order of magnitude larger than that predicted by models without PV neutral weak currents.[2] Since the structure of the "neutral currents" has not yet been experimentally elucidated it would be extremely interesting to test these ideas by searching for the large enhancements on the $\Delta T = 1$ PV interaction predicted by Weinberg-Salam type models.[2]

Apparently the most promising opportunity for such a measurement occurs in ^{18}F which seems ideally suited for the task (see Fig. 7.2-1). There a nearly degenerate doublet of J=0 levels is found with a splitting of only 39 keV. The 1042 keV J^π, $T=0^+,1$ level will only mix with the 1081 keV $J^\pi, T=0^-,0$ level under the action of a $\Delta T = 1$ PV weak force. Consider the parity properties of the 1081 and 1042 keV γ-ray transitions. Under a $\Delta T = 1$ PV interaction the 0^+ and 0^- levels will mix so that

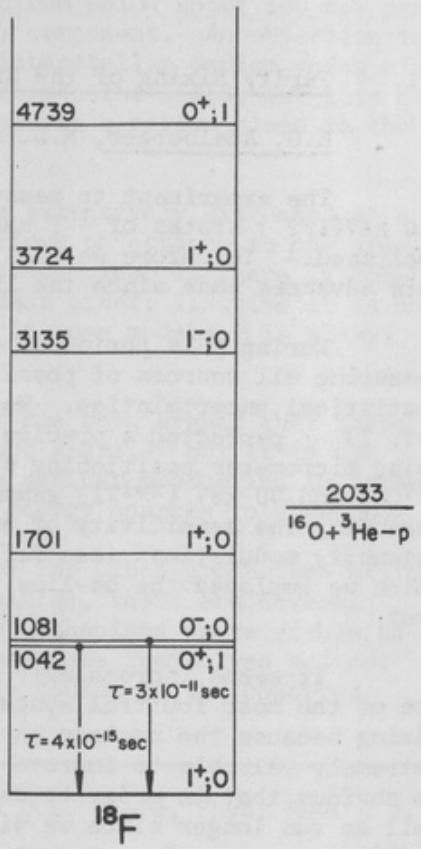

Fig. 7.2-1. A diagram of the low lying J=0 and J=1 levels of ^{18}F. The parity mixing between the 1042 and 1081 MeV levels can be detected by measuring the circular polarization of the 1081 keV gamma ray.

$$|1081\rangle = |-\rangle + \varepsilon|+\rangle$$
$$|1042\rangle = |+\rangle - \varepsilon|-\rangle \qquad \text{where } \varepsilon = \frac{\langle -|H_{PV}|+\rangle}{39 \text{ keV}}$$

The transitions to the ground state, $|0\rangle$, are then

$$\langle 0|E1 + M1|1081\rangle = E1 + \varepsilon \cdot M1$$
$$\langle 0|E1 + M1|1042\rangle = M1 - \varepsilon \cdot E1$$

where

$$E1 = \langle 0|E1|-\rangle$$
$$M1 = \langle 0|M1|+\rangle.$$

The isospin forbidden E1 transition is very retarded $\tau_{1081} = 3 \times 10^{-11}$ sec, while the isospin favored M1 transition is very fast $\tau_{1042} = 4 \times 10^{-15}$ sec. From these lifetimes we have $M1 \approx 100\ E1$. The PV circular polarization (CP) of

the 1081 and 1042 keV gamma rays is therefore

$$CP_{1081} \approx 2\varepsilon \cdot \frac{M1}{E1} \approx 200\varepsilon$$

$$CP_{1042} \approx 2\varepsilon \cdot \frac{E1}{M1} \approx \frac{\varepsilon}{50} .$$

Using shell model wave functions Gari *et al.*[3] predict that $CP_{1081} = 3.6 \times 10^{-4}$ in the Cabbibo model, while it grows to $CP_{1081} = 5.7 \times 10^{-3}$ in the Weinberg-Salam model.

We are working on an experiment to measure CP_{1081} with a sensitivity of $\sim 2 \times 10^{-3}$. The CP will be determined by a pair of transmission type Compton polarimeters viewed by 15% Ge(Li) detectors feeding two fast ADC's. Since we have good energy resolution we are able to make a relative measurement of CP_{1081} by comparing it to CP_{1042} which acts as a normalizer. The basic design for eliminating systematic errors is quite similar to that employed in the Seattle measurement of parity mixing in ^{19}F.[4] In both experiments there are 2 detectors, 2 gamma rays (one a normalizer which should have no true PV effects) and two conditions between which one switches repetitively (in this case the direction of $\vec{B}$ on the polarimeters). The system is highly effective at suppressing experimental asymmetries.

The ^{18}F activity is induced in a thick water target by a 3.8 MeV ^{3}He beam using the $^{16}O(^{3}He,p)$ reaction. The water circulates through the target past an entrance window of 7.5×10^{-5} cm thick nickel foil. High beam currents (50 μA would be ideal) are desirable in order to achieve statistical accuracy. The water circulates in order to cool the foil, dissipate the beam power (∿200 watts at 50 μA) and carry away the β^+ activity which would jam our counters with intense 511 keV gamma rays. Our Ge(Li) spectra taken with the flowing target contain almose exclusively ^{18}F gamma rays with copious production of both the 1081 and 1041 keV gammas. We also see 5 MeV gammas from ^{15}O produced via the $^{16}O(^{3}He,\alpha)$ reaction.

A system of automatic fast-acting vacuum and water valves plus an in-line cold trap has been assembled. It is remarkably effective in preventing water from reaching the vacuum pumps in event of a foil rupture. In a first trial at the California State University at Los Angeles KN4000 Van de Graaff accelerator our foils withstood beam currents of 5 μA but ruptured at higher intensities. These failures were probably caused by poor epoxy connections between the foil and its holder. Subsequent trials using 2.0 MeV α beams from the Kellogg Laboratory 3 MV generator showed that the foils would survive currents of 3 μA of these more heavily ionizing particles but that the bombardment produced bubbles in the water. The bubbles may be due to electrolysis of the water by the ionization of the beam and may be the limiting factor in our present current handling capacity. When we determine what intensity we can ultimately handle we can fix the optimum length of our polarimeter magnets. The cross-over from the source-strength limited regime to the count-rate limited regime occurs at ∿10 μA.

* Supported in part by the National Science Foundation at California Institute of Technology, Pasadena.
† Permanent address: California Institute of Technology, Pasadena.
‡ Permanent address: California Institute of Technology, Pasadena, and California State University at Los Angeles.
1. E.M. Henley, Comments on Nuclear and Particle Physics *4*, 206 (1970).
2. M. Gari and J.H. Reid, Phys. Lett. *53B*, 237 (1974).
3. M. Gari, J.B. McGrory and R. Offerman, to be published.
4. E.G. Adelberger, H.E. Swanson, M.D. Cooper, J.W. Tape, and T.A. Trainor, Phys. Rev. Lett. *34*, 402 (1975).

8. SCATTERING AND REACTIONS

8.1 Back-angle Excitation Functions of $\alpha + {}^{39}K$ and $\alpha + {}^{40,44}Ca$ Scattering between 20 and 27 MeV

T.H. Braid*, K.A. Eberhard, T. Renner*, J.P. Schiffer*, and S. Vigdor*

Detailed back-angle excitation functions for $\alpha + {}^{39}K$ and $\alpha + {}^{40,44}Ca$ elastic and inelastic scattering have been measured with the Argonne National Laboratory FN tandem accelerator in the energy range 20 through 27 MeV in an attempt to study the reaction mechanism of these reactions at energies and angles where large anomalies have been observed by several previous workers. Statistical fluctuations are observed for all three reactions. In Fig. 8.1-1 excitation functions for $\alpha + {}^{39}K$ and $\alpha + {}^{40}Ca$ at 175°(lab) are compared. The cross section fluctuations are more strongly damped for $\alpha + {}^{39}K$ than for $\alpha + {}^{40}Ca$ because of the large target thickness of ^{39}K (^{39}K: ∿ 400 μg/cm^2; ^{40}Ca: ∿20 μg/cm^2) and because of a large number of so-called effective channels in case of $\alpha + {}^{39}K$ due to the spin 3/2 of ^{39}K. In general, the fluctuations for $\alpha + {}^{40}Ca$ and $\alpha + {}^{39}K$ are clearly less pronounced than those for $\alpha + {}^{44}Ca$, where the backward rise is absent. The compound contribution to the elastic scattering at back angles in ^{40}Ca and ^{39}K is a few % of the cross section, in ^{44}Ca the percentage is larger though the absolute magnitude of the compound contribution is comparable. The backward rise in elastic alpha scattering from ^{40}Ca (^{39}K) seems thus to be caused primarily from a direct contribution, not from a fluctuating compound one.

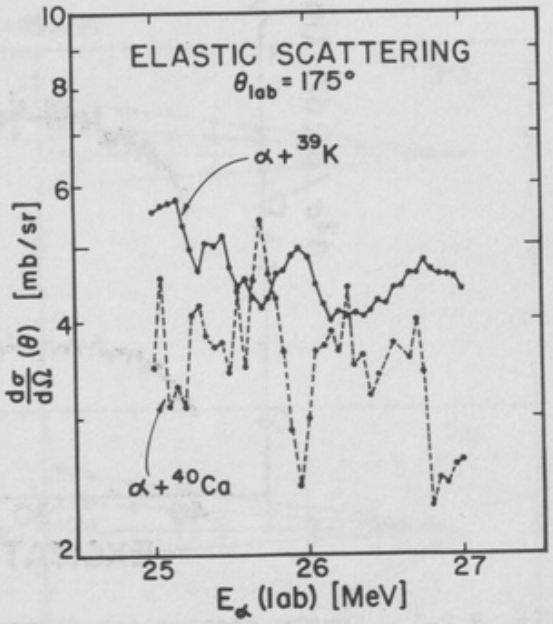

Fig. 8.1-1. Excitation functions for $\alpha + {}^{39}K$ and $\alpha + {}^{40}Ca$ elastic scattering at 175°.

* Permanent address: Argonne National Laboratory, Argonne, Illinois.

8.2 Highly Inelastic Deuteron Scattering

M. Baker, K. Ebisawa, D. Johnson*, I. Halpern, D. Hendrie†, H. Wieman, and M.S. Zisman

We have previously reported[1] making measurements of inelastic deuteron spectra over the full range of outgoing energies from the Coulomb barrier to the elastic peak. Cross sections were obtained at a number of angles for targets

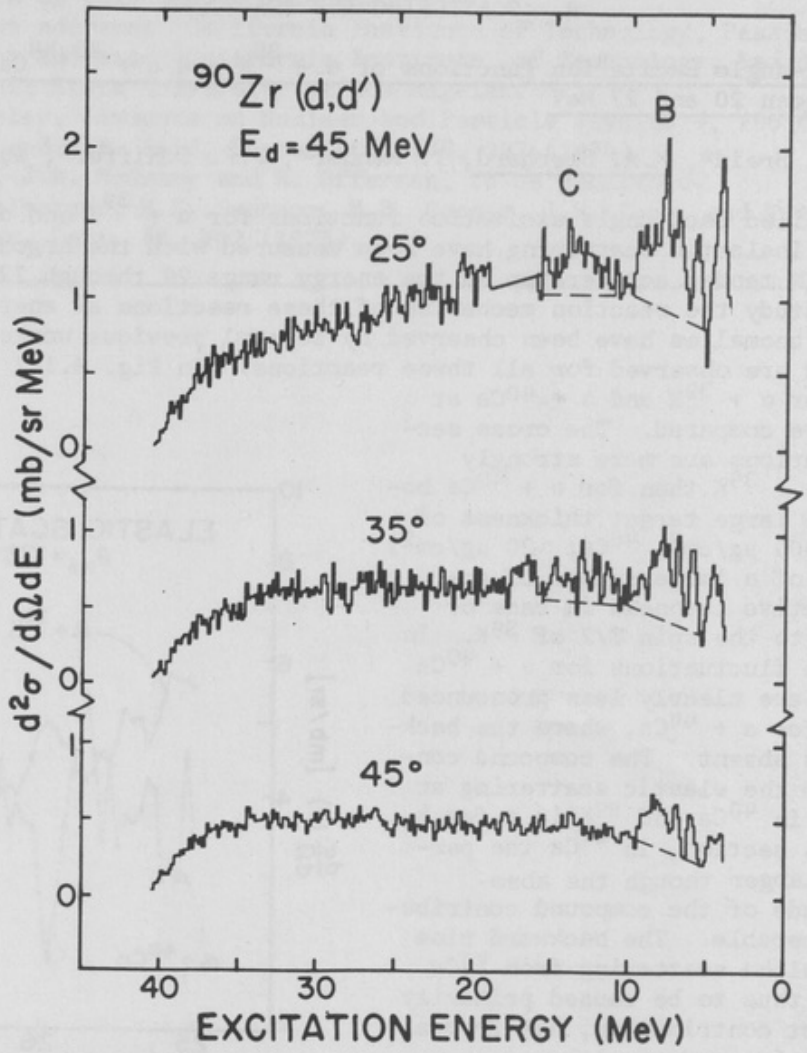

Fig. 8.2-1. Energy spectra for deuterons emitted by ^{90}Zr when bombarded with 45 MeV deuterons.

with masses varying from A = 27 to A = 208. Measurements were made at the Univsity of Washington Van de Graaff accelerator with 22 MeV deuterons and at the Lawrence Berkeley Laboratory using 45 MeV deuterons. Analysis of the data has now been completed and the cross sections have been compared with a collective model prediction.

Description of the Data

Most of the spectra, like the ^{90}Zr spectra shown in Fig. 8.2-1, are smooth and fairly free of prominent structure except at the lowest excitation energies. Above 10 MeV excitation at the most forward angles measured, the structure observed is a relatively small effect, seldom more than a 20% variation

on an otherwise smooth spectrum. At larger angles this fractional variation is even smaller. Aside from the 20% fluctuations in the energy spectra the double differential cross sections are observed to have a nearly exponential dependence on both excitation energy and scattering angle. This characteristic of the data is made obvious in Fig. 8.2-2 where the cross sections have been averaged over 5 MeV intervals of excitation, thereby suppressing the small variations due to structure in the spectra. Shown with the measured cross sections is the least squares fit to the data with the parameterized form

$$d^2\sigma/d\Omega dE = ae^{c(\theta-\theta_0)(E_x-E_0)}$$

where E_x is the excitation energy in the residual nucleus, and θ is the inelastic deuteron scattering angle. The parameters a, c, θ_0, and E_0 depend on the target and incident energy. The fit shown was made using the forward angle data only. As may be observed from Fig. 8.2-2, the full angular distribution including back

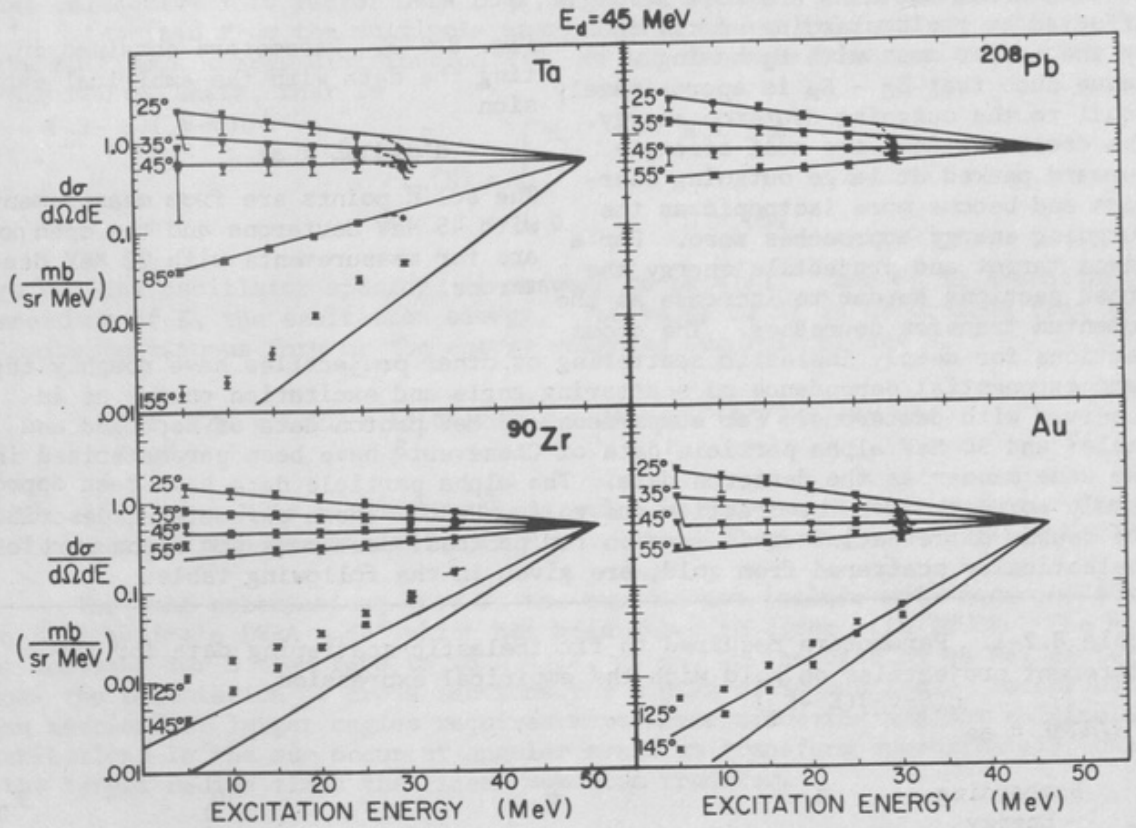

Fig. 8.2-2. Inelastic deuteron cross sections averaged over 5 MeV of excitation. Shown with the data is a fit to the empirical expression

$$d^2\sigma/d\Omega dE = ae^{c(\theta-\theta_0)(E_x-E_0)}$$

angle measurements cannot be exactly represented by an exponential dependence on angle. The deviation from an exponential dependence on excitation energy occurs only at the higher excitation energies near the Coulomb barrier cutoff for outgoing deuterons. All the inelastic data except for aluminum, the lightest target measured, were found to closely conform to the simple exponential dependence on excitation energy and scattering angle. The parameters for fitting the data (shown in Fig. 8.2-3) are largely independent of target. The strongest A dependence is found for c which tends to increase with increasing A. The cross sections are more strongly affected by the bombarding energy than by the target mass with E_0 having a value such that $E_0 - E_x$ is approximately equal to the outgoing deuteron energy. The cross sections are most strongly forward peaked at large outgoing energies and become more isotropic as the outgoing energy approaches zero. For a given target and projectile energy the cross sections appear to increase as the momentum transfer decreases. The cross sections for deeply inelastic scattering of other projectiles have roughly the same exponential dependence on scattering angle and excitation energy as is observed with deuterons. For comparison, 62 MeV proton data of Bertrand and Peele[2] and 90 MeV alpha particle data of Chenevert[3] have been parameterized in the same manner as the deuteron data. The alpha particle data have been approximately corrected for the fraction due to $(\alpha, {}^5He)$.[4] These parameters, describing the double differential cross section for protons, deuterons and alpha particles inelastically scattered from gold, are given in the following table.

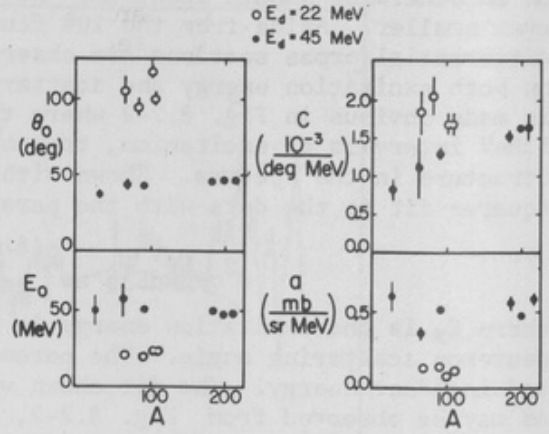

Fig. 8.2-3. Parameters obtained in fitting the data with the empirical expression

$$d^2\sigma/d\Omega dE = ae^{c(\theta-\theta_0)(E_x-E_0)}.$$

The solid points are from measurements with 45 MeV deuterons and the open points are for measurements with 22 MeV deuterons.

Table 8.2-1. Parameters required to fit inelastic scattering data for three different projectiles on gold with the empirical expression

$$d^2\sigma/d\Omega dE = ae^{c(\theta-\theta_0)(E_x-E_0)}$$

	Bombarding Energy (MeV)	a (mb/sr MeV)	c $(\text{MeV deg})^{-1}$	θ_0 (deg)	E_0 (MeV)
p	62	4.6 ±1.0	$(1.01\pm0.04)\times10^{-3}$	20±2	62±5
d	45	0.45±0.02	$(1.61\pm0.14)\times10^{-3}$	46.5±0.8	46.8±2.9
^{4}He	90	1.2 ±0.05	$(2.25\pm0.12)\times10^{-3}$	28±2	78±5

It is clear that for a given excitation energy the alpha particle, with its higher momentum, has an angular distribution that varies more rapidly with angle than the deuteron and proton angular distributions.

Collective Model Prediction of Inelastic Cross Sections

We have compared our data with an isoscalar collective model estimate of the highly inelastic cross section. The calculation is essentially the same as that used by M.B. Lewis[5] to investigate inelastic proton scattering. In this approach the theoretical double differential cross section is expressed as

$$d^2\sigma/d\Omega dE = \sum_L F_L \, d\sigma^{DWBA}/d\Omega_L$$

a sum over multipole contributions where $d\sigma^{DWBA}/d\Omega_L$ is the output from a conventional collective form factor DWBA code, such as DWUCK.[6] The strength function, F_L, is determined from the multipole energy-weighted sum rule and an estimate of the multipole energy distribution.[5,8] We use the same energy distribution as was assumed by Lewis, that is

$$F_L(E) = \begin{cases} S_L & E < L\hbar\omega \\ 0 & E > L\hbar\omega \end{cases}$$

where $\hbar\omega$, the oscillator spacing, is assumed to be $41/A^{1/3}$ and S_L is a constant independent of E, the excitation energy. The value of S_L is determined from the following continuous form of the energy weighted sum rule of Ref 5.

$$\int_0^\infty F_L \, E dE = L(2L + 1)(\hbar^2/2MR^2)4\pi/3A \simeq 2L^2(\hbar^2/2MR^2)4\pi/3A.$$

In this expression M is the nucleon mass and A is the target mass number. The value chosen for the target radius is $R = 1.2\ A^{1/3}(f)$ giving $S_L = 0.145/A\ MeV^{-1}$.

The DWBA calculations used in the sum did not include spin and were done with Braithwaite's DWBA code[7] which has been shown to agree with DWUCK. The sums were computed for L transfers up to L = 14, which, in the case of 45 MeV deuterons, allows the calculation of cross sections for angles of 50° or less. To calculate cross sections at larger angles requires more terms since the maximum multipole contributions in the sum occur at angular momentum transfers approximately equal to the target radius times the linear momentum transfer.

The results of the calculation are compared with the data in Figs. 8.2-4 and 8.2-5. Clearly the calculation gives too flat an angular distribution and the calculated cross sections decrease too rapidly with increasing excitation energy. However the model at least qualitatively accounts for differences observed in the highly inelastic cross sections measured with other projectiles. As noted earlier in the comparison of inelastic proton, deuteron and alpha particle scattering, the cross section varies more rapidly with angle for particles

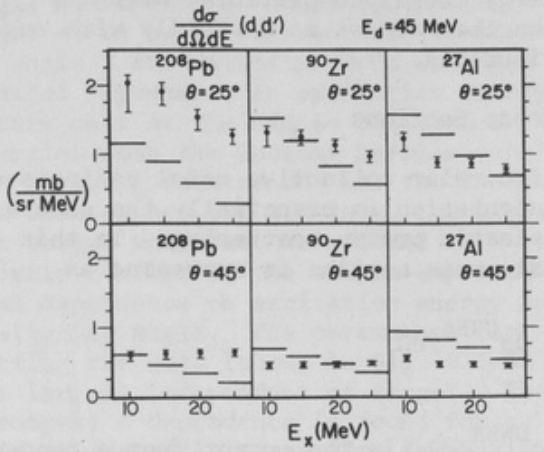

Fig. 8.2-4. Collective model DWBA prediction of inelastic deuteron spectra shown with data averaged over 5 MeV of excitation.

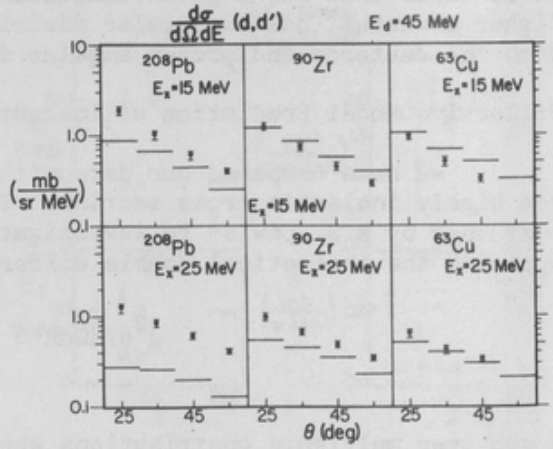

Fig. 8.2-5. Measured angular distributions at 15 and 25 MeV excitation shown with cross sections calculated with collective model DWBA. The data have been averaged over 5 MeV of excitation.

with higher momenta. Fig. 8.2-6 shows that the isoscalar collective model DWBA calculation qualitatively reproduce this effect. The calculated cross sections do not, however, show as large a difference between deuteron and alpha particle scattering as is observed in the data.

Discussion

In the model calculation there is some flexibility in choosing the energy distribution of the strength function but for the higher mass targets it is not possible to find a distribution that gives both a larger cross section at high excitation and a more strongly forward peaked angular distribution as is required to fit the data. In the calculation shown, the full sum rule strength for the lower multipoles is already exhausted. To increase the predicted cross section, therefore, requires increased contributions from the higher multipoles. Increasing this contribution, however, will change the angular distribution in the wrong direction since the high multipole parts add to the cross section most strongly at larger angles where the momentum transfer is large.

Part of the discrepancy may be due to ambiguities in the optical model parameters. Two optical model sets for deuterons on gold, which vary in potential depth by around 30% yet give nearly equal elastic cross sections, were found to produce variations in the inelastic prediction of about 50%. This appears to be the largest flexibility in the calculation.

In this model only scalar excitations have been included so, in principle, the discrepancy between the observed cross section and the prediction could in part be due to isovector excitations. Scattering of isospin zero projectiles can couple to isovector modes only if associated with the isovector excitation

there is a displacement of the total nucleon density. (This is a consequence of nuclear force charge independence.)

The coupling predicted for hydrodynamic models is strongly dependent on the details of the model. In the giant dipole models considered by Satchler[8] the coupling is zero for constant total density models and largest for the Goldhaber-Teller model in which rigid proton and neutron spheres oscillate against each other. An estimate of the coupling potential for inelastic excitation of the giant dipole resonance in ^{208}Pb by isospin zero projectiles has been made using the proton and neutron densities determined by S.D. Schery *et al.*[9] from the $^{208}Pb(p,n)^{208}Bi^{IAS}$ quasielastic scattering reaction. The potential obtained is ∿1/3 that coupling to isoscalar excitations. For lighter targets it is expected that the neutron radius will not extend so far beyond the proton radius and consequently the coupling to isovector modes will be still smaller. It appears that the excitation of isovector resonances is insufficient by itself to explain the discrepancy observed between the measured cross sections and the sum rule predictions for collective scalar excitations.

We have also left out other kinds of excitations, for example spin excitations for incident protons. Finally, we must call attention to our having left out effects due to multiple interactions, i.e., multiple scatterings of the projectile moving through the nucleus. These are likely to contribute more significantly to the higher excitations being studied here than they do to low-lying excitations. The large magnitude of the integrated inelastic cross sections in itself implies a relatively large contribution from such multiple events.

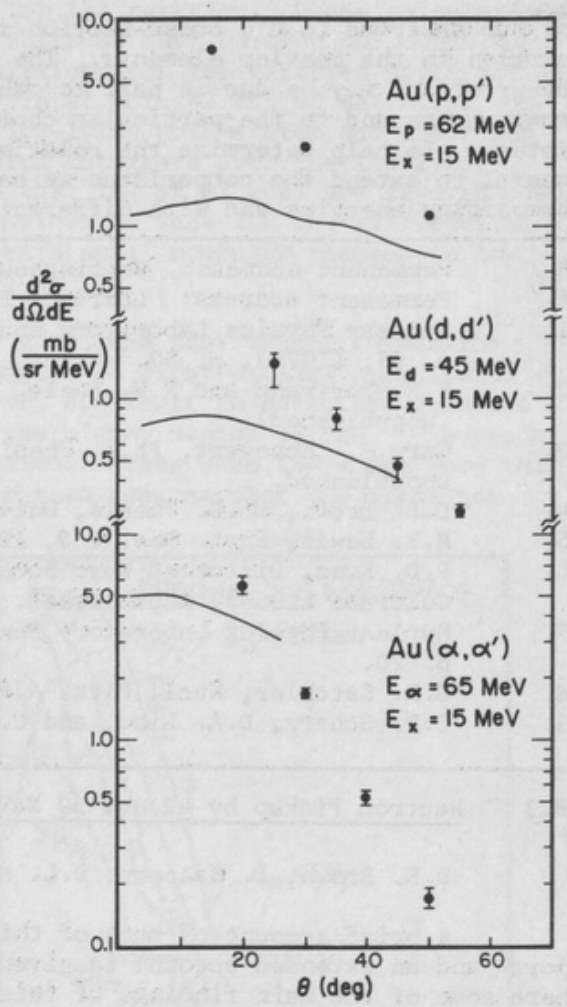

Fig. 8.2-6. Angular distributions predicted by collective model DWBA for 62 MeV protons, 45 MeV deuterons and 65 MeV alpha particles inelastically scattered from Au to 15 MeV of excitation. The proton cross sections measured by F.E. Bertrand and R.W. Peele were taken from Ref. 2 and the alpha particle inelastic cross sections measured by G. Chenevert were taken from Ref. 3.

To summarize -- we have calculated the contributions to the inelastic spectra and angular distributions of isoscalar shape oscillations induced by incident projectiles and have found that the calculations account for the most

of our observed (d,d') cross-section in the lighter elements and for a substantial portion in the heavier elements. The discrepancy between the calculations and observations may be due in part to other types of excitations, to multiple scatterings and to the particular choice that was made of optical model parameters. To help determine the relative importance of these effects, it will be useful to extend the comparisons we have made of scatterings studied at different bombarding energies and with different projectiles.

---

* Permanent address: Westinghouse Hanford Company, Richland, Washington.

† Permanent address: Lawrence Berkeley Laboratory, Berkeley, CA 94720.

1. Nuclear Physics Laboratory Annual Report, University of Washington (1974), p. 65; (1973), p. 57.
2. F.E. Bertrand and R.W. Peele, ORNL Report No. ORNL-4460 (1969) (unpublished).
3. Gary M. Chenevert, Ph.D. Thesis, University of Washington (1969), unpublished.
4. D.R. Brown, Ph.D. Thesis, University of Washington (1974),unpublished.
5. M.B. Lewis, Phys. Rev. C *9*, 1878 (1974).
6. P.D. Kunz, Distorted Wave Born Approximation Code, University of Colorado (1969), unpublished.
7. Nuclear Physics Laboratory Annual Report, University of Washington (1969), p. 20.
8. G.R. Satchler, Nucl. Phys. *A195*, 1 (1972).
9. S.D. Schery, D.A. Lind, and C.D. Zafiratos, Phys. Rev. C *9*, 416 (1974).

8.3 Neutron Pickup by 42 and 90 MeV Alpha Particles

D.R. Brown, I. Halpern, D.L. Hendrie*, and H. Homeyer†

A brief account of much of this work appears in last year's Annual Report[1] and an extended account is given in the thesis of D.R. Brown.[2] We summarize here some of the main findings of this investigation with special emphasis on those points not discussed in last year's report.

The most conspicuous feature in the two dimensional plot of energies E_α vs E_n obtained in the coincidence observation of α particles and fast neutrons in α particle bombardments of various nuclei are the peaks which correspond to the (α,^{5}He g.s.) reaction. (Here g.s. stands for the ground state). These peaks are somewhat different in character for ^{12}C and ^{103}Rh targets than they are for the main target studied, ^{208}Pb. The peaks from carbon are sharper than the others and we attribute this to the reduced effect on final α and n energies from nuclear Coulomb fields for those breakups of ^{5}He which happen to occur close to the target nucleus. The other target for which we have comparably detailed data, ^{103}Rh, shows peaks elongated in a direction that corresponds to pickups which leave the ^{102}Rh in a broad distribution of low-lying excited states. This is not unexpected in view of the greater low-lying level density in ^{103}Rh compared with either ^{12}C or ^{208}Pb.

Since our last account, a publication[3] has appeared confirming our coincidence identification of the (α,^{5}He) reaction and there also have appeared two

calculations[4,5] of expected cross-sections for the reaction. These calculations share some features with DWBA calculations which we have carried out ourselves.[2] Figure 8.3-1 shows the results of our calculations for the expected differential cross-section for ^{5}He g.s. production in ^{208}Pb at both 42 and 90 MeV. The computations were carried out for the various low-lying hole states and their sum compares favorably with our observations which integrate over the low-lying states of the residual nucleus. The reason that low $\Delta\ell$ pickups are favored over those involving higher angular momentum transfers is that the $(\alpha,^{5}\text{He})$ reaction in the forward direction tends to involve quite small momentum changes to low residual excitations.

In addition to the production of ^{5}He g.s., one must expect to see the production of higher states in ^{5}He, for example the first excited $p_{1/2}$ state. The cross-section for such states is, however, difficult to establish from the observations because of the great width of the higher states of ^{5}He. One needs sharp kinematic signatures to identify a residual state when there are more than two particles in the final state. It is for such reasons that one might not

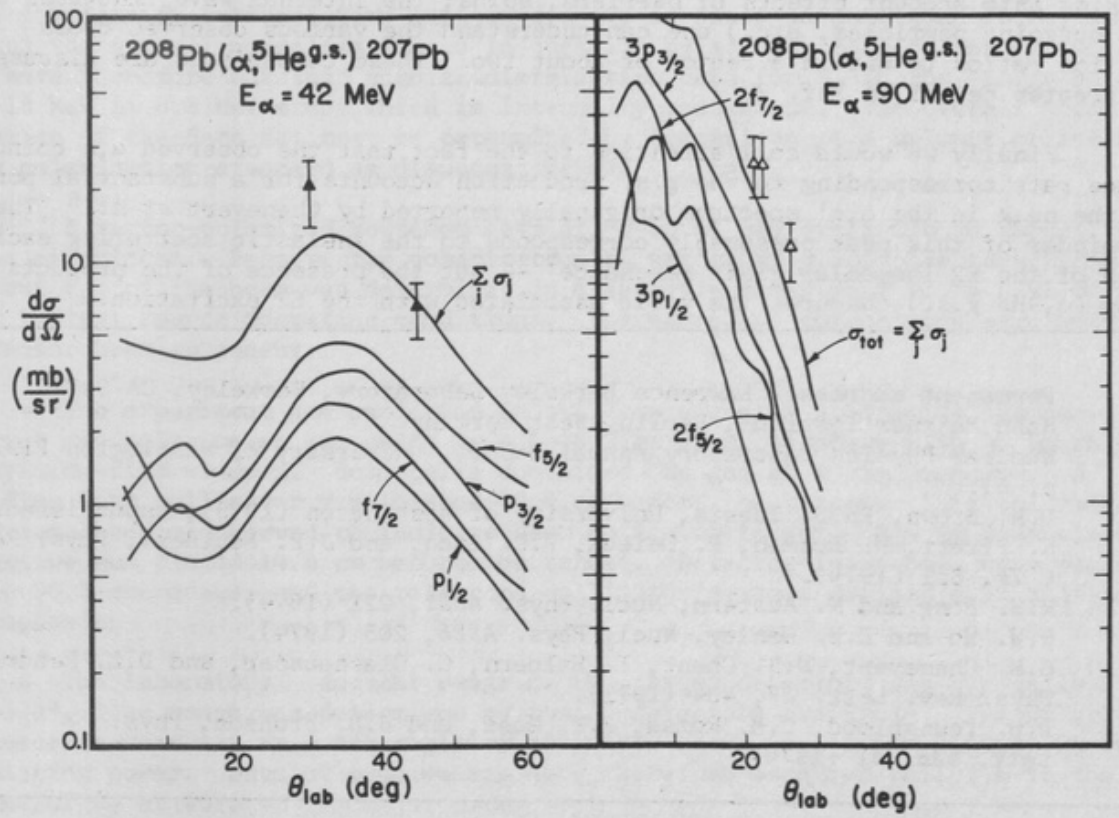

Fig. 8.3-1. A comparison of calculations of the angular distributions of the $(\alpha,^{5}\text{He g.s.})$ reaction to low-lying single hole states in ^{207}Pb with the observations. The observations correspond to the sum of cross-sections to the various single-hole states and seem to agree reasonably with expectations both at 42 MeV and 90 MeV.

expect to see much structure in an E_α vs E_n plot that corresponds to the reaction $\alpha + A \rightarrow (A - 2) + \alpha + n + n$ since here there are 4 particles in the final state. Yet we observe clear evidence for this reaction proceeding through the sequence $(A-2) + {}^6He^*(1.8\ MeV)$ with the $^6He^*$ going to ^5He g.s. + n and ^5He g.s. finally breaking up into α + n. The appearance of structure in this 4 particle final state is due to things, first the sharpness of the $^6He^*$ state involved in the sequence and, second, the limited phase space into which the $^6He^*$ can break up. The break-up apparently goes through $^5He_{g.s.}$ + n rather than, say, α + d neutron presumably because of the inhibition of the latter by a $\Delta\ell = 2$ centrifugal barrier. Moreover the $^6He^*$ decay energy is so low (0.83 MeV) that only a narrow portion of the width of the ^5He ground state can be populated. The upper portions of this level are not populated because of centrifugal barrier inhibition against low energy neutron emission. The observations of this pickup to the 1.8 MeV state in ^6He show that the cross-section is substantial approaching that of the one-neutron pickup to ^5He g.s.

It should be mentioned that the one and two neutron pickup cross-sections by α particles can be compared to the corresponding ones with protons and that (taking into account effects of barriers, spins, the internal wave functions of the outgoing particles, etc.) one can understand the various observed cross-section ratios to within a factor of about two. These comparisons are discussed in greater detail in Ref. 2.

Finally we would call attention to the fact that the observed α,n coincidence rate corresponding to ^5He g.s. production accounts for a substantial portion of the peak in the α,α' spectrum originally reported by Chenevert *et al.*[6] The remainder of this peak presumably corresponds to the inelastic scattering excitation of the E2 isoscalar giant resonance[7] -- but the presence of the products from (α,^5He g.s.) obscures the yield associated with the E2 excitation.

---

* Permanent address: Lawrence Berkeley Laboratory, Berkeley, CA 94720

† Hahn Meitner Institut, Berlin, West Germany.

1. Nuclear Physics Laboratory Annual Report, University of Washington (1974), p. 67.
2. D.R. Brown, Ph.D. Thesis, University of Washington (1975), unpublished.
3. C. Pirart, M. Bosman, P. Leieux, P.C. Macq, and J.P. Meulders, Phys. Rev. C *10*, 651 (1974).
4. W.S. Pong and N. Austern, Nucl. Phys. *A221*, 221 (1974).
5. H.W. Ho and E.M. Henley, Nucl. Phys. *A225*, 205 (1974).
6. G.M. Chenevert, N.S. Chant, I. Halpern, C. Glashausser, and D.L. Hendrie, Phys. Rev. Lett. *27*, 434 (1971).
7. D.H. Youngblood, C.M. Rozsa, J.M. Moss, and J.D. Bronson, Phys. Lett. *53B*, 51 (1974).

---

9. REACTIONS WITH POLARIZED PROTONS AND DEUTERONS

9.1 Vector Analyzing Power for Elastic Scattering of Deuterons from ^{4}He

N.L. Back, J.E. Bussoletti, L.D. Knutson, K-L Liu, and T.A. Trainor

In recent years there have been reports of vector-analyzing-power measurements for d-α scattering over a broad range of energies (3-45 MeV).[1,3-7] Phase shifts have been determined in the energy region 3-11.5 MeV and extrapolated to higher energies based on measurements made near 20 MeV.[1,2,4] These data confirm the excellent properties of this reaction as a polarization analyzer over the entire energy range.

A program has recently been initiated to develop the polarized deuteron beam capability of the Lamb-shift ion source at this Laboratory. It is planned to use d-α scattering as a monitor of the beam vector polarization at energies up to 18 MeV. A survey of the available data in the region 14-18 MeV has shown inconsistencies of the order of 0.05 in A_y at some energies and angles. Also, the phase shift extrapolation mentioned above is based on data near 20 MeV for which the overall normalization is in question by as much as a factor of two.[4,6] We have therefore obtained angular-distribution data for A_y in the energy range 14-18 MeV in 0.5 MeV steps which is internally consistent. The overall normalization of the data set must be determined by comparison to a primary or secondary polarization standard as discussed below.

A vector-polarized deuteron beam of 40-50 nA was available on target for this experiment. Beam vector polarization P_z was about 0.50. The tensor component P_{zz} of the beam was determined in a separate experiment to be 0.01 or less for typical source operating conditions. Therefore, no corrections were made for a tensor beam component.

The experiment was performed in a 152 cm diameter scattering chamber. The target and polarimeter gas cells were both 5 cm diam cylinders with 25 μm thick polyimide film windows. Both cells contained ^{4}He gas at 1 atm pressure. A 2.4 mm diam beam collimator was located 40.6 cm before the target. This collimator was insulated and served to indicate beam motion on target. A 4 mm diam cleanup aperture was placed 14.6 cm before the target. Detector telescopes were placed at a 20.3 cm radius, and the telescope collimator systems defined a 1° half-angle acceptance.

The laboratory angular range of the target detectors was typically 35° to 120°. The range was determined by the ΔE detectors available. The polarimeter telescopes were set at a lab angle of 90° where there is a broad minimum in the analyzing power. Data at each energy were therefore measured relative to the value of A_y at 90°.

The last focusing and steering elements preceding the scattering chamber used were about 8 m from the target. This large distance combined with the large chamber geometry and relatively tight beam collimation greatly reduced fluctuations in the data due to beam motion on target.

Relative normalizations between data sets at different energies were

obtained by inserting a 0.033 mm thick rolled brass degrading foil between target and polarimeter gas cells. The energy loss in the foil was slightly less than 1 MeV at the energies used. The ratios of asymmetries measured with the foil in gave energy-to-energy normalizations. The foil was periodically swung out of the beam to provide checks on data consistency. Both target and polarimeter telescopes were at a lab angle of 90° for these measurements.

The energy-to-energy normalization measurements indicated that there is no variation in the value of A_y at 90° over the energy range 14-18 MeV to within a statistical error of 0.005 in A_y.

A tentative overall normalization of the entire data set is therefore established by fixing the value of A_y (90° lab) = -0.400 over the energy range 14-18 MeV. This value is derived from the data of Ohlsen *et al.*[6] at 12, 14, and 17 MeV for which a spin-filter type Lamb-shift source was used. As discussed in their paper the quench-ratio method of determining the beam polarization serves as a secondary polarization standard. Current best estimates of the error associated with the quench-ratio method for a spin-filter source yield an absolute normalization error in A_y (90° lab) of ±.010. This error is in addition to the statistical errors associated with the asymmetry measurements reported here.

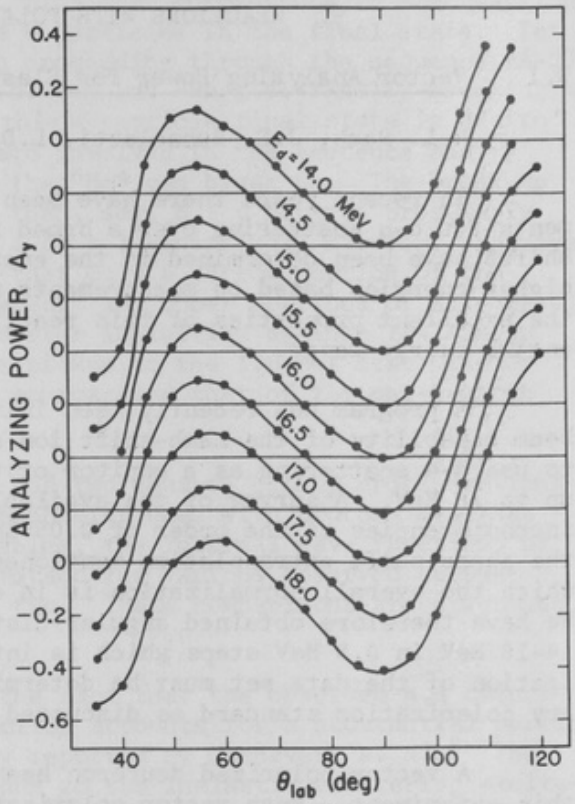

Fig. 9.1-1. Vector analyzing power A_y for the reaction $^4He(\vec{d},d_0)^4He$.

The normalized data set is shown in Fig. 9.1-1. Smooth curves have been drawn through the data points to guide the eye. In drawing these curves no attempt was made to represent the deep minimum in A_y near 35° lab.

The general trend of the data shows a very smooth energy dependence at all angles. The forward minimum at about 35° lab tends to become shallower and the backward maximum at about 120° lab tends to increase with increasing energy up to 18 MeV. Statistical errors in A_y are typically 0.005 to 0.008.

It is planned to parameterize these data by continuing phase-shift sets determined at lower energies.

1. L.G. Keller and W. Haeberli, Nucl. Phys. *A156*, 465 (1970).
2. P.A. Schmelzbach, W. Grüebler, V. König, and P. Marmier, Nucl. Phys. *A184*, 193 (1972).
3. W. Grüebler, V. König, P.A. Schmelzbach and P. Marmier, Nucl. Phys. *A134*, 686 (1969).
4. J. Arvieux, P. Darriulat, D. Garreta, A. Papineau, A. Tarrots, and J. Teston, Nucl. Phys. *A94*, 663 (1967).
5. C.C. Chang, H.F. Glavish, R. Avida, and R.N. Boyd, Nucl. Phys. *A212*, 189 (1973).
6. Gerald G. Ohlsen, P.A. Louoi, G.C. Salzman, U. Meyer-Berkhout, C.K. Mitchell, and W. Grüebler, Phys. Rev. C *8*, 1262 (1973).
7. H.E. Conzett, W. Dahme, Ch. Leemann, J.A. Macdonald and J.P. Meulders, Report LBL-1666, 1972, Lawrence Berkeley Laboratory, Berkeley, CA.

9.2 Depolarization in the Elastic Scattering of 17 MeV Polarized Protons from ^{9}Be

M.P. Baker, J.S. Blair, J.G. Cramer, J.W. Tape, T.A. Trainor, W.G. Weitkamp, and H. Wieman

Measurements of the angular distribution of the Wolfenstein depolarization parameter D(θ) for proton-elastic scattering from ^{9}Be has continued during the last year. As described previously,[1] the reaction was initiated by polarized protons and the polarization of those protons elastically scattered by the ^{9}Be analyzed using a high-resolution, silicon polarimeter. The polarimeter has a measured analyzing power of ∿+0.4 and an efficiency equal to 1-2 ∿ 10^{-5} with 170-keV resolution. Data has now been accumulated at angles between 70° and 120° in 10° steps with uncertainties ranging from 0.05 to 0.08. Theoretical comparisons to the measured depolarization-parameter angular distribution have been made using a multipole expansion of the elastic-scattering amplitude in terms of the amount of angular momentum, J, transferred to the target nucleus during the scattering process.[2] The indications are that the J = 2 contribution to the proton-elastic scattering amplitude for ^{9}Be can yield large deviations from unity in the depolarization parameter and thus mask the smaller depolarization effects due to the J = 1 (spin-spin) components.

Recall that the depolarization parameter, D(θ), is related to directly measurable quantities by the expression:[3]

$$p_f(\theta) = \frac{A(\theta) + p_i\, D(\theta)}{1 + p_i A(\theta)}$$

where $p_f(\theta)$ is the polarization produced at the angle θ in the elastic scattering of an incident proton beam of polarization p_i, A(θ) is the analyzing power for elastic scattering at the angle θ. Thus a determination of D requires the measurement of p_f, A and p_i.

A schematic diagram of the experimental apparatus used for the depolarization measurements is shown in Fig. 9.2-1. The beam polarization, p_i, was continuously monitored by a carbon polarimeter located upstream from the ^{9}Be target.

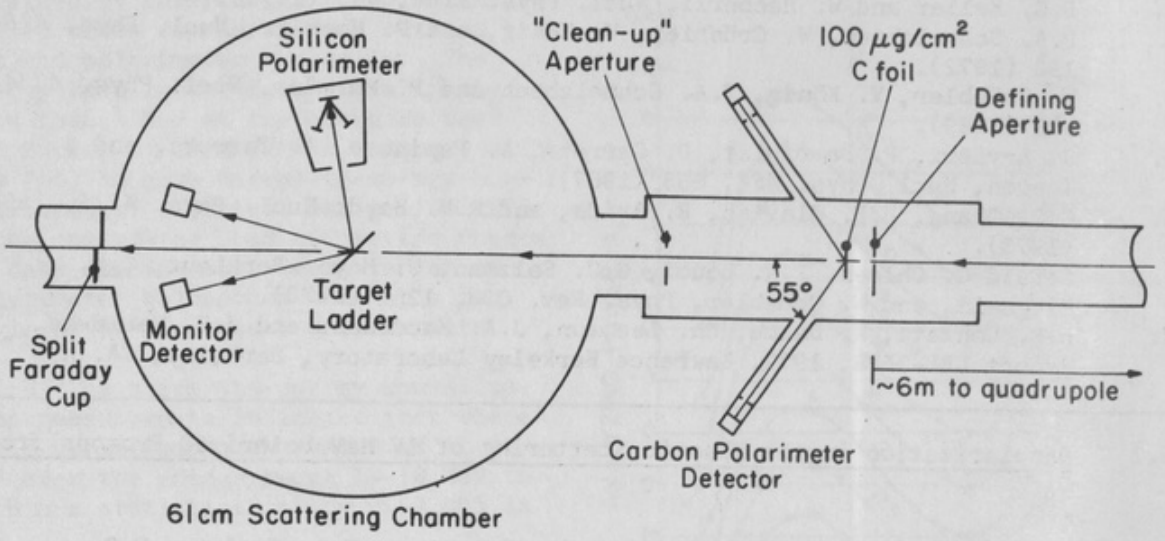

Fig. 9.2-1. Schematic diagram of scattering chamber and ancillary experimental apparatus used for depolarization measurements.

The polarization produced in (p_f) and the analyzing power of (A) the elastic scattering reaction on ^{9}Be was measured in the silicon polarimeter mounted on a rotatable arm in the scattering chamber. The beam passing through the target was collected by a split Faraday cup located directly down stream. The currents from the two halves of the cup were fed back to a regulator which controlled the current in the bending magnet immediately upstream from the scattering chamber in order to maintain the position of the beam on target. Monitor detectors were mounted at ±13° and used to measure the stability of the beam position and/or angle and to provide a check on the current integration system.

A more detailed diagram of the reflection-geometry, silicon polarimeter is shown in Fig. 9.2-2. This polarimeter is identical to that described last year[4] except for a minor change in the side-detector shielding. In an effort to reduce the fast neutron flux incident upon the side detectors, a 4 cm thick Fe shield was constructed to replace the existing 2 cm thick Pb shield. The permanent magnets used for electron suppression were then mounted directly on the Fe shield.

The quantity p_f was determined by comparing double-scattering events in the left and right side detectors. Since the analyzer detector was thick enough to stop all the single-scattered particles of interest, the quantity A was obtained by comparing the "singles" elastic scattering peak areas for the incident beam spin direction up and down.

The measured values of the depolarization parameter for proton-elastic scattering from ^{9}Be at ∿17 MeV obtained to date are given in Table 9.2-1. Although the uncertainty is rather large, the result obtained at a laboratory scattering angle of 120° represents the largest deviation from unity in the

depolarization parameter ever observed for proton-elastic scattering from a "heavy" nucleus.

Table 9.2-1. Measured values of the depolarization parameter for proton-elastic scattering from ^{9}Be at 17 MeV.

θ_L	A	D
70°	0.304	0.87 ± 0.06
80°	0.215	0.93 ± 0.06
90°	0.096	0.86 ± 0.05
100°	-0.003	0.92 ± 0.07
110°	-0.178	1.03 ± 0.08
120°	-0.226	0.78 ± 0.07

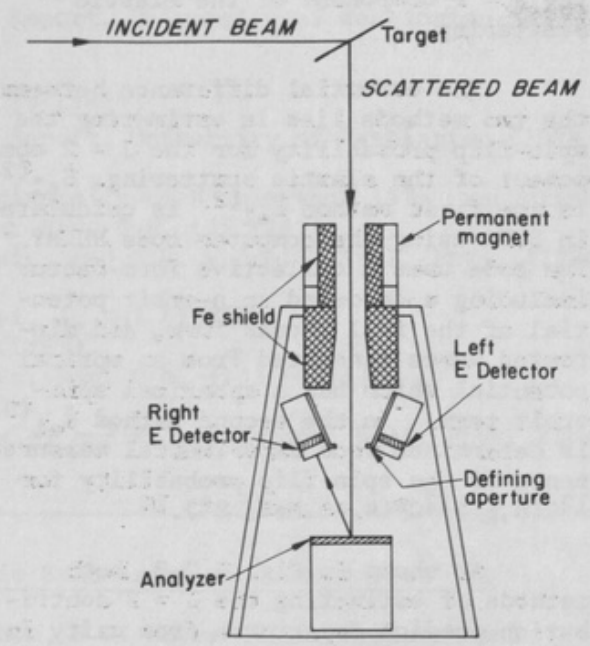

Fig. 9.2-2. High-resolution silicon polarimeter developed for use in the depolarization measurements.

Figure 9.2-3 shows a comparison between the experimental data and the predictions for the depolarization parameter using several theoretical models. The analysis presented here is based on a multipole expansion of the elastic-scattering amplitude in terms of the amount of angular momentum, J, transferred to the target nucleus. (Details of the theoretical analysis can be found in Refs. 2 and 5.) In this expansion the J = 0 term results from the standard optical model potential and can produce no spin flip (the spin-flip probability, S, is related to the depolarization parameter, D, by the relation S = ((1 - D)/2)). Only the terms in the expansion with J > 0 can produce spin flip (J_{max} = 2I, where I is the spin of the target) and to the extent that such terms form an important part of the elastic scattering amplitude, substantial spin flip probabilities are expected.

The J = 1 prediction is the result of a DWBA calculation using the computer code SPINSOR.[6] A standard optical model potential[7] was used to generate the distorted waves and the J = 1 spin-spin interaction was composed of spherical and tensor forms. The largest reasonable estimates[8] for the strengths of the spin-spin interactions have been assumed in the calculation. The data generally indicate much larger departures from unity than those predicted for the J = 1 contribution.

The predictions for the J = 2 contributions to the spin-flip probability, on the other hand, have more nearly the magnitude of what has been observed. As discussed in more detail in Ref. 2, two methods have been developed for estimating the role of the J = 2 terms in the elastic scattering process. Both methods rely on a comparison of the strong inelastic scattering to the $5/2^-$, 2.43 MeV state in ^{9}Be (which involves the transfer of two units of angular momentum) to

the J = 2 component of the elastic scattering.

The essential difference between the two methods lies in estimating the spin-flip probability for the J = 2 component of the elastic scattering, $\hat{S}_{el}^{(2)}$. In the first method $\hat{S}_{el}^{(2)}$ is calculated in DWBA using the computer code HELMY.[9] The code uses a collective form-factor including a deformed spin-orbit potential of the full Thomas form, and distorted waves generated from an optical potential which has a spherical spin-orbit term. In the second method $\hat{S}_{el}^{(2)}$ is determined from experimental measurements of the spin-flip probability for $^{12}C(p,p')^{12}C^*(4.43\ MeV, 2^+)$.[10]

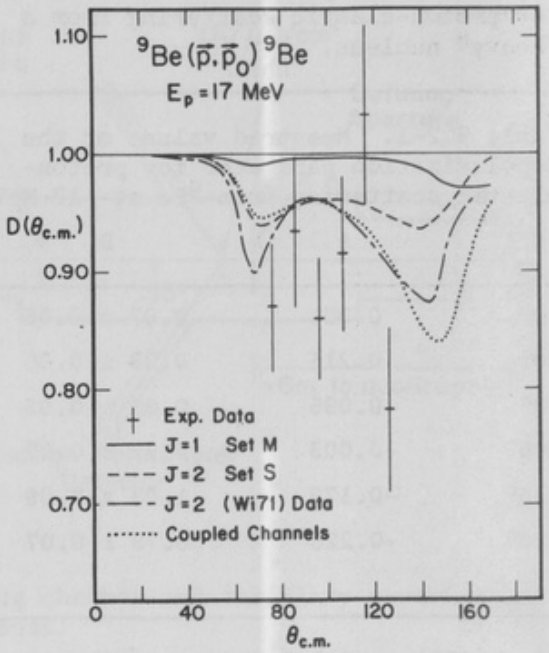

Fig. 9.2-3. Comparison between measured and calculated values of the depolarization-parameter angular distribution for proton-elastic scattering from ^9Be at ∿17 MeV. Several calculational procedures are used to derive the curves shown as discussed in the text.

As shown in Fig. 9.2-3, both methods of estimating the J = 2 contribution predict departures from unity in D significantly larger than those computed for the J = 1 component. The second method yields depolarization predictions which more closely approximate the magnitude of the experimental observations. Also shown for comparison are the results of a coupled-channels calculation in which the effects of the J = 2 contribution to the scattering are included. The prediction is quite similar to that determined from the ^{12}C inelastic data with a somewhat deeper back-angle dip. The parameters of Votava *et al.*[12] were used for these calculations and the deformation of the spin-orbit potential was not included.

In summary, one can say that the J = 2 contribution to the scattering amplitude is a much more likely mechanism than the J = 1 term for producing the observed departures from unity in the depolarization parameter. If this is the case, then the effects of the J = 1 term are likely to be masked by the J = 2 component for all targets with spin one or greater. A careful measurement of the depolarization parameter angular distribution for a spin 1/2 target may help clarify the role of the J = 1 and 2 components in the elastic scattering amplitude.

In order to further test the theoretical ideas discussed here, additional depolarization measurements on ^9Be at more backward angles are planned for the near future.

1. Nuclear Physics Laboratory Annual Report, University of Washington (1974), p. 75.
2. Section 9.6 of this report.
3. G.G. Ohlsen, Rep. Prog. Phys. *35*, 17 (1972).
4. Nuclear Physics Laboratory Annual Report, University of Washington (1974), p. 21.
5. Michael P. Baker, Ph.D. Thesis, University of Washington, 1975, unpublished.
6. A.H. Hussein and H.S. Sherif, Phys. Rev. C *8*, 518 (1973).
7. D.G. Montague, R.K. Cole, P.S. Lewis, and C.N. Waddell, Nucl. Phys. *A199*, 433 (1973).
8. G.R. Satchler, Particles and Nuclei, *1*, 397 (1971).
9. H. Sherif, Nucl. Phys. *A131*, 532 (1969).
10. M.A.D. Wilson and L. Schecter, Phys. Rev. C *4*, 1103 (1971).
11. W.J. Thompson, private communication.
12. H.J. Votava, T.B. Clegg, E.J. Ludwig, and W.J. Thompson, Nucl. Phys. *A204*, 529 (1973).

9.3 The Analyzing Power for the Elastic Scattering of Protons from ^{12}C

M.P. Baker, J.G. Cramer, J.S. Dunham, H.O. Meyer*, T.A. Trainor, and W.G. Weitkamp

Last year we reported the measurement of analyzing power excitation functions for $^{12}C + \vec{p}$ at three back angles between 11.5 and 17.7 MeV.[1] We also reported the measurement of six angular distributions in the same energy region. After a phase shift analysis was begun on these data, it became apparent that more data would be necessary in order to obtain reliable fits. In particular, we found that it would not be possible to obtain good fits for regions like those at 13.2 and 15.2 MeV without several complete angular distributions spaced rather closely in energy throughout the entire structure.

Using the same experimental setup, we have now measured complete angular distributions ($\geq$ 12 angles) at nearly 40 energies in the region from 11.5 to 18.0 MeV. Also, complete analyzing power excitation functions for six back angles have been obtained for this energy region.

The new data obtained at forward angles above 17 MeV shows a prominent structure corresponding to the 17.67 MeV 1/2- state seen by LeVine and Parker.[2] No evidence for the 17.8 MeV 3/2+ state can be found in our data.

We are now completing the phase shift analysis, obtaining far more satisfactory fits than was possible with the limited amount of data available last year.

* Department of Physics, University of Basel, Basel, Switzerland.
1. Nuclear Physics Laboratory Annual Report, University of Washington (1974), p. 88.
2. M.J. Levine and P.D. Parker, Phys. Rev. *186*, 1021 (1969).

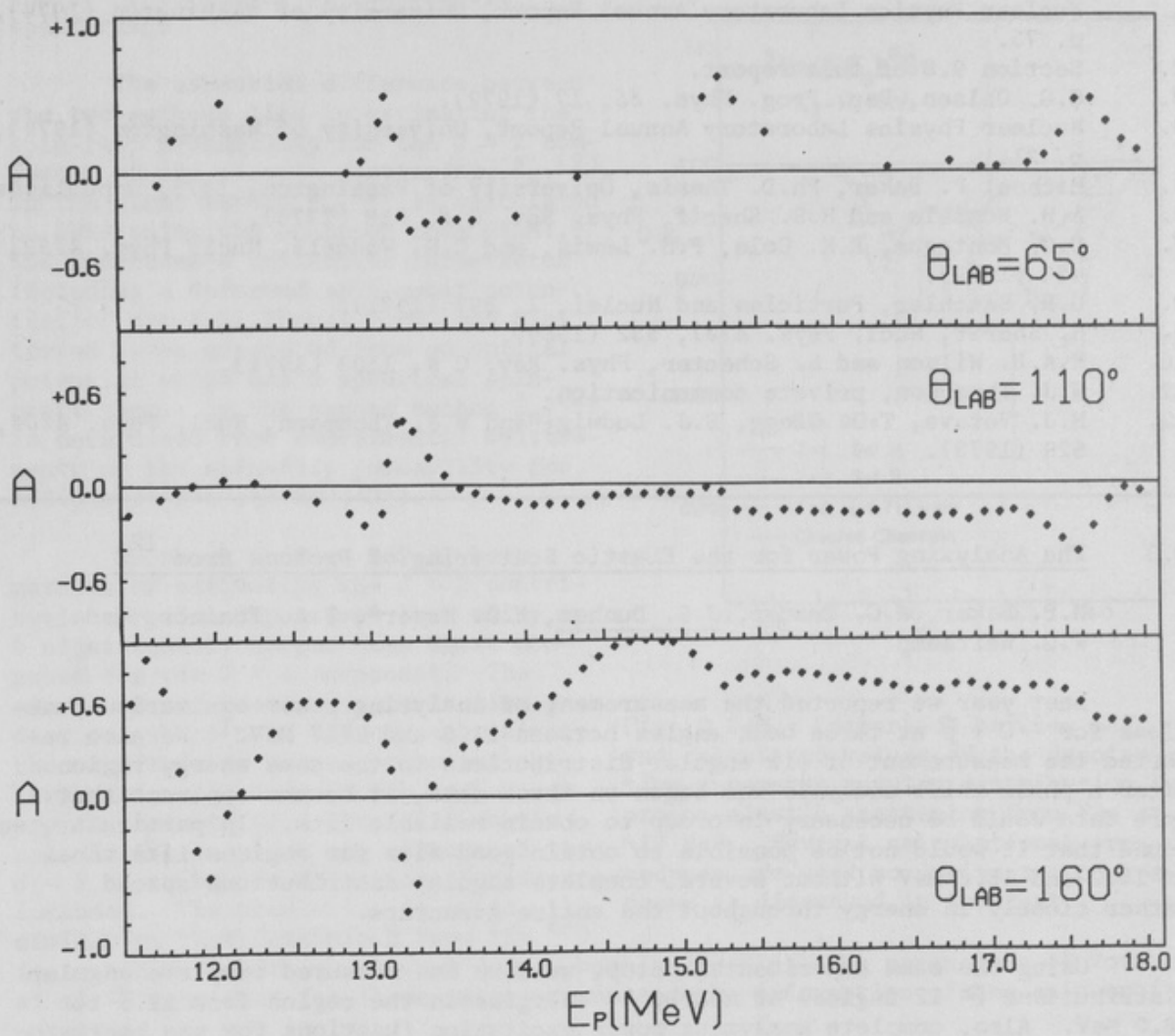

Fig. 9.3-1. Analyzing power excitation functions for three angles in the reaction $^{12}C(\vec{p},p_0)$ from 11.5 to 18.0 MeV.

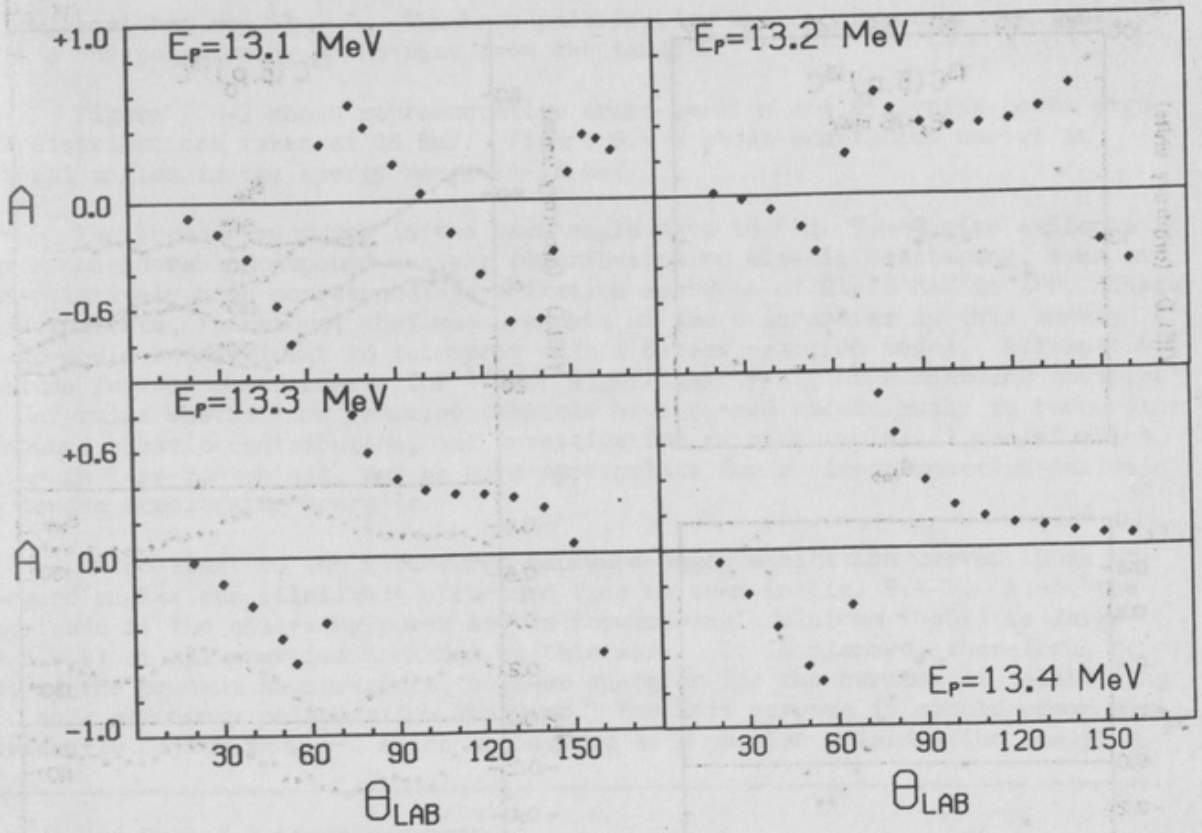

Fig. 9.3-2. Angular distributions of the analyzing power for the $^{12}C(\vec{p},p_0)$ reaction around the structure at 13.2 MeV.

9.4 Analyzing Power for Elastic Scattering of Protons from ^{13}C

N.L. Back, J.E. Bussoletti, J.G. Cramer, L.D. Knutson, and T.A. Trainor

Recent measurements of the D parameter for $^{9}Be(\vec{p},\vec{p}_0)^{9}Be$[1] have shown large deviations from unity at backward angles, corresponding to a considerable spin-flip probability. Such deviations cannot be accounted for by spin-spin forces and are substantially larger than those predicted by the recently developed "quadrupole" spin-flip mechanism.[2] It is therefore possible that several different mechanisms, including possible compound nuclear contributions, are involved in the large observed spin-flip probability.

Because the quadrupole spin-flip mechanism cannot contribute to depolarization in the case of elastic proton scattering from a spin-1/2 nucleus there would be less ambiguity in the analysis of D-parameter measurements for such a case. A program was therefore initiated to measure cross sections and analyzing powers for $^{13}C(p,p_0)$ as a preliminary to D-parameter measurements. The choice of ^{13}C seemed to be ideal since the target is relatively easily available, and the first excited state (3.09 MeV) is well separated from the spin-1/2 ground

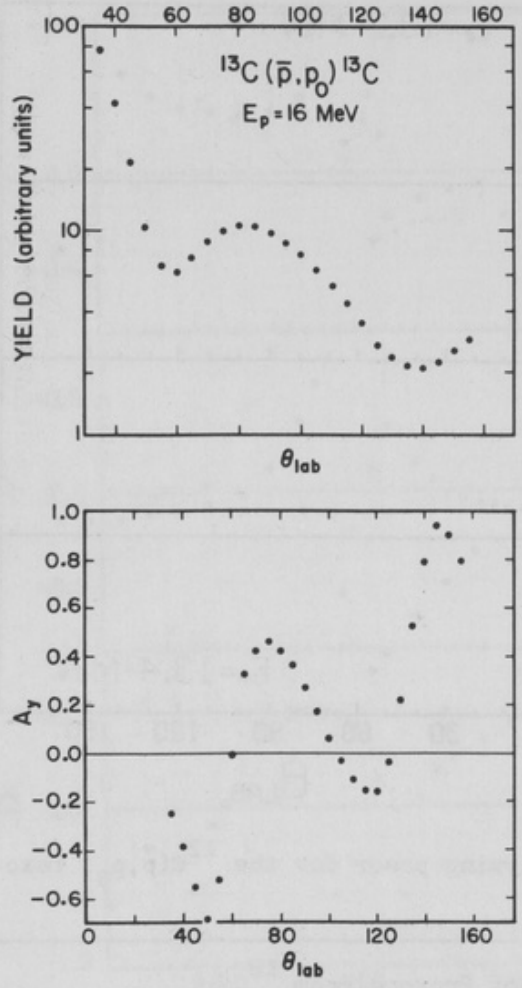

Fig. 9.4-1. Cross-section and analyzing-power angular distributions for $^{13}C(\vec{p},\vec{p}_0)^{13}C$ at E_p = 16 MeV.

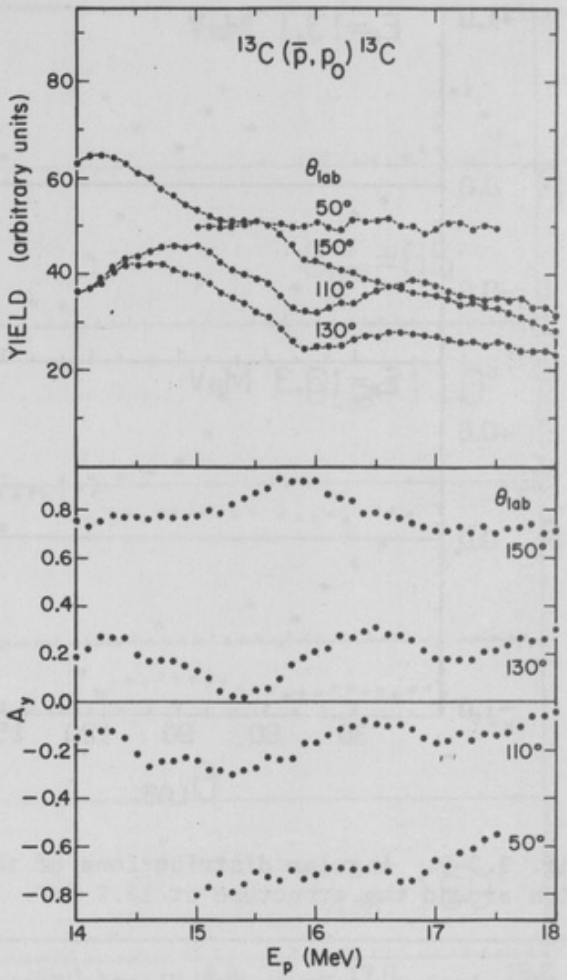

Fig. 9.4-2. Cross-section and analyzing-power excitation curves for $^{13}C(\vec{p},\vec{p}_0)^{13}C$ from 14-18 MeV.

state. The latter is important because of significant energy straggling in thick targets and broadening of elastic and inelastic peaks in the polarimeter. The cross-section and analyzing-power data are required in order to extract D-parameter values from polarimeter data and to obtain finite-geometry corrections.

Excitation curves were obtained in 100 keV steps from 14 to 18 MeV at lab angles of 30°, 50°, 70°, 110°, 130°, and 150°. Also, angular distributions in 5° steps were obtained every 250 keV in the energy range 16-17 MeV. Statistical uncertainties are typically ±0.7% for cross section data and ±0.01 for analyzing power data.

Data were obtained with a 150 cm diam scattering chamber. Three symmetric detector pairs with 2° acceptance angle were used. The target was 100 μg/cm^2

thick, enriched to 97% ^{13}C. The beam polarization was continuously monitored with a ^{4}He polarimeter downstream from the target.

Figure 9.4-1 shows representative cross-section and analyzing-power angular distributions taken at 16 MeV. Figure 9.4-2 shows excitation curves at several angles in the energy range 14-18 MeV.

The broad structures in the back angle data in Fig. 9.4-2 give evidence for a considerable compound nuclear contribution to elastic scattering, even at the relatively high corresponding excitation energies of 21-25 MeV in ^{14}N. These data indicate, therefore, that measurements of the D parameter in this energy range would be difficult to interpret with a direct reaction model. Alternatives include further measurements for ^{13}C at significantly higher bombarding energies to determine whether new reaction channels have opened sufficiently to reduce the compound elastic contribution, and investigation of other spin-1/2 nuclei which, although less convenient, may be more appropriate for a direct reaction analysis at tandem accelerator energies.

In contrast to the structured backward-angle excitation curves those at forward angles are relatively structure free as seen in Fig. 9.4-2. Also, the magnitude of the analyzing power at the forward-angle minimum ($\sim 50^{\circ}$) is large (0.6-0.8) at all energies included in this work. It is planned, therefore, to extend the present measurements to lower energies for the purpose of calibrating ^{13}C as a secondary polarization analyzer. For this purpose it should prove significantly better than ^{12}C which has served as a popular polarization analyzer.

---

1. See Sec. 9.2 of this report.
2. See Sec. 9.6 of this report.

9.5 Analyzing Powers in the $^{40}Ca(\vec{p},p')^{40}Ca$ Reaction between 16.0 and 18.0 MeV

N. Back, J.S. Blair, J. Bussoletti, B. Cuengco, L. Knutson, T. Trainor, and J. Wiborg

We have completed the analysis of the angular distributions for 17.5 MeV polarized protons in the reactions $^{40}Ca(\vec{p},p')$ and $^{48}Ca(\vec{p},p')$[1] by obtaining optical model fits to the elastic scattering cross section and polarization. DWBA calculations,[2] using these optical model parameters, failed to reproduce the observed inelastic cross sections and analyzing powers. This failure leads us to suspect large non-direct contributions to the inelastic scattering. However, previous measurements[1] of cross section excitation functions on ^{48}Ca and ^{40}Ca showed little evidence for isolated resonance contributions in the energy range of 16 MeV to 18 MeV. For this reason we have investigated the analyzing power excitation function of ^{40}Ca + p in the hope that the analyzing powers might be more sensitive to the presence of non-direct reaction mechanisms.

The analyzing power excitation function of the $^{40}Ca(\vec{p},p')^{40}Ca^{*}$ reaction was measured from E_p = 16.0 MeV and E_p = 18.0 MeV. The data in the 16.0 to 17.0 MeV region were obtained in 100 keV steps while the 17.0 to 18.0 MeV region was

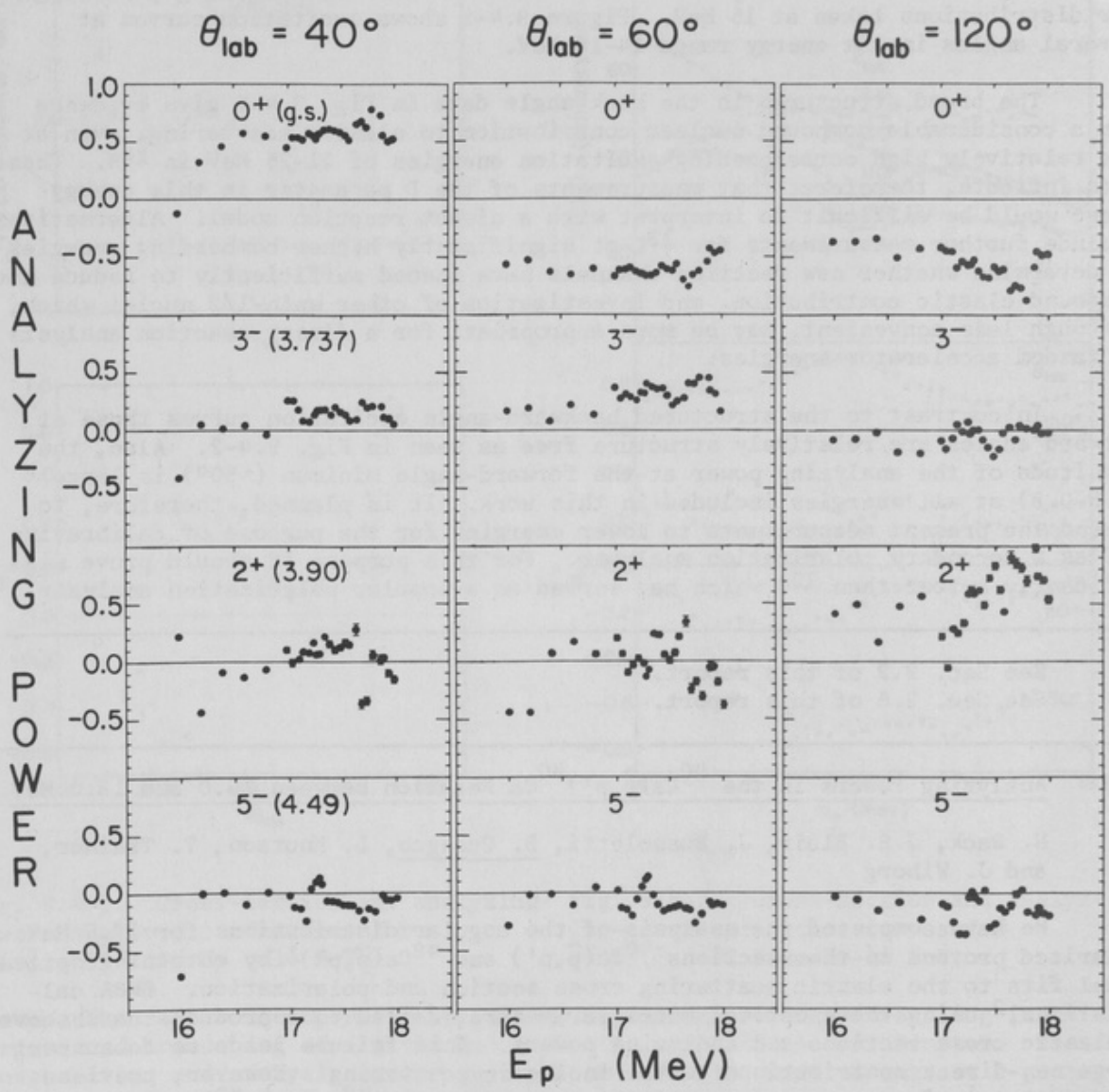

Fig. 9.5-1. Analyzing power excitation functions of the $(0.0)0^+$, $(3.737)3^-$, $(3.903)2^+$, and $4.491)5^-$ states for the $^{40}Ca(p,p')^{40}Ca$ reaction measured at 40°, 60°, and 120°.

measured in 50 keV steps. Left and right counters were set at laboratory angles of 40°, 60°, and 120°. The discrepancy between the calculated and measured analyzing powers at E_p = 17.5 MeV were most severe for these angles. A ^{12}C polarimeter with detectors set at 55° was used to continuously monitor the beam polarization.

If direct reaction were the dominant reaction mechanism we would expect a slow variation of the analyzing power with energy over a width of several MeV. Our measurements show that this is not the case. For inelastic scattering to the $^{40}Ca(3.737)3^-$, the $^{40}Ca(3.903)2^+$, and the $^{40}Ca(4.491)5^-$ states, we observe significant fluctuations with a width of several hundred keV. The results of our measurements are shown in Fig. 9.5-1.

These fluctuations, observed in the analyzing power excitation functions, tend to corroborate our suspicions of non-direct reaction contributions. The structure in the $^{40}(4.491)5^-$ excitation function are particularly suggestive of interfering resonances at 17.2 and 17.7 MeV.

At present the situation is by no means clear. It would be desirable to extend the excitation function to higher energies, but our machine is limited to 18 MeV. We intend to proceed by examining the excitation function in more detail at other angles. We also plan to examine the analyzing power excitation function of other nuclei in the ^{40}Ca mass region to determine whether the fluctuations are common to all nuclei in this region.

---

1. Nuclear Physics Laboratory Annual Report, University of Washington (1974), p. 78; (1973), p. 78.
2. H. Sherif and J.S. Blair, Phys. Lett. *26B*, 489 (1968); H. Sherif, Nucl. Phys. *A131*, 532 (1969).

9.6 The Depolarization of Elastically Scattered Nucleons and Quadrupole Spin-Flip

M.P. Baker, J.S. Blair, and H.S. Sherif*

Stimulated by the observation in this Laboratory of large depolarization of protons elastically scattered from ^9Be,[1] we have re-examined the possible mechanisms for producing such depolarization. The traditional approach has attributed depolarization to the presence of explicit terms in the optical potential coupling the spin of the projectile to that of the target nucleus;[2] such terms may in turn be related to spin dependent interactions in the two-nucleon system.[3] While fits to existing depolarization data can be obtained by adding spin-spin terms to the optical potential, the required strengths of such terms are much larger than those resulting from the known two-nucleon interactions.

Faced with this contradiction, we then realized that there was another direct mechanism, hitherto overlooked, which could contribute to depolarization. This mechanism involves the transfer of two units of angular momentum to the nucleus in the presence of a distorting (spherical) potential which contains the

usual spin-orbit coupling; it is closely related to the phenomenon of quadrupole spin flip seen in the inelastic excitation of 2^+ levels of even mass targets. This process can, in principle, occur in any situation where $I > 1/2$; it will be most important when a collective description for the quadrupole interaction is appropriate so that the quadrupole contribution is enhanced.

Numerical calculations of the depolarization parameter, $D(\theta)$, (or equivalently, the spin-flip probability $S \equiv (1 - D)/2$, have been made using several procedures which are concrete embodiments of the quadrupole spin-flip effect sketched in the preceding paragraph. For the case of ^{9}Be, ^{10}B, and ^{27}Al targets, our numerical calculations approximate the observed depolarization.

In the most theoretical of these calculations, the rotational model has been adopted for the target nuclei ^{9}Be and ^{10}B; the strength of the deformation parameter β_2 is varied so that there is a modest fit to the inelastic scattering cross section to the first excited state within the rotational band; the predicted magnitudes of quadrupole contribution to the elastic scattering and the elastic depolarization are then uniquely specified for the optical parameters chosen.

An alternative procedure, which we feel has at least equal merit, makes use of experimentally measured quadrupole spin flip probabilities in neighboring spin-zero nuclei. To establish this procedure it is advantageous first to make an exact multipole decomposition[5] of the elastic amplitudes and to explore some of its consequences; specifically, for elastic scattering of a spin-1/2 projectile from a nucleus with angular momentum I, the elastic amplitude may be expanded:

$$f_{M'\mu'M\mu} = \sum_{J=0}^{2I} \sum_{m} (IJM',-m|IM)(2J+1)^{1/2} f^{(J)}_{m\mu'\mu}; \qquad (1)$$

here M and M' are the projections of I on the z axis before and after scattering, μ and μ' are the corresponding nucleon spin projections, J is the angular momentum transferred to the nucleus and m is its projection. This decomposition enables us to define precisely the contributions to the elastic cross sections and spin-flip probabilities owing to specific values of angular momentum transfer; this decomposition is tailor-made for theoretical discussions of direct processes in that the Clebsch-Gordan coefficient in Eq. (1) will naturally occur in a direct-interaction expression for the amplitude.

Particularly simple expressions for spin dependent observables result when one chooses a coordinate system whose z axis is perpendicular to the reaction plane. On using the Bohr theorem,[6] we see that there will be spin-flip; i.e., $\mu' \neq \mu$, if and only if the values of m are odd. (The spin projection μ' is now superfluous and is thenceforth deleted.)

With this decomposition, the elastic scattering cross section itself may be written

$$\sigma_{e\ell} = (2)^{-1} \sum_{J\mu m} |f^{(J)}_{m\mu}|^2 \equiv \sum_{J} \sigma^{(J)}_{e\ell} \qquad (2)$$

where use has been made of the orthogonality property of the Clebsch-Gordan

coefficients. Similarly, the elastic spin-flip probability becomes

$$S = (2\sigma_{e\ell})^{-1} \sum_{J\mu, m \text{ odd}} |f_{m\mu}^{(J)}|^2 \equiv (\sigma_{e\ell})^{-1} \sum_{J=1}^{2I} \sigma_{SF}^{(J)} \equiv \sum_{J=1}^{2I} S^{(J)}. \qquad (3)$$

It is interesting to note that, of all readily determined observables, spin-flip is a unique indicator of effects which may be attributed to the non-zero spin of a target nucleus; contrariwise, elastic cross sections, analyzing powers, and polarizations all have monopole as well as higher multipole contributions. The spherical and tensor spin-spin potentials, when considered in DWBA, lead only to J = 1. Clearly there can be J = 1 but no J = 2 spin-flip when I = 1/2; depolarization experiments on nuclei with I = 1/2 and on neighboring nuclei with I > 1/2 could enable one to assess crisply how much of the spin-flip mechanism should be attributed to dipole (J = 1) and how much to quadrupole (J = 2) components.

In order to proceed further in the evaluation of the J = 2 spin-flip probabilities, it is helpful to rearrange the last equation in the form of a product of ratios. Invariably, when $\sigma_{e\ell}^{(2)}$ is appreciable, there will be at least one low-lying level for which there is strong J = 2 excitation. Denoting the angular momentum of that reference state by $\bar{I}$ and the inelastic differential cross section to that level by $\sigma_{\bar{I}I}$, we may write

$$S^{(2)} = \frac{\sigma_{\bar{I}I}}{\sigma_{e\ell}} \frac{\sigma_{e\ell}^{(2)}}{\sigma_{\bar{I}I}} \frac{\sigma_{SF}^{(2)}}{\sigma_{e\ell}^{(2)}}. \qquad (4)$$

This form has the virtue that it involves three ratios, the first of which can be evaluated using easily obtained experimental data. Insofar as the excitation is direct and the excitation energy of the reference level is small compared to the bombarding energy, the second ratio should vary only slightly with angle. Its value may be calculated with a specific nuclear model; for example, the rotational model predicts that this is well approximated as a ratio of Clebsch-Gordan coefficients:

$$\frac{\sigma_{e\ell}^{(2)}}{\sigma_{\bar{I}I}} \simeq \frac{(I2K0|IK)^2}{(I2K0|\bar{I}K)^2}. \qquad (5)$$

In some cases the ratio may be deduced[7,8] from measurements of elastic and inelastic scattering by the nucleus in question as well as by neighboring zero-spin nuclei.

On considering the third ratio of Eq. (4), which is conveniently termed the intrinsic J = 2 spin-flip probability, $\hat{S}^{(2)}$, we come to the point where we make use of measured inelastic quadrupole spin-flip probabilities, $S_{in}^{(2)}$; specifically, our recommendation is that $\hat{S}^{(2)}$ be replaced by $S_{in}^{(2)}$ for a neighboring zero-spin nucleus. The basis for this substitution is that, on adopting standard collective models and assuming the scattering process to be sudden, we can prove the theorem that $\hat{S}^{(2)} = S_{in}^{(2)}$ for a hypothetical zero spin nucleus whose optical model and collective parameters are those adopted for the

non-zero spin nucleus in question. Provided that the actual scattering from a neighboring zero-spin nucleus is well approximated by this collective description, using the same optical parameters, that the spins of valence nucleons play no role in determining $S_{in}^{(2)}$ does not vary much with excitation energy, then substitution of measured inelastic spin-flip probabilities for $\hat{S}^{(2)}$ should be a fairly reasonable procedure. We note further that in the limit of DWBA, the ratios $\hat{S}^{(2)}$ and $S_{in}^{(2)}$ are independent of nuclear matrix elements.

These procedures have been applied to several examples. Application to the measurements, carried out at this Laboratory, of depolarization with the target nucleus ^{9}Be is presented elsewhere in this report.[1] The measurements of D with the smallest stated errors have been those made by a group at Saclay.[9] For ^{9}Be at 21.4 ± 2.3 MeV they found $D(\theta_{lab} = 58°) = 0.940 \pm 0.016$. Using ^{9}Be cross sections[10] measured at E_{lab} = 21.0 MeV and the Seattle group's measurements[4] of $S_{in}^{(2)}$ for ^{12}C at 20.0 MeV and that angle, 0.122, we predict that D = 0.924. The departures of D from unity predicted by DWBA or coupled-channel calculations are roughly half as much at this angle. For ^{10}B at 19.8 ± 1.3 MeV, the Saclay group finds $D(\theta_{lab} = 60°) = 0.926 \pm 0.012$; again using the measured inelastic spin-flip cross sections[4] for ^{12}C and cross section measurements[11] at 17.95 MeV, we predict D(60°) = 0.94.

Measurements of D, with somewhat greater stated uncertainty, have been reported[12] for ^{9}Be at E_{lab} = 24.7 MeV; these are compared in Fig. 9.6-1 to various predictions. Except for those based on $S_{in}^{(2)}$ measured[13] at 26.2 MeV, the predictions lie within the stated errors. We note that all procedures predict large depolarization at back angles.

There are some non-rotational nuclei for which the ratio $(\sigma_{el}^{(2)}/\sigma_{II})$ can be estimated by comparing the observed elastic and inelastic cross sections of neighboring odd and even nuclei.[7] Thus, a comparison of cross sections[15] for scattering of α particles by

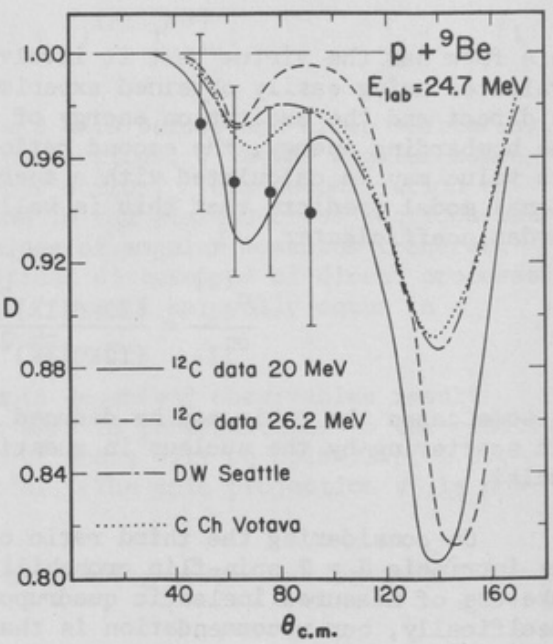

Fig. 9.6-1. Measurements of $D(\theta)$ for ^{9}Be at E_{lab} = 24.7 MeV (Ref. 12) compared to predictions based on measurements of $S_{in}^{(2)}$ for ^{12}C at 20.0 MeV (Ref. 4) or 26.2 MeV (Ref. 13), on DWBA calculations of $\hat{S}^{(2)}$ using the parameters of Ref. (1) or on coupled channel calculations of σ_{SF} which use the parameters of Ref. 14 but with complex coupling and $\beta_2 = 0.90$. The various calculations give spin-flip cross sections, σ_{SF}, with little angular structure except that they go to zero at 0° and 180°; much of the structure in $D(\theta)$ then arises from that of the measured $\sigma_{el}(\theta)$.

^{27}Al and ^{26}Mg indicates that this ratio is 0.6 for ^{27}Al, the reference state being the $7/2^+$ level at 2.21 MeV. The Saclay group[9] finds $D(\theta_{lab} = 43°) = 0.964 \pm .020$ for ^{27}Al at $E_{lab} = 18.0 \pm 0.9$ MeV. Inelastic spin-flip measurements are not available for the neighboring nuclei ^{26}Mg and ^{28}Si near this energy; the values of $S_{in}^{(2)}$ for ^{32}S at $E_{lab} = 17.57$ MeV are stated to be[16] only (0.04 ± 0.015) at this forward angle but rise to 0.43 at 140°. Using these and measured cross sections at $E_{lab} = 17.5$ MeV,[17,18] we estimate that $D(43°) = 0.974$ and $D(140°) = 0.92$.

Recent measurements[19] have been reported of the depolarization of 16.5 MeV proton scattered elastically from ^{14}N. When expressed in terms of the spin-flip cross sections, the values found are quite large; in the neighborhood of 60° the spin-flip cross sections are almost 1 mb, two to three times the values for ^{9}Be in this range. Such large values are hard to explain with the quadrupole mechanism since they require either very large values for $\sigma^{(2)}$ or very large intrinsic J = 2 spin-flip probabilities. The first possibility seems quite unlikely since, in contrast to ^{9}Be, collective descriptions have not been successful for ^{14}N. The second possibility also seems remote; although large intrinsic quadrupole spin-flip probabilities are calculated at back angles, we have not seen any cases where these probabilities exceed 0.2 around 60° and more typically the values lie around or under 0.1. Further, the direct J = 1 contributions to spin-flip are expected to be small; for the isospin-zero target ^{14}N, the direct contribution to the spin-tensor optical interaction from a pure OPEP two-nucleon tensor interaction will vanish since that interaction is also proportional to the isospin operator of the target nucleon. We speculate that the large spin-flip cross sections in ^{14}N reflect instead compound nuclear contributions. The substantial depolarization of low energy neutrons[20] has been explained by considering such compound nuclear contributions; it is an unwelcome thought that such contributions may also be present at higher energies.

In concluding, we remark that there is much uncertainty in our various predictions of the quadrupole contribution to depolarization. But, except for the case of ^{14}N, our estimates do approximate the observed depolarization. At the least they indicate that extraction of the properties of spin-spin potentials from depolarization experiments will be very difficult to achieve in the presence of the large quadrupole spin-flip effect.

---

1. Sec. 9.2 of this report.
2. A.H. Hussein and H.S. Sherif, Phys. Rev. C *8*, 518 (1973).
3. G.R. Satchler, Particles and Nuclei *1*, 397 (1971).
4. W.A. Kolasinski, J. Eenmaa, F.H. Schmidt, H. Sherif, and J.R. Tesmer, Phys. Rev. *180*, 1006 (1969).
5. K.T.R. Davies and G.R. Satchler, Nucl. Phys. *53*, 1 (1964).
6. A. Bohr, Nucl. Phys. *10*, 486 (1959).
7. G.R. Satchler and C.B. Fulmer, Phys. Lett.*50B*, 309 (1974).
8. J.S. Blair and I.M. Naqib, Phys. Rev. C *1*, 569 (1970).
9. R. Beurtey, P. Catillon, and P. Schnabel, J. Phys. (Paris) *31*, Supp. No. 5-6, C2, 96 (1970) and P. Catillon in *Polarization Phenomena in Nuclear Reactions*, ed. by H.H. Barschall and W. Haeberli (University of Wisconsin Press, Madison, Wisc., 1971) p. 657.

10. D.G. Montague, R.K. Cole, P.S. Lewis, C.N. Waddell, and D.L. Hendrie, Nucl. Phys. *A199*, 433 (1973).
11. G. Schrank, E.K. Warburton, and W.W. Dachnik, Phys. Rev. *127*, 2159 (1962).
12. J. Birchall, H.E. Conzett, J. Arvieux, W. Dahme, and R.M. Larimer, Phys. Lett. *53B*, 165 (1974).
13. J.J. Kolata and A. Galonsky, Phys. Rev. *182*, 1073 (1969).
14. H.J. Votova, T.B. Clegg, E.J. Ludwig, and W.J. Thompson, Nucl. Phys. *A204*, 529 (1973).
15. I.M. Naqib, Bull. Am. Phys. Soc. *7*, 73 (1962).
16. M.A.D. Wilson and L. Schecter, Phys. Rev. C *4*, 1103 (1971).
17. G.M. Crawley and G.T. Garvey, Phys. Rev. *167*, 1070 (1968).
18. I.E. Dayton and G. Schrank, Phys. Rev. *101*, 1358 (1956).
19. T.B. Clegg, R.A. Hardkopf, and G.G. Ohlsen, Bull. Am. Phys. Soc. *19*, 1021 (1974).
20. K. Katori, T. Naguta, A. Uchida, and S. Kobayashi, J. Phys. Soc. Japan *28*, 1116 (1970).

10. HEAVY ION REACTIONS

10.1 X-ray Technique for Measurement of Heavy Ion Nuclear Charge Distributions

P. Dyer, L. Graham, and R. Vandenbosch

In order to better understand the reaction mechanism for deeply inelastic scattering of very heavy ions (see Sec. 10.10 of this report), it is of interest to measure the nuclear charge distribution of the reaction products as a function of angle and particle energy. The ability of conventional (dE/dx)-E counter telescopes to resolve particles of adjacent nuclear charge decreases as the nuclear charge increases. We are therefore developing a new technique[1] for measuring the nuclear charge distribution of high-Z reaction products.

This Z identification is based on observation of x-rays characteristic of the nuclear charge of a particular reaction product; it consists of a radiator foil followed by a silicon particle detector and a solid state x-ray detector (see Fig. 10.1-1). When a high-energy, heavy ion passes through the radiator foil (prior to being stopped in the particle detector), there is a high probability that a K electron will be knocked out of the projectile, and that the filling of this vacancy will result in the emission of a characteristic K x-ray. Such x-rays are observed in coincidence with the particle. With present solid-state x-ray detectors, it is possible to resolve K_α x-rays of adjacent-Z elements.

This technique was first tested with a 108-MeV silver beam from the NPL tandem, obtained with the new sputtering source. A beam of 10^4 particles/sec was sent directly into the detection system. We observed Ag K_α and K_β x-rays in coincidence with Ag particles.

A similar detection system has now been tested in a scattering geometry at the LBL Super-HILAC. Thin lead and samarium targets were bombarded by beams of 500 and 700 MeV ^{84}Kr. Scattered particles were observed by a detection system consisting of a 5 mg/cm^2 tin radiator foil, a 200 μ thick transmission-mounted silicon detector, and a 1 cm diameter, 0.5 cm thick Si(Li) x-ray detector placed about 10 cm from the target. A spectrum of x-rays in coincidence with particles is shown in Fig. 10.1-2. For this spectrum, particles were detected at an angle of 30° from a lead target (where the scattering is Coulomb), and the detector system was rotated and shielded such that the x-ray detector could not see x-rays from the target.

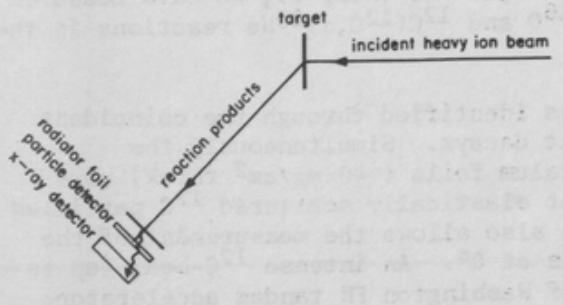

Fig. 10.1-1. Schematic diagram of configuration for detection of x-rays in coincidence with heavy ions.

Future experimental configurations will reflect a compromise between resolution (which is degraded by Doppler broadening) and high efficiency, and will deal with background due to high yields of target x-rays. Use of fast timing techniques will be required for geometries where the x-ray detector can see

the target. Since a xenon beam has recently become available at the Super-HILAC, we will use this system for Z-identification of Xe as well as Kr-induced reactions.

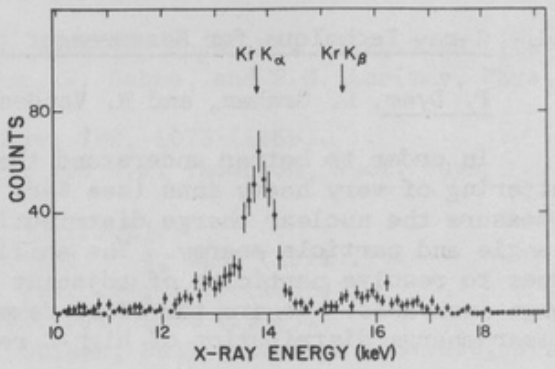

Fig. 10.1-2. Energy of x-rays from the radiator foil in coincidence with particles scattered from a 500-MeV ^{84}Kr beam incident on a lead target. Arrows indicate the expected positions of Kr lines, including a calculated Doppler shift of 1.2 keV but not including atomic shifts due to L-shell vacancies. The separation between K_α lines of adjacent-Z elements here is 0.73 keV.

---

1. This detection technique was conceived in collaboration with J. Pedersen of the Niels Bohr Institute, Copenhagen.

10.2 Correlated Structure in the $^{12}C(^{12}C,^{8}Be)^{16}O$ and $^{12}C(^{12}C,\alpha)^{20}Ne_{g.s.}$ Reactions between 17 and 26 MeV (c.m.)

K.G. Bernhardt and K.A. Eberhard

Strongly correlated structures in reactions leading to the compound nucleus ^{24}Mg at excitation energies between 32 and 40 MeV have been recently observed by several workers. In addition to the excitation functions for $^{12}C(^{12}C,^{8}Be)^{16}O$ (Ref. 1), $^{12}C(^{12}C,\alpha)^{20}Ne$ (Ref. 2), and $^{10}B(^{14}N,\alpha)^{20}Ne$ (Ref. 3), we have measured angular distributions for the $^{12}C(^{12}C,^{8}Be)^{16}O$ and $^{12}C(^{12}C,\alpha)^{20}Ne$ reactions in the energy range of interest.

The particle unstable ^{8}Be nucleus was identified through the coincident detection of the two α-particles by which it decays. Simultaneously the $^{12}C(^{12}C,\alpha)^{20}Ne$ reaction was measured. Tantalum foils ($\sim$40 mg/cm^2 thick) were mounted in front of the detectors to prevent elastically scattered ^{12}C particles from entering the detector. This technique also allows the measurement of the $^{12}C(^{12}C,\alpha)^{20}Ne$ and $^{12}C(^{12}C,^{8}Be)^{16}O$ reactions at 0°. An intense ^{12}C-beam (up to 500 nA) was available from the University of Washington FN tandem accelerator.

The most prominent structure in the $^{12}C(^{12}C,\alpha)^{20}Ne$ and $^{12}C(^{12}C,^{8}Be)^{16}O$ excitation functions is observed at $E_{^{12}C}$(c.m.) = 18.5 MeV. In the $^{10}B(^{14}N,\alpha)^{20}Ne$ and $^{12}C(^{12}C,^{8}Be)^{16}O$ excitation functions a correlated structure is found at

$E_{^{12}C}$(c.m.) = 25.5 MeV. Angular distributions for the $^{12}C(^{12}C,\alpha)^{20}Ne$ and $^{12}C(^{12}C,^{8}Be)^{16}O$ reactions have been measured at incident energies (c.m.) of 17.75, 18.5, 22, and 25.5 MeV.

In Fig. 10.2-1 angular distributions for the ground state transitions at an incident energy of 18.5 MeV (c.m.) are shown with the square of the Legendre polynomials P^2_{10} and P^2_{12}, respectively.

As can be seen from Fig. 10.2-1, the $^{12}C(^{12}C,\alpha)^{20}Ne$ reaction is dominated by the ℓ = 10 partial wave in contrast to the $^{12}C(^{12}C,^{8}Be)$ reaction, which is dominated by the ℓ =12 partial wave. This behavior casts considerable doubt on previous interpretations of the observed correlated structure at this energy as being due to intermediate resonances in ^{24}Mg. Further investigations of these puzzling "resonances" are in progress.

1. K.A. Eberhard *et al.*, Phys. Lett. to be published.
2. H.T. Fortune *et al.*, preprint, Argonne National Laboratory, 1975.
3. N. Marquardt *et al.*, Phys. Rev. Lett. *33*, 1389 (1974).

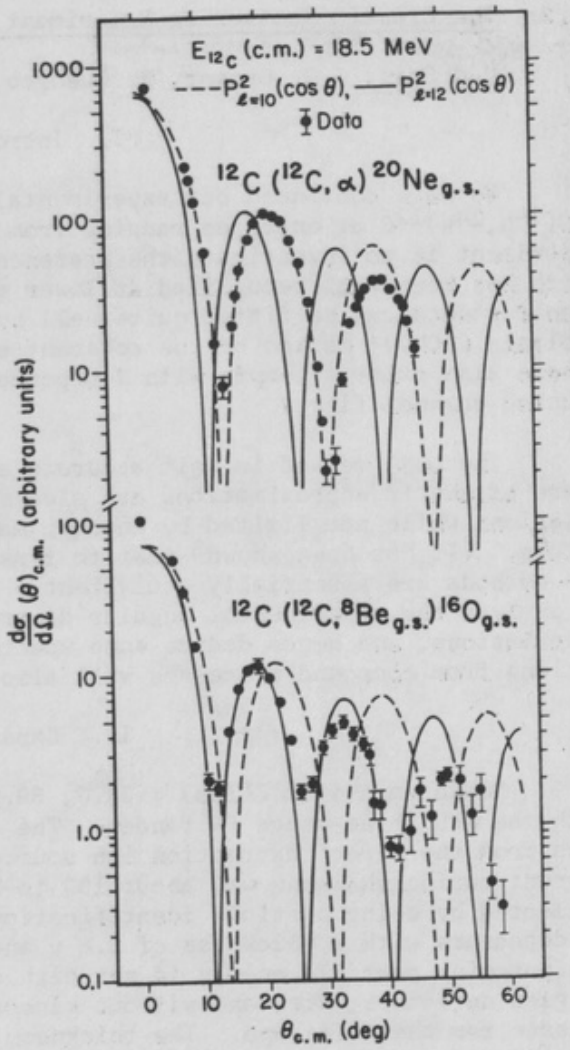

Fig. 10.2-1. Measured angular distributions for the $^{12}C(^{12}C,\alpha)^{20}Ne_{g.s.}$ (top) and $^{12}C(^{12}C,^{8}Be_{g.s.})^{16}O_{g.s.}$ (bottom) reactions at $E_{^{12}C}$(c.m.) = 18.5 MeV and corresponding Legendre polynomials. Experimental errors are smaller than the point size unless given by error bars.

10.3 The Elastic Scattering Experiment $^{12}C(^{14}N, ^{14}N)^{12}C$

Y-d Chan, J.G. Cramer, B. Cuengco, K-L Liu, J. Wiborg, M.S. Zisman

I. Introduction

We have continued our experimental elastic scattering studies of $^{12}C(^{14}N,^{14}N)^{12}C$ at energies ranging from 33.0 to 46.0 MeV. One purpose of this experiment is to investigate the presence of the elastic transfer mechanism, which has been well recognized at lower energies. Most of the existing elastic transfer data can be fitted quite well by the Linear Combination of Nuclear Orbitals (LCNO)[1] method or the coherent elastic plus DWBA transfer method.[2] (There also exist attempts with ℓ-dependent optical model and more sophisticated coupled channel fits.)

The LCNO method is most accurate at energies close to the Coulomb barrier where adiabatic approximations are always valid. On the other hand, DWBA calculations while not limited by energy, may be limited by their first order nature. (It has been shown[3] that to first order in the exchange potential, these two methods are essentially equivalent.) It is therefore also one of our interests to analyze the experimental angular distributions by means of full recoil DWBA calculations, and hence deduce some spectroscopic information. Possible contributions from compound processes will also be estimated.

II. Experiment

Measurements at E(lab) = 33.0, 38.0, 41.0, 44.0, and 46.0 MeV were made with the NPL three-stage FN tandem. The ^{14}N beam was obtained by extracting NH^- ions from the direct extraction ion source of this Laboratory. Typical beam current during the runs was about 100 to 250 nA. Most of the data points were collected by doing particle identification with a ΔE, E silicon detector telescope. ΔE detectors with a thickness of 9.8 μ and 10.5 μ were used. In regions where the outgoing particle energy is not high enough to pass through the ΔE detector, singles detectors, with and without kinematic coincidence, were set up to compensate for the telescope. The thickness of the ^{12}C target was about 100 $\mu g/cm^2$ and the particle identification was done with the on-line data collection program PPID[4] and its modified version PID-SSSS. Besides integrating the beam current, a monitor detector was mounted at 15°(lab) in the scattering plane for normalization purposes.

A summary of the data is shown in Fig. 10.3-1. Lower energy data from other laboratories can be found in Ref. 5. The angular distributions look quite similar for all energies in the forward hemisphere with peaks and valleys shifting with increasing energy toward the forward region as one would expect. However, backward angle points are less unified and show some irregularities.

III. Data Fitting

1. Optical Model Parameters

Optical model potential parameters were extracted by numerically searching on forward angle points for each energy. The outcome of such searches in our case always ends up with a very small diffuseness a_w for the imaginary potential. This is probably due to the fact that a very sharp-edged well is required to reproduce the strong diffractive behavior of the data in the forward hemisphere, as can be demonstrated by the strong absorption model. Several sets of these parameters are summarized in Table 10.3-1, with comparable chi-squares.

2. DWBA Fits

Simple DWBA heavy-ion calculations are notorious for always tending to underestimate the magnitude of the 2-nucleon transfer cross section. It seems that we also have encountered this difficulty. The full recoil DWBA code LOLA[6] was used to calculate the transfer amplitude. The two $1p_{1/2}$ proton and neutron were assumed to form a $3S_1$ state,[7] and the cluster transfer approximation was used. The actual parameters for the calculations are shown in Table 10.3-1. The final differential cross section was calculated according to the following formula:

$$\frac{d\sigma}{d\Omega}(\theta) = \left| f_{el}(\theta) + S \frac{2J_N+1}{2J_C+1} W f^{LOLA}_{\Delta\ell=0}(\pi-\theta) \right|^2$$

where f_{el} is the elastic amplitude, $f^{LOLA}_{\Delta\ell=0}$ is the $\Delta\ell = 0$ elastic transfer amplitude, and W is the appropriate Wigner coefficient. S here denotes the spectroscopic factor. It was found that the DWBA calculations can roughly reproduce the angular distribution pattern but the magnitude was smaller than that suggested by the data. Also the magnitude of the DWBA cross section depends quite sensitively on the optical potential parameters used, as can be seen in Fig. 10.3-2.

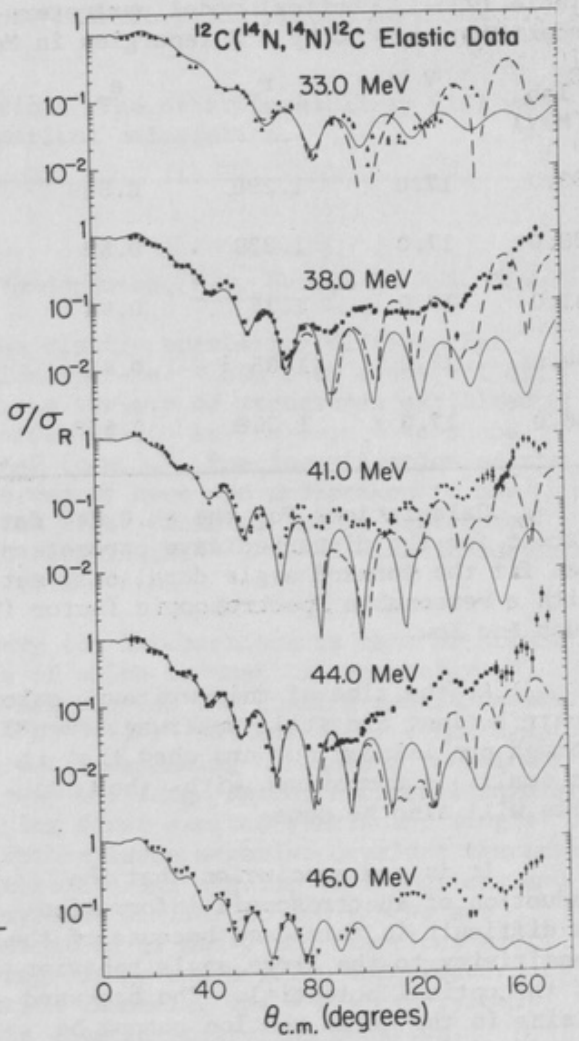

Fig. 10.3-1. Elastic scattering data for $^{12}C(^{14}N,^{14}N)^{12}C$. The solid lines are optical model best fits for the forward angle points. The dashed curves are the coherent sum of elastic and DWBA fits.

Table 10.3-1. Optical model parameters used in the DWBA calculations of the scattering of ^{12}C by ^{14}N (energies in MeV, length in fermis).

E_{lab} (MeV)	V	r_v	a_v	W	r_w	a_w	S
33.0	17.0	1.296	0.589	3.766	1.428	0.04	0.6
38.0	17.0	1.339	0.52	4.178	1.421	0.178	0.6
41.0	17.0	1.35	0.48	4.552	1.406	0.173	0.6
44.0	17.0	1.35	0.48	5.646	1.404	0.207	0.6
46.0	17.0	1.358	0.553	6.876	1.456	0.178	---

Calculations for the 44.0 MeV data set were done with identical parameters except for the distorted wave parameters. Even though both parameter sets (A & B) can fit the forward angle data, only set B can reproduce the transfer strength with a reasonable spectroscopic factor (S ≈ 0.6), while the set A prediction is much too low.

At the time of this writeup, calculations on possible compound elastic contributions are still underway, even though preliminary numbers show that it is small. A comparison with the LCNO fits will also be done.

It is our conclusion that the deduction of spectroscopic information is difficult in this case because of the sensitivity to the large angle behavior of the optical potential. The backward rising in the cross section cannot be accounted for by assuming only a simple scattering mechanism compound elastic contribution. In other words, elastic transfer remains the dominant mechanism in this energy range.

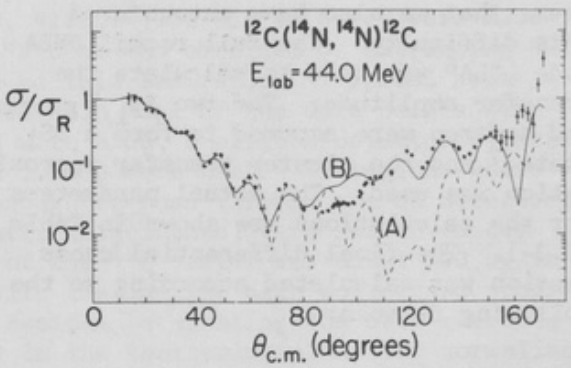

Fig. 10.3-2. DWBA fits for the 44.0 MeV $^{12}C(^{14}N,^{14}N)^{12}C$ data. The dashed line is calculated from set A, and the solid line from set B.
Set A: V=17.0 MeV, r_v=1.35 f, a_v=0.48 f
W=5.646 MeV, r_w=1.404 f, a_w=0.207 f
Set B: V=90.0 MeV, r_v=1.294 f, a_v=0.116 f
W=28.3 MeV, r_w=1.42 f, a_w=0.116 f
All bound state parameters are identical.

1. W. von Oertzen, Nucl. Phys. *A148*, 529 (1970).
2. C.A. McMahon and W. Tobocman, Nucl. Phys. *A202*, 561 (1973).
3. G. Baur and C.K. Gelbke, preprint (1971).
4. Nuclear Physics Laboratory Annual Report, University of Washington (1974), p.

5. W. von Oertzen, H.G. Bohlen, preprint "Elastic transfer in heavy ion scattering", 1975.
6. R.M. DeVries, unpublished.
7. From the $N + 2L = \sum_i (n_i + 2l_i)$ relation. The other possibility (1P) was found to be negligible by actual numerical calculation.

10.4 Elastic Scattering of ^{18}O from ^{12}C

K.G. Bernhardt, K.A. Eberhard*, R. Vandenbosch, M.P. Webb, and M.S. Zisman

The dramatic energy dependence of the elastic scattering differential cross-sections observed for several heavy ion systems[1-3] has been a subject of continued interest. Equally surprising is the variety of structures exhibited; from narrow structures with widths on the order of 100 keV or less,[1] to shape resonances characterized by widths of 2-3 MeV (c.m.).[3] The investigation of the elastic scattering of ^{18}O from ^{12}C which we report here was undertaken to see which, if any, types of structure this system might exhibit, but in particular to see if resonant behavior similar to that seen in the $^{12}C + ^{16}O$ elastic scattering at 19.7 MeV (c.m.)[2] is also present in this system.

The dominant physical process in heavy ion interactions is that of strong absorption of the projectile, a consequence of which is that the character of the elastic scattering is dominated by the behavior of the grazing partial waves. As is evidenced in the study of the $^{16}O + ^{16}O$,[3] $^{18}O + ^{18}O$[4] and $^{12}C + ^{20}Ne$[5] systems, the elastic scattering is affected greatly depending on whether the direct reaction channels are capable of carrying away the large entrance channel angular momentum. Those systems exhibiting high lying first excited states and single and multi-nucleon transfer reactions with rather large negative Q values characteristically show strongly oscillatory elastic scattering angular distributions and excitation functions. On the other hand, systems similar to $^{12}C + ^{20}Ne$ are characteristic of the more usual strong absorption in heavy ion reactions and exhibit rather featureless elastic scattering energy and angular dependence. Based on the energetics of the direct reaction channels, the $^{18}O + ^{12}C$ system should resemble the $^{12}C + ^{20}Ne$ system in its elastic scattering behavior.

Less predictable is the occurrence of intermediate structure which manifests itself in excitation functions through the presence of peaks with widths approximately 500 keV which are cross correlated in angle for a given channel and cross correlated in different exit channels. The fact that such structure appears almost exclusively when ^{12}C is involved kindled our interest in the $^{18}O + ^{12}C$ system.

Beams of ^{18}O from the direct extraction ion source were used to bombard thin ($\sim$100 $\mu g/cm^2$) ^{12}C targets. A kinematic coincidence measurement was performed with an eight-detector array which allowed the simultaneous measurement of four excitation functions. The heavy ion surface barrier detectors subtended a solid angle of 0.01 msr with an angular acceptance of 0.2° (lab). A monitor counter was included when measuring the angular distributions. The target thickness was determined by low energy, forward angle elastic scattering where the cross sections were known to be Rutherford. The energy spread due to the finite target

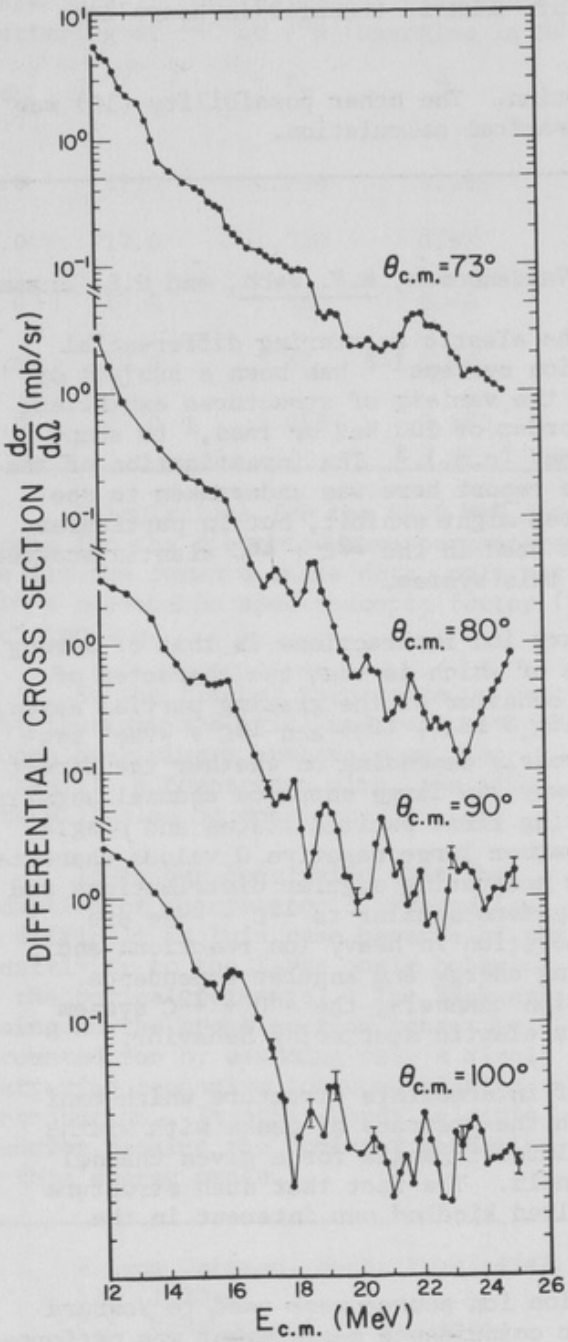

Fig. 10.4-1. $^{18}O + ^{12}C$ elastic scattering excitation functions at those angles where the even partial waves are expected to be enhanced.

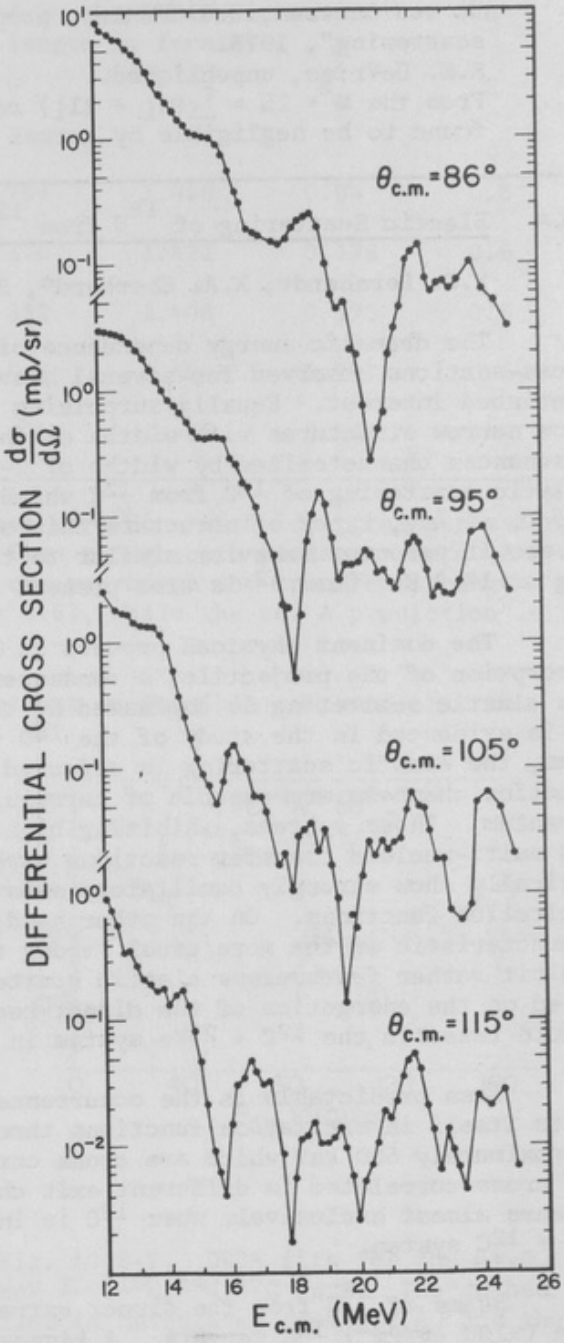

Fig. 10.4-2. $^{18}O + ^{12}C$ elastic scattering excitation functions at those angles where the odd partial waves are expected to be enhanced.

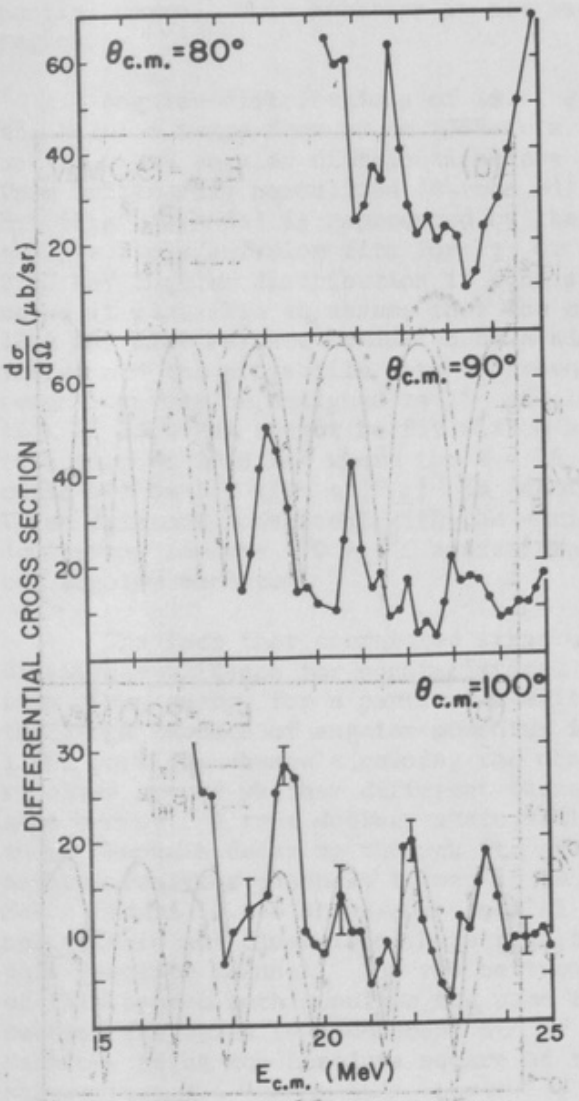

Fig. 10.4-3. Linear plot of $^{18}O + ^{12}C$ elastic scattering excitation function.

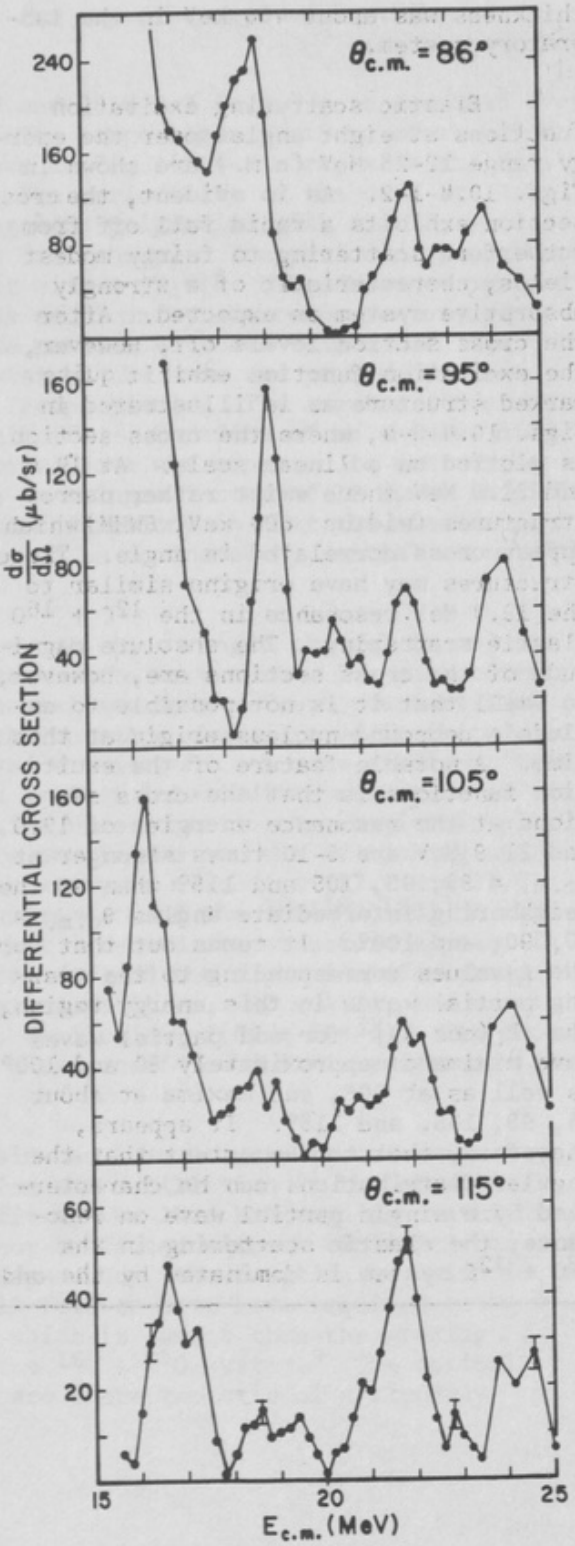

Fig. 10.4-4. Linear plot of $^{18}O + ^{12}C$ elastic scattering excitation function. Note the larger cross sections at these angles than at those where the even partial waves are enhanced.

thickness was about 400 keV in the laboratory system.

Elastic scattering excitation functions at eight angles over the energy range 12-25 MeV (c.m.) are shown in Figs. 10.4-1-2. As is evident, the cross section exhibits a rapid fall off from Rutherford scattering to fairly modest yields, characteristic of a strongly absorptive system as expected. After the cross section levels off, however, the excitation function exhibit quite marked structure as is illustrated in Figs. 10.4-3-4, where the cross section is plotted on a linear scale. At 19.0 and 21.8 MeV there exist rather narrow structures (widths 600 keV, FWHM) which appear cross correlated in angle. These structures may have origins similar to the 19.7 MeV resonance in the $^{12}C + ^{16}O$ elastic scattering. The absolute magnitude of the cross sections are, however, so small that it is not possible to exclude a compound nucleus origin at this time. A notable feature of the excitation functions is that the cross sections at the resonance energies of 19.0 and 21.8 MeV are 5-10 times stronger at $\theta_{c.m.}$ = 85, 95, 105 and 115° than at the neighboring intermediate angles $\theta_{c.m.}$ = 80, 90, and 100°. It turns out that for the ℓ-values corresponding to the grazing partial waves in this energy region, the $|P_L(\cos\theta)|^2$ for odd partial waves have minima at approximately 80 and 100° as well as at 90°, and maxima at about 85, 95, 105, and 115°. It appears, therefore, that to the extent that the angular distributions can be characterized by a single partial wave on resonance, the elastic scattering in the $^{18}O + ^{12}C$ system is dominated by the odd

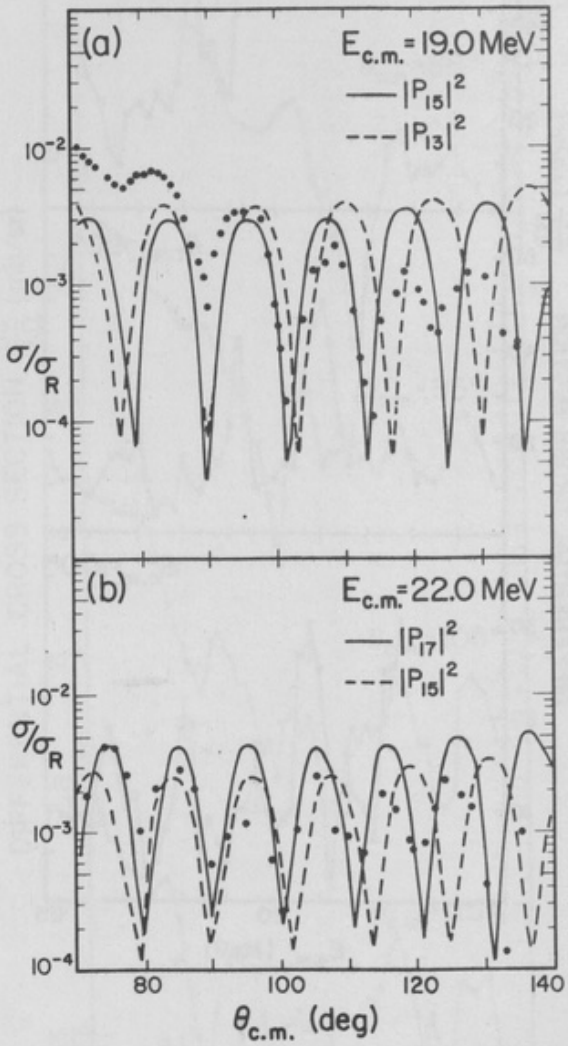

Fig. 10.4-5. a) 19.0 MeV angular distribution for $^{18}O + ^{12}C$. The solid curve is an arbitrarily normalized $|P_{15}|^2$. The dashed curve is an arbitrarily normalized $|P_{13}|^2$. b) 22.0 MeV angular distribution. The two curves represent arbitrarily normalized $|P_{15}|^2$ (---) and $|P_{17}|^2$ (——).

partial waves. This behavior is not known for any other system in this mass region.

Angular distributions of 19.0, 22.0 and 23.0 MeV (c.m.) were measured over the angular range from 40 to 135° (c.m.). The large angle portions of the 19.0 and 22.0 MeV angular distributions are shown in Fig. 10.4-5 along with the fits from arbitrarily normalized $|P_\ell(\cos\theta)|^2$. The periodicity of the data at 19.0 MeV (Fig. 10.4-5a) is reproduced by the Legendre polynomial with $\ell = 15$, with qualitatively inferior fits for P_{13} or P_{17} (not shown). The periodicity of the 22.0 MeV angular distribution is consistent with a $|P_{17}|^2$. The above comparison makes it plausible to assume that the cross sections at the resonance energies 19.0 and 21.8 MeV are dominated by a single partial wave and (since both the target and the projectile have 0^+ ground states) the spin and parity of these resonances may be assigned as 15^- and 17^-, respectively. The angular distribution at 23.0 MeV cannot be fit with a single $|P_\ell|^2$. Portions of an angular distribution at 20.6 MeV where the $\ell = 16$ partial wave was expected to contribute could not be fit with a $|P_{16}|^2$ in addition to being a factor of 10 lower in yield. These data are consistent with the excitation functions in that the elastic scattering for the $^{18}O + ^{12}C$ system appears to be dominated by partial waves with odd angular momentum.

The fact that correlated structure exists in a single channel is not indisputable evidence for nonstatistical intermediate structure. The enhancement at a given energy for a particular exit channel may only reflect the fact that the large amounts of angular momentum in the entrance channel have inhibited light particle channels causing the observed enhancement. A more stringent test revolves around whether different channels exhibit intermediate structure at the same energy. A true doorway state would give rise to resonant behavior in all those channels decaying through it. We are now in the process of looking at several reaction channels to see if such behavior is evident at 19.0 and 21.8 MeV. Figure 10.4-6 shows some initial measurements of the $^{12}C(^{18}O,^{16}O)^{14}C$ channel. It is not clear from these results that intermediate structure appears in this reaction channel. The two neutron transfer and the alpha transfer channels of this system both populate the same final state (i.e., $^{16}O + ^{14}C$), the cross section for which is a coherent sum of two amplitudes, $f(\theta) + f(\pi-\theta)$. The cross section, being the absolute square of the above, could exhibit interference structure.

In addition an optical model analysis has been started to determine whether the combination of strong absorption and oscillation in the elastic scattering can be fitted. A preliminary fit to the 19.0 MeV angular distribution is shown in Fig. 10.4-7. These data can not be fitted without explicitly or implicitly including an angular momentum dependence, the function of which is to reproduce the back angle oscillations. All fits to date have required an ℓ_c value in the angular momentum form factor which is larger than the grazing ℓ, contrary to what was found in the fit to the $^{16}O + ^{16}O$ system.[3] The optical potential parameters shown in Fig. 10.4-7 are characteristic of a strongly absorptive interaction.

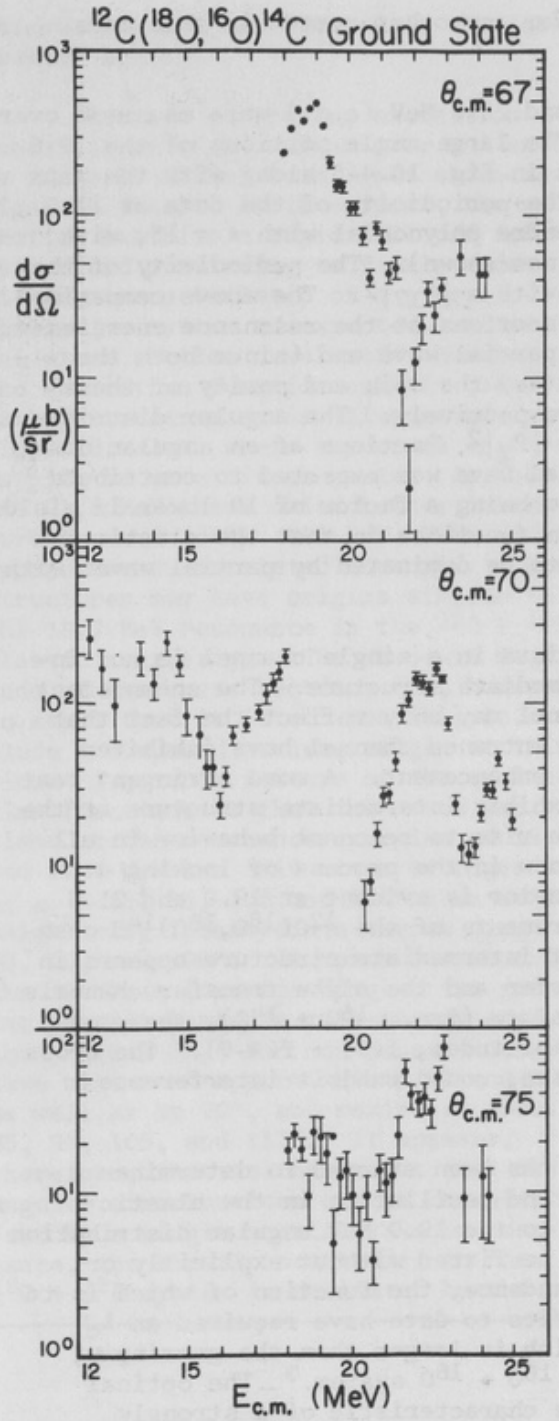

Fig. 10.4-6. Excitation functions for the reaction $^{12}C + ^{18}O \rightarrow ^{14}C + ^{16}O$.

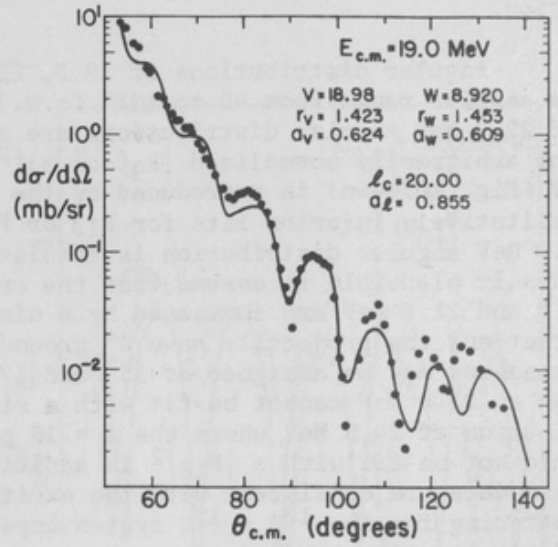

Fig. 10.4-7. Optical model fit to the 19.0 MeV elastic scattering angular distribution for $^{18}O + ^{12}C$.

---

* Permanent address: Sektion Physik Universität München, D-8046 Garching, Germany.

1. W. Reilly, R. Wieland, A. Gobbi, M.W. Sachs, J.V. Maher, D. Mingay, R.H. Siemssen and D.A. Bromley, Proc. of International Conf. on Nuclear Reactions Induced by Heavy Ions, Heidelberg, Germany, ed. R. Bock and W.R. Hering (North-Holland Pub. Co., Amsterdam,1970).
2. R.E. Malmin, Ph.D. Thesis, ANL PHY-1972F.
3. J.V. Maher, M.W. Sachs, R.H. Siemsen, A. Weidinger, and D.A. Bromley, Phys. Rev. *188*, 1665 (1969).
4. R.W. Shaw, Jr., R. Vandenbosch, and M.K. Mehta, Phys. Rev. Lett *25*, 457 (1970).
5. R. Vandenbosch, M.P. Webb, and M. S. Zisman, Phys. Rev. Lett. *33*, 842 (1974).

10.5 Elastic Scattering of ^{16}O from ^{14}C

K.G. Bernhardt, K.A. Eberhard*, R. Vandenbosch, and M.P. Webb

Studies of elastic scattering in the $^{16}O + {}^{16}O$,[1] $^{18}O + {}^{18}O$,[2] and $^{12}C + {}^{20}Ne$[3] systems have shown that the direct reaction channels can play an important role in determining the angular momentum dependence of the elastic scattering. The pronounced structure in the elastic scattering excitation functions of the $^{16}O + {}^{16}O$ system could only be reasonably reproduced with an optical model having an explicitly ℓ-dependent absorptive potential. The function of this potential was to allow the grazing partial waves a greater than usual transparency.[4] The lack of similar structure in the $^{18}O + {}^{18}O$ and $^{12}C + {}^{20}Ne$ systems demonstrates that the origin of this ℓ-dependence is not a consequence of scattering identical bosons nor is it dependent on the angular momentum dependence of the level density of the compound nucleus or of its decay widths. The results of all these experiments may be qualitatively understood by considering the energetics of the reaction channels coupled most directly to the entrance channel (i.e., inelastic excitations and single and multi-nucleon transfers). Systems such as $^{16}O + {}^{16}O$ which exhibit a high lying first excited state and transfer channels with large negative Q-values cannot carry away (through these direct reaction channels) the large amount of orbital angular momentum brought in by grazing collisions. Such a system is said to be angular momentum mismatched. The $^{18}O + {}^{18}O$ and $^{12}C + {}^{20}Ne$ systems are characterized by low lying excited states and more favorable Q-values in the direct reaction channels resulting in elastic scattering characteristic of the more usual strongly absorptive heavy ion interactions.

We have initiated an investigation of the $^{16}O + {}^{14}C$ system which, as regards its behavior of the direct reaction channels, is somewhat similar to the $^{16}O + {}^{16}O$ system. Initial measurements have concentrated on the energy dependence of the elastic scattering. A 75 $\mu g/cm^2$ ^{14}C target[5] on a 200 $\mu g/cm^2$ Al backing was bombarded with an ^{16}O beam from the direct extraction ion source of the University of Washington's FN tandem Van de Graaff. A kinematic coincidence measurement was made with an eight detector array allowing the simultaneous measurement of four excitation functions. The details of the experimental setup are described in Sec. 10.4 of this report.

Although a complete work-up of the experiment has not been completed at this time, a partial analysis has revealed the following qualitative features. In the energy region between 20 and 30 MeV (c.m.) and at center-of-mass angles of 65, 85, 95, and 105 degrees, the excitation functions exhibit structure with widths consistent with shape resonant behavior with peak cross-sections on the order of 3 mb/sr. Although the structure is not as dramatic as in the $^{16}O + {}^{16}O$ system, the rather large cross-section is consistent with behavior characteristic of an angular momentum mismatched system. The angles in this initial measurement allow the enhancement of odd over even partial waves and were chosen to compare the $^{16}O + {}^{14}C$ elastic scattering with the $^{18}O + {}^{12}C$ results, a system which exhibits the anomalous behavior of having its elastic scattering dominated by odd partial waves. A more direct comparison of the $^{16}O + {}^{14}C$ system with the $^{16}O + {}^{16}O$ results can be made at those angles where the even partial waves are enhanced. Such a measurement is planned for the near future.

* Permanent address: Sektion Physik, Universität München, D-8046 Garching, Germany.

1. J.V. Maher, M.W. Sachs, R.H. Siemssen, A. Weidinger, and D.A. Bromley, Phys. Rev. *188*, 1665 (1969).
2. R.W. Shaw, Jr., R. Vandenbosch, and M.K. Mehta, Phys. Rev. Lett. *25*, 457 (1970).
3. R. Vandenbosch, M.P. Webb, and M.S. Zisman, Phys. Rev. Lett. *33*, 842 (1974).
4. R.A. Chatwin, J.S. Eck, D. Robson, and A. Richter, Phys. Rev. C *1*, 795 (1970).
5. Our thanks to Dr. A. McDonald of Chalk River for providing the ^{14}C targets.

10.6 Elastic Scattering of ^{16}O on ^{20}Ne

R. Vandenbosch, M.P. Webb, and M.S. Zisman

In recent years there has been a great deal of interest in the study of elastic scattering of heavy ions of nearly comparable mass such as $^{16}O + ^{16}O$, $^{16}O + ^{18}O$, and $^{18}O + ^{18}O$.[1-3] The first of these systems, $^{16}O + ^{16}O$, has shown a clearcut need for modification of the standard optical model treatment of heavy ion elastic scattering in order to reproduce the observed[1] highly oscillatory angular distributions and excitation functions. The proposed[4] explanation for this oscillatory behavior, as opposed to the more usual structureless angular distributions characteristic of a strongly absorptive heavy ion interaction, is that the grazing partial waves are weakly absorbed.

The physical justification for the weak absorption is that few exit channels are available which can carry off the rather large entrance channel grazing angular momentum, L_g (for which $T_L = 0.5$). As pointed out by Shaw *et al.*,[3] the important exit channels in determining the absorption of the grazing partial waves (or the L-dependence of the optical potential) are not the compound nuclear channels but rather the reaction channels coupled directly to the entrance channel such as the inelastic scattering and α-particle transfer channels. This hypothesis was recently investigated by looking at the elastic scattering in the $^{12}C + ^{20}Ne$ system,[5] which forms the same compound nucleus as $^{16}O + ^{16}O$ at about the same excitation energy and with the same angular momentum. The data indicate[5] that $^{12}C + ^{20}Ne$ is indeed strongly absorbing and verify the idea of Shaw *et al.*[3] that it is the direct reaction channels which are dominant in this case.

If the correlation between L-dependence and the existence of momentum-matched direct reaction channels suggested by Shaw *et al.* holds true generally, one would expect no marked L-dependence in any elastic system containing the deformed ^{20}Ne nucleus. This is because the 2^+ and 4^+ inelastic excitations are nearly always capable of carrying off the entrance channel grazing angular momentum, and furthermore the cross sections to these states are particularly large due to the collective nature of ^{20}Ne. To test this we have investigated the elastic scattering of the $^{16}O + ^{20}Ne$ system. In addition, this system offers the possibility of showing effects due to the "elastic transfer" of an α-particle,

a mechanism which is unobservable in an identical particle system such as $^{16}O + ^{16}O$. Unfortunately, the $^{20}Ne(^{16}O,^{20}Ne)^{16}O$ reaction, which is indistinguishable from back angle elastic scattering, can give rise to angular distributions having back angle oscillations that look very similar to the effects of an L-dependence in the optical potential. This makes it somewhat difficult, in practice, to determine unambiguously which mechanism is responsible for any observed structure, as was demonstrated in a careful study of the analogous $^{12}C + ^{16}O$ system undertaken by Malmin.[6]

The experiment was performed with ^{16}O beams of 45, 55, and 63 MeV incident on a specially designed[7] thin-window ^{20}Ne gas cell used previously for the $^{12}C + ^{20}Ne$ experiment.[5] After passing through the entrance foil and target gas, the calculated energies in the center of the cell were 40.7, 51.1, and 59.4 MeV, respectively. In order to cover a large angular range, the data were measured with a detector telescope consisting of an 11.2μ ΔE and 60μ E counter. By performing a standard power law identification in the SDS-930 computer, both ^{16}O and recoil ^{20}Ne could be observed simultaneously at forward lab angles. At the highest energy, this allowed us to obtain data from $\theta_{c.m.}$ = 36 to 140° in 2° steps.

Angular distributions for all three energies are shown in Fig. 10.6-1. The solid curves represent a simultaneous fit to all data sets obtained with a modified version of the optical model code GENOA.[8] As can be seen, the predictions of the standard optical model fit the data moderately well at forward angles but are much too low at back angles. In an attempt to improve these fits, the higher energy sets were searched individually. At 51.1 MeV it was possible to find a potential (dashed curve in Fig. 10.6-1) which fit the data at least qualitatively over the whole angular range, albeit with an imaginary diffuseness which is probably unreasonably sharp. However, all attempts to obtain such a fit to the 59.4 MeV data failed. This is because any potential which predicts approximately the correct magnitude at back angles greatly overpredicts the forward angle structure.

We next investigated the data in terms of an extended optical model which employed an L-dependent imaginary potential. Having argued that L-dependence is unlikely to occur in this system, we however show in Fig. 10.6-2 fits to the 51.1 and 59.4 MeV data using this model. The parameters for the two potentials are given in the figure. Clearly, the overall quality of the fits is markedly better than that obtained from a standard optical model treatment, although the detailed behavior is still not reproduced exactly. Attempts to find an L-dependent potential which fits all three energies simultaneously (that is, using a common real and imaginary potential and independent L_c and L parameters) have thus far been unsuccessful. This failure may not be surprising if the observed L-dependence in the potentials is merely mocking up some other effect, such as elastic transfer.[9]

We turn next to a consideration of the elastic α-transfer process as an explanation for the observed back angle enhancements in the 59.4 MeV $^{16}O + ^{20}Ne$ elastic scattering. This process has previously been suggested in the analogous $^{12}C + ^{16}O$ system studied by von Oertzen.[10] Using the distorted wave Born approximation (DWBA) to calculate the $^{20}Ne(^{16}O,^{20}Ne)$ part of the transition matrix gives

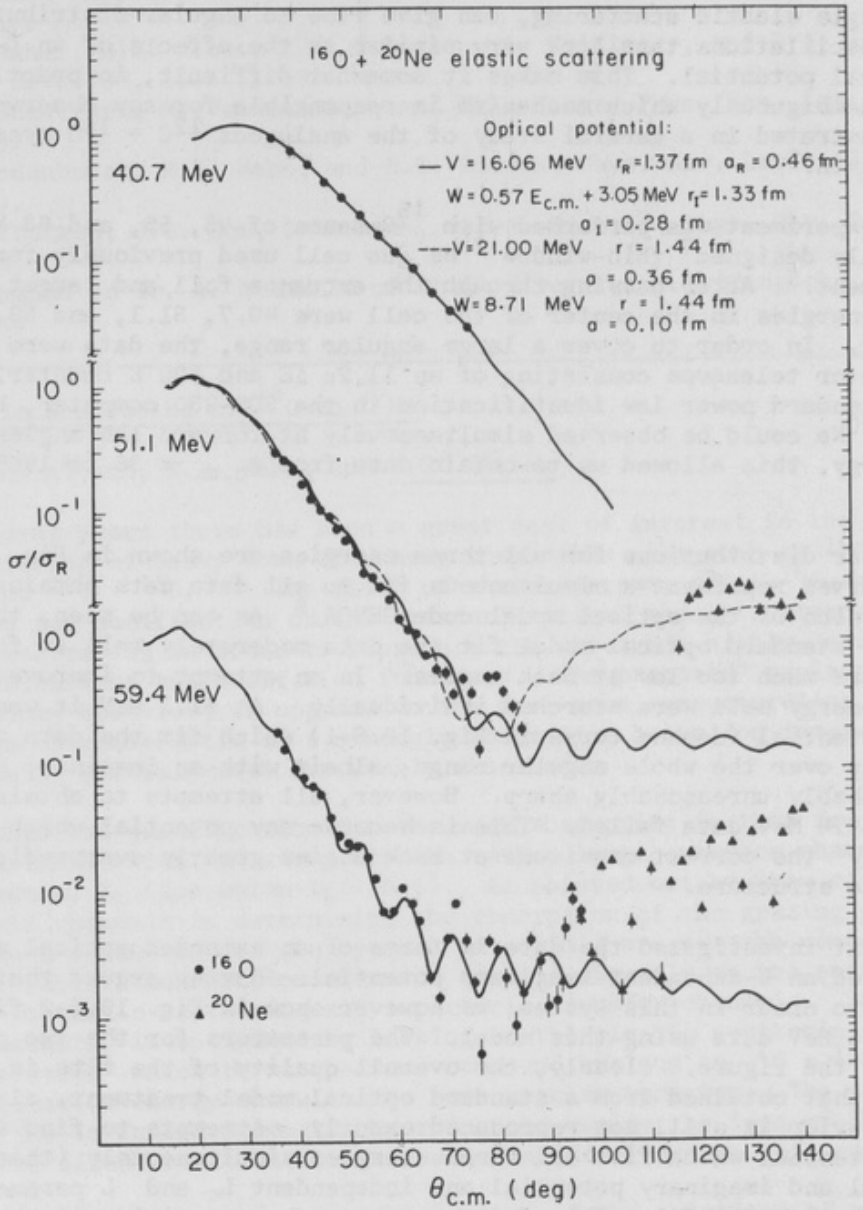

Fig. 10.6-1. $^{16}O + {}^{20}Ne$ elastic scattering data at 40.7, 51.1 and 59.4 MeV. The solid curve is a fit to all three ^{16}O data sets using the standard optical model. The dashed curve is a fit to the 51.1 MeV data including the back angle ^{20}Ne points.

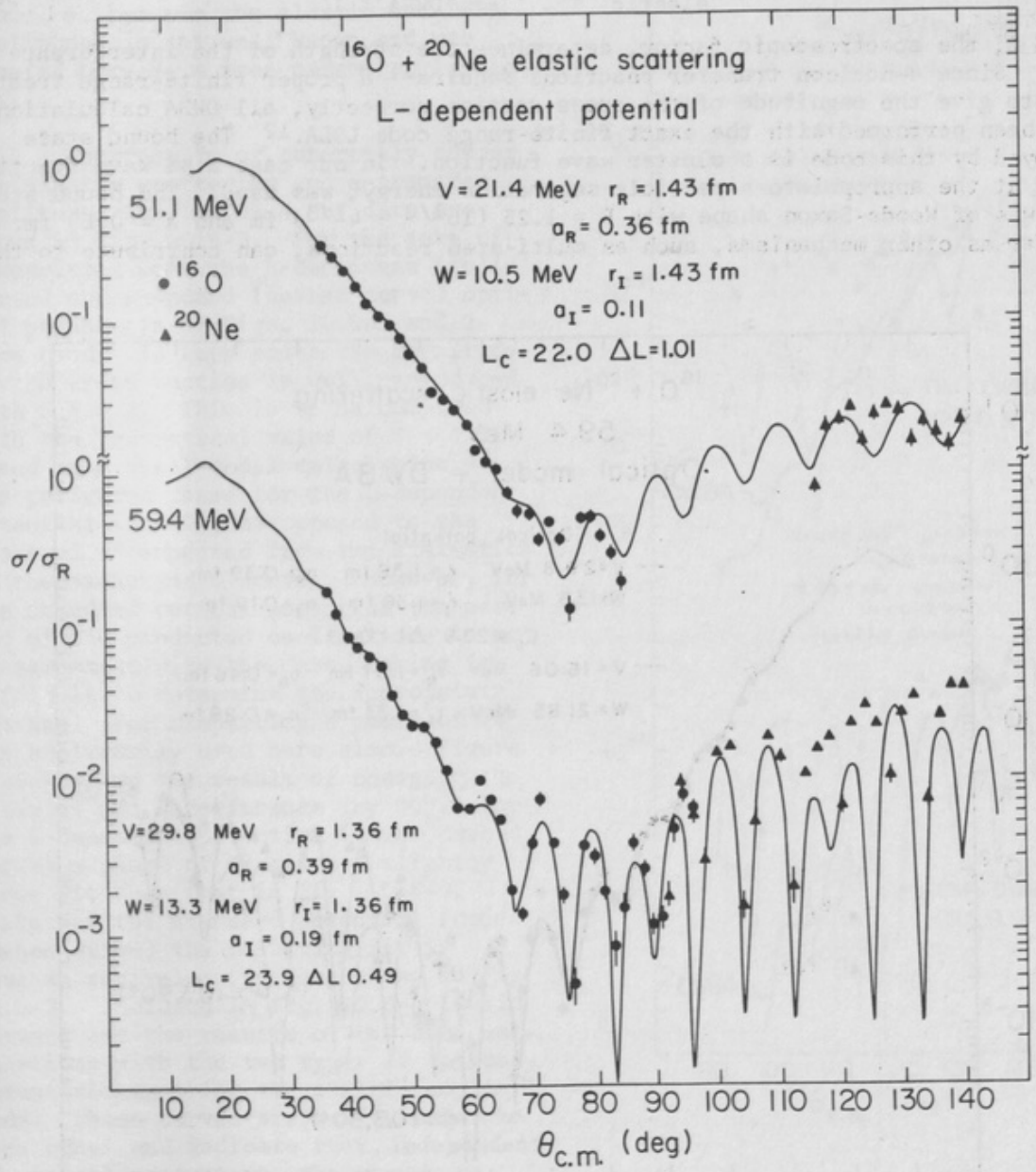

Fig. 10.6-2. Fits to the $^{16}O + ^{20}Ne$ data using an L-dependent optical model.

$$T(\theta) = T_{elastic}(\theta) + Se^{i\alpha} T_{DWBA}(\pi-\theta) \qquad (1)$$

where S, the spectroscopic factor, determines the strength of the interference term. Since 4-nucleon transfer reactions require[11] a proper finite-range treatment to give the magnitude of the cross section correctly, all DWBA calculations have been performed with the exact finite-range code LOLA.[12] The bound state employed by this code is a cluster wave function. In our case a 4S wave function, bound at the appropriate α-particle separation energy, was used. The bound state well was of Woods-Saxon shape with $R = 1.25\ (16^{1/3} + 4^{1/3})$ fm and a = 0.65 fm. Insofar as other mechanisms, such as multi-step reactions, can contribute to the

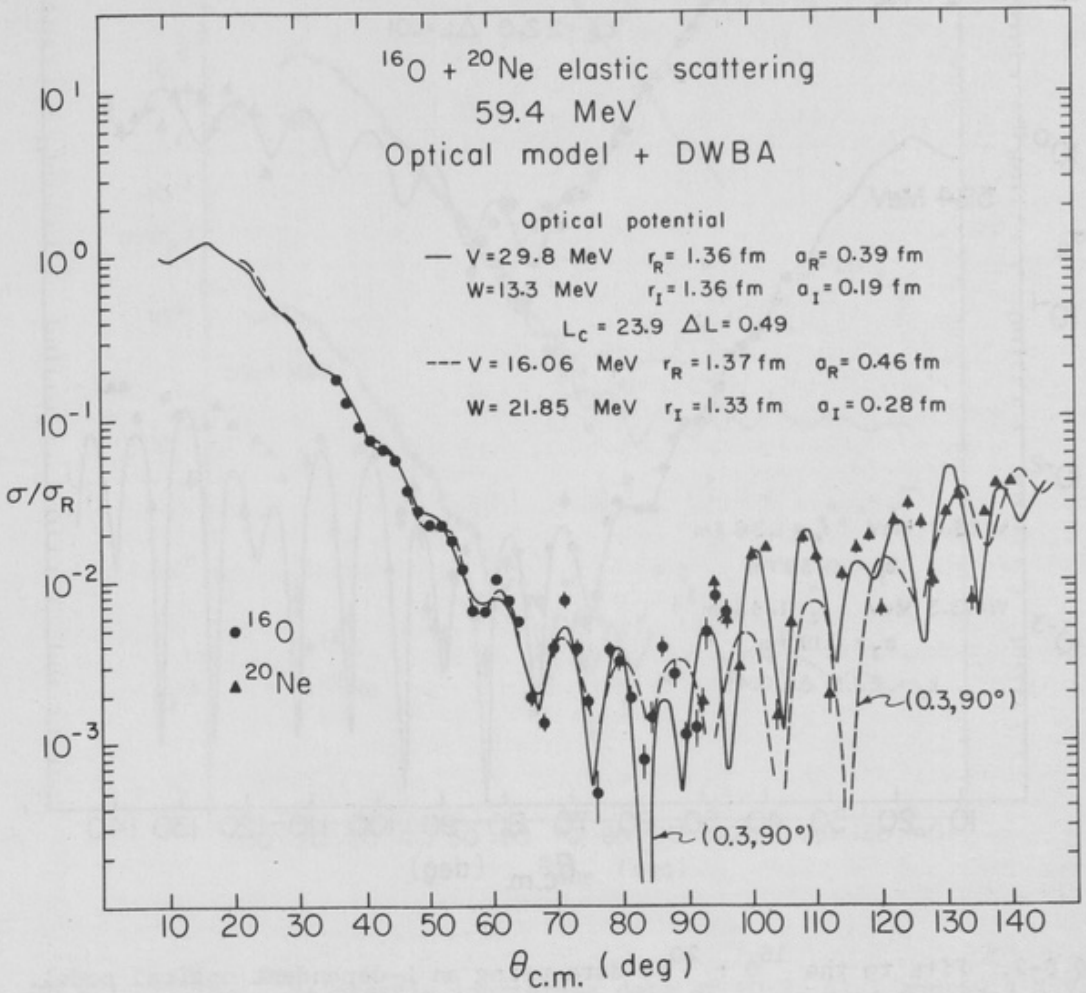

Fig. 10.6-3 Fits to the 59.4 MeV $^{16}O + ^{20}Ne$ data with the elastic transfer mechanism. The dashed curve refers to the standard optical potential from Fig. 10.6-1 and the solid curve to the L-dependent optical potential from Fig. 10.6-2. The spectroscopic factor and phase are indicated for each curve.

observed cross section, the relative phase, α, between the elastic and DWBA amplitudes is not well known and was treated here as a free parameter in the fit.

The results of coherently adding the elastic scattering and α-transfer amplitudes for the 59.4 MeV data are shown in Fig. 10.6-3. For the sake of comparison, both the L-dependent (solid curve) and standard (dashed curve) optical potentials of Figs. 10.6-1 and 2 were used. In both cases the magnitude of the cross section is well reproduced with S = 0.3. This is to be compared with the theoretical value of S = 0.21 based on a shell-model calculation.[13] The preferred phase for the L-dependent potential was 90°, as opposed to the phase of 0° expected from the statistics of the exchanged 0^+ cores. However, for the standard optical potential the period of the predicted oscillations is not in agreement with the data, making it difficult to determine the appropriate phasing. For simplicity a phase of 90° was arbitrarily used here also. Figure 10.6-4 shows the result of changing the phase of the interference by 90°. For the L-dependent potential (lower dashed curve) a phase of 0° gives a slightly worse fit than that in Fig. 10.6-3, while for the standard potential (upper dashed curve) the resulting fit is roughly equivalent to that shown in Fig. 10.6-3. Included in Fig. 10.6-4 (solid curves) are the results of the DWBA calculations with the two types of optical potentials ignoring the elastic amplitude. These curves are very similar to each other and indicate that, independent of optical parameters, the structure seen in the data is <u>not</u> explained by the transfer reaction alone.

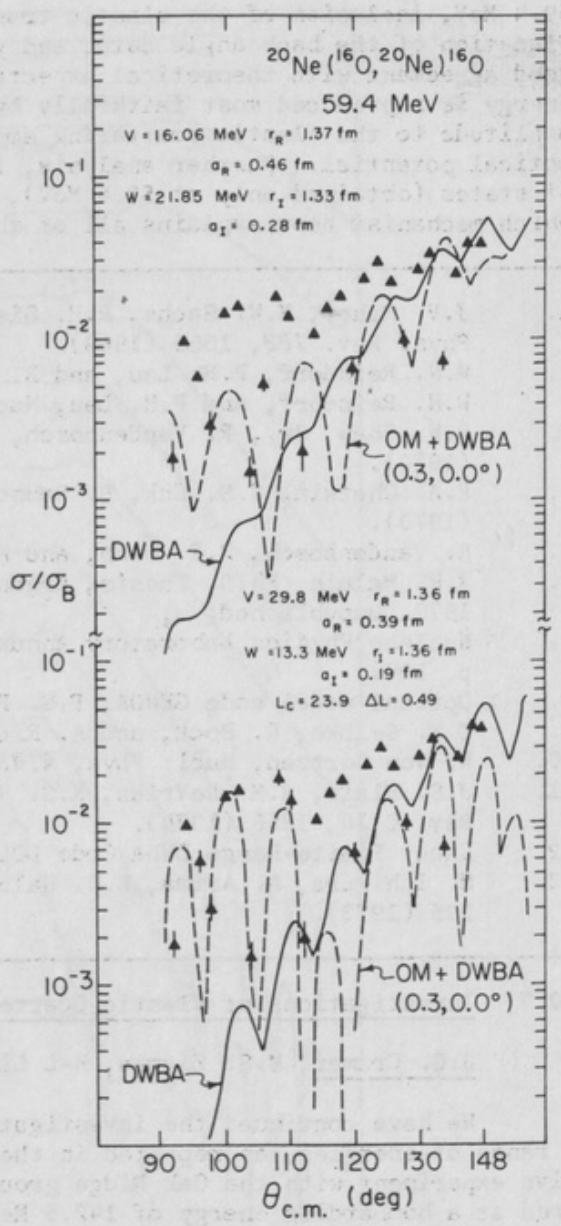

Fig. 10.6-4. (Dashed curves). Effect of varying the phase shown in Fig. 10.6-3. (Solid curves). Results of DWBA calculations ignoring the elastic scattering amplitude.

In summary, our present results indicate that the back angle enhancements seen in $^{16}O + ^{20}Ne$ elastic scattering cannot be explained consistently by a standard optical model calculation. Extension of the optical model to include an L-dependent imaginary potential, however, does give qualitative agreement to the 51.1 and 59.4 MeV data. At

59.4 MeV, inclusion of the elastic transfer process also gives a reasonable explanation of the back angle data, and yields a spectroscopic factor in fairly good agreement with theoretical expectations. The back angle structure at this energy is reproduced most faithfully by coherently adding the elastic transfer amplitude to the elastic scattering amplitude calculated with an L-dependent optical potential. Further analysis, including the inelastic data to the 2^+ and 4^+ states (obtained only at 59.4 MeV), is being carried out in order to determine which mechanism best explains all of the observed data.

---

1. J.V. Maher, M.W. Sachs, R.H. Siemssen, A. Weidinger, and D.A. Bromley, Phys. Rev. *188*, 1665 (1969).
2. W.N. Reisdorf, P.H. Lau, and R. Vandenbosch, to be published; R. Vandenbosch, W.N. Reisdorf, and P.H. Lau, Nucl. Phys. *A230*, 59 (1974).
3. R.W. Shaw, Jr., R. Vandenbosch, and M.K. Mehta, Phys. Rev. Lett. *25*, 457 (1970).
4. R.A. Chatwin, J.S. Eck, D. Robson, and A. Richter, Phys. Rev. C *1*, 795 (1970).
5. R. Vandenbosch, M.P. Webb, and M.S. Zisman, Phys. Rev. Lett. *33*, 842 (1974).
6. R.H. Malmin, Ph.D. Thesis, Argonne National Laboratory Report No. ANL-1972, unpublished.
7. Nuclear Physics Laboratory Annual Report, University of Washington (1974), p. 100.
8. Optical model code GENOA, F.G. Perey (unpublished).
9. C.K. Gelbke, R. Bock, and A. Richter, Phys. Rev. C *9*, 852 (1974).
10. W. von Oertzen, Nucl. Phys. *A148*, 529 (1970).
11. J.S. Blair, R.M. DeVries, K.G. Nair, A.J. Baltz, and W. Reisdorf, Phys. Rev. C *10*, 1856 (1974).
12. Exact Finite-Range DWBA Code LOLA, R.M. DeVries (unpublished).
13. M. Ichimura, A. Arima, E.C. Halbert, and T. Terasawa, Nucl. Phys. *A204*, 225 (1973).

10.7 Investigations of Elastic Scattering of ^{16}O by ^{28}Si

J.G. Cramer, M.S. Zisman, K-L Liu, Y-d Chan, B. Cuengco, and J. Wiborg

We have continued the investigation of $^{16}O + ^{28}Si$ elastic scattering over a range of energies, as reported in the previous Annual Report.[1] In a collaborative experiment with the Oak Ridge group,[2] we have also obtained new data measured at a bombarding energy of 142.5 MeV, and have included this data in a global analysis of the data set. The analysis of this data set shows a strong preference for very shallow potentials. Figure 10.7-1 illustrates this preference: the data set is shown with two theoretical predictions, one with a potential 15 MeV deep and one with a potential which is 50 MeV deep. Both of these potentials are members of the same family of ambiguous potentials. As can be seen, the data taken at lower energies are reproduced well by both potentials, but the 50 MeV deep potential fails badly in predicting the 81 and 142.5 MeV data. We interpret this effect to be a manifestation of the absence of nuclear rainbow scattering[2] in the high energy data, which implies a shallow potential.

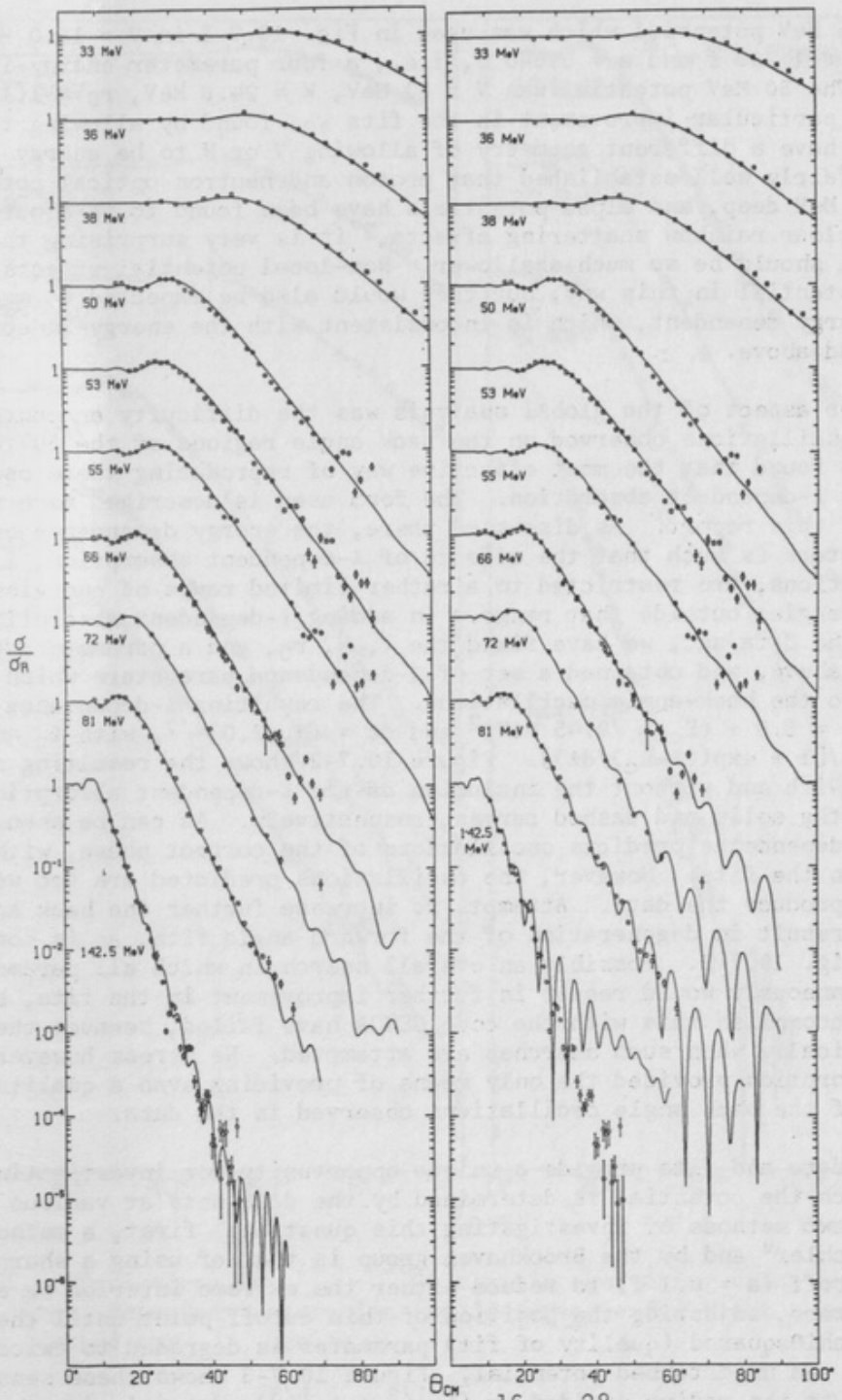

Fig. 10.7-1. Comparison of predictions for $^{16}O + ^{28}Si$ elastic scattering with 15 MeV potential (left) and 50 MeV potential (right). See text.

The 15 MeV potential which was used in Fig. 10.7-1 is V = 15.0 MeV, W = 9.33 MeV, r_0 = 1.263 f and a = 0.640 f, i.e., a four parameter energy-independent potential. The 50 MeV potential was V = 50 MeV, W = 24.8 MeV, r_0 = 1.135 f, a = 0.640 f. No particular improvement in the fits was found by allowing the imaginary potential to have a different geometry of allowing V or W to be energy dependent. Since it is fairly well established that proton and neutron optical potentials are about 50 MeV deep, and alpha potentials have been found to be about 120 MeV deep from nuclear rainbow scattering effects,[2] it is very surprising that a heavy ion potential should be so much shallower. Non-local potential effects[3] could reduce the potential in this way, but they would also be expected to make the potential energy dependent, which is inconsistent with the energy-independent potential used above.

Another aspect of the global analysis was the difficulty encountered in fitting the oscillations observed on the back angle regions of the 50 to 66 MeV data. It was found that the most effective way of reproducing these oscillations was to employ ℓ-dependent absorption. The form used is described more fully in Sec. 10.12 of this report. As discussed there, the energy dependence of the ℓ-cutoff parameters is such that the effects of ℓ-dependent absorption, i.e., back angle oscillations, are restricted to a rather limited range of energies, with no effects at energies outside that range. In adding ℓ-dependent absorption to the analysis of the data set, we have fixed the V, W, r_0, and a parameters to the values given above, and obtained a set of ℓ-dependence parameters which give improved fits to the back-angle oscillations. The resulting ℓ-dependence parameters are $\ell_c = 8.0 + (E_{c.m.}/9.45\ \text{MeV})^2$ and $d\ell = (\ell_c/2.0)^{1/2}$, with ℓ_c and $d\ell$ in $W(r,\ell) = W(r)/[1 + \exp((\ell-\ell_c)/d\ell)]$. Figure 10.7-2 shows the resulting fits to the data set with and without the inclusion of the ℓ-dependent absorption, as indicated by the solid and dashed curves, respectively. As can be seen, the inclusion of ℓ-dependence predicts oscillations of the correct phase, with a net improvement in the fits. However, the oscillations predicted are too weak to accurately reproduce the data. Attempts to increase further the back angle oscillations result in degeneration of the forward angle fits, as is somewhat apparent in Fig. 10.7-2. Possibly an overall search in which all parameters are varied simultaneously would result in further improvement in the fits, but attempts to accomplish this with the code GENOA have failed, because the program behaves erratically when such searches are attempted. We stress however that ℓ-dependent absorption provided the only means of providing even a qualitative explanation of the back angle oscillations observed in the data.

These data and fits provide a unique opportunity for investigating the degree to which the potential is determined by the data sets at various energies. We have used two methods of investigating this question: first, a method suggested by Satchler[4] and by the Brookhaven group is that of using a sharp Woods-Saxon type cutoff (a = 0.1 f) to reduce either the extreme interior or exterior potential to zero, adjusting the position of this cutoff point until the boundaries at which the chi0squared (quality of fit) parameter is degraded to twice the value obtained with the unperturbed potential. Figure 10.7-3 shows these sensitivity limits, given as the radius divided by $(A_1^{1/3} + A_2^{1/3})$, determined vs bombarding energy plotted vertically. Also given for comparison are the critical radius, defined as the semiclassical distance of closest approach for the grazing partial wave, and the location of the nuclear surface region, defined as $R_0 \pm a$. We see

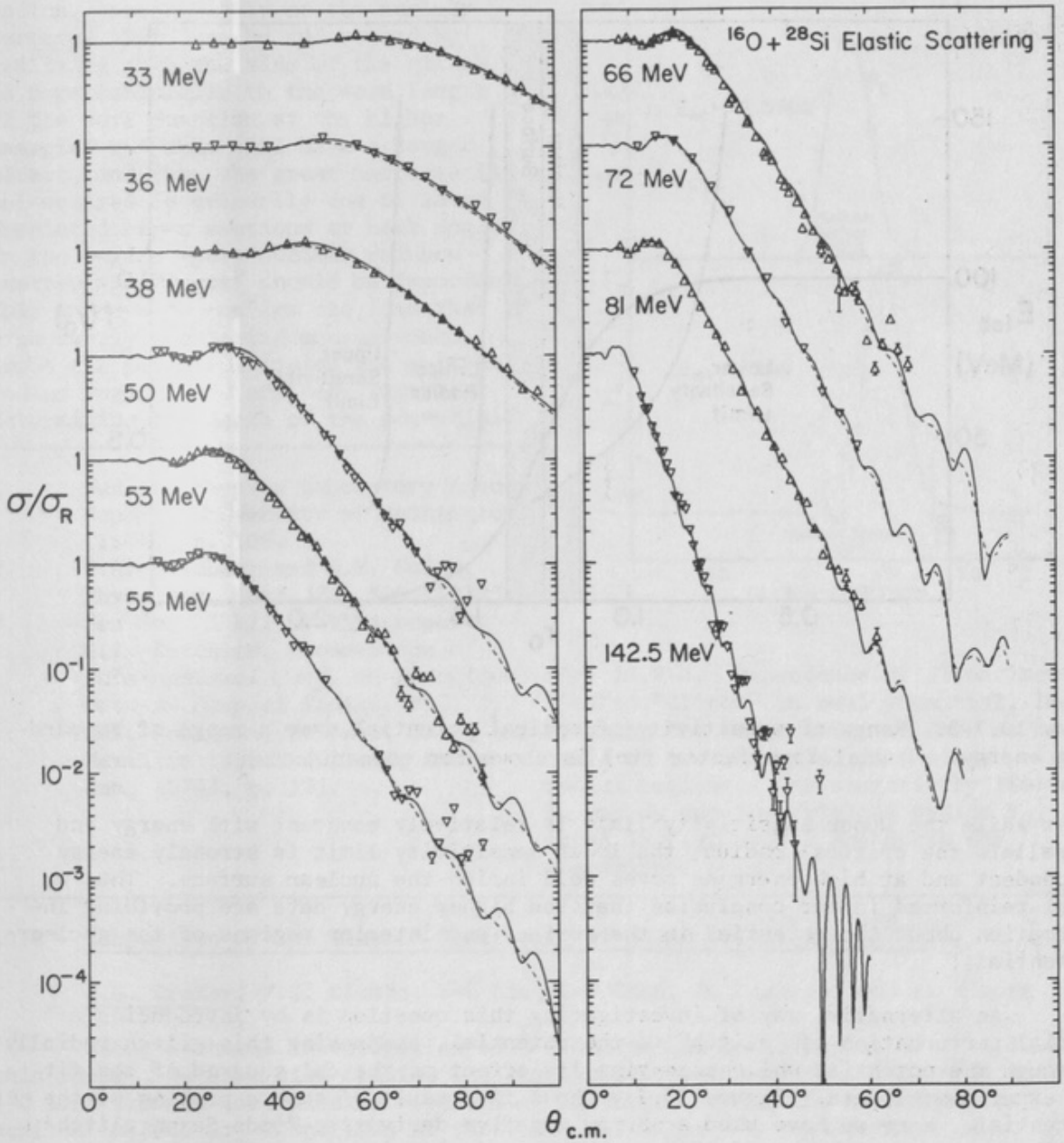

Fig. 10.7-2. Predictions for $^{16}O + ^{28}Si$ elastic scattering using an optical potential with ℓ-dependent absorption (solid curve) and without ℓ-dependent absorption (dashed curve). See text.

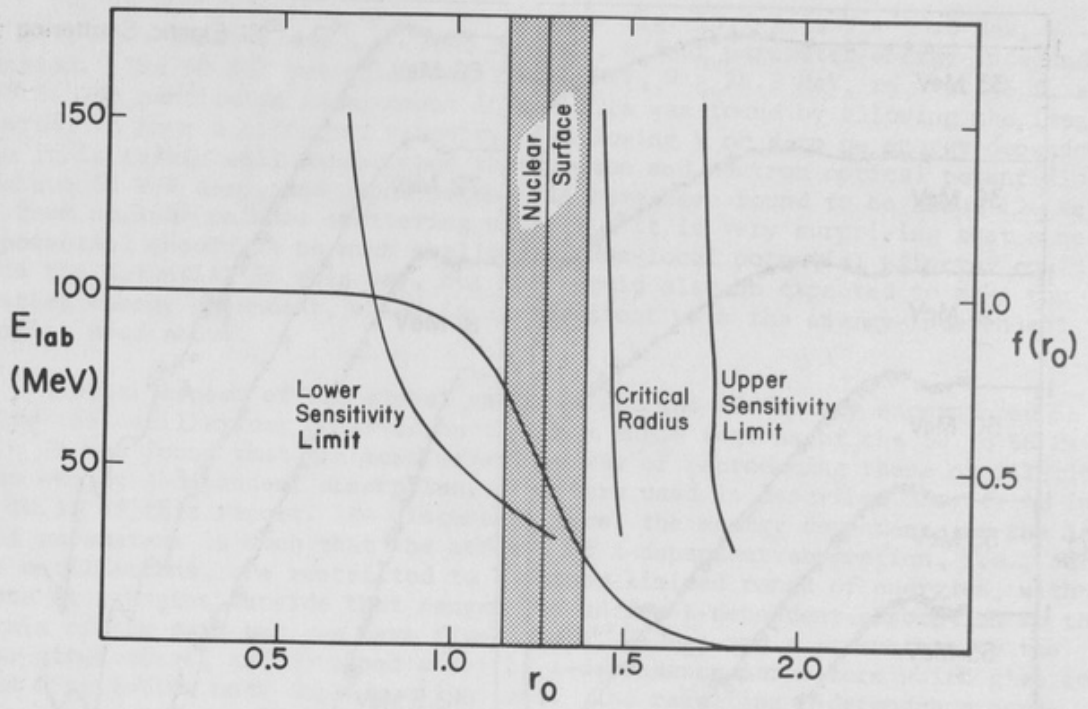

Fig. 10.7-3. Range of sensitivity of optical potential over a range of bombarding energy. Radial form factor f(r) is shown for comparison.

that while the upper sensitivity limit is relatively constant with energy and parallels the critical radius, the lower sensitivity limit is strongly energy dependent and at high energies moves well inside the nuclear surface. Thus we feel reinforced in our conclusion that the higher energy data are providing information about the potential in the surface and interior regions of the nuclear potential.

An alternative way of investigating this question is by introducing a radial perturbation of "glitch" to the potential, and moving this glitch radially through the potential while observing its effect on the chi-squared of the fit to experimental data. Figure 10.7-4 shows the result of such a probing of the potential. Here we have used a narrow negative derivative-Woods-Saxon glitch which carves a notch out of the potential, reducing it to zero and then bringing it back to its normal value over a radial region about 0.2 f wide. In Fig. 10.7-4 the chi-squared of the fit is plotted vs the radial position of the glitch divided by $(A_1^{1/3} + A_2^{1/3})$ for the highest and lowest energy members of the data set. For the 33 MeV data we see that the chi squared increases by about a factor of 6 due to the perturbation of the glitch, and is most strongly affected when the glitch is located at the critical radius R_c which was defined above. We see on the other hand that the chi-squared for the 142.5 MeV data set is increased by almost four orders of magnitude by the glitch, and peaks well inside the critical

radius, approximately at the nuclear surface. This can be understood by realizing that the size of the glitch is more comparable to the wave length of the wave function at the higher energies and thus will have a larger effect, and that the great increase in chi-squared is primarily due to large predicted cross sections at back angles, in the region where nuclear rainbow scattering effects[2] should be important. This appears to confirm the idea that high energy scattering measurements probe the potential inside the critical radius region, and are very important in determining the depth of the potential.

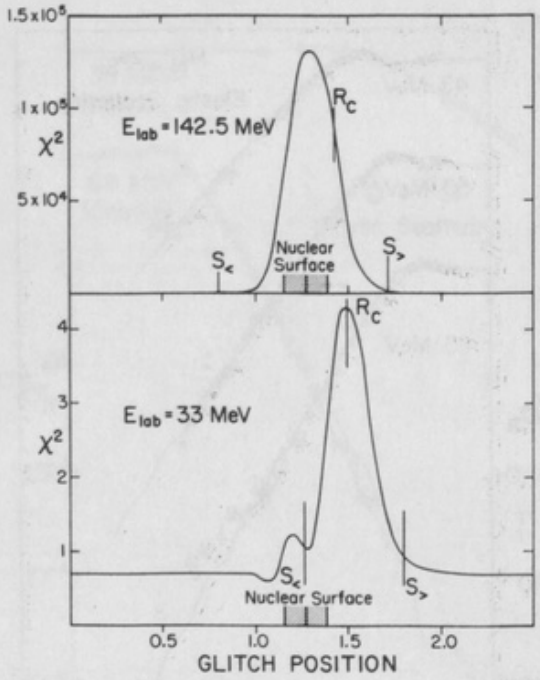

Fig. 10.7-4. Dependence of χ^2 on location of "Glitch" in real potential, indicating the sensitivity of data to details of the potential in various radial regions. The sensitivity limits $S_<$ and $S_>$ and the critical radius R_C shown in Fig. 10.7-3 are shown for comparison.

1. Nuclear Physics Laboratory Annual Report, University of Washington (1974), p. 108.
2. D.A. Goldberg and S.M. Smith, Phys. Rev. Lett. *33*, 500 (1972).
3. See Sec. 10.11 of this report.
4. G.R. Satchler, *Proceedings of International Conf. on Reactions between Complex Nuclei, Vol. 2*, Eds. Robinson, McGowan, Ball, and Hamilton (North-Holland, Amsterdam, 1974), p. 171.

10.8 Comparison of the Elastic Scattering of N and O Ions from ^{28}Si

J.G. Cramer, M.S. Zisman, K-L Liu, Y-d Chan, B. Cuengco, and J. Wiborg

Along with the investigation of ^{16}O scattering described in Sec. 10.7 of this report, we have also studied the elastic scattering of ^{14}N, ^{15}N, ^{17}O, and ^{18}O ions from an isotopically separated ^{28}Si target, using the techniques described in Ref. 1. Comparison of these data with the ^{16}O data permits us to investigate the question of whether the scattering of neighboring ions such as the N and O isotopes can be described by the same potential. This is related to the question of whether there may be significant differences in the entrance and exit channel potentials used in the analysis of heavy ion transfer reactions.

To begin this comparison we have attempted to use the potential determined by fitting the $^{16}O + ^{28}Si$ data to predict the scattering of these ions. It was immediately found that the ℓ-dependent absorption used in the ^{16}O potential generated predictions with large oscillations at back angles which are not present

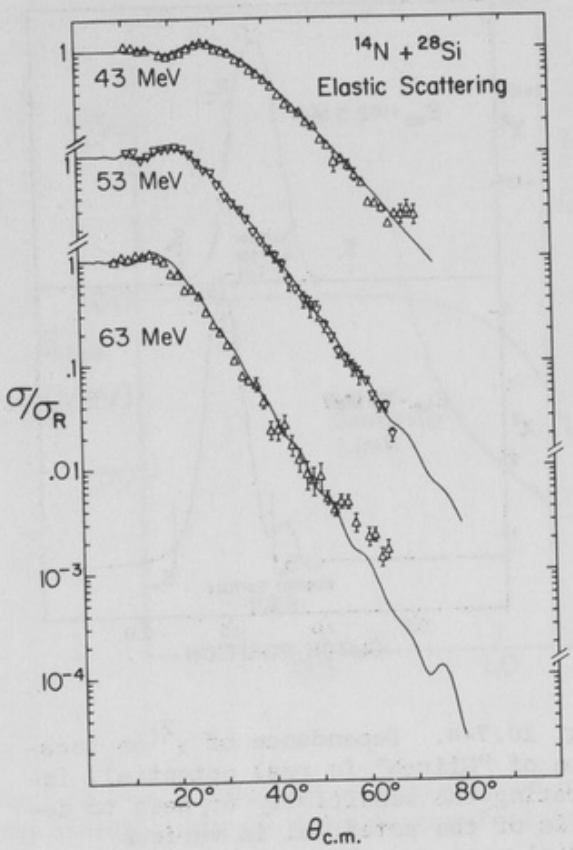

Fig. 10.8-1. Angular distributions of $^{14}N + ^{28}Si$ elastic scattering at 43 MeV, 53 MeV, and 63 MeV. Solid curve is calculation using ^{16}O potential.

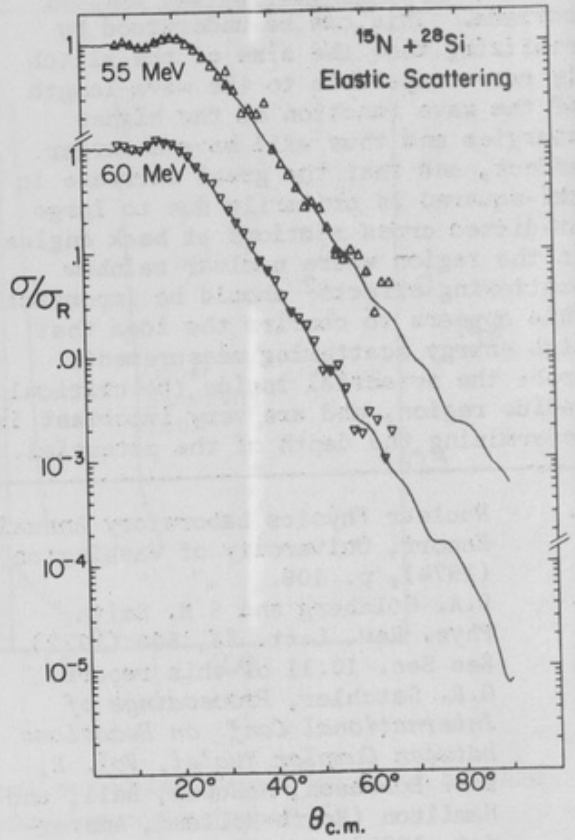

Fig. 10.8-2. Angular distributions of $^{15}N + ^{28}Si$ elastic scattering at 55 MeV and 60 MeV. Solid curve is calculated using ^{16}O potential.

in the data. However, the ^{15}N and ^{14}N data sets could be fairly well described with the ^{16}O potential when the ℓ-dependent absorption was omitted. This is illustrated in Figs. 10.8-1 and 2. It is worth noting that both data sets show some tendency toward oscillation at back angles which might be better reproduced if some ℓ-dependent absorption were included.

On the other hand, it was found that neither the ^{17}O nor the ^{18}O data could be adequately described by the ^{16}O potential, with or without the inclusion of ℓ-dependent absorption, and it was necessary to search for a new potential to fit these data sets. These potentials are given in Table 10.8-1. Figures 10.8-3 and 4 show the ^{17}O and ^{18}O data, with the solid curves produced by the fitted potentials given in Table 10.8-1 and the dashed curve produced by the ^{16}O potential. It is curious to note that the ^{17}O data at back angles is <u>larger</u> than the ^{16}O predictions while the ^{18}O data at back angles is <u>smaller</u> than the ^{16}O predictions. This is reflected in the potentials given in Table 10.8-1 in that the

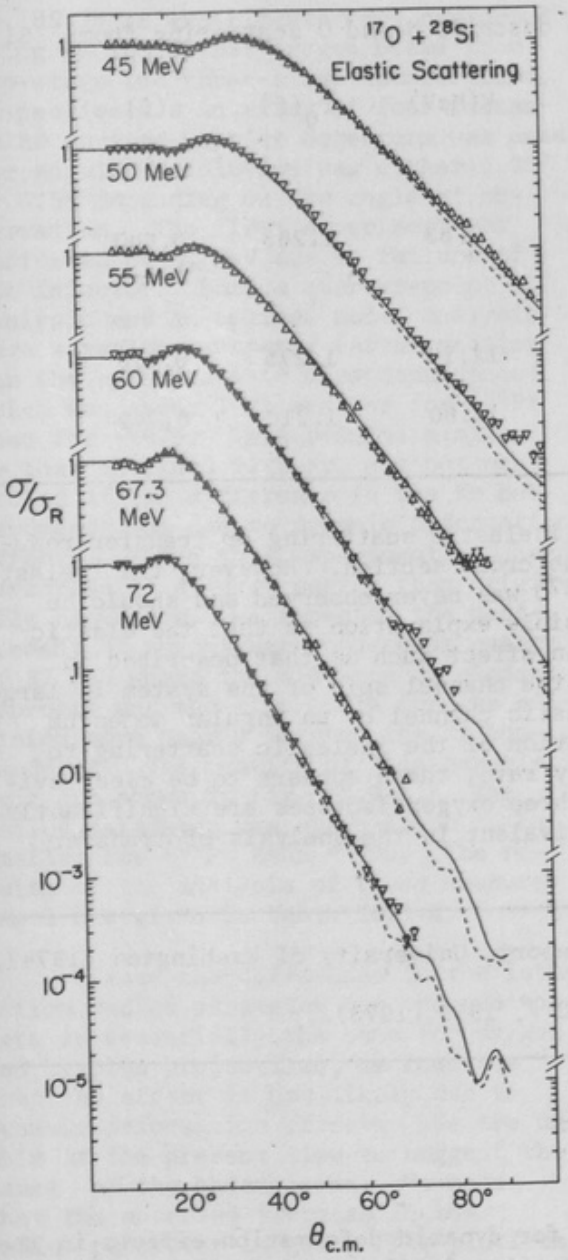

Fig. 10.8-3. Angular distribution of $^{17}O + ^{28}Si$ elastic scattering at 45 MeV, 50 MeV, 55 MeV, 60 MeV, 67.3 MeV, and 72 MeV. Solid curves are calculated using ^{17}O potential and dashed curves are calculated using ^{16}O potential given in Table 10.8-1.

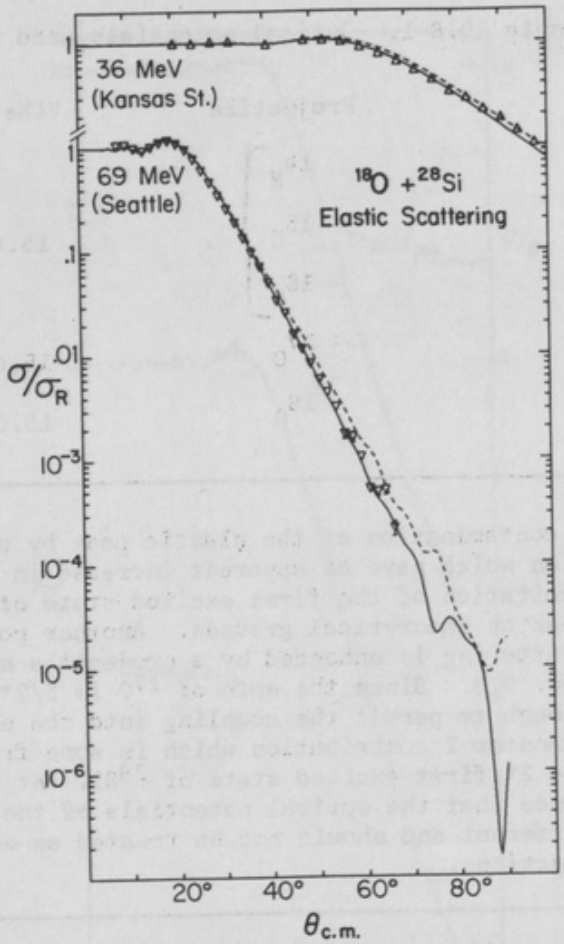

Fig. 10.8-4. Angular distributions of $^{18}O + ^{28}Si$ elastic scattering at 36 MeV and 69 MeV. 36 MeV data is taken from Ref. 2. Solid curves are calculated using ^{18}O potential and dashed curves are calculated using ^{16}O potential from Table 10.8-1.

^{17}O potential has a smaller diffuseness than the ^{16}O potential while the ^{18}O potential has a larger diffuseness. It is not particularly surprising that a projectile which has two nucleons outside a closed shell appears more diffuse than a closed shell projectile like ^{16}O. It is rather surprising, however, that ^{17}O appears less diffuse than ^{16}O. It is possible that this is an artifact of

Table 10.8-1. Optical potentials used to describe N and O scattering from ^{28}Si

Projectile	V(MeV)	W(MeV)	r_0(f)	a(f)
^{14}N, ^{15}N, ^{16}O	15.0	9.33	1.263	0.640
^{17}O	15.0	12.14	1.275	0.626
^{18}O	15.0	11.60	1.210	0.742

a contamination of the elastic peak by an inelastic scattering or transfer reaction which gave an apparent increase in the cross section. However, the inelastic excitation of the first excited state of ^{17}O was never observed and should be weak on theoretical grounds. Another possible explanation is that the elastic scattering is enhanced by a projectile spin effect such as that described in Sec. 9.6. Since the spin of ^{17}O is $5/2^+$, the channel spin of the system is large enough to permit the coupling into the elastic channel of an angular momentum transfer 2 contribution which is some fraction of the inelastic scattering to the 2^+ first excited state of ^{28}Si. At any rate, there appears to be clear evidence that the optical potentials of the three oxygen isotopes are significantly different and should not be treated as equivalent in the analysis of transfer reactions.

1. Nuclear Physics Laboratory Annual Report, University of Washington (1974), p. 108.
2. D.S. Gale and J.S. Eck, Phys. Rev. C *7*, 1950 (1973).

10.9 Elastic Scattering of ^{16}O from ^{208}Pb

R. Vandenbosch and M.P. Webb

An experiment whose aim was to look for dynamic deformation effects in the near-barrier scattering of very heavy projectiles is discussed in Sec. 10.10 of this report. An apparent difference in the interaction radius between ^{194}Pt and ^{208}Pb was observed. Although this difference was in the expected direction and of the order of magnitude expected for dynamic deformation effects, the smallness of the difference prompted the suggestion[1] that a control experiment with a lower-Z projectile should be performed. If the observed effect was due to the deformation of the target nucleus by the Coulomb potential of the Kr projectile (Z = 36), the use of a lower-Z projectile such as oxygen (Z = 8) should give a much smaller effect. We have therefore studied the elastic scattering of oxygen from ^{194}Pt and ^{208}Pb targets.

These experiments were performed using 81 and 87 MeV oxygen beams from two-stage and three-stage acceleration, respectively. An array of four rectangular surface-barrier detectors was used. The angular resolution was either 0.36° or 0.5° depending on the angle of observation. The first experiment was performed at 81 MeV due to failure of the injector. Both a quarter-point analysis and an optical model analysis gave a radius parameter (after scaling for the expected $A^{1/3}$ mass dependence) which was about 1-2% smaller for ^{194}Pt than for ^{208}Pb. This result, similar to that obtained with Kr, was not expected if the difference in the Kr bombardments was due to dynamic deformation effects. Since this experiment had been performed at a lower energy than originally hoped for, we repeated the measurement at the higher bombarding energy of 87 MeV where the distance of closest approach and the time scale for the collision more nearly matched the Kr bombardment. The results of this experiment are shown in Fig. 10.9-1. The radius parameter was again found to be smaller for ^{194}Pt than ^{208}Pb. The results of the analysis of these measurements are given in Table 10.9-1.

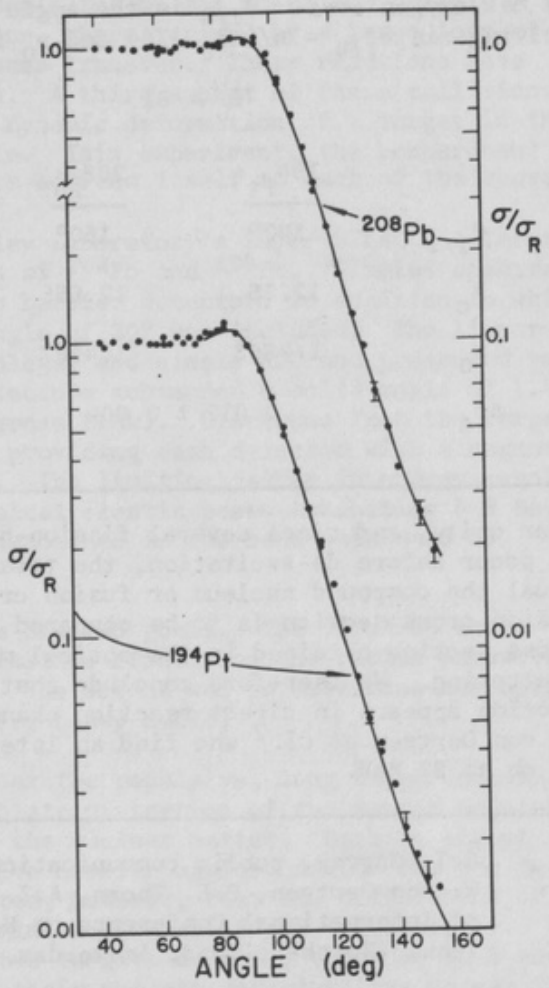

Fig. 10.9-1. Elastic scattering angular distributions (plotted as ratio of observed cross section to Rutherford cross section) for 87 MeV ^{16}O incident on ^{194}Pt and ^{208}Pb. The full curves are optical model fits with V = 40 MeV, a_v = 0.49, W = 60 MeV, a_w = 0.36 and $r_w = r_v + 0.14$ f. The r_v values giving the best fits shown are 1.291 for ^{194}Pt and 1.310 for ^{208}Pb.

Since the difference in the interaction radius parameter for the two targets is essentially the same for oxygen and krypton projectiles, we conclude that the effect is not likely due to dynamic deformation effects. We are unable at the present time to suggest the cause of the observation. We note that the observed increase in the radius parameter in going from platinum to lead is contrary to the general trend for the radius parameter (when scaled in this manner) to decrease with increasing mass number.

During the course of these measurements we also measured the differential fission cross sections at 81 MeV. Integration of these cross sections gives a total fission cross section of 83 mb. Since the fission branching ratio Γ_f/Γ_T for the compound nucleus formed in the oxygen plus lead system is expected to be

Table 10.9-1. Results of quarter-point analysis of elastic scattering of 81 and 87 MeV oxygen ions. $\theta_{1/4}$ is the angle for which $\sigma/\sigma_R = 1/4$, R_c is given by solving $\sin \theta_{1/4} = \eta/(kR_c - \eta)$ and r_0 is defined by $R_c = r_0(A_1^{1/3} + A_2^{1/3})$.

	$E_L = 81$		$E_L = 87$	
	^{194}Pt	^{208}Pb	^{194}Pt	^{208}Pb
$\theta_{1/4}$	142°	160°	111.4°	117
R_c	12.35	12.656	12.30	12.65
r_0	1.4863	1.4987	1.4805	1.498
Δr_0	0.012 ± 0.004		0.017 ± 0.006	

near unity, and since several fission-neutron emission competitions are expected to occur before de-excitation, the total fission cross section should nearly equal the compound nucleus or fusion cross section. This value of 83 mb for the fusion cross section is to be compared with a value of 190 mb for the absorption cross section obtained in the optical model calculation fits to the elastic scattering. We therefore conclude that a good fraction of the absorption cross section appears in direct reaction channels. Such a result has been obtained by von Oertzen *et al.*[2] who find an integrated direct reaction cross section of 94 mb at 82 MeV.

1. G.T. Garvey, public communication.
2. W. von Oertzen, C.E. Thorn, A.Z. Schwarzschild, and J.D. Garrett, Proc. of International Conference on Reactions between Complex Nuclei, Nashville, Tenn. (North-Holland, Amsterdam, 1974), p. 83.

10.10 Elastic and Deeply Inelastic Scattering of ^{84}Kr from ^{208}Pb and ^{194}Pt

T.D. Thomas*, R. Vandenbosch, and M.P. Webb

We have completed a series of experiments designed to obtain a deeper understanding of the elastic scattering, reaction mechanisms and interaction potentials generated in collisions between very heavy ions and heavy targets. The optical model potential required to reproduce the elastic scattering provides an indication of the effective interaction potential and provides a test of the phenomenological potentials used in semiclassical friction models. The relative absence[1] of complete fusion reactions in ^{84}Kr bombardment of heavy targets marks a significant departure from reaction mechanisms generally observed in light particle interactions. Compound nucleus formation represents a major fraction of the total reaction cross section for reactions involving light ions and heavy targets, while approximately only half of the reaction cross section goes into

complete fusion for ^{40}Ar induced reactions. For ^{84}Kr bombardment of heavy targets the total reaction cross section is dominated by the so-called "deeply inelastic"[2] or "strongly damped"[3] collisions, characterized by a large loss of relative kinetic energy but rather small mass transfer. These reactions have also been labeled "quasifission" reactions. A third aspect of these collisions involves the feasibility of measuring the dynamic deformation of a target in the strong Coulomb field of a high Z projectile. This experiment, the bombardment of ^{208}Pb and ^{194}Pt by ^{84}Kr, was designed to address itself to each of the above.

^{84}Kr beams from the Lawrence Berkeley Laboratory's Super-HILAC accelerator were used to bombard 50-100 $\mu g/cm^2$ targets of ^{208}Pb and ^{194}Pt. Singles spectra were obtained from two solid state surface barrier detectors in addition to which a monitor counter at a fixed laboratory angle of 30° was included. The linear signals were digitized by an analog multiplexer and single ADC and presented to a PDP 15 computer. The angle-defining detectors subtended a solid angle of 1.4 msr with an angular acceptance of 0.75 degrees (lab). Electrons from the target were suppressed by biasing the target and providing each detector with a magnet and a thin Ni covering foil ($\sim$100 $\mu g/cm^2$). The limiting factor in energy resolution appeared to be beam related, with typical elastic peaks exhibiting 6-8 MeV widths (FWHM). In addition, two energy components in the beam separated by several MeV could normally be observed.

Our elastic scattering studies have had two goals. The first of these was to look for evidence for dynamic deformation effects on the radius parameter characterizing the interaction potential. The second was to determine the optical potential for the elastic scattering of very heavy nuclei.

It was suggested some years ago[4] that the repulsive, long range Coulomb field of the projectile might induce an oblate distortion of the target requiring a smaller distance of approach to overlap the nuclear matter. Such an effort would result in an increase in the effective barrier against fusion for the two nuclei. More recent calculations[5] indicated, however, that the diffuseness of the attractive nuclear potential would diminish such an effect considerably. We have done a careful comparative study of two targets as close together in Z and A as possible but which differ greatly in their nuclear deformability to see if the effect is as small as the above two mutually self-cancelling deformation processes would suggest. These targets were ^{194}Pt, a transitional region nucleus very soft with respect to the oblate distortion degree of freedom and ^{208}Pb, a doubly closed shell nucleus rather rigid with respect to distortion.

We have measured elastic scattering angular distributions at 494 (Fig. 10.10-1) and 510 MeV. To minimize experimental problems the measurements were taken by alternating the Pb and Pt targets at each angle. The results of both a sharp-cutoff analysis and an optical model analysis show that the radius parameter, r_0, where $R = r_0(A_1^{1/3} + A_2^{1/3})$; is approximately 1.5% smaller for ^{194}Pt than for ^{208}Pb; a result in agreement with dynamic deformation predictions.[4] In a sharp-cutoff analysis such a difference corresponds to a difference in quarter-point angle of 3°, whereas we believe that we can determine the quarter-point angle to better than a degree. The above results were confirmed in the 510 MeV measurements. These results correspond to an increase in the barrier height (in the sharp-cutoff model) of about 4 MeV (less than 2%). This is considerably less than early estimates[4] neglecting the effects of the diffuse nuclear potential,

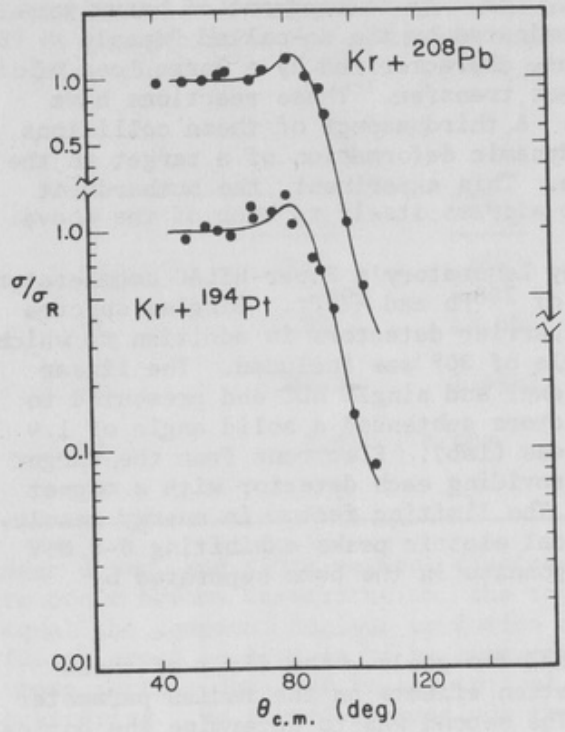

Fig. 10.10-1. Ratio of elastic scattering cross sections to Rutherford scattering cross section as a function of angle for the two targets, ^{194}Pt and ^{208}Pb. The bombarding energy was 494 MeV.

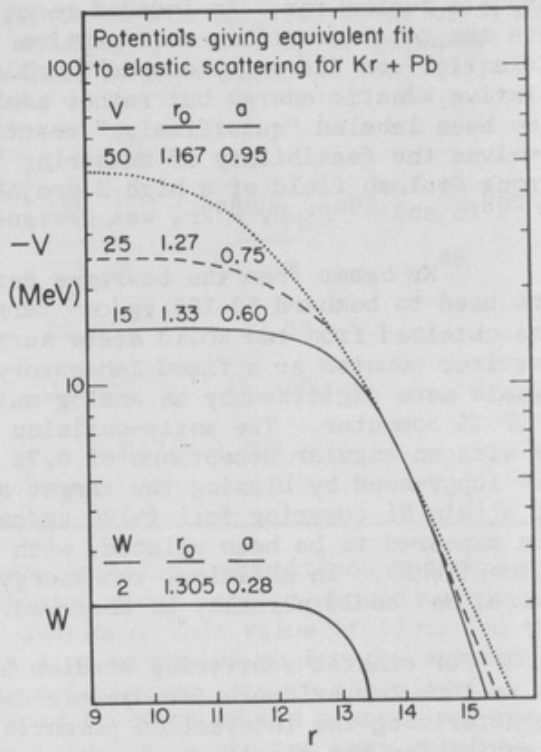

Fig. 10.10-2. Real part of the optical potentials giving an equivalent fit to the elastic scattering. The imaginary potential shown at the bottom of the figure was held fixed in this particular set of calculations.

thus tending to confirm the cancellation process. It is not clear, however, that the small residual effect observed can in fact be attributed to dynamic deformation effects. A "control" experiment where ^{16}O was scattered off the same targets gave a similar difference in r_0 in spite of the fact that the Z of the projectile was smaller by a factor of 4.5. These results are discussed in Sec. 10.9 of this report.

The elastic scattering data for the Pb target has been subjected to a fairly extensive optical model analysis using the program described in Sec. 4.7 of this report. The analysis shows that it is necessary to use an optical potential that is somewhat transparent for the grazing partial waves. This is indicated by the need to have an imaginary potential which falls off more rapidly with distance than does the real part of the potential. The ambiguities in the potentials which fit the elastic scattering show that it is only sensitive to the tail of the potential in the region where the separation is about 14 fermis. Some examples of equivalent potentials from a preliminary analysis are shown in Fig. 10.10-2.

Perhaps the most surprising phenomenon arising from ^{84}Kr induced reactions is the relative absence of fusion-fission events and the concomitant dominance of the reaction cross section by deeply inelastic collisions. This novel reaction mechanism is characterized by: 1) a strong damping of the incident kinetic energy, the outgoing kinetic energy being consistent with the value calculated for Coulomb repulsion between the two fragments; 2) relatively little mass transfer and 3) angular distributions which are strongly peaked at angles near the grazing angle indicative of a relatively fast reaction (not characterized by a $1/\sin\theta$ angular distribution expected for fission fragments from a compound nucleus formed in a heavy ion induced reaction). The above results have stimulated classical explanations based on a large nuclear viscosity which generate a strong thermalization of the incident kinetic energy during the short interaction period of the collision.

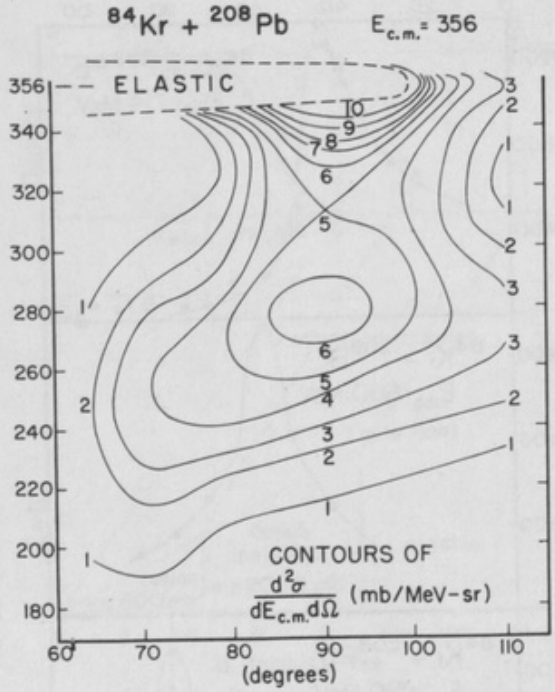

Fig. 10.10-3. Contours of $d^2\sigma/dE_{c.m.}d\Omega$ for 494 MeV (lab) bombardment of ^{84}Kr on ^{208}Pb.

As part of our experiment we obtained angular distributions for deeply inelastic scattering at 494, 510, and 714 MeV. The deeply inelastic events manifest themselves in singles spectra as a peak reduced in energy from the ^{84}Kr elastic peak and well separated at all angles measured except those near the grazing angle where higher energy multinucleon transfer reactions (quasi-elastic reactions) fill in the valley between the deeply inelastic and elastic peaks. This is illustrated in Fig. 10.10-3 which shows contours of $d^2\sigma/dE_{c.m.}d\Omega$. The integrated cross sections for the deeply inelastic process contains quasi-elastic contributions at angles very near the grazing angle. There is also evidence in Fig. 10.10-3 for a recession in energy of the deeply inelastic peak at angles both smaller and larger than the grazing angle. This suggests that the trajectories for these angles correspond to a greater overlap of the matter density of the projectile and target, increasing the possibility of energy loss. The deeply inelastic angular distributions for ^{84}Kr + ^{208}Pb are presented in Fig. 10.10-4 along with the ^{84}Kr + ^{209}Bi data of Wolf *et al.*[3] The angular distributions peak at angles close to those for which σ/σ_R for the elastic channel begins to fall. The rapid decrease in cross section of small angles argues against an orbiting picture[6] of the interaction. The angle integrated cross section for the deeply inelastic events are plotted in Fig. 10.10-5 as a function of laboratory energy. Included is the prediction of the total absorption cross section calculated from an optical model used to fit the elastic scattering data. As is evident, the deeply inelastic yield accounts for virtually all of the cross section. At 714 MeV an estimate of the upper limit to the fusion cross section gave ~600 mb. This estimate was made

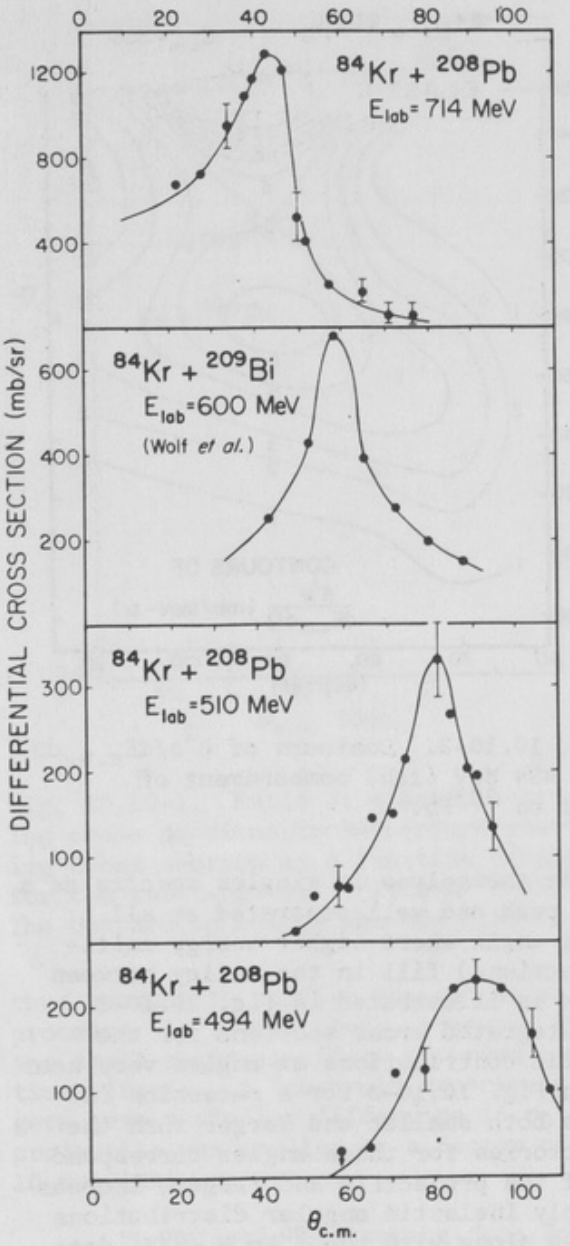

Fig. 10.10-4. Deeply inelastic angular distributions for $^{84}Kr + ^{208}Pb$. Included are the $^{84}K + ^{209}Bi$ results of Wolf *et al.*[3]

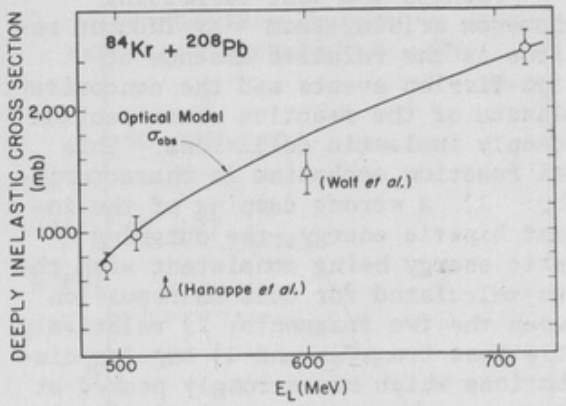

Fig. 10.10-5. Angle integrated cross sections for the deeply inelastic scattering of $^{84}Kr + ^{208}Pb$ as a function of energy. Our values also include the quasielastic events which fill the valley between the deeply inelastic and elastic peaks at angles near the grazing angle. The solid line is an optical model prediction of the total absorption cross section.

by assuming that the large-angle tail seen in the 714 MeV data is due to a $1/\sin\theta$ type angular distribution resulting from fusion-fission events. This upper limit, however, does not detract from the fact that the total reaction cross section at 714 MeV (more than 200 MeV (c.m.) above the barrier for head on collisions) is dominated by non-fusion processes. At energies near 500 MeV the large preponderance of the deeply inelastic process relative to complete fusion can be explained by considerations based on the highly distorted trajectories and the density distributions at the distance of closest approach, as illustrated in Fig. 10.10-6. It is seen that a relatively large range of impact parameters, and hence a large cross section, is associated with a rather narrow range of distances of closest approach.

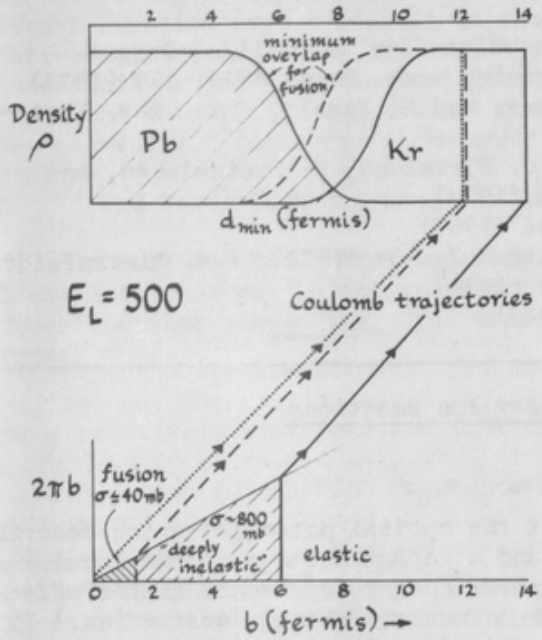

Fig. 10.10-6. The lower part of the figure shows the division of impact parameters between the elastic, deeply inelastic and possibly fusion processes. The arrows connect the impact parameters dividing these regions with the distance of closest approach indicated at the top of the figure. The full curves at the top show the target and projectile charge density profiles at the distance of closest approach for the impact parameter corresponding to the division between elastic and deeply inelastic processes. The dotted line shows the density distribution for the distance of closest approach for a head-on collision.

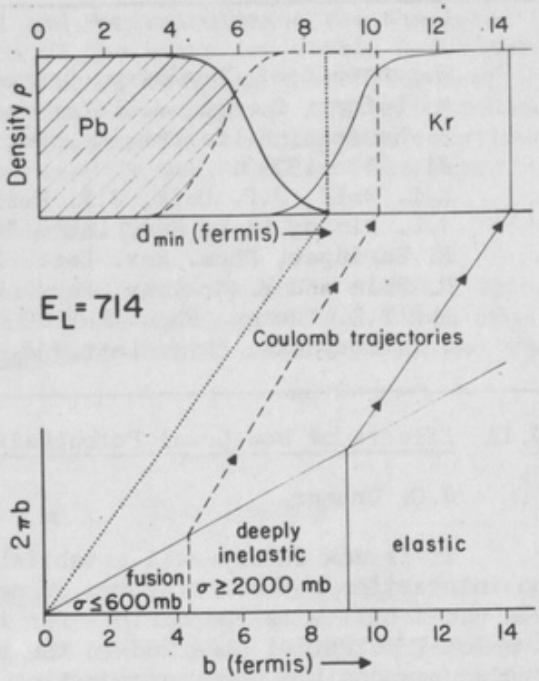

Fig. 10.10-7. Similar to Fig. 10.10-6, except the bombarding energy is now 714 MeV. The assumption of Coulomb trajectories is a much poorer assumption at this energy for the smaller impact parameters. It is clear however that at this energy there is a sizable range of impact parameters which should lead to a distance of closest approach where sufficient overlap to saturate the nuclear density will occur.

Assuming Coulomb trajectories, the impact parameters required to account for the observed deeply inelastic cross section lead to distances of closest approach for which the nuclear density in the overlap region does not saturate. In effect, almost all the collisions are grazing collisions. The situation at 714 MeV is depicted in Fig. 10.10-7. More trajectories have the necessary energy to overcome the strong Coulomb repulsion and overlap the matter densities to the point where fusion might be expected to set in. A possible explanation of the absence of fusion may be that few if any of the trajectories bring the centers of mass as close together as would be required to be inside the fission saddlepoint of the compound system (if indeed there is a barrier against fission for this high Z^2/A system).

* Department of Chemistry, Oregon State University, Corvallis, Oregon.
1. M. Lefort, C. Ngô, J. Péter and B. Tamain, Nucl. Phys. *A216*, 166 (1973).
2. F. Hanappe, M. Lefort, C. Ngô, J. Péter, and B. Tamain, Phys. Rev. Lett. *32*, 738 (1974).
3. K.L. Wolf, J.P. Unik, J.R. Huizenga, J. Birkelund, H. Freissleben, and V.E. Viola, Phys. Rev. Lett. *33*, 1105 (1974).
4. R. Beringer, Phys. Rev. Lett. *18*, 1006 (1967).
5. H. Holm and W. Greiner, Phys. Rev. Lett. C *2*, 404 (1970); P.W. Riesenfeldt and T.D. Thomas, Phys. Rev. C , 2448 (1970).
6. J. Wilczynski, Phys. Lett.*47B*, 45 (1973).

10.11 Effects of Non-Local Potentials in Heavy Ion Reactions

J.G. Cramer

It is now fairly well established that the optical potential which describes the interaction between a proton or neutron and a target nucleus is non-local.[1] This non-locality is responsible for the negative energy dependence of the effective local potential observed in the analysis on nucleon elastic scattering.[1] It is also responsible for the reduction of the wave function in the nuclear interior[2] which had prompted the use of radial cutoffs in DWBA calculations which did not include non-local corrections.

Non-local potentials are functions of two radial variables rather than one. The usual potential term in the Schroedinger equation, which has the form $V(\vec{r})\psi(\vec{r})$, is replaced by an integral of the form $\int V(\vec{r},\vec{r}')\psi(\vec{r}')d\vec{r}'$. Thus, since the wave function $\psi(r)$ usually changes rapidly compared to the potential, this integral has the effect of averaging away some fraction of the potential term, thereby reducing the effective potential. If the averaging interval (or non-local "range") becomes comparable to the wave length of the wave function, this reduction can be sizable and the effective potential reduced by orders of magnitude.

Since the wave lengths characteristic of heavy ion reactions are usually much smaller than in light ion reactions (due to the larger masses and higher energies involved) non-local effects for a given non-local range would be expected to be more important for heavy than light ions. Whether such effects are, in fact, important remains an open question which can best be answered by experiment. One must, however, understand which experimentally observable effects would be produced by non-local heavy ion potentials. It is the purpose of this paper to investigate this question and to test the approximations which have been developed for calculating such effects in light ion reactions.

To begin this investigation it was necessary to write an optical model program which could solve the integro-differential non-local Schroedinger equation in the heavy ion domain. The work of Perey and Buck,[1] based on the assumption of a separable Gaussian form for the non-local potential, was taken as a starting point. It was soon found that the methods presented in that work

for computing an approximate local potential and for calculating the non-local kernel function were divergent in some region of the heavy ion domain and alternative methods had to be devised. Further, it was found that their method of numerically solving the inhomogeneous Schroedinger equation was highly unstable for short wave lengths, and a new numerical procedure for solving this equation was necessary. These new techniques are discussed in Sec. 4.11 of this report.

A. The Perey-Buck Non-Local-to-Local Potential Transformation

Perey and Buck[1] have suggested a transformation by means of which a non-local potential may be transformed into an effective local potential which produces the same scattering. The transformation including Coulomb effects has the form:

$$u_L = u_N \exp(-\alpha(\varepsilon - u_L)) \qquad \alpha < 1$$
$$u_L = \frac{1}{\alpha} \ln(u_L/u_N) + \varepsilon \qquad \alpha \geq 1 \qquad (1)$$

where $\alpha = (k\beta/2)^2$, $u_L = U_L/E_{c.m.}$, $u_N = U_N/E_{c.m.}$, and $\varepsilon = 1 - V_{Coul}/E_{c.m.}$ Here $k = p/h$ is the wave number, β is the non-local range, U_L and U_N are the (complex) local and non-local optical potentials, $E_{c.m.}$ is the kinetic energy of the system in the center of mass system, and V_{Coul} is the Coulomb potential. Both of these expressions are transcendental, and must be iterated to generate a local potential U_L from a given non-local potential U_N.

It can be seen from the exponential form of (1) that, since U_L is normally an attractive, i.e., negative, potential, the exponential factor will be less than one, so that the local potential will usually be less than the non-local potential in magnitude. Further, since $E_{c.m.}$ enters into various factors in this relation, the reduction factor will depend on energy. Since both U_L and V_{Coul} are functions of the radius, the reduction factor will also depend on radius, so that the shape of U_L will be different from that of U_N.

To test the accuracy of the transformation for heavy ions, we have considered two types of comparisons: (1) a comparison of the elastic scattering prediction of the transformed potential with that of an exact non-local elastic scattering calculation, and (2) a comparison of the transformed potential with the "trivially equivalent" local potential[2] which is the exact equivalent of a non-local potential for a given partial wave. Comparison of elastic scattering cross section predictions (1) shows excellent agreement in all cases tested. Since this method of comparison is rather insensitive to the details of non-local wave functions, and since a full non-local optical model calculation is very time consuming, this method of comparison is rather limited in its utility.

The basis of comparison (2) is that an equivalent potential can be defined by $V_{eq} = [\int V(r,r')\Psi_\ell(r')dr']/\Psi_\ell(r)$. This equivalent potential is strongly ℓ-dependent, is not well behaved, and will have cusps and poles when the wave function has minima and zeroes, but it is a local potential which contains <u>all</u> of the features of a non-local potential and may be directly compared with the transformed potential. Figure 10.11-1 shows a comparison between the transformed potential and the trivially equivalent potential for several different ℓ-values.

For this comparison and those which follow we have used the scattering of ^{16}O from ^{48}Ca at 48 MeV as a test case. This system was chosen because it is light enough so that relatively few partial waves are needed in the calculations, because the non-local effects are tested more severely with the relatively deep potential (V = 100 MeV) used in the elastic scattering analysis, and because significant deviations between experimental transfer data and DWBA calculations have been noted.[5] The potential used is V = 100 MeV, W = 40 MeV, r_0 = 1.22 f, a = 0.49 f. For all comparisons we have chosen ℓ-values near the grazing ℓ-value. As can be seen, the equivalent potentials have large excursions and cusps, but generally average through the transformed potential. This demonstrated the kind of approximation which is being used by employing the transformed local potential.

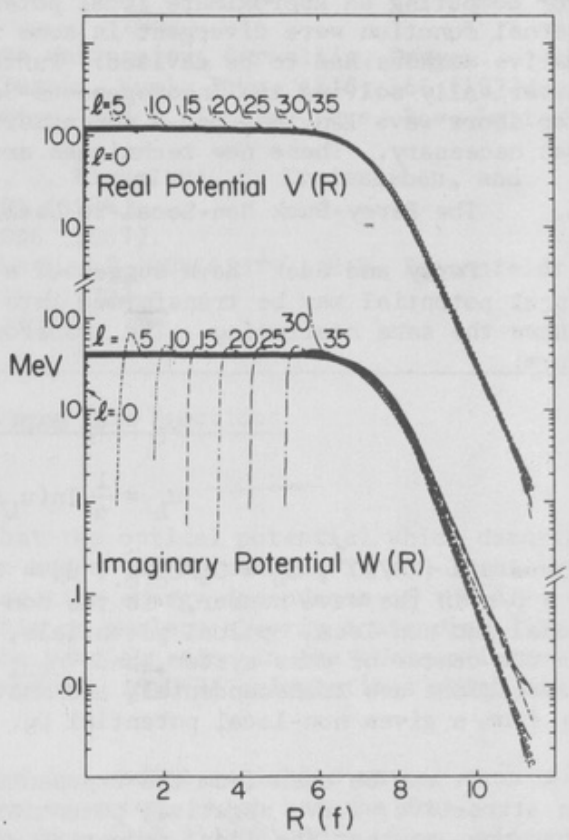

Fig. 10.11-1. Comparison of local equivalent potential (circles) with non-local effective potentials (dashed curves) for ^{16}O + ^{48}Ca scattering.

B. The Local Energy Approximation

As mentioned above, one of the effects of a non-local potential is the reduction of the wave function in the interior of the nucleus, which is sometimes called the Perey effect.[2-4] The use of an effective local potential such as the transformed potential described above does not reproduce this effect, since the transformed potential only gives an approximation to the external behavior of the wave function. Thus an additional approximation is required to simulate the reduction of the internal wave function produced by a non-local potential. Such an approximation is not required for the analysis of elastic scattering, which depends only on the behavior of the external wave function, but is needed when analyzing transfer reactions, where overlaps between bound state wave functions and distorted waves in the nuclear interior make important contributions to the cross sections. The approximation which is conventionally used on light ion reactions is called the Local Energy Approximation.[3,4] Its derivation is given in Ref. 3. It has the form:

$$\Psi_{NL}(r) \simeq \Psi_L(r)[1 - (\tfrac{1}{2}\beta k)^2(V_L(r)/E_{c.m.})]^{-1/2}.$$

Since $V_L(r)$ is in general an attractive potential and therefore negative, the denominator will be greater than 1 and the wave function will be reduced. Further, since $V_L(r)$ is complex, the approximate non-local wave function will not only be reduced in magnitude but also shifted in phase by the transformation. The local energy approximation gives the appearance of being energy-dependent,

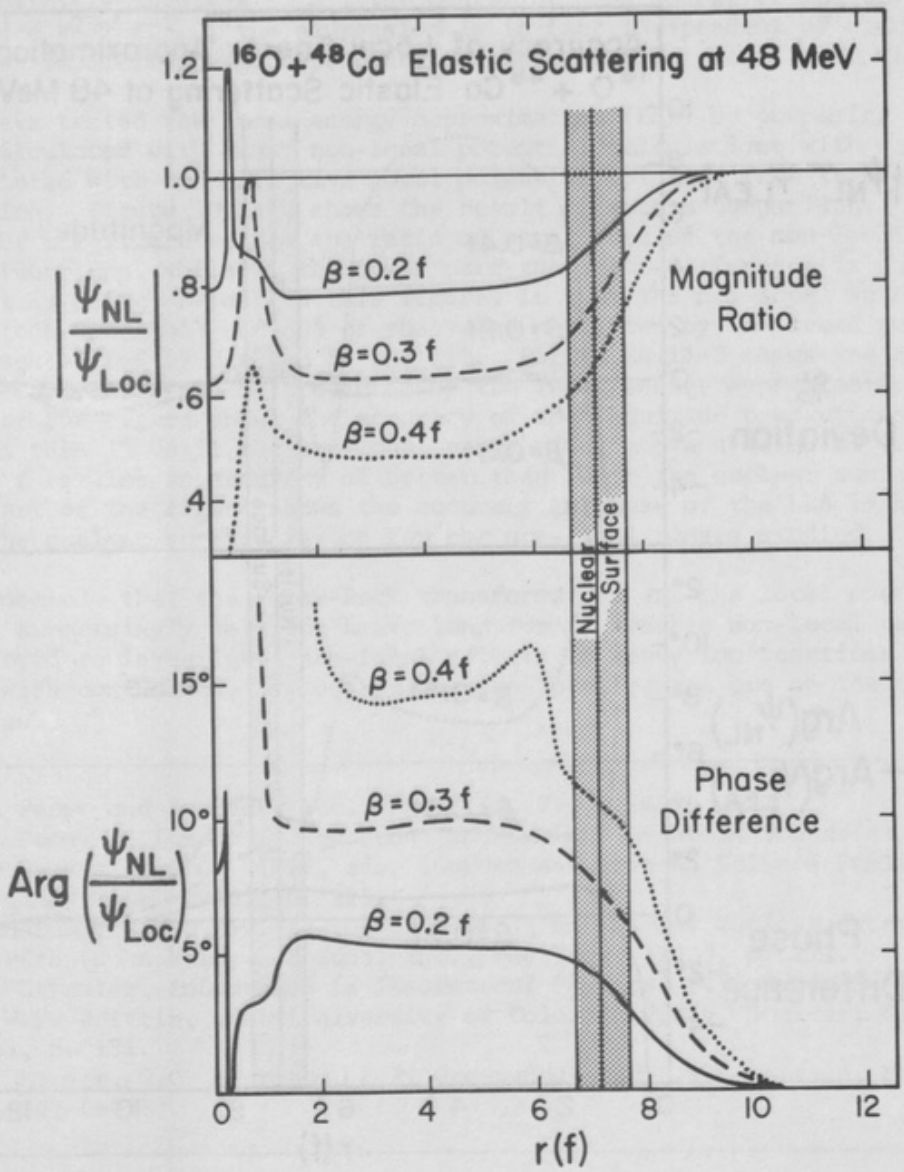

Fig. 10.11-2. Comparison of local and non-local wave functions for $^{16}O + ^{48}Ca$ scattering.

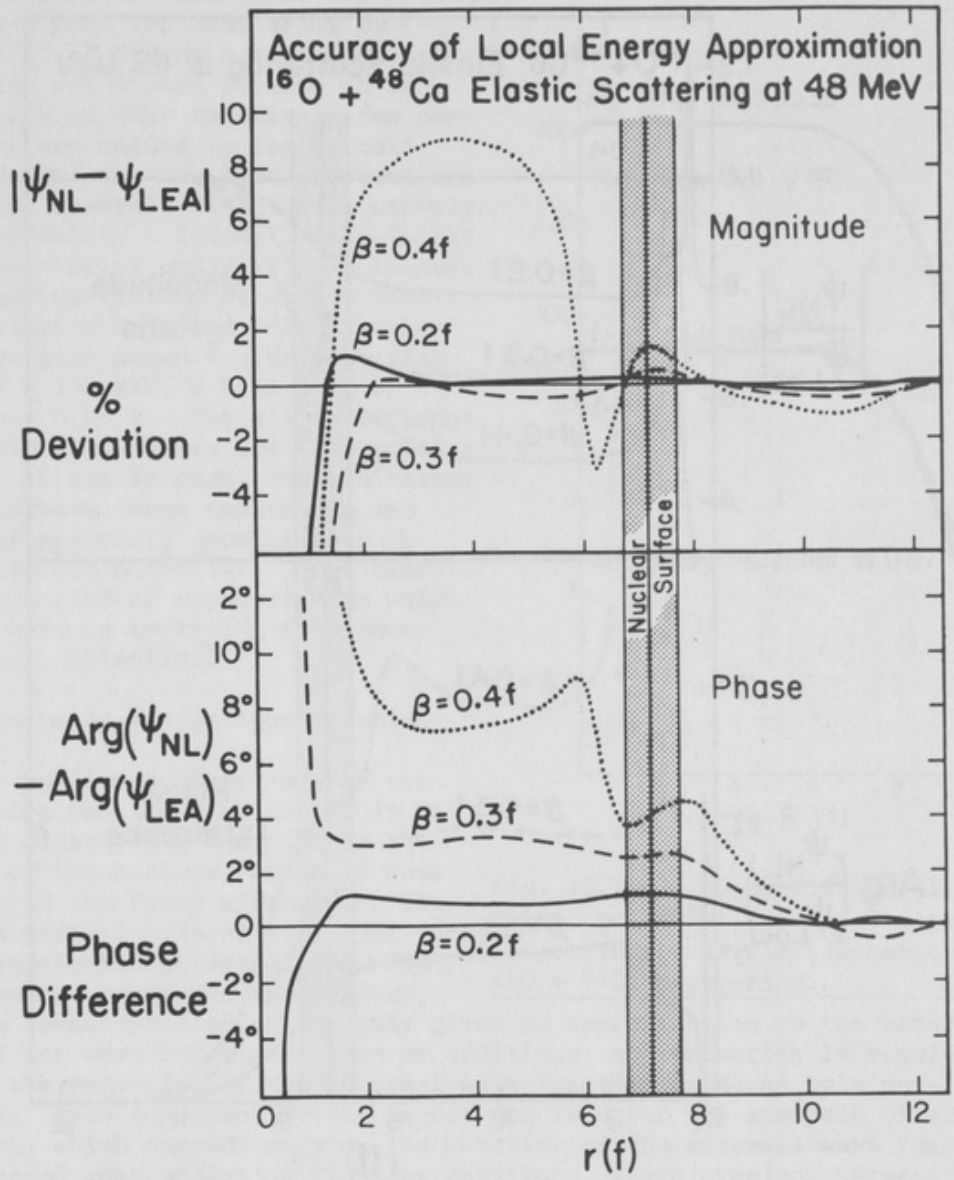

Fig. 10.11-3. Effectiveness of local energy approximation in simulating the non-local damping of the wave function.

since it explicitly involves $E_{c.m.}$, the center of mass energy of the system. However, since $k^2 \approx E_{c.m.}^{-1}$, the expression is in fact independent of energy, except for the implicit energy dependence of the equivalent local potential $V_L(r)$.

We have tested the local energy approximation (LEA) by comparing wave functions calculated with exact non-local potential calculations with wave functions calculated with the effective local potential obtained from the Perey-Buck Transformation. Figure 10.11-2 shows the result of such a comparison. In the upper part of the figure we see the ratio of magnitudes of the non-local and local wave functions, while in the lower part the phase difference is shown. The Perey Effect is quite obvious in this figure, in that the non-local wave function is reduced to between 80% and 50% of the value predicted by the local potential and its phase shifted by between 5° and 15°. Figure 10.11-3 shows the accuracy to which these effects can be predicted by the local energy approximation. The upper part of the figure shows the accuracy of the magnitude predictions of the LEA are less than 1% until the non-local range rises above a value of 0.3 f, and even at 0.4 f retains an accuracy of better than 5% in the nuclear surface region. The lower part of the figure shows the accuracy in phase of the LEA is between 1° and 5° in the nuclear surface region for the non-local ranges studied.

We conclude that the Perey-Buck transformation and the local energy approximation work surprisingly well for heavy ions for reasonable non-local ranges, and can be employed to investigate non-local effects in heavy ion reactions and scattering with confidence, as long as the non-local ranges are on the order of 0.4 f or less.

---

1. F.G. Perey and B. Buck, Nucl. Phys. *32*, 353 (1962).
2. F.G. Perey in *Direct Interactions and Nuclear Reaction Mechanisms*, E. Clemental and C. Villi, eds. (Gordon and Breach, Science Publications, Inc., New York, 1963), p. 125.
3. N. Austern, Phys. Rev. *137*, B752 (1965), and *Direct Nuclear Reaction Theories* (John Wiley and Sons, Inc., New York, 1970), p. 111.
4. G.R. Satchler, in*Lectures in Theoretical Physics*, P.D. Kunz, D.A. Lind, and W.E. Brittin, eds. (University of Colorado Press, Boulder, Colorado, 1966), p. 151.
5. H.J. Körner, G.C. Morrison, L.R. Greenwood, and R.H. Siemssen, Phys. Rev. C *1*, 107 (1973).

10.12 A New Form of Energy Dependence for Angular-Momentum Dependent Absorption

J.G. Cramer

Chatwin, Eck, and Robson[1] have suggested that the absorptive part of the heavy-ion nucleus optical potential should depend on angular momentum and should be reduced as the angular momentum of the system increases beyond some critical angular momentum value. Unfortunately, there is a problem in applying this concept to most physical situations, and that is that such angular momentum dependence is intrinsically energy dependent in a way that is not well understood.

Chatwin, Eck, and Robson have suggested an energy dependence of the form:

$\ell_c = k\bar{R}(1 + \bar{Q}/E_{c.m.})^{1/2}$ and $d\ell$ = constant, where k is the wave number, $E_{c.m.}$ is the center of mass energy of the system, $\bar{R}$ and $\bar{Q}$ are adjustable parameters, and ℓ_c and $d\ell$ are parameters defining the angular momentum dependence of the imaginary potential as:

$$W(r,\ell) = W(r)/(1 + \exp((\ell - \ell_c)/d\ell)).$$

Malmin[2] has suggested an alternative form for ℓ_c which is:

$$\ell_c = \ell_0 + k\bar{R}(1 - 2\eta/k\bar{R})^{1/2}$$

where ℓ_0 and $\bar{R}$ are adjustable parameters and $\eta = ZZ'e^2/hV$ is the Sommerfeld parameter. Both of these forms can be subsumed under the more general 3-parameter form:

$$\ell_c = \ell_0 + k\bar{R}(1 + \bar{Q}/E_{c.m.})^{1/2} \qquad (1)$$

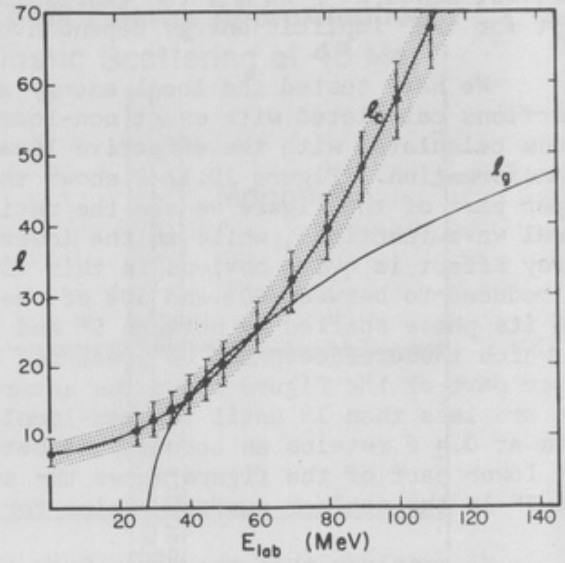

Fig. 10.12-1. Plot of grazing angular momentum ℓ_g and angular momentum cutoff ℓ_c for $^{16}O + ^{28}Si$.

which reduces to the Chatwin form with $\ell_0 = 0$ and to the Malmin form with $\bar{Q} = -E_{c.m.}(2\eta/k\bar{R}) = -ZZ'e^2/\bar{R}$. These forms were chosen by those authors so that the energy dependence of ℓ_c would resemble the energy dependent behavior of the grazing angular momentum ℓ_g in a heavy ion scattering. Figure 10.12-1 shows the grazing angular momentum ℓ_g for the case of $^{16}O + ^{28}Si$ scattering. As can be seen, it is roughly parabolic in ℓ with the axis of the parabola parallel to the energy axis.

In measurements of the elastic scattering of ^{16}O from ^{28}Si reported in Sec. 10.7, the angular distributions at bombarding energies of 50, 53, 55, and 66 MeV (lab) showed pronounced oscillations at cross sections below 10^{-2} of Rutherford. These oscillations proved to be quite intractible to optical model analysis with either 4-parameter or 6-parameter potentials. It was found, however, that the inclusion of angular momentum dependence in the imaginary potential greatly improved the agreement between the data and the calculations. An angular momentum diffuseness parameter $d\ell$ of about 2.8 seemed to provide good fits to the oscillations. Searches of individual data sets were performed, searching on ℓ_c while holding $d\ell$ fixed at 2.6, 2.8, and 3.0. The same values of ℓ_c were obtained in each set of searches, demonstrating that the two parameters $d\ell$ and ℓ_c are not strongly correlated.

The values of ℓ_c determined in this way (Fig. 10.12-1) showed a curvature which was opposite that of the grazing angular momentum. For this reason, they could not be reasonably fitted with the 3-parameter Chatwin-Malmin energy dependence expression given above, and it was necessary to find an alternative form to represent them. It appeared that what was needed was a form of energy dependence which was parabolic in energy rather than ℓ, and so an expression of the form

$\ell_c = A + BE_{c.m.} + CE_{c.m.}^2$ was fitted to the values of ℓ_c which had been determined. It was found that the B coefficient was nearly zero and could be eliminated. This led to a new 2-parameter form, which in analogy with the Chatwin-Malmin form,[1] is written $\ell_c = \ell_0 + (E_{c.m.}/\bar{Q})^2$. This expression was fitted to the values of ℓ_c determined previously, and this fit curve is shown in Fig. 10.12-1.

It was noted, on employing this form of ℓ_c and seeking a best value of $d\ell$, that the low energy data seemed to have a preference for lower values of $d\ell$ than did the high energy data. This suggested that $d\ell$ might be dependent on energy, or alternatively on the value of ℓ_c. Various functions of energy and ℓ_c were investigated, but the best ones seemed to be $d\ell = AE_{c.m.}$ or alternatively $d\ell = (\ell_c/\ell_1)^{1/2}$. We have elected to use the latter because of its implications of a statistical undertainty. Thus, the suggested forms of the angular momentum dependence parameters are:

$$\ell_c = \ell_0 + (E_{c.m.}/\bar{Q})^2 \quad \text{and} \quad d\ell = (\ell_c/\ell_1)^{1/2} \tag{2}$$

where ℓ_0, ℓ_1 and $\bar{Q}$ are adjustable parameters.

We have used these functions to obtain optimum fits to the $^{16}O + ^{28}Si$ data mentioned previously, keeping the other optical model parameters fixed and using those given in Sec. 10.7. Fits to these data with and without ℓ-dependent absorption are shown in Fig. 10.7-2. The parameters used for the ℓ-dependence are: $\ell_0 = 8.0$, $\bar{Q} = 9.45$ MeV, $\ell_1 = 2.0$. Such ℓ-dependent absorption has sometimes been observed to produce large cross sections near 180°. We have investigated the 180° predictions of the ℓ-dependent potentials employed in this analysis, and find predicted 180° elastic cross sections which are less than 5 μb/sr for all energies greater than 40 MeV.

---

1. R.A. Chatwin, J.S. Eck, and D. Robson, Phys. Rev. C *1*, 795 (1970).
2. R.E. Malmin, Ph.D. Thesis, Argonne Physics Division Imformal Report PHY-1972F (1972, unpublished).

---

11. RADIATIVE CAPTURE

11.1 Direct and Semi-Direct Electric Dipole and Quadrupole Radiative Capture of Protons

K.A. Snover and K. Ebisawa

In general, a good reaction theory for radiative proton capture in the region of and above the giant-dipole resonance is lacking. It is commonly the case that comparison between experiment and theory goes little beyond the point of comparing experimentally measured total cross sections (predominantly E1) with strength distributions calculated in a bound-state approximation. Some continuum calculations are available, mostly in light nuclei and done in the particle-hole approximation. However, these calculations are generally quite complicated and it is often difficult to gain physical insight into the qualitative reasons for differences in calculated vs measured quantities. Also, theorists who do these calculations are often unable to keep pace with the experimentalist who produces measurements in new nuclei and of new quantities such as analyzing powers with polarized protons.

The lack of a good reaction theory is a particularly serious drawback when it comes to understanding E2 strength observed in radiative capture. The E2 strength shows up predominantly in its interference with the E1 and it is necessary to understand the E1 amplitudes in order to extract the E2 strength. In a very limited number of special cases one can do this from information gained experimentally using polarized beams, but in general this is not possible. Thus a a model which can help limit the complexity of the problem could be enormously useful.

Initially we did some calculations of total cross sections for direct E2 capture, and angular distributions of direct E2 interfering with direct E1, and the results looked quite promising. It seemed most appropriate to look for a relatively simple theoretical approach which incorporates direct and resonance capture together in a natural way. The "semidirect" theory[1-4] of radiative nucleon capture has these features, and has been developed for the calculation of total cross sections for electric dipole capture through the Giant-Dipole Resonance (GDR). The theory has to date been applied[1-5] almost exclusively to the calculation of sizes and shapes of neutron and proton capture total cross sections, where it has met with reasonable success.

We have taken the "semidirect" theory of E1 capture and extended it to include direct (and collective) E2 and to calculate angular distributions of cross sections and analyzing power for radiative proton and neutron capture. As a first step, we have applied the theory to the $^{15}N(p,\gamma_0)^{16}O$ reaction where we find most of the essential features of the measurements are given correctly by the calculations.

The direct capture calculation is handled in a manner similar to Donnelly,[1] with 2 important differences. First, a fractional-parentage expansion of the final state is carried out at the beginning. Since the electromagnetic operator is a sum of 1-body operators, this immediately selects out those parts of the final state which have as parentage the target ground-state configuration plus a

nucleon. This simplifies considerably the angular momentum algebra. Secondly, the angular momentum algebra is reduced using standard Racah techniques, to yield an expression for the differential cross section in terms of a Legendre polynomial expansion in the angle of the emitted γ-ray. This expression involves the usual 3J and 6J symbols which come from contraction of angular momentum coupling coefficients, and the reaction matrix elements which are proportional to the radial matrix element

$$R^{d}_{\substack{\ell j \\ LJ\mathcal{L}}} \equiv \int_0^\infty \frac{\chi_{\ell j}(r) f_{\mathcal{L}}(r)}{r} \frac{U_{LJ}(r)}{r} r^2 dr$$

where $\chi_{\ell j}(r)$ is a scattering wave function calculated in the optical model, U_{LJ} $U_{LJ}(r)$ is a bound-state wave function, and $f_{\mathcal{L}}(r) = r^{\mathcal{L}}$ for electric capture of multiple order $\mathcal{L}$ (in the long-wave length approximation). The proportionality factor between R and the reaction matrix element (the S_t factor of Carr and Baglin[7]) involves statistical and phase space factors, angular momentum coupling factors involving L and J, the spectroscopic factor for the final state, and a phase factor $\exp(i\sigma_\ell)$ (σ_ℓ = Coulomb phase) corresponding to the proper asymptotic normalization of $\chi_{\ell j}(r)$.

Introduction of a collecting E1 resonance in the semidirect theory amounts to replacing the direct E1 radial matrix element R^d above by

$$R^d + \frac{\alpha \cdot R^c}{E - E_R + i\Gamma_R/2}$$

for $\mathcal{L} = 1$. The factor $\alpha \cdot R^c$ represents the collective resonance amplitude which comes from the product of formation and decay matrix elements

$$\langle \psi_i | \sum_{k\ell} v_1(\vec{r}_k - \vec{r}_\ell) | \psi_{coll} \rangle \langle \psi_{coll} | E1 | \psi_f \rangle$$

where $|\psi_i\rangle$ is the initial scattering state of target plus projectile, $|\psi_f\rangle$ is the final bound state of the residual nucleus, $|\psi_{coll}\rangle$ is the collective E1 resonance state and v_1 is the isospin-dependent part of the residual nucleon-nucleon interaction involving $\vec{\tau}_k \cdot \vec{\tau}_\ell$. Several different prescriptions are available for handling the collective E1 amplitude, all of which reduce the problem to the calculation of a collective radial matrix element R^c which is exactly the same as the expression for R^d given above except that one has a collective form factor $f^c(r)$ which replaces the direct term $f_{\mathcal{L}}(r) = r$ for E1. The factor α is related to the strength of v_1.

The form of $f^c(r)$ depends on the particular theoretical prescription. Four different prescriptions stand out.

(1) The simplest is that given by Brown[1] in the original paper on the subject. The residual interaction is taken to be of schematic form $v_1 = \vec{r}_i \cdot \vec{r}_j$ as in the schematic model for $|\psi_{coll}\rangle$. The result is $f^c(r) = r$, the same as the direct. In this case the total amplitude above may be written as

$$R^d(1 + \alpha/E - E_R + i\Gamma_R/2)$$

and α is given by just the upward energy shift ΔE in the collective state due to the interaction v_1. Although the schematic form of v_1 used here has a somewhat unrealistically long range, this approach has the advantage that it treats consistently the collective state and the residual interaction.

The other approaches all deal with v_1 in zero-range and treat $|\psi_{coll}\rangle$ differently: (2) Here one assumes $|\psi_{coll}\rangle \propto E1|\psi_f\rangle$ which leads to[3] $f^c(r) = r\rho_0(r)$ where $\rho_0(r)$ is the ground-state density. This result is similar to what is obtained with a hydrodynamic model of oscillating neutron and proton fluids within a fixed sphere (the "Jensen-Steinwedel" model).

(3) $|\psi_{coll}\rangle$ is determined[2] from the oscillation of rigid neutron and proton spheres, in which the deviation from sphericity occurs in the surface region (the "Goldhaber-Teller" model). Here $f^c(r) = -d\rho_0(r)/dr$. In (4) a harmonic-oscillator model for $|\psi_{coll}\rangle$ yields[4] $f^c(r) = r\rho_0(r) + \beta(-d\rho_0(r)/dr)$ where β is specified by the model ($\beta \simeq 2.2$ for ^{16}O). All of the above approaches assume a volume form for the isospin term in the optical potential. In (2) -(4) the form factor is surface peaked, although of somewhat different shape. In (1) only the tail of the bound state wave function cuts off the contribution of $f^c(r)$ at large r. All of the calculations include in addition to the direct term only the diagram which looks like

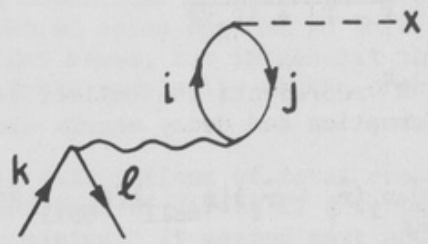

in which the project k annihilates the target hole ℓ creating a particle-hole excitation ij which annihilates by emitting a photon (a similar diagram obtains for closed-shell targets). Antisymmetry and exchange effects are essentially ignored. The effect of core-polarization is small in the resonance region, but may be significant[4] far away from resonance (this will be dealt with explicitly later on).

The form factor calculated in the zero-range approximations (2) -(4) is just the transition density for E1 decay of the collective state, which may also be obtained from microscopic calculations. The generalization to collective E2 states yields $\pm r^2$, $\pm r^2\rho_0(r)$ and $\pm(-d\rho_0(r)/dr)$ for the form factor in cases (1)-(3) above, with the + sign for an isovector excitation (in which case the strength parameter α involves v_1 as in the E1 case) and the - sign for isoscalar excitations, which involve the central interaction v_0.

Finally, one can show that for measurements with polarized protons the calculated coefficients of associated Legendre polynomials in the expansion of the analyzing power are simply related to the Legendre coefficients of the cross section. The calculated differential cross section involves terms of the sort $P_k \mathrm{Re} S_t S_{t'}^*$, where t and t' correspond to different reaction channels. If the beam is partially polarized, one cah show that the cross section is given exactly as before, except for replacing

$$P_k \mathrm{Re} S_t S_{t'}^* \rightarrow P_k \mathrm{Re} S_t S_{t'}^* + f \vec{P}\cdot\hat{n}\, P_k^1 \mathrm{Im}\, S_t S_{t'}^*,$$

where $\vec{P}$ is the polarization of the beam and $\hat{n}$ is a unit vector along $\vec{k}_p \times \vec{k}_\gamma$. The factor f is given by

$$f = [j'(j'+1) + \ell(\ell+1) - j(j+1) - \ell'(\ell'+1)]/k(k+1)$$

where j is the total angular momentum quantum number of the projectile. This factor seems to differ by an overall sign from a similar expression given by Devons and Goldfarb.[8] In particular, for the proton spin polarized perpendicular to the reaction plane, we may write

$$\sigma(\theta) = [\sigma\uparrow(\theta) + \sigma\downarrow(\theta)]/2 = A_0[1 + \sum_{i=1}^{4} a_i P_i(\cos\theta)]$$

and

$$[\sigma\uparrow(\theta) - \sigma\downarrow(\theta)]/2P = A_0 \sum_{i=1}^{4} b_i P_i^1(\cos\theta)$$

where P represents the polarization of the beam, and $\uparrow$ lies along the direction of $\hat{n}$. Here we have restricted one multipole order to be ≤ 2.

We chose the $^{15}N(p,\gamma_0)^{16}O$ reaction for a first test of the calculations primarily because of the extensive experimental measurements available, including detailed measurements[9] with polarized beam[10] from E_p = 8.7 to 15.7 MeV, and cross section measurements[11] up to 30 MeV. In Figs. 11.1-1 to 11.1-3 we display calculated vs experimental quantities for this reaction in and above the Giant-Dipole Resonance (GDR). The calculated quantities include direct and collective E1 strength (calculated in approximation (1) above) and direct E2 only. The calculations shown in the figures actually use a more exact form[1] for the radial dependence of the E1 and E2 operators which yields results differing by ~10% from the long-wave length approximation.

Now there are two possible (complex) reaction amplitudes for E1, which we label $s\cdot\exp(i\phi_s)$ and $d\cdot\exp(i\phi_d)$ and we compare calculated vs experimental values in Fig. 11.1-1. Here we have normalized $s^2 + d^2 = 1$ (the overall strength is not shown). Experimental values have been extracted from the published data by our analysis, and represent the "dominant d-wave" solution.[10] The calculation predicts d-wave dominance, but tends to underestimate the relative amount of s-wave amplitude. On the other hand, the relative phase agrees very well with experiment.

Since there is a mathematical ambiguity involved in extracting s, d and

$\phi_d - \phi_s$ from the experimental data, it is worthwhile comparing directly the calculated and measured a_2 and b_2 coefficients (shown in Figs. 11.1-2 and 11.1-3), which are dominated by E1. The a_2 is fit very well in the GDR region, while the b_2 is underestimated by about 30%, due to the underestimate of the s-wave amplitude.

Calculations of the E1 amplitudes for prescriptions (2) - (4) above all give very similar phase differences (within ±5° of 120°). The surface form factor (3) gives the same s-wave relative strength as case (1), s ≈ 0.29, case (2) yields s = 0.18 and case (4) yields s = 0.20. Thus among cases (2) - (4) the "surface" derivative form factor (3) works best, and gives a fit comparable to case (1). That the data yield significantly higher s values than any of these cases may indicate an explicit inadequacy in the calculation. Absolute strength factors α for each of the four cases are generally compatible with a strength of the isospin term in the optical potential of $v_1 \approx 100$ MeV, where we have chosen E_R and Γ empirically to give a reasonable fit to the gross structure in the total cross section.

Also shown in Fig. 11.1-1 are the results of a recent coupled channels calculation[12] which extends just into the lower side of the GDR. The results are very similar to those of the present calculation.

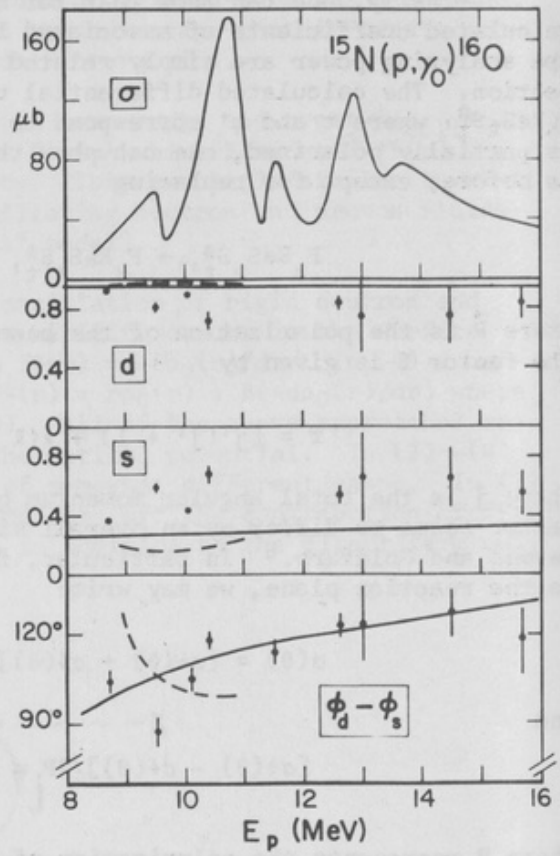

Fig. 11.1-1. The upper curve shows the measured total cross section for the $^{15}N(p,\gamma_0)$ reaction. The lower portions of the figure display measured (points) and calculated (solid curve) E1 reaction amplitudes s and d and the phase difference $\phi_d - \phi_s$. Dashed curves come from a coupled channel calculation (see text).

Of particular interest in Fig. 11-1.2 is the region above the GDR. Now the E1 calculation does not of course reproduce the structure in the GDR total cross section, now does it give exactly the tail at higher energies (probably due at least in part to the inadequacy of the Breit-Wigner approximation for the resonance energy denominator). In order to better understand the E2, we have empirically adjusted the calculated E1 amplitudes by a real energy dependent but channel independent normalization factor adjusted to give the correct total cross section (above $E_p = 16$ MeV this factor is within 20% of unity), and the curves shown in Figs. 11.1-2 and 11.1-3 contain this renormalization. The direct E2 cross section rises from 0.3 μb at 10 MeV to 0.8 μb at 20 MeV followed by a smooth decrease to 0.6 μb at 30 MeV, and its effect on the angular distribution is to

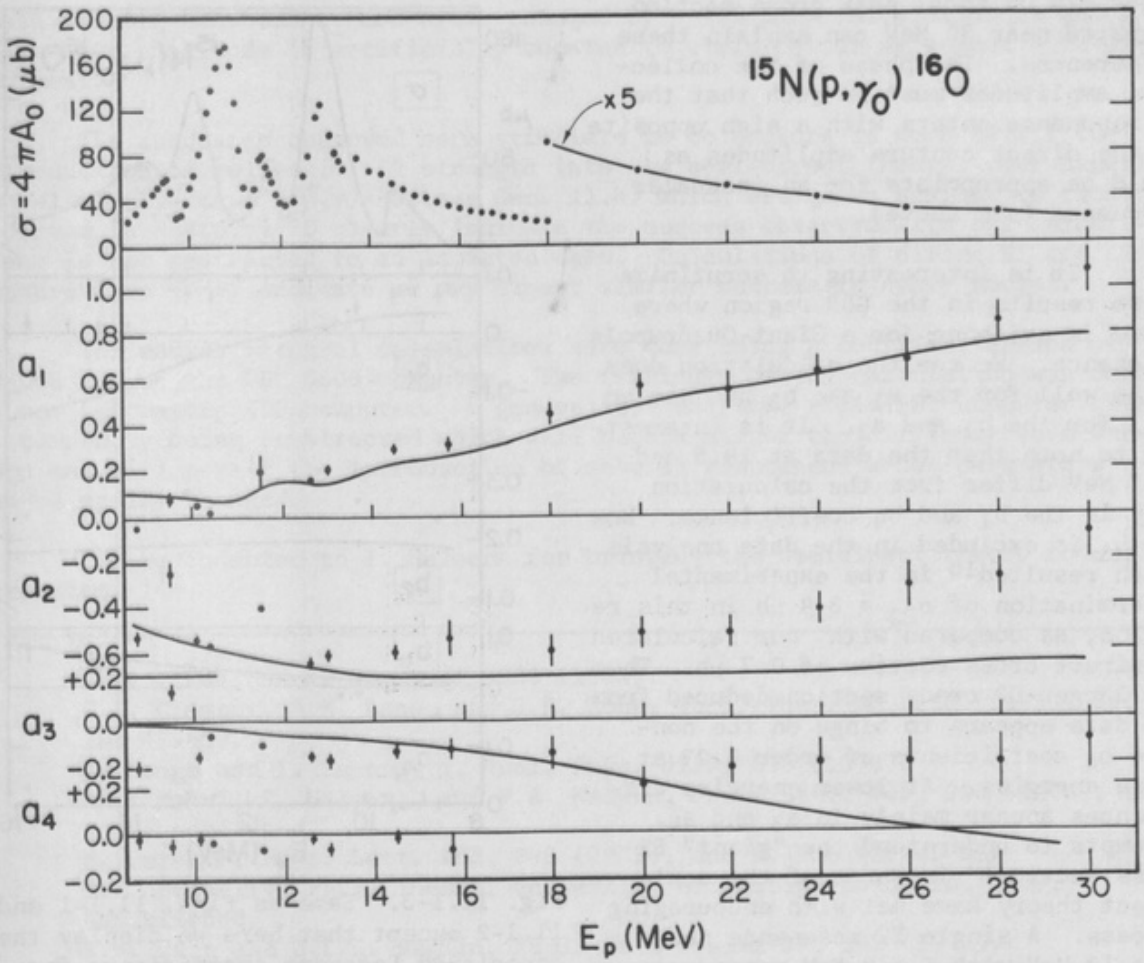

Fig. 11.1-2. Same as Fig. 11.1-1 except that here we display the measured (points) vs calculated Legendre coefficients for the cross section.

produce a large positive a_1 coefficient in agreement with experiment, and a large negative a_3 coefficient which is much bigger than the measured values at the higher energies. Thus direct E2 alone is more than sufficient to account for the size of the odd a_i above 15 MeV. The trend of a_2 toward zero from E_p = 22 to 30 MeV is not reproduced, although the calculated a_2 does become slightly less negative at large E_p due to the growing relative importance of E2 (about 15% of σ_{total} is due to E2 direct at 30 MeV). Thus for E_p = 22-30 MeV it is tempting to associate the discrepancies in the measured vs calculated a_2 and a_3 with the presence of collective E2 strength.

A rough estimate shows that one can resolve these discrepancies by the introduction of collective E2 strength at the higher energies which is about the same cross section as the direct. Specifically a broad (4-6 MeV) E2 resonance of

about 3/4 μb total peak cross section situated near 30 MeV can explain these differences. The phase of the collective amplitudes must be such that the E2 resonance enters with a sign opposite to the direct capture amplitudes as would be appropriate for an isoscalar resonance (see above).

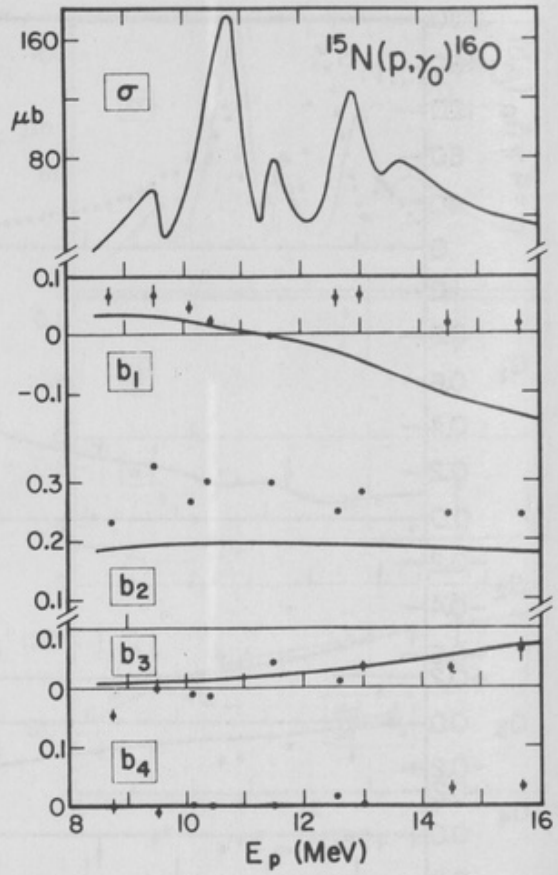

Fig. 11.1-3. Same as Figs. 11.1-1 and 11.1-2 except that here we display the associated Legendre coefficients for the analyzing power.

It is interesting to scrutinize these results in the GDR region where there is evidence for a Giant-Quadrupole Resonance. We see the calculation does quite well for the a_1 and b_3 but not so well for the b_1 and a_3. It is interesting to note that the data at 14.5 and 15.7 MeV differ from the calculation only in the b_1 and b_4 coefficients. Now the b_1 is excluded in the data analysis which resulted[10] in the experimental determination of σ_{E2} = 3-4 μb in this re region, as compared with our calculated E2 direct cross section of 0.7 μb. Thus the larger E2 cross section deduced from the data appears to hinge on the non-zero b_4 coefficients of order 0.03 at these energies. At lower energies differences appear mainly in a_3 and a_4. Attempts to understand the "giant" E2 cross section[10] in terms of the semi-direct theory have met with encouraging success. A single E2 resonance near E_p = 13 MeV with $\Gamma \sim 4$ MeV reproduces the cross section quite well using a strength factor that may be reasonable if the resonance is isoscalar. The p/f ratio, which is found experimentally to be of order unity, is calculated here to be ~0.2-0.4, depending on the form factor. The E2 resonance is more sensitive to the form factor than is the E1. For example, using $d\rho_0(r)/dr$ for the form factor, an increase of 0.5 fm in r_0 increases p/f to 0.6. The E1-E2 phase differences which can in principle yield valuable information about the resonance properties, including the isospin, are in our analysis of the data not sufficiently well-determined to allow information to be extracted. We will soon attempt fits to the a_i and b_i by varying the resonance parameters.

We should point out that a variety of checks have been made to insure that the results presented here are not strongly sensitive to small changes in parameters that are not well known. The above results were calculated using optical potentials determined[13] from p + ^{16}O elastic scattering -- they differ by $\lesssim$ 10% from calculations performed with the Watson[14] potentials. Long wave length approximations vs a more exact radial dependence for the $E\mathcal{L}$ operators has a similar

small effect. The odd a_i are again changed by $\lesssim$ 10% in a calculation in which the s-wave amplitude is artificially boosted to yield better agreement with experiment.

The successes observed here stimulate us to explore in more detail the introduction of collective E2 strength into the semi-direct theory. Our experimental results on $^{14}C(\vec{p},\gamma)^{15}N$ (see Sec. 11.4) which are quite similar to those observed in $^{15}N(p,\gamma)^{16}O$ clearly indicate the success observed with our calculations is not restricted to an isolated case. Calculations of direct E1 and E2 capture into ^{209}Bi indicate we may expect similar success in heavy nuclei.

The radial integral calculations were done using a modified version of ABACUS run on the CDC 6600 computer. The remainder of the calculation was done on our Laboratory XDS computer. A generalized and more efficient computer code is currently being constructed which will handle all of the different form factors and will permit the introduction of several resonances whose parameters can be easily changed.

We are indebted to I. Halpern for bringing the semidirect theory to our attention.

---

1. G.E. Brown, Nucl. Phys. *57*, 339 (1964).
2. C.F. Clement, A.M. Lane, and J.R. Rook, Nucl. Phys. *66*, 273 (1965); *66*, 293 (1965).
3. G. Longo and F. Saporetti, Nucl. Phys. *A199*, 530 (1973).
4. J. Zimanyi, I. Halpern, and V.A. Madsen, Phys. Lett. *33B*, 205 (1970), and to be published.
5. M. Potokar, Phys. Lett. *46B*, 346 (1973), and M. Potokan *et al.*
6. T.W. Donnelly, Ph.D. Thesis, University of British Columbia, 1969, unpublished.
7. R.W. Carr and J.E.E. Baglin, Nucl. Data Tables *10*, 143 (1971).
8. S. Devons and L.J.B. Goldfarb, *Handbuch der Physik*, Vol. 42 (Springer-Verlag, 1957) 362.
9. W.J. O'Connell, Ph.D. Thesis, Stanford University 1969, unpublished.
10. S.S. Hanna *et al.*, Phys. Rev. Lett. *32*, 114 (1974), and Conference on Nuclear Structure, Amsterdam, Sept. 1974, to be published.
11. P. Paul, K.A. Snover, and E.K. Warburton, Sec. 11.5 of this report, and to be published.
12. K. Ramaratarам, C.L. Rao and S. Ramaratarам, Phys. Rev. C *11*, 450 (1975).
13. B.M. Skwiersky, C.M. Baglin, and P.D. Parker, Phys. Rev. C *9*, 910 (1974).
14. B.A. Watson, Phys. Rev. *182*, 977 (1969).

11.2 Measurement of T-matrix Elements by (p,γ) Reactions with E1, M1 and E2 Radiation

J. Bussoletti

The form of the T-matrix describing the (p,γ) reaction is particularly simple for the two cases of: 1) a spin zero target and a spin 1/2 final state; and 2) a spin 1/2 target and a spin zero final state. For the particular case

of E1 and E2 radiation a $(\vec{p},\gamma)$ reaction is characterized by an angular distribution of the form:

$$Y(\theta) = c\, A_0[1 + \sum_{L=1}^{4} a_L P_L(\cos\theta) + \vec{p}\cdot\hat{n} \sum_{L=1}^{4} b_L P'_L(\cos\theta)].$$

$\hat{n}$ is a unit vector perpendicular to the scattering plane and $\vec{p}$ is the beam polarization. The angular distribution contains in general 9 independent coefficients while only 7 quantities are needed to specify the two complex amplitudes in the T-matrix for each of the two modes of decay.

If M1 radiation is also present, the angular distribution has the same complexity but the T matrix now requires eleven numbers to specify it. The $(\vec{p},\gamma)$ reaction does not provide sufficient information to determine the T-matrix elements. This unfortunately means that all analyses of $(\vec{p},\gamma)$ reactions are subject to the assumption that there is no M1 mode of decay. A consistency check can be made by omitting the a_1 and b_1 coefficients (those most sensitive to the presence of M1 amplitudes) from a matrix element determination and checking that the a_1 and b_1 parameters are well reproduced by the first. This is however only a sufficiency condition; in no way does it eliminate the possibility of the presence of M1 radiation. Moreover, admixtures of M1 radiation could well have a large effect on the size of the E2 cross section deduced from $(\vec{p},\gamma)$ measurements.

For these reasons, an inquiry into what measurements would constitute a determination of the T-matrix for the more complex case of E1, E2 and M1 radiation was made. It was hoped that by combining measurements of polarized proton capture with measurements of the plane polarization of gamma radiation following capture of an unpolarized proton would determine a large enough set of parameters to completely specify the T-matrix elements.

The angular distribution of plane polarized photons from a (p,γ) reaction with unpolarized protons was calculated from relations given in Devons and Goldfarb.[1] Assuming E2 is the highest multipolarity the angular distribution is given by

$$Y(\theta) = c\, A_0[1 + \sum_{L=1}^{4} a_L P_L(\cos\theta) + \varepsilon \cos 2\psi \sum_{L=2}^{4} c_L P_L^2(\cos\theta)$$

where ε is the analyzing efficiency of the plane polarimeter and ψ is an azimuthal angle about an axis defined by the outoing photon momentum.

There are a total of 12 coefficients thus determined, 5 a's, 4 b's, and 2 c's, but not all of them are independent since

$$c_4 = \frac{1}{4} a_4$$

$$c_3 = -\frac{1}{6} a_3.$$

Thus there are only 10 independent quantities in terms of which the matrix elements must be computed, leaving one matrix element parameter unspecified.

This means that in order to measure enough parameters one must measure the plane polarization of outgoing photons produced in the capture of a polarized proton. At this time this seems experimentally unfeasible.

1. S. Devons and L.J.B. Goldfarb, *Handbuch der Physik*, Vol. 42 (Springer-Verlag, 1957) 362.

11.3 A Survey of the $^{14}C(\alpha,\gamma_0)^{18}O$ Reaction

E.G. Adelberger, A.B. McDonald*, K. Ebisawa, and K.A. Snover

We have undertaken a survey of the $^{14}C(\alpha,\gamma_0)^{18}O$ reaction from E_α = 8.5 to 23.0 MeV (E_x = 13 to 24 MeV) with the main purpose of comparing these results with the detailed $^{12}C(\alpha,\gamma_0)^{16}O$ measurements made in this Laboratory.[1] The data were taken with a target consisting of about 340 μg/cm^2 of ^{14}C deposited upon a 3 mg/cm^2 gold backing. Data were taken with a $LiCO_3$-paraffin absorber between the target and the γ-ray spectrometer to suppress the strong background from the $^{14}C(\alpha,n)^{17}O$ reaction. The yield was measured at θ_γ = 130°, an angle where both E1 and E2 radiation contribute, and where the neutron background was relatively low. The buildup of carbon on the target was monitored during the course of the run and was found to contribute a negligible amount to the measured γ_0 yield except in the region 18.2-19.0 MeV where a correction was applied to the data. The

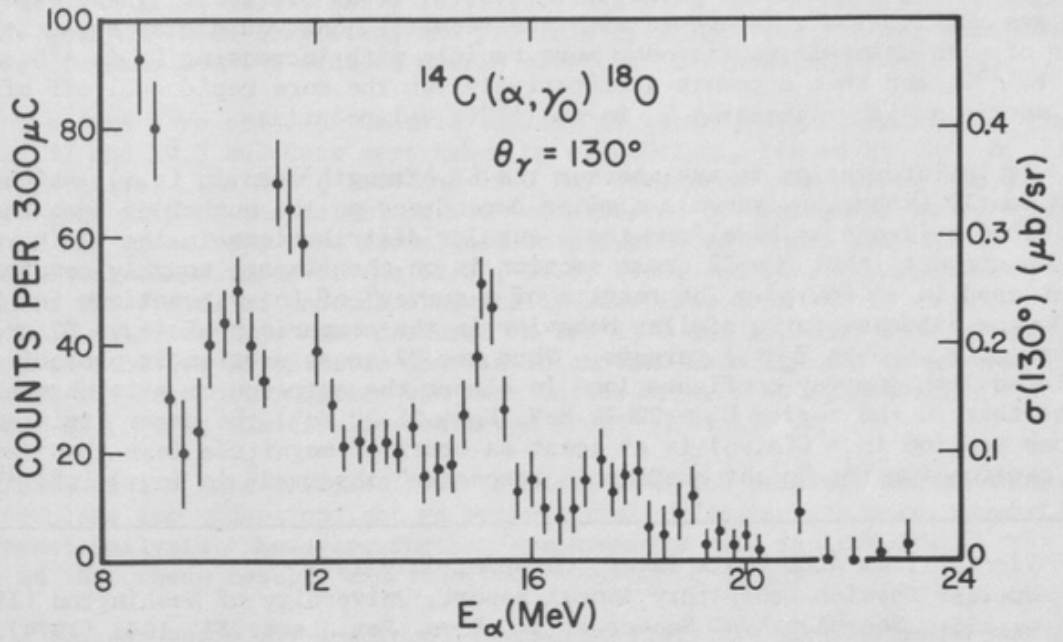

Fig. 11.3-1. Excitation curve for $^{14}C(\alpha,\gamma_0)^{18}O$ at θ_γ = 130°. The absolute cross section scale on the right is accurate to ±40%.

resulting yield curve is shown in Fig. 11.3-1. The absolute cross section scale was determined approximately by comparison to $^{12}C(\alpha,\gamma_0)^{16}O$, using the nominal ^{14}C target thickness quoted above, and is believed to be accurate within ±40%. Angular distributions measured at E_α = 8.85, 15.1 and 18.0 MeV indicate the radiation is predominantly E1, with ∿10-20% E2 contribution.

One of the most striking features of these data is the absence of any measurable yield in the Giant-Dipole Resonance region (E_x = 21-24 MeV, E_α = 19-23 MeV), in spite of the fact that population of the T=1 component of the GDR is isospin allowed. The cross section here is ≲ .03 μb/sr (at 130°), compared to typical (p,γ) GDR cross sections of ∿6 μb/sr at a comparable angle, indicating a strong nuclear structure inhibition of α-decay of the GDR. This is consistent with (α,γ) measurements in the 2s1d shell which do not show a GDR shape, and have been interpreted as proceeding ∿100% by compound nucleus formation (which should be relatively unimportant in the case of ^{18}O). In fact, the suggestion of Ref. 3 that a significant non-statistical contribution to GDR α-decay may exist (in $^{60}Ni(\alpha,\gamma_0)^{56}Fe$) is not supported by the present results. Thus the absence of the GDR in $^{12}C(\alpha,\gamma_0)^{16}O$ is probably not governed much by its isospin purity.

The average cross section for $^{14}C(\alpha,\gamma_0)$ for E_α = 10-20 MeV is about a factor of 3 bigger than for $^{12}C(\alpha,\gamma_0)$, and falls faster with increasing E_α, becoming smaller than the ^{12}C cross section for E_α = 19-23 MeV. For these "compound" resonances with $J^\pi = 1^-$ and T = 1, one would expect the α-partial widths to be much larger in $^{14}C(\alpha,\gamma_0)$ compared with $^{12}C(\alpha,\gamma_0)$ since only the former reaction is isospin allowed. However the number of open channels at a given α-energy is significantly greater in ^{18}O compared to ^{16}O, and this will act to increase the resonance total widths and depress the $^{14}C(\alpha,\gamma_0)$ cross sections. These expectations are qualitatively in accord with the results. One would also expect the number of open channels to increase more rapidly with increasing E_α in ^{18}O compared to ^{16}O, and this accounts qualitatively for the more rapid fall off of cross sections with increasing E_α in the $^{14}C(\alpha,\gamma_0)$ reaction.

It is interesting to ask whether the E2 strength seen in (α,γ), which is predominantly isoscalar, shows a similar dependence on the number of open channels. The limited evidence we have from the 3 angular distributions in the $^{14}C(\alpha,\gamma_0)$ reaction suggests that the E2 cross section is on the average roughly comparable to that seen in $^{12}C(\alpha,\gamma_0)$. The results of a survey[4] of (α,γ) reactions for 24 ≤ A ≤ 60 show evidence for a similar behavior in the comparison of (α,γ) E2 cross sections on T_z = 0 vs T_z = 1 targets. Thus the E2 cross section is probably associated with doorway configurations in either the entrance or exit channels. We note that in the region E_x ∿ 22-24 MeV (E_α ∿ 21-23 MeV) the upper limit on the E2 cross section in $^{14}C(\alpha,\gamma_0)$ is at least an order of magnitude less than the cross section for the "giant quadrupole resonance" observed[5] in (p,γ) into ^{16}O.

---

* Visitor from AECL Chalk River, Ontario, July 1974.

1. Nuclear Physics Laboratory Annual Report, University of Washington (1974), p. 135. See also K.A. Snover *et al.*, Phys. Rev. Lett. *32*, 1061 (1974).
2. L. Meyer-Schutzmeister, Z. Vager, R.E. Segal, and P.P. Singh, Nucl. Phys. *A108*, 180 (1968); G.S. Foote, D. Branford, D.C. Weisser, N. Shikazono and F.C.P. Huang, J. Phys. A *7*, 64 (1974).

3. G.S. Foote, D. Branford, R.A.I. Bell, and R.B. Watson, Nucl. Phys. , 505 (1974).
4. S.S. Hanna, contribution to Amsterdam Conference on Nuclear Spectroscopy, Amsterdam, 1974.
5. S.S. Hanna *et al.*, Phys. Rev. Lett. *32*,114 (1974).

11.4 The $^{14}C(\vec{p},\gamma)$ Reaction through the Giant Dipole Resonance at ^{15}N

E.G. Adelberger, J.E. Bussoletti, K. Ebisawa, A.D. McDonald, K.A. Snover, and T.A. Trainor

There is a great deal of interest presently in searching for giant quadrupole resonances in nuclei, in analogy with the giant dipole state. Resonances of the E2 mode have been found in certain nuclei, but the systematics of these structures are not yet sufficiently well established to indicate that the structure is as general a property of nuclear forces as the giant dipole resonance is. The main difficulty in studying these high-lying resonances is the problem of obtaining a unique multipolarity decomposition of the observed structures. One fruitful approach has been the use of reactions with a photon in one of the entrance or exit channels to limit the multipolarity. Even here, the multipoles can be separated only in a few cases, one of which is the reaction $(\vec{p},\gamma)$ on a target with spin 0 leading to a final state with spin 1/2. (See however Sec. 11.2 of this report.)

We are presently investigating the reaction $^{14}C(\vec{p},\gamma)^{15}N$. Measurements of angular distributions of both cross section and analyzing power have been completed at E_p = 11.0, 12.37, 13.7, 14.5, 15.4 and 16.3 MeV; a preliminary analysis of these data has been completed, and preliminary values for the Legendre expansion coefficients and the deduced matrix elements have been obtained.

The data were obtained under a variety of experimental conditions. The 11.0, 12.37 and 13.7 MeV data were taken by sequentially recording data in each spin orientation. The 14.5, 15.4 and 16.3 MeV data were taken using the device for fast spin flip of the polarized beam constructed by H. Swanson *et al.*[1] The yields of the gamma rays were normalized to accumulated charge for the 11.0 and 13.7 MeV data, while those of the 12.37, 14.5, 15.4, and 16.3 MeV runs were normalized to the yields of protons elastically scattered from ^{14}C to an angle of 160°. Beam polarizations were measured in the 11.0 and 13.7 MeV runs by switching the beam to a helium polarimeter located in another beam line; a continuous monitor at the beam polarization was made in the other runs by measuring the asymmetry of protons elastically scattered from ^{14}C at 160°.

Some of the data suffered from problems with the particle normalizations. These problems are understood and we believe their effects have been removed by our present analysis. However, further measurements will include checks to assure us that these results are free from systematic errors.

A typical gamma ray spectrum is shown in Fig. 11.4-1. The gamma ray yields were analyzed by the procedure explained in Sec. 4.6 of this report. Angular distributions consisted of measurements of gamma ray yields at angles of 43°, 55°,

75°, 90°, 110°, 125° and 137° with respect to the beam direction.

In Table 11.4-1 and Fig. 11.4-2 the extracted Legendre polynomial coefficients are presented for both the cross section and analyzing power (see Sec. 11.1 for definitions). The non-zero a_3 and b_3 coefficients establishes unambiguously the presence of E2 radiation. The variations in the a_2 and b_2 coefficients indicates significant structure in the E1 amplitudes as well.

The reaction process for E1 and E2 capture is completely specified in this case by four complex reaction amplitudes: $s_{1/2}$ and $d_{3/2}$ for E1 capture and $p_{3/2}$ and $f_{5/2}$ amplitudes for E2 capture. These matrix elements were extracted by performing a χ^2 fit to the extracted Legendre coefficients. All nine coefficients were used to obtain the seven parameter matrix element fit; reasonable χ^2 were obtained assuming no M1 radiation was present.

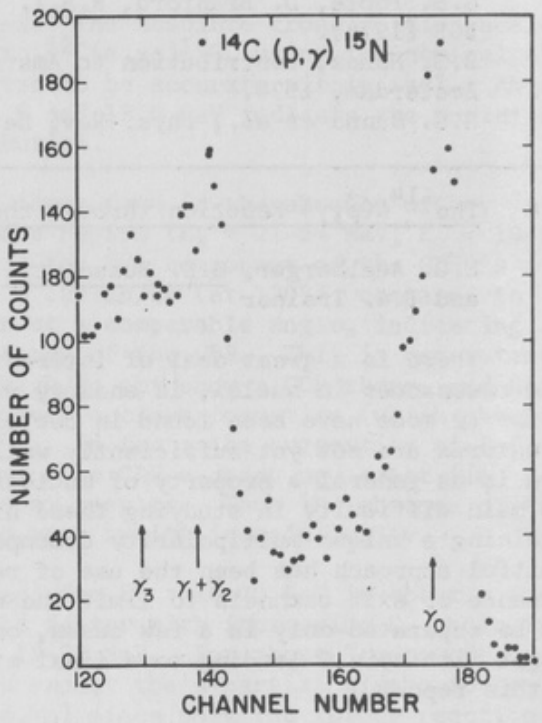

Fig. 11.4-1. Gamma ray spectrum from the $^{14}C(p,\gamma)^{15}N$ reaction at E_p = 16.3 MeV, θ = 75°, spin ↑.

In Table 11.4-2 we listed the matrix elements we obtain from the fit. The errors on the matrix elements do not include the covariance terms of the Legendre fit; these can have a serious effect on the magnitude of the errors as our Legendre fit coefficients are strongly correlated. The errors listed in the table are based on the statistical variance of the Legendre coefficients; a more detailed error analysis is in progress. Two solutions have been obtained at each energy for the matrix element fit; one corresponds to mostly s-wave and the other to mostly d-wave E1 capture. Because of the non-linearity of the equations defining the matrix elements, there may be other solutions for the matrix elements, though a cursory search has not revealed any others for the 9-equation fits.

We compare in Fig. 11.4-3 the 90° cross section obtained by M. Harakeh *et al.*[2] with the partial wave contributions to the cross section. In the following we will discuss only solution 1 (essentially all theoretical models predict d-wave dominance in the GDR); the conclusions are essentially the same for solution 2 if we interchange s and d. We assume no crossing of solutions as a function of energy. The structures of 11.0 and 13.7 MeV are associated with an increase in the d-wave amplitude and are thus to be identified as j = 3/2 structures. The plateau at 14.5 MeV arises from an increase in the s-wave amplitude and thus indicates a J = 1/2 structure. At 12.37 MeV we see a slight change in the relative contributions of the two partial cross sections and at 16.3 MeV the peak seems to be due to an increase in both the s-wave and d-wave cross sections. This

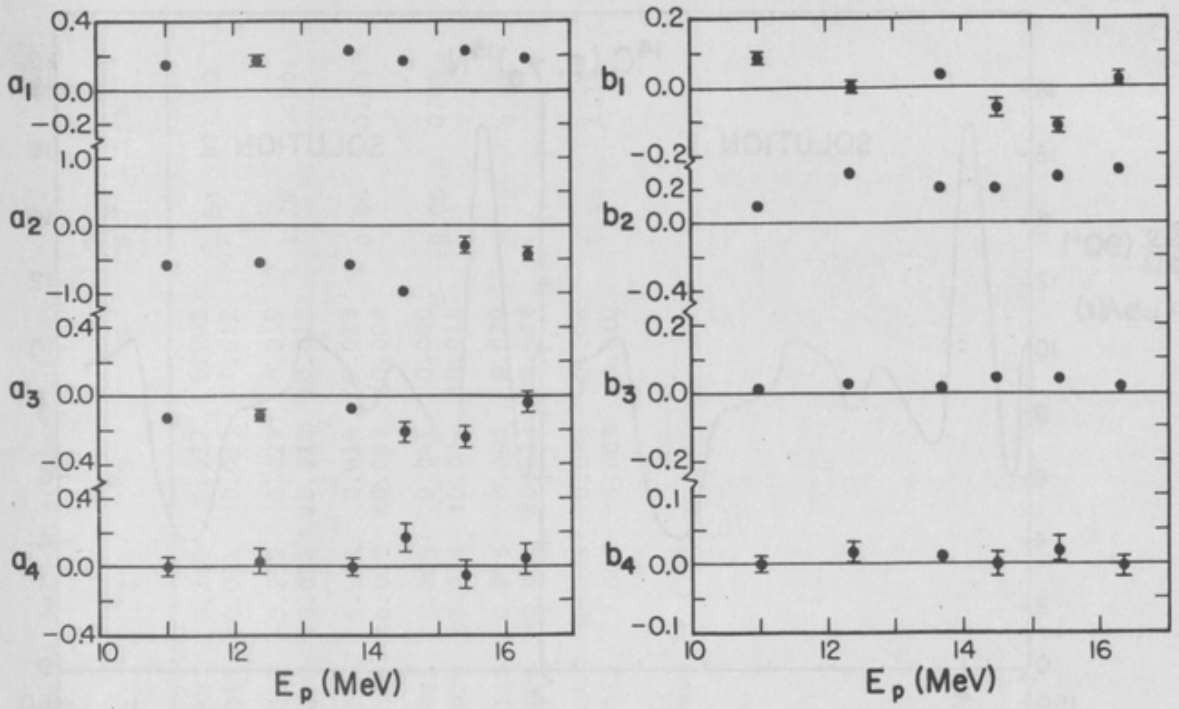

Fig. 11.4-2. Legendre polynomial expansion coefficients of the cross section and analyzing power as a function of energy for the $^{14}C(p,\gamma)^{15}N$ reaction.

illustrates the power of the measurement with polarized protons in separating out the contributions to the reaction process of different electric multipoles and of different spin components of each multipole. The assumption of no crossing of solutions is subject to experimental verification -- this will require measurements in finer energy steps. It is interesting to note that the average percentage of s^2 in E1 capture over this energy range is quite large, $\gtrsim$ 1/5. This may be compared to the result of recent 2h-1p calculations[2] of the GDR absorption strength which indicate 1/3 of the total dipole strength built on the $1/2^-$ ground state of ^{15}N is spin $1/2^+$ (the rest is $3/2^+$). However, it must be noted that most of the $1/2^+$ strength calculated in Ref. 2 must be due to configurations of the sort $[dp^{-2}]_{J=1/2}$, which will not have a simple overlap with the ^{14}C ground state plus a proton. On the other hand, these configurations are just the sort that will couple to the proton channel via the isovector particle hole interaction between the proton projectile and the target nucleons such as is treated macroscopically in the model calculations of Sec. 11.1, and it may well be that this latter effect is the dominant one. There is also the interesting feature in the data that the average percentage of s^2 in the cross section increases significantly at the higher energies. Although this is getting into the region where T = 3/2 strength is expected to be predominant, there is no indication from the Harakeh calculations that the fraction of spin 1/2 strength is different for the T = 3/2 and T = 1/2 components. It will also require more data to make sure that this effect is not due just to local structure.

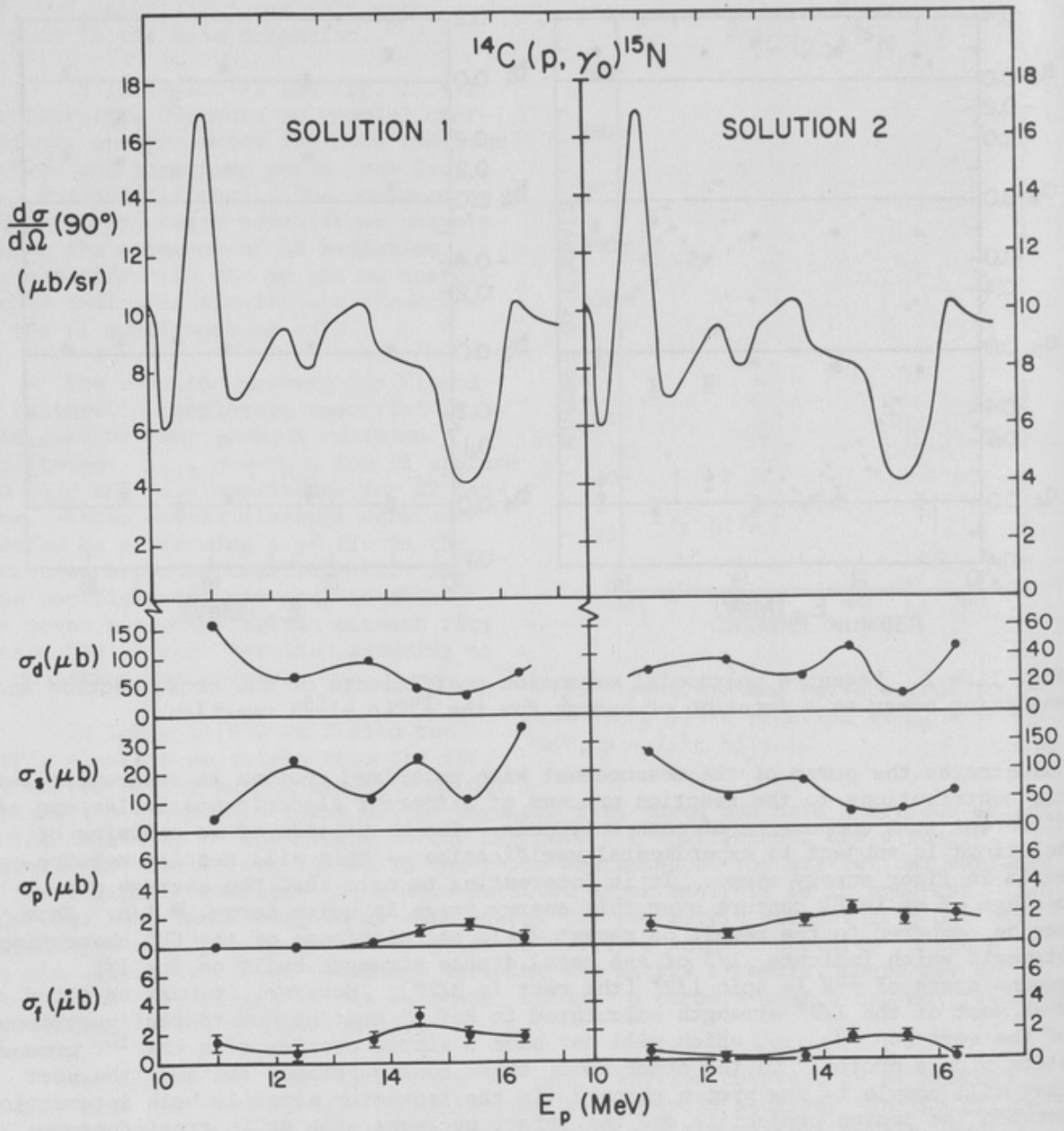

Fig. 11.4-3. Top section: The 90° cross section for the $^{14}C(p,\gamma_0)^{15}N$ reaction (Ref. 2). Bottom section: Partial cross sections for s- and d-wave (E1) capture, and p- and f-wave (E2) capture, as determined from the present measurements.

Table 11.4-1. $^{14}C(\vec{p},\gamma)^{15}N$ Angular Distribution Coefficients

E_p	$4\pi A_0(\mu b)$	a_1	a_2	a_3	a_4	b_1	b_2	b_3	b_4	$\chi^2_N(a)$	$\chi^2_N(b)$
11.0	165.	0.148 ±0.017	-0.587 ±0.048	-0.128 ±0.030	-0.003 ±0.045	0.083 ±0.015	0.102 ±0.011	0.012 ±0.010	0.001 ±0.012	0.64	1.20
12.37	91.	0.184 ±0.022	-0.559 ±0.066	-0.115 ±0.043	0.030 ±0.063	0.006 ±0.019	0.292 ±0.013	0.028 ±0.012	0.018 ±0.015	1.10	1.06
13.70	108.	0.230 ±0.016	-0.557 ±0.049	-0.067 ±0.032	0.003 ±0.047	0.033 ±0.010	0.201 ±0.007	0.019 ±0.007	0.013 ±0.008	0.80	0.83
14.50	69.	0.168 ±0.028	0.956 ±0.088	-0.210 ±0.066	0.179 ±0.084	-0.065 ±0.024	0.204 ±0.013	0.041 ±0.014	0.000 ±0.018	0.06	0.45
15.40	45.	0.215 ±0.041	-0.290 ±0.100	-0.237 ±0.078	-0.053 ±0.088	-0.115 ±0.020	0.275 ±0.015	0.046 ±0.013	0.020 ±0.018	0.03	0.85
16.30	111.	0.237 ±0.018	-0.310 ±0.051	-0.067 ±0.036	0.035 ±0.050	0.044 ±0.013	0.279 ±0.008	0.028 ±0.009	-0.006 ±0.010	1.48	1.13

(a) Chi-squared for fit to yield angular distribution: $Y\uparrow + Y\downarrow$
(b) Chi-squared for fit to analyzing power: $Y\uparrow - Y\downarrow$

Table 11.4-2. Matrix elements from Legendre polynomial fit to $^{14}C(\vec{p},\gamma_0)$ angular distribution.

Solution 1

E_p	s	p	d	f	$\phi_p-\phi_s$	$\phi_d-\phi_s$	$\phi_f-\phi_s$	χ^2_N
11.0	0.168 ±0.024	0.033 ±0.018	0.981 ±0.080	0.096 ±0.016	- 6 ±37	119 ±11	176 ±16	0.036
12.37	0.513 ±0.061	0.019 ±0.055	0.854 ±0.043	0.085 ±0.043	62 ±183	109 ±8	126 ±41	0.809
13.7	0.320 ±0.021	0.054 ±0.025	0.938 ±0.012	0.118 ±0.015	96 ±18	108 ±7	134 ±11	0.878
14.5	0.606 ±0.057	0.121 ±0.057	0.824 ±0.048	0.213 ±0.068	-91 ±42	145 ±14	77 ±19	2.518
15.4	0.473 ±0.052	0.179 ±0.069	0.841 ±0.058	0.202 ±0.065	-86 ±10	88 ±8	18 ±9	0.240
16.3	0.452 ±0.018	0.047 ±0.031	0.881 ±0.015	0.127 ±0.018	93 ±25	83 ±5	110 ±12	0.438

Solution 2

E_p	s	p	d	f	$\phi_p-\phi_s$	$\phi_d-\phi_s$	$\phi_f-\phi_s$	χ^2_N
11.0	0.899 ±0.018	0.087 ±0.015	0.427 ±0.033	0.052 ±0.019	-61 ±8	158 ±3	121 ±21	0.035
12.37	0.766 ±0.063	0.085 ±0.054	0.637 ±0.068	0.019 ±0.051	-27 ±33	122 ±4	88 ±182	0.808
13.7	0.854 ±0.024	0.124 ±0.019	0.496 ±0.034	0.037 ±0.023	-30 ±6	138 ±2	-332 ±27	0.878
14.5	0.625 ±0.057	0.186 ±0.058	0.808 ±0.049	0.159 ±0.067	56 ±24	146 ±3	232 ±26	2.461
15.4	0.815 ±0.070	0.192 ±0.059	0.517 ±0.062	0.189 ±0.069	69 ±12	109 ±2	174 ±13	0.243
16.3	0.863 ±0.020	0.133 ±0.022	0.487 ±0.025	0.022 ±0.030	-36 ±8	110 ±4	182 ±56	0.438

These results bear a rather close quantitative similarity with those obtained[3] in the $^{15}N(p,\gamma_0)^{16}O$ reaction, at least for the E1 amplitudes, indicating that, although the shape of the total cross section is quite different, the relative properties (s/d and $\phi_d - \phi_s$) are quite similar. This similarity should follow quite naturally in the semi-direct calculations where the only differences in the 2 cases come from changes in reaction matrix elements due to small differences in potentials and binding energies (we are now in the process of making such calculations).

The E2 cross section shows a gradual increase from 11.0 MeV to 15.4 MeV and begins to decrease at 16.3 MeV. At the higher energies the cross section is quite a bit larger than that calculated for direct E2 capture (1-1.5 μb), and hence indicates a significant presence at collective E2 strength. In order to establish the decrease in the E2 strength additional measurements at higher energies will be undertaken.

1. Nuclear Physics Laboratory Annual Report, University of Washington (1974), p.
2. M. Harakeh, Ph.D. Thesis, SUNY, Stony Brook, N.Y., 1974, unpublished.
3. S.S. Hanna *et al.*, Phys. Rev. Lett. *32*, 114 (1974).

11.5 The $^{15}N(p,\gamma_0)^{16}O$ Reaction above the Giant-Dipole Resonance

P. Paul†, K.A. Snover, and E.K. Warburton††

We report here the results of measurements of radiative proton capture into ^{16}O made at Brookhaven National Laboratory. The measurements were made from E_p = 18 to 30 MeV (corresponding to E_x = 29 to 40 MeV) using the proton beam from the Brookhaven Double Emperor facility and detecting the capture γ-rays in a large NaI spectrometer. The target consisted of a cylindrical gas cell 30 cm long, with Kapton entrance and exit foils. The γ-detector was collimated so that it could not see γ-rays produced in the entrance and exit foils. Angular distributions were measured in steps of 2 MeV, and consisted of 4 or 5 points between the angles of 45° and 135°. Measured angular distributions were corrected for extended geometry effects and fit to a Legendre polynomial expansion with $\ell_{max} = 3$. The statistical accuracy and angular range of the data were not sufficient to determine an a_4 coefficient.

The results are shown in Fig. 11.2-2 of Sec. 11.2 of this report. The data below E_p = 18 MeV are taken from Refs. 1 and 2, and the data above 18 MeV constitute the present results. Most notable is the smooth behavior of the angular distribution coefficients with increasing E_p, and the smooth decrease in the total cross section. Thus there is no evidence in these data for resonance structure in either the E1 or E2 amplitudes in this energy range. Several calculations[3] which predict an isoscalar E2 resonance near $E_x \approx 22$ MeV, in the region where a large amount of strength is seen[2] in (p,γ), predict a concentration of isovector strength in the E_x = 30-35 MeV region, in contrast with the present results. However, the calculations of Kuo and Osnes[4] illustrate the large differences in predicted collective energies obtained using harmonic oscillator single-particle energies (2 hω = 28 MeV) as compared with empirical single particle (s.p.) energies. The empirical s.p. energies are significantly greater

than the harmonic oscillator values -- for example, the unperturbed $0f_{7/2}\ 1p_{3/2}^{-1}$ is ∿37 MeV based on empirical s.p. energies.[4] The net effect of the higher s.p. energies in the calculations of Ref. 4 is to shift the isovector collective strength up into the E_x = 40-50 MeV region and to spread it out. However, in the process the isoscalar E2 strength gets shifted to ∿30 MeV and remains concentrated. Thus the theoretical expectations for the presence or absence of E2 resonance strength in this energy range are still not clear.

In Sec. 11.1 these data are discussed in light of model calculations including direct E2, where it is found that the introduction of a modest amount of collective E2 strength at the highest energies (in addition to the direct E2) is sufficient to explain the data.

Finally it is worth noting that similar measurements[5] of (p,γ) made on ^{11}B and ^{14}N targets bear a striking quantitative similarity to the results presented here for $^{15}N(p,\gamma)^{16}O$.

---

† Permanent address: State University of New York at Stony Brook.
†† Permanent address: Brookhaven National Laboratory, Upton, L.I., N.Y.

1. W.J. O'Connell, Ph.D. Thesis, Stanford University, 1967, unpublished.
2. S.S. Hanna *et al.*, Phys. Rev. Lett. *32*, 114 (1974).
3. S. Krewald and J. Speth, Phys. Lett. *52B*, 295 (1974); S. Krewald, Amand Faessler and J. Speth, preprint.
4. T.T.S. Kuo and E. Osnes, Nucl. Phys. *A205*, 1 (1973).
5. P. Paul, K.A. Snover and E.K. Warburton, to be published.

11.6 Radiative Proton Capture on ^{205}Tl

K. Ebisawa, K.A. Snover, and J. Bussoletti

In the last few years several experimental observations of broad collective resonances associated with electromagnetic-multipoles have been reported. Among them, collective E2 resonances have been investigated in inelastic scattering of electrons,[1] protons,[2] Helium-3 and Helium-4,[3] and in radiative proton capture.[4] However, very little evidence has been found for the Isovector Giant Quadrupole Resonance (GQR) above the Giant Dipole Resonance (GDR) which is expected at an excitation energy of about 120-130 $A^{-1/3}$ MeV.[5] It is important to search for the GQR systematically in a wide range of nuclei since, if it exists, it should be expected to be a general feature of nuclei.

The present report is part of the continuing study of the isovector GQR by radiative proton capture.[6] Here we present results of a study of the reaction $^{205}Tl(p,\gamma)^{206}Pb$. If we consider the capture gamma rays to the ground state of ^{206}Pb to be either electric dipole or electric quadrupole, the angular distribution of these gamma rays can be written

$$W(\theta) = \sum_{i=0}^{4} A_i P_i(\cos\theta)$$

where

$$A_0 = (p_{1/2})^2 + (p_{3/2})^2 + (d_{3/2})^2 + (d_{5/2})^2$$

$$A_1 = 2.449(p^*_{1/2}\, d_{3/2}) + 2.546(p^*_{3/2}\, d_{5/2}) + 0.346(p^*_{3/2}\, d_{3/2})$$

$$A_2 = -0.5(p_{3/2})^2 + 0.5(d_{3/2})^2 + 0.571(d_{5/2})^2 - 1.414(p^*_{1/2}\, p_{3/2}) + 0.350(d^*_{3/2}\, d_{5/2})$$

$$A_3 = -1.131(p^*_{3/2}\, d_{5/2}) - 2.0(p^*_{1/2}\, d_{5/2}) - 2.078(p^*_{3/2}\, d_{3/2})$$

$$A_4 = -0.572(d_{5/2})^2 - 2.799(d^*_{3/2}\, d_{5/2}).$$

Here $p_{1/2}$, $p_{3/2}$, and $d_{3/2}$, $d_{5/2}$ represent the reaction amplitudes associated with E1 and E2 radiation respectively. The interference between E1 and E2 appears only in the A_1 and A_3 coefficients, and these coefficients will generally have contributions from both resonance and direct capture. The A_4 coefficient involves the E2 amplitudes only, and we neglect it compared with the A_0 term. The four complex matrix elements on which the A coefficients depend can be completely determined from radiative capture measurements using a polarized proton beam; i.e., seven parameters may be determined from the measured five A_i and four B_i coefficients.[7] For the capture gamma rays to other states, e.g., those feeding the first excited state, the angular distribution coefficients are more complicated and individual reaction matrix elements cannot be uniquely determined from them. However even here the odd Legendre coefficients still arise only from the interference between E1 and E2. The following quantities are defined from the measurements in connection with A_i coefficients

$$\sigma \equiv 4\pi A_0 \simeq 2\pi[W(55°) + W(125°)]$$

$$A \equiv [W(55°) - W(125°)]/2P_1(\cos 55°) \simeq A_1 - 0.68\, A_3$$

and

$$a = A/A_0,$$

where we have neglected the A_4 coefficient.

The present measurements were performed with the proton beam from the three stage FN tandem Van de Graaff accelerator. A collimated beam passing through 6.4 mm diameter double collimators struck a 3.2 mg/cm^2 ^{205}Tl target which had been evaporated onto a 20 μg/cm^2 carbon backing foil. The target chamber was lined with lead shielding to prevent background reactions due to scattered beam. Gamma rays were detected by the 25 cm × 25 cm NaI detector[8] with its plastic anti-coincidence shield. Typical running conditions with the ^{205}Tl target

involved about 8×10^4 pulses per second in the NaI above $E_\gamma \approx 250$ keV, which resulted in a detector resolution slightly worse than the 3.1% which had been determined at low count rate and at E_γ = 15.1 MeV using the $^{12}C(p,p'\gamma)^{12}C$ reaction. As shown in Fig. 11.6-1, the statistics were not good enough to separate the transition gamma rays to the ground state (γ_0) from those to excited states ($\gamma_1,\gamma_2,\cdots$,etc.). In this report the total yield $W(\theta)$ was obtained by simply summing counts from the ground state energy to 1.5 MeV above the ground state in each energy spectrum. This method of analysis introduces an energy dependent efficiency into the yield estimates which depends on the γ_1/γ_0 ratio. This effect should be small ($\sim$10-20%) and will be removed in a more detailed analysis by making line shape fits to the data. Gamma-ray spectra were taken at 55° and 125° with respect to the proton beam at energies from E_p = 7.0 MeV to 23 MeV. Absolute cross sections were estimated using the nominal target thickness determined by weighting, along with a counting efficiency estimated by comparison to $^{89}Y(p,\gamma)^{90}Zr$.

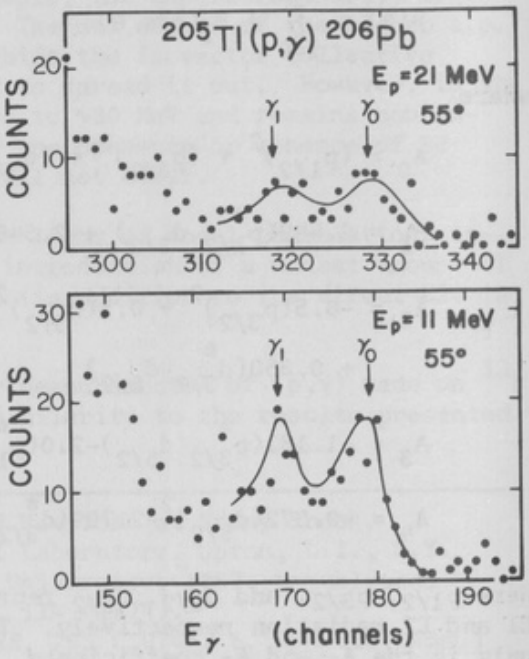

Fig. 11.6-1. Typical spectra from the $^{205}Tl(p,\gamma)^{206}Pb$ reaction. Top half counts per 300 μC, bottom half counts per 400 μC.

The excitation function of A_0 in Fig. 11.6-2 shows that the cross-section for $^{205}Tl(p,\gamma)$ is rather small throughout the entire energy region. The Giant Dipole Resonance which peaks at $E_\gamma \approx$ 13 MeV in total photoabsorption measurements is not apparent in the figure because of strong suppression by the Coulomb barrier for the incoming protons. The Coulomb penetrability for the protons increases by a factor of 10 from E_p = 8 MeV to E_p = 15 MeV. From 7 to 15 MeV the total cross section 4 A_0 increases smoothly due to increasing penetrability except around E_p = 13 MeV where there is structure due to isobaric analog resonances. At higher energy the total cross section decreases by a factor of 3 up to E_p = 23 MeV.

The asymmetry factor A_1 which arises from the interference between E1 and E2, has a very broad peak around $E_p \sim$ 16 MeV ($E_\gamma \sim$ 23 MeV). The width of this peak appears to be much broader than that seen in $^{208}Pb(p,\gamma)^{209}Bi$.[4] In fact, no peak is evident in the fractional asymmetry a. The smoothly increasing asymmetry a has been observed in various radiative proton capture reactions, and may be due in large part to the interference of direct E2 with E1.[9] Detailed quantum mechanical calculations including direct capture are necessary to deduce the effects of a collective E2 resonance. Initial estimates of the amount of direct E2 in the $^{208}Pb(p,\gamma)^{209}Bi$ reaction show that it is responsible for a large fraction of the measured asymmetry.

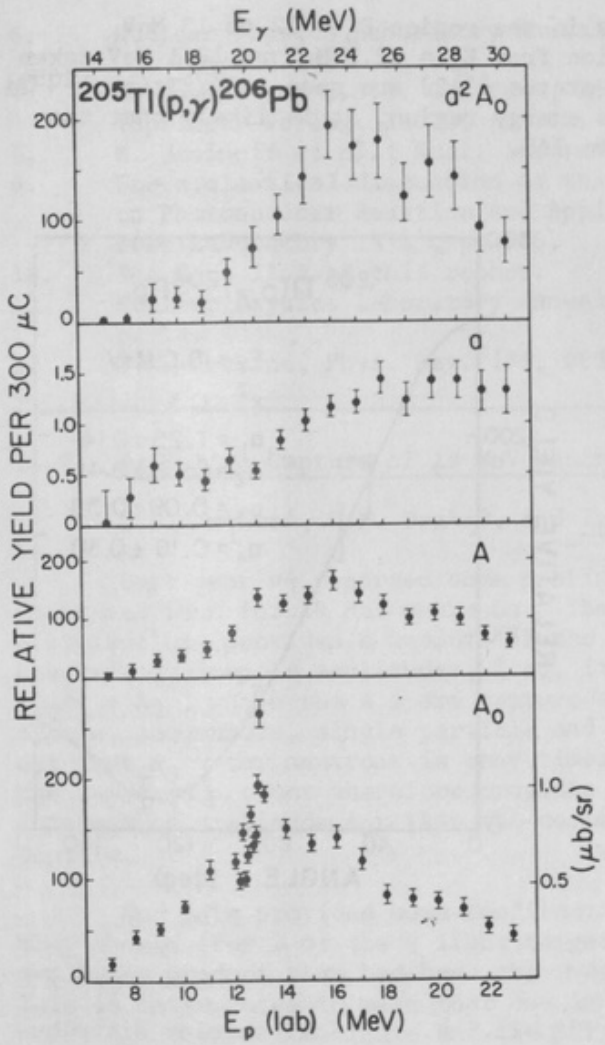

Fig. 11.6-2. Excitation functions for the ^{205}T (p,γ)^{206}Pb reaction for $\gamma_0+\gamma_1$.

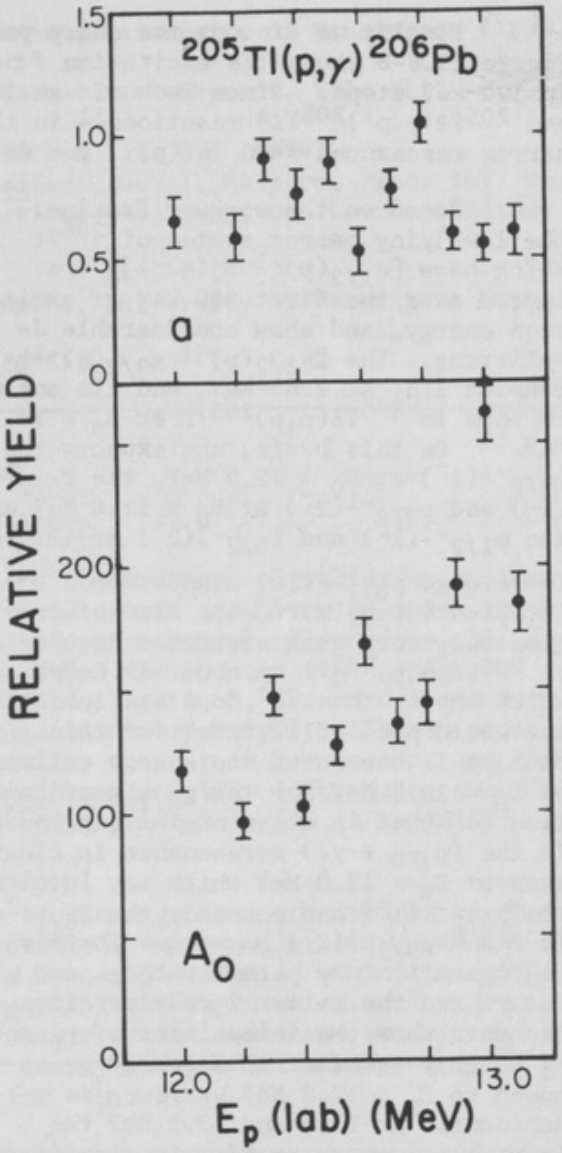

Fig. 11.6-3. Excitation functions for ^{205}T (p,γ)^{206}Pb reaction from E_p = 12.0 to E_p = 13.1 MeV.

Following the discussion of Ref. 4 (see also 1974 Annual Report, p. 145) one can show that well above the region of structure in the El amplitudes, the quantity a^2A_0 is less sensitive to variations in the El amplitudes, and involves the E2 amplitudes quadratically. This quantity is also shown in Fig. 11.6-2 and exhibits a broad peak at $E_\gamma \sim 24$ MeV. Particularly notable is the absence of a 3-4 MeV wide resonance such as was seen[1] in ^{208}Pb(p,γ)^{209}Bi. The slower energy variation seen here may be due at least in part to direct contributions -- we must await the result of detailed calculations to determine this.

Finally we discuss the sharp peaks in the region E_p = 12 to 13 MeV. Figure 11.6-3 shows the excitation function from E_p = 12.2 MeV to 13.1 MeV taken in 100 keV steps. Since isobaric analog states (IAS) are seen in ^{205}Tℓ(p,p)^{205}Tℓ and ^{205}Tℓ(p,p')^{205}Tℓ* reactions[11] in this energy region, it is likely that the narrow resonances seen in (p,γ) are due to IAS.

Based on the work of Erskine,[12] the low-lying parent states of ^{206}Tℓ which have $[s_{1/2}(p)^{-1}\ \ell j(n)^{-1}]_J$ are spread over the first 800 keV of excitation energy, and show considerable J-splitting. The $[s_{1/2}(p)^{-1}\ g_{9/2}(n)^{-1}]_{4^+,5^+}$ doublet lies at 2.59 MeV, and its analog is seen in ^{205}Tℓ(p,p)^{205}Tℓ at E_p = 14.73 MeV.[11] On this basis, one expects the $p_{3/2}^{-1}(1^-)$ at E_p = 12.9 MeV, the $f_{5/2}^{-1}$ (3-) and $p_{3/2}^{-1}(2^-)$ at E_p = 12.8 MeV and the $p_{1/2}^{-1}(1^-)$ and $f_{5/2}^{-1}(2^-)$ at 12.4 MeV (Here e.g. $p_{3/2}^{-1}(1^-)$ stands for $[s_{1/2}(p)^{-1}\ p_{3/2}(n)^{-1}]_{1^-}$). In this region only very weak structure is seen in ^{205}Tℓ(p,p)^{205}Tℓ at about 12.6 MeV, which may be the 1^-2^- doublet (in fact one would predict 12.6 MeV for this doublet if one based the energy estimate on E_p = 14.9 MeV for the $g_{9/2}$ configuration as found in other nuclei near ^{208}Pb). In the $(p,\gamma_0 + \gamma_1)$ a resonance is clearly seen at E_p = 13.0 MeV which may involve the $p_{3/2}^{-1}(1^-)$ and possibly the $f_{5/2}^{-1}$ (3^-) and $p_{3/2}^{-1}(2^-)$ as well. The first configuration may permit both γ_0 and γ_1 decays and the latter 2 only permit γ_1. The data show the intensities of γ_0 and γ_1 roughly equal at this energy as opposed to $E_p \sim 12.2$ MeV where γ_0 is dominant. At 12.3 and 12.6 MeV the $(p,\gamma_0 + \gamma_1)$ cross section is significantly larger than at adjacent energies, perhaps due to additional IAR. It is particularly surprising that the strongest (p,γ) resonance is apparently not seen at all in (p,p).

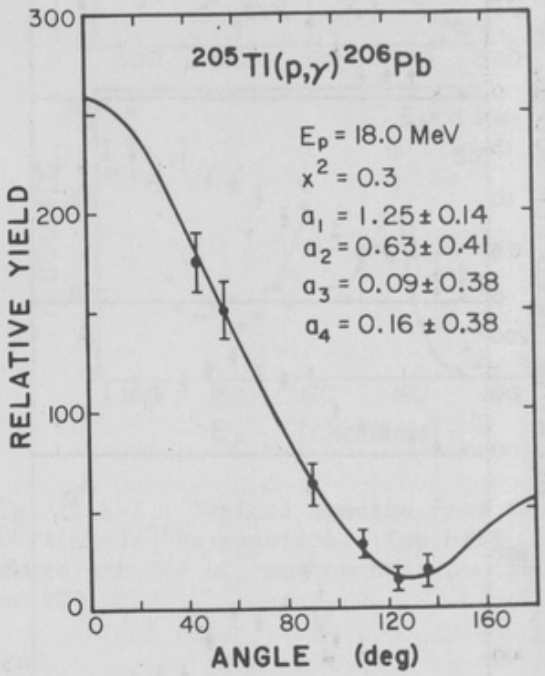

Fig. 11.6-4. Typical angular distribution of the gamma rays. Solid line shows the least squares fit to a Legendre expansion.

1. M. Nagao and Y. Torizuka, Phys. Rev. Lett. *30*, 1068 (1973); S. Fukuda and Y. Torizuka, Phys. Rev. Lett. *29*, 1109 (1973).
2. M.B. Lewis, F.E. Bertrand, and D.J. Horen, Phys. Rev. C *8*, 398 (1973).
3. J.M. Moss *et al.*, Phys. Rev. Lett. *34*, 748 (1975); S. Moalem *et al.*, Phys. Rev. Lett. *31*, 482 (1973).
4. K.A. Snover *et al.*, Phys. Rev. Lett. *32*, 317 (1974); S.S. Hanna *et al.*, Phys. Rev. Lett. *32*, 114 (1974).
5. A. Bohr and B.R. Mottelson, Nuclear Structure, Vol. II (to be published).

6. Nuclear Physics Laboratory Annual Report, University of Washington (1974), pp. 142 and 145.
7. S. Devons and L.J.B. Goldfarb, Encyclopedia of Physics, Vol. XLII (Springer-Verlag, 1957), p. 362.
8. M. Hasinoff *et al.*, Nucl. Instrum. Method *117*, 375 (1974).
9. For a classical discussion of this effect, see I. Halpern, Proc. Int. Conf. on Photonuclear Reaction and Applications, Asilomar, CA (Lawrence Livermore Laboratory 1973), p. 675.
10. See Sec. 11.1 of this report.
11. Nuclear Physics Laboratory Annual Report, University of Washington (1969), p. 79.
12. J.R. Erskine, Phys. Rev. *138*, B851 (1965).

11.7 Radiative Capture of 14 MeV Neutrons

E.D. Arthur*, D.M. Drake*, and I. Halpern

Last year we reported some preliminary measurements on radiative capture cross-sections for 14 MeV neutrons. The front-to-back asymmetry in these angular distributions provides a measure of the interference between electric dipole and electric quadrupole amplitudes, i.e., it measures the product $(A_D^{SP} + A_D^C) \times (A_Q^{SP} + A_Q^C)$ where the A's are capture amplitudes and D, Q, SP and C stand for dipole, quadrupole, single particle and collective respectively. It was pointed out that A_Q^{SP} for neutrons is many times smaller than it is for protons and that the measured product therefore provides considerably better information about the interesting amplitude A_Q^C than the corresponding product in proton radiative capture.

Our data provided some confirmation of these general conclusions in that they showed (for 3 of the 4 light targets studied) much smaller values of the amplitude product than had been observed in comparable studies with protons. This is interpreted to mean that one is observing the captures at excitations where A_Q^C does not dominate and the large values of the amplitude product for protons are to be attributed to the rather energy-independent amplitude A_Q^{SP} which is large for protons and very small for neutrons.

One puzzling result was the sizable and negative value of the amplitude product observed for $^{12}C(n_{14},\gamma_0)$. The yield ratio $(Y(55°)-Y(125°))/(Y(55°)+Y(125°))$ had the value -0.15 ± 0.06. The excitation energy involved here is about 18 MeV, a few MeV below the giant dipole resonance in carbon. One must interpret the large value of the observed interference as an indication of the presence of a large amount of collective capture at the excitation energy in ^{13}C reached in this experiment. The sign of the interference is however something of a puzzle. One can show that below the giant dipole resonance, isoscalar quadrupole capture would give a positive interference product and isovector quadrupole capture would give a negative one. It is expected that the giant isoscalar quadrupole lies below the dipole giant resonance while the isovector quadrupole resonance lies above it. Hence one expects a positive interference product. One is driven to conclude that in ^{13}C the isoscalar and isovector strengths are not neatly separated into distinct resonances but are broad and overlapping and that we

therefore happen to be picking up a piece of the isovector strength far from the centroid of this strength. This view is consistent with other studies of radiative capture in light nuclei, some of them discussed elsewhere in this section of the Annual Report, which show that in light nuclei the quadrupole strengths are more widely distributed than in heavy nuclei. It would be interesting to study other nuclei in this mass region and to see how rapidly the observed backward folding of the angular distribution in $^{12}C(n,\gamma)$ changes with incident neutron energy in the neighborhood of 14 MeV.

---

* Permanent address: Los Alamos Scientific Laboratory, Los Alamos, NM.

---

12. FISSION

12.1. Determination of $J^{\pi} = 1^{-}$ Fission Barrier Parameters from Photofission Cross Sections in ^{238}U and ^{232}Th

P. Dickey

The selectivity with which photons excite 1^{-} states in an even-even compound nucleus makes them an ideal probe for studying the fission of nuclei through transition states of a single spin and parity. The parameterization of the shape of the fission barriers as a function of deformation in terms of smoothly joined parabolas (see Fig. 12.1-1) allows an exact calculation of the quantum mechanical penetrability through these barriers. The comparison of calculated penetrabilities with penetrabilities inferred from photofission cross sections yields information about the heights and thicknesses of the components of the double humped fission barrier. Such an analysis has been made for new photofission data obtained at the University of Illinois bremsstrahlung monochomator facility.

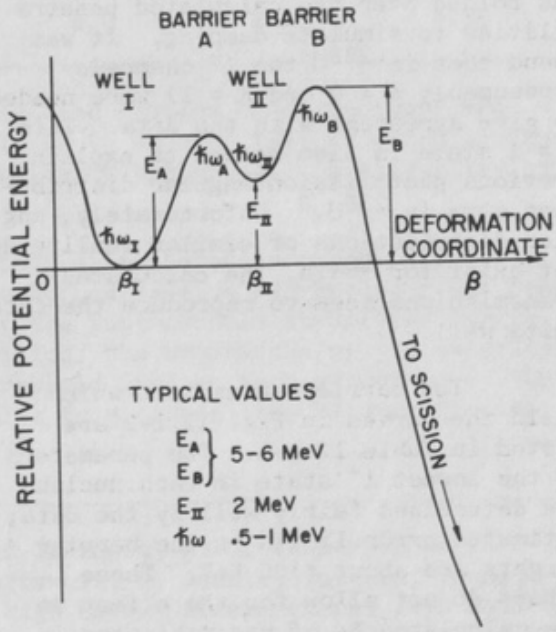

Fig. 12.1-1. Double humped fission barrier.

The photofission cross sections[1] were obtained last year at Illinois by measuring the yield of fission neutrons produced when targets of ThO_2 and UO_3 were irradiated with the bremsstrahlung photon beam produced by the superconducting electron linac.[2] Tagged photons with about 1.5% energy resolution between 5 and 8 MeV were defined by concident detection of the post bremsstrahlung electrons and the fission neutrons.

The fission transmission (or barrier penetrability) and the photofission cross section are related by

$$\sigma_f(E) = \sigma_a(E) \frac{T_f}{T_f + T_\gamma + T_n}$$

where $\sigma_a(E)$ is the total photon absorption cross section, T_f is the sum of barrier penetrabilities for participating fission channels, and T_γ and T_n are effective gamma ray and neutron transmissions. At energies not higher than 600 keV above the photoneutron threshold, the photon interaction cross section was assumed equal to that predicted by extrapolating the giant resonance. At higher energies, measured values for the fission plus photoneutron cross section from

the Illinois experiment were used for $\sigma_a(E)$. The gamma ray transmission was taken from Huizenga and Vandenbosch.[4] The total neutron transmission was calculated[5] by summing optical model transmission coefficients[6] to known states in the residual nuclei ^{237}U and ^{231}Th.

The model calculations were performed on the SDS-930 off-line computer using a modified version of a computer program by Ron Aley based on work of Bang and Wong.[7] The fission barrier model parameters are defined in Fig. 12.1-1. The important low-lying 1^- fission barriers in even-even nuclei are expected to have K = 0 and K = 1 (corresponding to the octupole and bending collective states), where K is the angular momentum projection along the nuclear symmetry axis. Initial values for the barrier heights were based on results of direct reaction fission studies[8] which predicted parameters for the 0^+ fission barriers in these nuclei. The parameters were adjusted to give agreement with the fission transmission data, as shown in Fig. 12.1-2. A Gaussian spreading function was folded over the calculated penetrabilities to simulate damping. It was found that in ^{238}U two 1^- channels (presumably K = 0 and K = 1) were needed to give agreement with the data. This K = 1 state is also needed to explain previous photofission angular distribution data in ^{238}U.[9] Unfortunately, angular distributions of similar quality do not exist for ^{232}Th. The calculated transmissions seem to reproduce the data quite well.

The barrier parameters which yield the curves in Fig. 12.1-2 are listed in Table 12.1-1. The parameters of the lowest 1^- state in each nucleus are determined fairly well by the data; estimated error limits on the barrier heights are about ±100 keV. These errors do not allow for the effect on the calculated T_f of uncertainties in the photon absorption cross section and the competing transmissions T_γ and T_n. Parameters of the K = 1 barriers are less well determined, particularly in thorium, where the K = 1 barrier was put in merely to show that it is not needed below 6.8 MeV. In uranium, however, the higher barrier of the K = 1 channel is probably known to about ±100 keV.

The barrier shapes deduced from the fits are consistent with the expected[10] near-degeneracy of the octupole and 0^+ barriers at the second maximum of the barriers because of the softness of the nucleus to octupole distortions at

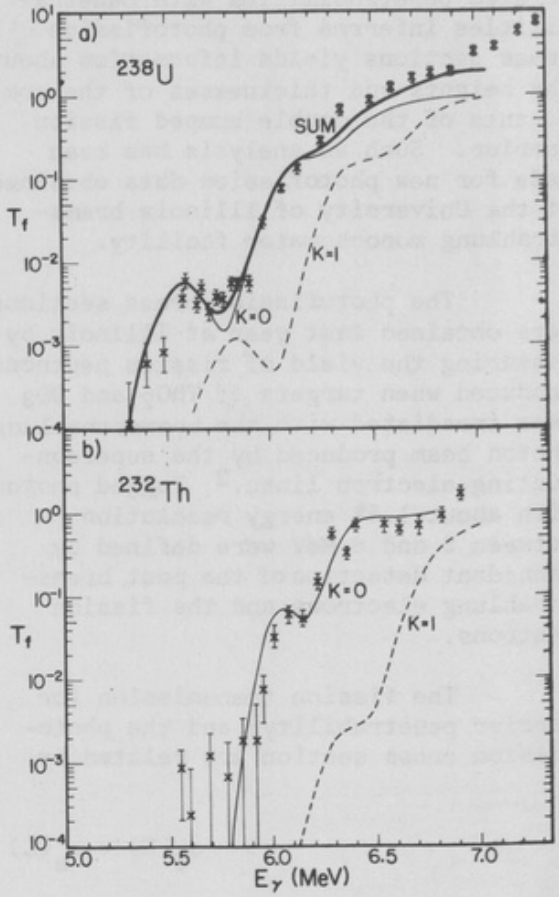

Fig. 12.1-2. Fission transmission factors for ^{238}U and ^{232}Th.

Table 12.1-1. Fission Barrier Parameters
(Energies given in MeV)

	J^π	K	E_A	E_{II}	E_B	$\hbar\omega_A$	$\hbar\omega_{II}$	$\hbar\omega_B$	Spreading Width
^{238}U	0^+	0	5.9	2.0	6.1	1.0	0.9	0.6	
	1^-	0	6.5	2.35	6.1	1.0	0.9	0.6	.23
	1^-	1	6.7	2.55	6.6	1.0	0.9	0.6	.25
^{232}Th	0^+	0	<5.5	3.0	6.1	0.9	1.5	0.5	
	1^-	0	6.3	3.1	6.3	0.9	1.2	0.45	.16
	1^-	1	6.5	3.3	6.9	0.9	1.0	0.5	.20

that quadrupole deformation. In both nuclei the fission cross sections are adequately described by one or two channels up to about 7 MeV, at which excitation a rapid rise in fission probabilty indicates the probable availability of two quasi particle states at the barrier.

Although structure has been seen before in photofission cross sections,[11] a fit to the cross section based on double humped fission barriers has not been previously made. This analysis shows that the subthreshold structures can be interpreted as fission resonances. In addition, the smoothness of the experimental barrier penetrabilities at neutron threshold implies that structure in the fission cross section at that energy results from competition between fission and neutron emission.

1. P.A. Dickey, thesis, University of Illinois, 1975, (unpublished).
2. A.O. Hanson, J.R. Harlan, R.A. Hoffswell, D. Jammik, and L.M. Young, Proc. of the 9th Int'l. Conf. on High Energy Accelerators, 1974 National Technical Information Service, Dept. of Commerce, TID 4500, 60th edition.
3. A. Veyssieri, H. Beil, R. Bergere, P. Carlos, A. Lepretre, and K. Kernbath, Nucl. Phys. *A199*, 45 (1973).
4. R. Vandenbosch and J.R. Huizenga, *Nuclear Fission*, Academic Press, New York (1973), p. 122.
5. H.C. Britt, private communication, 1974.
6. L. Rosen, J.C. Berg, and A.S. Goldhaber, Ann. Phys. *34*, 96 (1965).
7. C.Y. Wong and J. Bang, Phys. Lett. *29B*, 143 (1969).
8. B.B. Back, Oley Hansen, H.C. Britt, and J.D. Garrett, Phys. Rev. *C9*, 1924 (1974).
9. J.W. Knowles, A.M. Khan, and W.G. Cross, Izv. Akad. Nauk SSSR, Ser. Fiz. *34*, 1627 (1970).
10. P. Moller and J.R. Nix, Proc. IAEA Sym. on Physics and Chemistry of Fission SM-174/202, Rochester (1973), p. 103.
11. J.W. Knowles and A.M. Khan, Nucl. Phys. *A179*, 333 (1972).

13. ATOMIC PHYSICS

13.1 Search for Electron Capture in the Alpha Decay of ^{210}Po

D. Burch and P. Dyer

The radioactive nucleus ^{210}Po decays with the emission of a single 5.3-MeV alpha particle. As the emitted alpha particle penetrates the successive atomic shells of the daughter atom, Pb, there is some probability that vacancies will be produced in the K, L, and M shells. The interaction is similar to "one-half" of an atomic collision at zero impact parameter. These probabilities have been measured by several groups and are: $P_K = 1.7 \times 10^{-6}$, $P_L = 7.7 \times 10^{-4}$, and $P_M = 1.8 \times 10^{-2}$. The vacancy production has been interpreted theoretically as direct ionization to the continuum; the agreement with experiment has been fairly good, discrepancies having been attributed to approximations in the calculations as opposed to the vacancy production mechanism itself.

Recently, however, Fischbeck and Freedman[1] performed an experiment unique in two ways: first, they used a high-resolution magnetic spectrometer which was sensitive to the charge state of the He ion and, in a second experiment, deduced P_L from coincidences between x-rays and knock-out electrons. They found that the number of He^{++} ions which had undergone an energy loss corresponding to L-shell ionization did agree with the number of electrons knocked out of the L shell, but the value of P_L implied by both of these data was only 35% of the value obtained from the ratio of L x-rays to alpha particles as measured in the earlier studies. As they pointed out, these data indicate that 65% of the L vacancy production occurs by electron capture forming He^+ and not by ionization, i.e., neither the electron nor the He^{++} ion would be present although the L x-ray would be, and experiments insensitive to the charge state could not distinguish these events.

Although the evidence for this process is strong, it remains indirect until the He^+ ions are observed in the predicted ratio. Since the implications of this work have a profound influence on inner-shell vacancy production in atomic collisions, we have begun work on an experiment designed to detect the He^+ ions and thus verify this important result.

A schematic diagram of the experiment is shown in Fig. 13.1-1. He ions emitted from a fractional monolayer source deposited on 0.5-mil Be are tightly collimated before entering a magnetic field of 8 kG, 4 inches long, and detected with a position sensitive detector. The ions are detected in coincidence with L x-rays detected behind the source with a thin NaI crystal. To protect the source from contamination which could strip off the He^+, the vacuum is maintained with an oil-free system at 1×10^{-8} Torr. The x-ray, alpha, and coincidence count rates obtained and the resolution of the magnet system are consistent with the design values, but progress on the actual measurement was interrupted by an unexpected problem. The Po source appears to "creep" readily along the source

holder and collimator system, and after one week the chamber was contaminated. This produced a position background in the particle detector high enough to prohibit any realistic search for the small He^+ component.

We feel that this problem can be solved with a redesign of the collimator section of the chamber, and work on this is in progress.

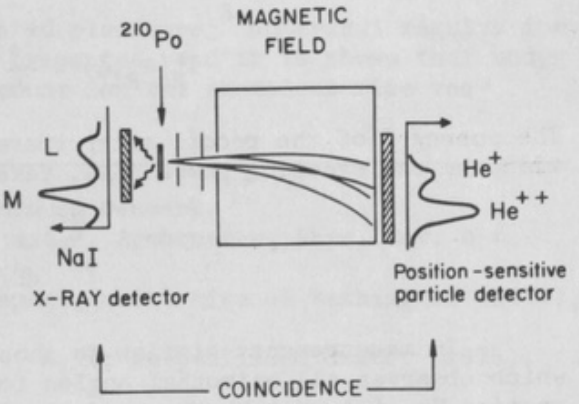

Fig. 13.1-1. Schematic diagram of the experiment to measure coincidences between He^+ and L x-rays in the decay of ^{210}Po.

1. H.J. Fischbeck and M.S. Freedman, Phys. Rev. Lett. *34*, 173 (1975).

13.2 Recoil Effects on the Impact Parameter Dependence of X-ray Production

D. Burch and Knud Taulbjerg*

The impact parameter dependence of inner-shell ionization can be determined by measuring coincidences between x rays and projectile ions as a function of scattering angle. When solid targets -- even very thin ones -- are used, there is a possibility that x-ray production in the target-recoil interaction will artificially increase the observed probability at small impact parameters. An unexpected rise of this type was reported by Stein *et al.*[1] for L x-ray production in I + Te collisions. This effect is of further interest in regard to coincidence studies of united-atom x-ray spectra which may be influenced by recoil contributions.[2]

The probability for x-ray production in the recoil interaction for a projectile at scattering angle θ, detected at the azimuthal angle ϕ after transferring an energy E_R to the recoil is given by

$$P_R(\theta,\phi,E_R) = \frac{1}{T_o}\int_0^{T_o} dT \int_0^{2TT_R(\theta_R,\phi)/T_o} dx\, N\sigma_s(E(x;E_R)), \qquad (1)$$

where σ_s is the x-ray production cross section in a collision between two target atoms and N is the number density of the target. In Eq. (1) we have averaged over the position of the primary collision and integrated the x-ray production cross section along the path of the recoil, assumed to be a straight line. The recoil path length for a primary collision in the center of a foil of thickness T_o positioned at the angle θ_T with respect to the beam axis is given by

$$T_R(\theta_R,\phi) = \frac{T_o}{2} \frac{\text{Sec } \theta_R \text{ Sec } \theta_T}{|\text{Tan } \theta_T - \text{Tan } \theta_R \text{ Cos } \phi|}. \quad (2)$$

The energy E of the recoil after traversing a distance x in the target is determined by the stopping power S(E), taken here from LSS theory:

$$\int_E^{E_R} dE/S(E) = x. \quad (3)$$

In measurements similar to those of Stein *et al.* employing a ring detector which observes all azimuthal angles for a given scattering angle, the recoil correction Eq. (1) must be averaged over the azimuthal angles:

$$P_R(\theta,E_R) = \frac{1}{2\pi} \int_0^{2\pi} d\phi \int_0^{2T_R(\theta,\phi)} dx \, N\sigma_s(x)\{1 - \frac{x}{2T_R(\theta,\phi)}\}, \quad (4)$$

where here the integral over the position of the primary collision has been evaluated. The integral over ϕ may also be evaluated, but the resulting expression is cumbersome; the remaining integral must be evaluated numerically.

An example of the results is shown in Fig. 13.2-1 for Al K x-ray production. This case was chosen since $\sigma_s(x)$ is known from threshold up to 40 MeV. Note that P_R is independent of the projectile character depending only upon the maximum energy transfer and the center of mass scattering angle. Experimental data are not available for direct comparison in this case, but rough estimates show that the recoil contribution is comparable to the primary probability for incident Al projectiles scattered to back angles in the geometry indicated in the caption to Fig. 13.2-1.

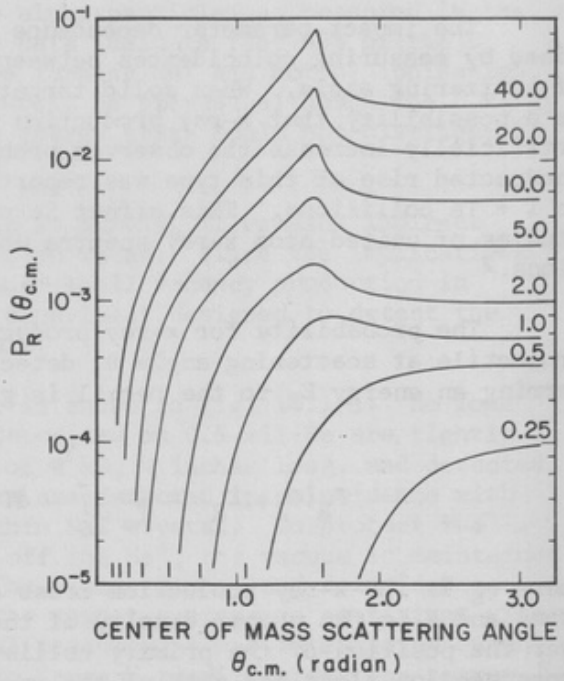

Fig. 13.2-1. Probability for Al K x-ray production in the recoil-target interaction as a function of the center of mass scattering angle. The target angle is 45° and the target thickness is 20 $\mu g/cm^2$. Results are shown for maximum energy transfers of 0.25 to 40 MeV. To first order the recoil probability is proportional to the target thickness.

Full details of this work are presented elsewhere;[3] numerical results for the collisions studied by Stein *et al.* are presented, and it is shown that under certain circumstances this effect could account for the anomalous rise they reported.

---

* Permanent address: University of Aarhus, Denmark.

1. H.J. Stein, H.O. Lutz, P.H. Mokler, and P. Armbruster, Phys. Rev. A *5*, 2126 (1972).
2. Nuclear Physics Laboratory Annual Report, University of Washington (1974), p. 161.
3. D. Burch and K. Taulbjerg, Phys. Rev. A, to be published August (1975).

13.3 End-point Energies of Molecular-Orbital X-ray Spectra

D. Burch and B. Müller

Although molecular-orbital (MO) x-ray spectra have been studied extensively by many groups now, there has been little attempt made to relate the observed shape and, in particular, the cut-off or end-point energy of the photon distribution to the correlation diagram of the collision system. We have worked on a simple method for making this comparison which yields end-point energy predictions in closed form for arbitrary collisions. Below we outline briefly this procedure for L-shell transitions ($2p\pi$ - $3d\delta$), using atomic units throughout.

The MO energy levels as a function of internuclear separation R (the correlation diagram) are represented by a model shape which has the correct values for small and large R and also the hydrogenic R^2 dependence at small R:

$$\varepsilon_{n\ell m}(R) = E_{n\ell}(\infty) + \frac{E_n(0) - E_n(\infty)}{1 + R^2/R_{n\ell}^2} . \qquad (1)$$

Here R = 0 and ∞ represent the united-atom (UA) and separated-atom (SA) limits, respectively. $R_{n\ell}$ is a scaling parameter which depends on the collision system and represents the value of R at which the MO level has reached $\sim 1/2$ of its UA value. The SA energies are those of the higher Z collision partner. $R_{n\ell}$ is evaluated from the hydrogenic result at small R where the energy levels are approximated by the addition of a quadrupole term:

$$\varepsilon'_{n\ell m} \approx E_{n\ell}(0) - k_{\ell m} Z_{n\ell} R^2 \left\langle \frac{1}{r^3} \right\rangle_{n\ell} \qquad (2)$$

Equation (2) is valid for $R \ll \langle r \rangle_{n\ell}$ evaluated in the UA limit and can be evaluated analytically using screened hydrogenic wave functions; the $k_{\ell m}$ are constants. The effective charge $Z_{n\ell}$ for each shell is determined from

$$E_{n\ell}(0) = \frac{Z_{n\ell}^2}{2n^2}, \tag{3}$$

which combined with the evaluation of Eq. (2) yields

$$\varepsilon'_{n\ell m}(R) \approx E_{n\ell}(0) - K_{n\ell m} R^2 E_{n\ell}^2(0). \tag{4}$$

For small R, Eq. (1) can be rewritten as

$$\varepsilon_{n\ell m}(R) \approx E_{n\ell}(0) - [E_{n\ell}(0) - E_{n\ell}(\infty)] \frac{R^2}{R_{n\ell}^2}, \tag{5}$$

or, comparing Eqs. (4) and (5), yields

$$R_{n\ell}^2 = \frac{E_{n\ell}(0) - E_{n\ell}(\infty)}{K_{n\ell m} E_{n\ell}^2(0)}. \tag{6}$$

Equations (1) and (6) provide a correlation diagram for the $n\ell$-th level at all R for any collision. We note that this formulation is not applicable to the $1s\sigma$ level.

In the static limit the end-point energy of the spectrum is given by

$$\varepsilon_{ep} = E_{UA} - \Delta\varepsilon \equiv \hbar\omega_s, \tag{7}$$

where

$$E_{UA} = E_{2p\pi}(0) - E_{3d\delta}(0), \tag{8}$$

and

$$\Delta\varepsilon = \frac{E_{2p}(0) - E_{2p}(\infty)}{1 + R_{2p}^2/R_{min}^2} \equiv \hbar\Delta\omega(0). \tag{9}$$

R_{min} is the distance of closest approach in a head-on collision which, for the slow collisions considered here, must be evaluated using screened interatomic potentials.

In collisions, however, the static limit is only a first approximation since the energy levels are changing with time along the trajectory of the collision which introduces a broadening of the end-point energy as a result of the uncertainty principle.

Macek and Briggs[1] have pointed out that the MO x-ray frequency distribution should be proportional to the square of the following amplitude:

$$D_c(\omega) = \int_{-\infty}^{\infty} dt\ \bar{\omega}(t) d_c(t)\ e^{i\omega t - i\int_0^{\tau} \bar{\omega}(t')dt'} . \qquad (10)$$

$d_c(t)$ is the dipole matrix element between the molecular orbitals which we have approximated as a constant, and

$$\bar{\omega}(t) = \omega_0 + \Delta\omega(t), \qquad (11)$$

where ω_0 is the SA transition energy. $\Delta\omega$ is given by Eq. (9) with R^2_{min} replaced by $R^2 = b^2 + v^2t^2$, i.e., a straight-line, constant-velocity approximation at impact parameter b. The resulting integral is complicated but can be evaluated analytically. The result is proportional to a Whittaker function divided by a gamma function; for the present work, however, we care only about the shape of this function for $\omega > \omega_s$. In this asymptotic region the intensity can be written as

$$I(\omega) \simeq e^{-(\omega-\omega_s)/\Gamma}, \qquad (12)$$

where

$$\Gamma = 2v(R_{2p}^2 + R_{min}^2)^{-1/2} \qquad (13)$$

is a measure of the spectral broadening above the static limit which is found to be proportional to the collision velocity. We then get the following simple expression for L transition end-point energies

$$\varepsilon_{ep} = E_{UA} - \Delta\varepsilon + \Gamma. \qquad (14)$$

Equation (14) has been compared to the data of Bissinger and Feldman[2] for ε_{ep} measured in 200-keV Z_1 + Si collisions with Z_1 = 16 to 22. The model calculations reproduce the data very well for the lower Z_1 collisions but overestimate ε_{ep} by 13% at Z_1 = 22. This discrepancy is significant considering the limited range of possible values which can be established from even simpler models. If we assume that the model shape given in Eq. (1) is appropriate, then these results indicate that Eq. (6) underestimates the dependence of R_{2p} on E_{2p} in that R_{2p} should decrease faster with increasing E_{2p}.

We feel the major purpose of this analysis has been achieved since the reproduction of the data is definitely sensitive to the shape of the correlation diagram. For example, an assumed pure R^2 dependence of the energy levels for all R values sampled in the experiment yields a Z_1 dependence of ε_{ep} distinctly different from the data. Work is now in progress toward improving the scaling law of Eq. (6) which should provide a better test for the overall analysis.

1. J.H. Macek and J.S. Briggs, J. Phys. B *7*, 1312 (1974).
2. G. Bissinger and L. Feldman, Phys. Rev. Lett. *33*, 1 (1974).

13.4 Multiple Scattering of Heavy Ions in Thick Absorbers

D. Burch and K. Green

Multiple scattering of heavy ions is important to both atomic and nuclear experiments with energetic heavy ions. Besides its practical importance, e.g., in strippers in heavy-ion accelerators, it also can be used to provide basic information on inter-atomic potentials. Recent experimental work,[1] for a variety of heavy ions and targets at MeV energies has shown that the Meyer theory[2] reproduces the half angle at half maximum, $\theta_{1/2}$, of the multiple scattering distributions to within ±20%. Scattering distributions have also been calculated by Sigmund and Winterbon[3] for a wider range of target thicknesses using several interatomic potentials. The theoretical results are tabulated.[2,3]

We have found that the following very simple semi-empirical formula reproduces the available experimental data to within ±20%:

$$\theta_{1/2}(\text{rad}) = \frac{2Z_1Z_2e^2}{Ea} \times 0.347\ \tau^{0.754}, \qquad (1)$$

where $a = 0.8853\ a_o(Z_1^{2/3} + Z_2^{2/3})^{-1/2}$, and $\tau = \pi a^2 Nx$, with N the particle density and x the thickness of the target. Other formulas have also been developed which reproduce the theoretical curves to within ±2%.

Existing data are for relatively small energy losses (the theory neglects all energy loss) typical of targets for nuclear experiments. We have begun measurements to extend these data to thick targets with up to 75% energy loss. The thick target data are useful for the analysis of detection efficiencies in particle telescope systems employing time of flight measurement since the second detector is well separated from the first transmission detector which is effectively a thick target. The thick target data are also important to experiments involving the channeling of heavy ions in crystals.

The experiment is relatively simple: a low intensity beam collimated to a very small angular divergence is incident directly onto a position sensitive detector, and spectra are accumulated with and without the insertion of the absorber under study. The primary concern is the production of an adequately collimated beam without excessive energy straggling from slit edges. Geometrical corrections to the spectra are required to account for the azimuthal variation of the position signal for a given scattering angle.

The spectrum for 30-MeV O ions passing through 10 μm of Si is shown in Fig. 13.4-1 compared with several theoretical curves as explained in the caption. The data indicate two rather surprising results: first, the semi-empirical formula, the Gaussian curve B using Eq. (1), which works well for low energy losses is also a good approximation to this thick target data using the incident energy. This may be fortuitous; if the result persists for other systems it must be

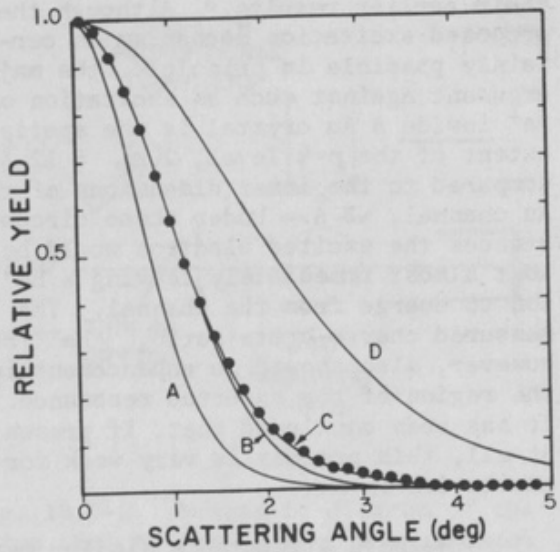

Fig. 13.4-1. Multiple scattering distribution for 30-MeV O ions in 10 μm (2.33 mg/cm^2) of Si in a random orientation. The open points are experimental. Curve A is from Ref. 3 using the incident energy 30 MeV, curve D is the same result using the exit energy 11.0 MeV, and curve C uses the average energy in the target, 20.5 MeV. Curve B is a Gaussian of the form $f(\theta) = \exp[-\ln(2)(\theta/\theta_{1/2})^2]$, where $\theta_{1/2}$ is determined from Eq. (1).

considered purely empirical. Secondly, the calculations of Sigmund and Winterbon,[3] using the average energy in the foil, reproduces the data nearly identically.

A systematic study is required to test these first results, and this work is in progress. We currently have data for 15 to 30 MeV oxygen ions at 5-MeV steps for 1 to 3 mg/cm^2 targets of Al, Ni and Au. Both the energy straggling and the multiple scattering data are being analyzed.

1. B.W. Hooten, J.M. Freeman, and P.P. Kane, Nucl. Instrum. Methods *124*, 29 (1975) and G. Spahn and K.O. Groeneveld, Nucl. Instrum. Methods *123*, 425 (1975).
2. L. Meyer, Phys. State. Sol. *44*, 253 (1971).
3. P. Sigmund and K.B. Winterbon, Nucl. Instrum. Methods *119*, 541 (1974).

13.5 Search for Coherent Excitation of X-ray Transitions in Channeled Ions

D. Burch, J.A. Cairns*, and A.D. Marwick*

In 1973 Okorokov *et al.*[1] reported a resonance-like enhancement of 10% in the incident energy dependence of the n=1 to n=4 (51 eV) excitation of He^+ ions channeled through thin Ag crystals at an energy of 570 keV. The effect was interpreted as a coherent Coulomb excitation of the ion by the periodic potential along the channel since the resonance energy corresponded to a frequency of collisions (ion velocity/interatomic spacing) very nearly equal to the characteristic frequency of the n=4 transition ($\Delta E/h$). This type of coherent excitation was, indeed, predicted by Okorokov in 1965.[1] The experiment was repeated by Gaillard *et al.*[2] using thin Au crystals and the resonance, even more pronounced, was again observed at the corresponding energy for the ⟨110⟩ axis of Au, ∿280 keV.

Recently, however, Berry and Gemmell *et al.*[3] and Gibson *et al.*[4] in an attempt to reproduce the Au measurements found no indication of a resonance; and subsequently Gaillard *et al.* have also reported that they are unable to reproduce

their earlier results.[3] Although the proposed excitation mechanism is certainly possible in principle, the major argument against such an excitation of He^+ inside a Au crystal is the spatial extent of the n=4 level, $2\langle r\rangle = 12$ Å, compared to the inner dimensions of the Au channel, ∿3 Å. Under these circumstances the excited electron would be lost almost immediately leaving a He^{++} ion to emerge from the channel. The measured charge-state ratio, He^{++}/He^+, however, also showed no enhancement in the region of the expected resonance.[3,4] It has been concluded that, if present at all, this process is very weak for He^+ excitation in Au.

We have attempted a similar measurement of the n=1 to n=2 excitation of C^{5+} ions channeled along the ⟨110⟩ axis of Au. In contrast to the He^+ example, the dimensions of the n=2 state of hydrogenic C, $2\langle r\rangle = 1$ Å, are compatible with the size of the Au channel.

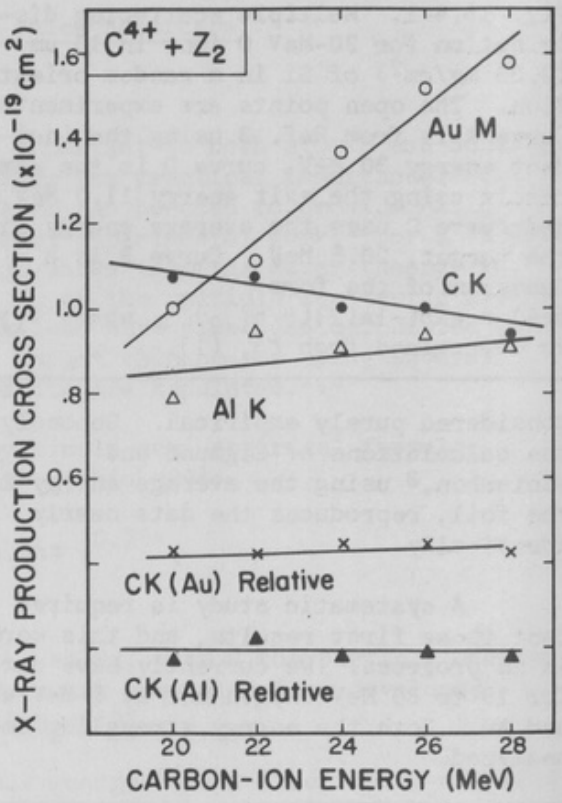

Fig. 13.5-1. X-ray production cross sections for C^{4+} ions on Au, C, and Al. The top three curves are for the target emission with experimental uncertainties of ±40%. The bottom two curves are relative yields of C K x rays from both the beam and from any impurity layers of C on the targets.

Preliminary measurements were m made at the University of Washington to investigate the feasibility of observing the 1s → 2p excitation by directly viewing the Au crystal. X-ray production cross sections for C ions incident on amorphous Au are shown in Fig. 13.5-1 compared with C and Al targets. It was found that the Au M x rays (∿2 keV) completely swamped the low yield of C K x rays, (∿280 eV) in the proportional counter spectrum and the relative C yield became even worse at higher energies. It appears that a direct observation of the crystal will require a Bragg spectrometer measurement, in which case the low intensity may still prohibit this measurement. If this approach is to be pursued it is mandatory that C build-up be completely suppressed.

Further measurements were carried out at the Harwell tandem using their existing channeling facilities. The intention of the experiment was to look for the resonance in the 1s → 2s excitation of a metastable state and observe this excitation by motional electric field quenching of the a $^2S_{1/2}$ state as developed in earlier Lamb shift studies.[5] Cross sections for the 1s → 2s excitation could be crudely estimated from low-energy He^+ data;[6] it was found that He^+ (1s → 2s) was, at the maximum in the cross section, ∿2 orders of magnitude lower than 2s formation by electron capture into He^{++}. Scaling this result to C according to the (1s → 2s) M1 transition rate, $\propto Z^{10}$, and the electron capture rate, $\propto Z^5$,

reduces the 2 orders of magnitude factor to something on the order of 1. The present measurements were carried out at 30 to 40 MeV, an energy range near the broad maximum in both the capture and excitation cross sections. In this energy range Kugel *et al.*[5] found ∿2% of the C^{6+} capture, in a near-equilibrium-thickness Ar gas, was to the 2s state. From the above comments we could very roughly expect a comparable intensity for the direct excitation of C^{5+} inside a Au channel.

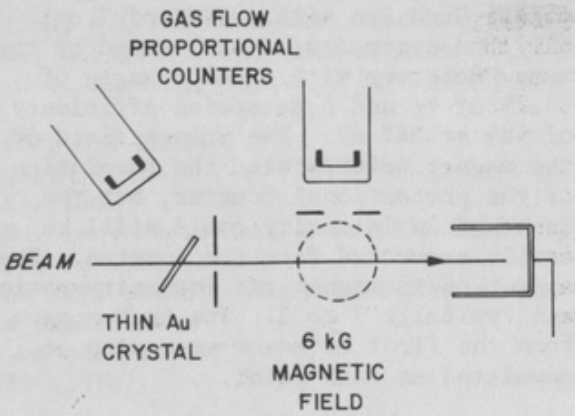

Fig. 13.5-2. Schematic diagram of the setup (not to scale) in the experiment to look for the 1s → 2s transition in C^{5+} passing through a gold crystal.

The Au crystals used were produced at Bell Laboratories,[7] the final measurement was for a 1700 Å crystal oriented along the ⟨110⟩ axis at 35.2°, or an effective thickness of 400 μg/cm^2 (∿720 atomic layers). The stopping power for charge state q+ inside the channel can be roughly estimated from related measurements[8] as

$$S_{channel}(q) \sim \frac{1}{2}\left(\frac{q}{Z}\right)^2 S_{random}. \qquad (1)$$

The 1s → 2s energy for C^{5+} is ΔE = 367 eV which combined with the ⟨110⟩ spacing, d = 2.884 A, implies a resonance energy of 40.7 MeV. The resonance energy can be expressed as

$$E_R(\text{MeV}) = 3.03 \times 10^{-6} \times M(\text{amu}) \times d^2(\text{Å}) \times \Delta E^2(\text{eV}). \qquad (2)$$

The energy loss in the channel is therefore expected to be ∿200 keV which might be considered a first order estimate of the minimum resonance width. The resonance width will also be affected by the thermal motion of the crystal atoms. For Au at room temperature the vibration amplitude is u_1 = 0.087 Å,[9] (3% of d) which from Eq. (2) suggests a maximum width of 6% of E_R or ∿2.5 MeV. We could than, very roughly, expect a resonance width between 0.2 and 2.5 MeV.

The experimental arrangement is shown schematically in Fig. 13.5-2. The C^{5+} beam was collimated to ±0.04° with two 1-mm apertures separated by 1.3 m. A third collimator after the Au crystal accepted only the well channeled beam. The channeling half angle[9] $\psi_{1/2}$ = 0.41°. Since the multiple scattering half angle[10] is 0.18°, no enhancement of beam intensity transmitted through this aperture was observed when the crystal was oriented along the ⟨110⟩ axis. An electromagnet was located 25 cm from the crystal and operated at 6 kG with 2.5-cm diameter pole pieces separated by 2.5 cm. The lifetime of C^{5+}(2s) is 2.6 μsec (66 m at 40 MeV) so there was no loss of intensity by double photon emission.

Loss of intensity does come about from collisional quenching and by Stark mixing in the fringe field of the magnet. The magnetic field was not optimized

in this regard. The field was approximately Gaussian with a FWHM of 7 cm; only the central 3 cm was viewed by the x-ray detector with a solid angle of ∿0.2% of 4π and a detection efficiency of ∿5% at 367 eV. The fringe field of the magnet deteriorated the resolution of the proportional counter, but the quenched 2s intensity could still be easily extracted from the spectra. The magnet-on to magnet-off intensity ratio was typically 7 to 1. The Au M x rays from the first detector were also accumulated at each point.

The chamber pressure was 5×10^{-6} Torr, and the crystal was completely surrounded by a LN cooled shield. Although no carbon build up could be detected visually, this pressure range is still perhaps marginal for this type of measurement. For example, at 5×10^{-5} Torr essentially all of the 2s production was collisionally quenched before reaching the magnetic field.

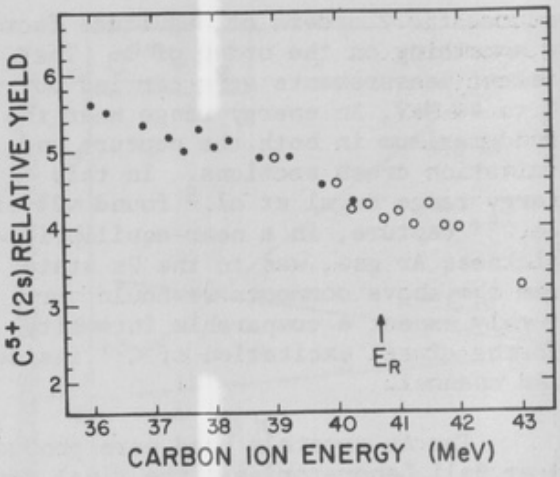

Fig. 13.5-3. Relative yield of C^{5+}(2s) from C beams incident along the ⟨110⟩ axis of Au. The open circles are for incident 5+ ions and the closed points are for 6+ ions which presumably reach the same equilibrium distribution as the 5+ beam just after entering the crystal. The yield from the 6+ beams was ∿20% higher than from incident 5+ beams and these data have been normalized as shown. The fluctuations in the data are outside of the statistical variation but were not reproducible, and their origin is uncertain.

The crystal was oriented using the Au M x-ray production. A 40% dip ($\chi_{min} = 0.6$) was observed at the ⟨110⟩ axis. Although this is not a large effect relative to the limits set by the thermal motion, this result is not surprising since the average impact parameter for M x-ray production in this collision is larger than the critical impact parameter for channeling. The results in fact suggest that model shapes of the impact parameter dependence of x-ray production might be tested by channeling measurements in similar heavy ion collisions. The shape of the channeling dip did not change throughout the duration of the measurements which amounted to a total dose of ∿10 μC of integrated beam.

Figure 13.5-3 shows the incident energy dependence of the 2s production. At 36 MeV, 3500 C^{5+} K x rays were observed per 0.1 μC of integrated beam current. Using the indicated detection efficiency and an assumed beam composition of 75% 6+ and 25% 5+ yields an absolute production efficiency for C^{5+}(2s) of ∿0.1%. This result has very large uncertainties but is consistent with the estimates since the losses mentioned above are not taken into account.

The data show no indication of a resonance in the expected region. This result must be considered preliminary and does not at all exclude the possibility of observing a coherent excitation in this collision if the experiment is refined.

* Permanent address: Metallurgy Division, A.E.R.E. Harwell, Didcot, U.K.
1. V.V. Okorokov *et al.*, Phys. Lett. *43A*, 485 (1973) and JETP Letters *16*, 415 (1972); see also V.V. Okorokov, Sov. J. Nucl. Phys. *2*, 719 (1966) and JETP Letters *2*, 111 (1965).
2. M.J. Gaillard *et al.*, Phys. Lett. *45A*, 306 (1973).
3. H.G. Berry *et al.*, Phys. Lett. *49A*, 123 (1974).
4. W.M. Gibson *et al.*, private communication.
5. H.W. Kugel, M. Leventhal, and D.E. Murnick, Phys. Rev. A *6*, 1306 (1972).
6. M.B. Shah and H.B. Gilbody, J. Phys. B *7*, L122 (1974).
7. We thank W.M. Gibson for providing us with these crystals and for extensive helpful discussions relating to this experiment.
8. C.D. Moak *et al.*, Phys. Rev. B, to be published.
9. D.S. Gemmell, Rev. Mod. Phys. *46*, 129 (1974).
10. See Sec. 13.4 of this report.

13.6 Search for the Double Photon Decay of $Pb^+(1s^{-1})$

D. Burch and J. Bussoletti

The two-photon decay mode of the 2s → 1s transition in hydrogenic ions has been observed for $Z \leq 18$ using beam foil spectroscopy.[1] The lack of dipole (2p → 1s) competition and the long lifetime of the excited 2s electron results in very clean spectra which facilitates these low count rate measurements. The transition rates and the photon energy distribution (measured only for He^+) agree well with the hydrogenic calculations.

Double photon decay has thus far not been observed in singly ionized $(1s^{-1})$ atoms. Recent theoretical work[2,3] has shown that the energy distribution of the photons, which is not sensitive to the details of the calculations, should be distinctly different from hydrogen as shown in Fig. 13.6-1. Also on general grounds, since the oscillator strength for any electron is primarily concentrated in the continuum spectrum, we can expect that the inhibition of this rate is an atom (relative to a hydrogenic ion) due to Pauli blocking will not be excessive.

The 2s → 1s transition rate for a double E1 decay has been calculated by Freund.[2] His result, after some manipulation and integration over the angular distribution, can be expressed as

$$\Gamma_{\gamma\gamma}(\text{eV}) = 9.37 \times 10^{-16}(\text{eV})^{-3}\, E_0^{\,3}\, g_{1s} g_{2s} I_\alpha \qquad (1)$$

where the transition energy $E_0 = E_{1s} - E_{2s}$ (note, $E_0 \sim (3/4)Z^2 \times 13.6$ eV) and I_α is the integral over the energy spectrum shown in Fig. 13.6-1 which, in our formulation, depends on the ratio of binding energies, $\alpha = E_{2s}/E_{1s}$. The continuum (total) oscillator strengths $g_{n\ell}$ are related to the photoabsorption cross section for the $n\ell$-th electron. Equation (1) can be compared to the hydrogenic value which includes virtual transitions through empty bound states:

$$\Gamma^H_{\gamma\gamma}(\text{eV}) = 5.41 \times 10^{-15}\, Z^6. \qquad (2)$$

Experimental observation of the two-photon decay of ($1s^{-1}$) states is hindered by the presence of the much more intense one-photon decay. The ratio $\Gamma_{\gamma\gamma}/\Gamma_{\gamma}$ is typically 10^{-6} for light atoms and 10^{-5} for heavy atoms. Although the intensity is low, fast coincidence electronics combined with "event-record" data acquisition appears to make these measurements feasible.

We have combined x-ray coincidence techniques developed earlier[4] with the computer program SCOSINDHAP[5] to obtain an upper limit on the two photon decay of a K vacancy in Pb^{+} created in the radioactive decay of a ^{207}Bi source. X-rays were detected in coincidence in a 180° geometry using two planar Ge(Li) detectors;[4] the limit on the two-photon decay was established relative to the single-photon decay, by requiring the summed energy of the two photons in true coincidence to be equal to $E_0 \pm$ the detector resolution. We find for $Pb^{+}(1s^{-1})$, from a total of 3×10^{8} single-photon decays, that

$$\frac{\Gamma_{\gamma\gamma}}{\Gamma_{\gamma}} \leq (1.5 \pm 0.3) \times 10^{-5}. \qquad (3)$$

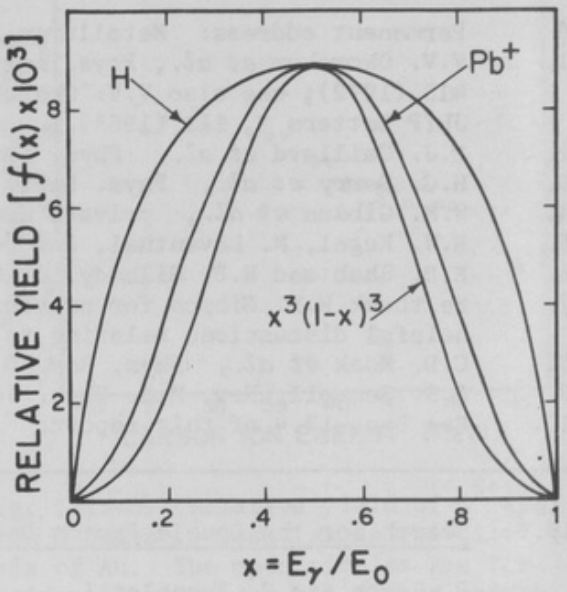

Fig. 13.6-1. The calculated energy spectrum of the double photon decay of the 2s → 1s transition in $Pb^{+}(1s^{-1})$. The photon energy E is normalized to the transition energy E_0 and is compared to the hydrogenic distribution and to a $E^3(E_0 - E)^3$ distribution characteristic of double-photon decay in nuclear transitions.

This value is a factor of 2 lower than the hydrogenic value, Eq. (2), but is still a factor of 2 higher than predicted by Eq. (1). We should note that in evaluating Eq. (1), we evaluated I_{α} numerically and determined the $g_{n\ell}$ from the Thomas-Reiche-Kuhn sum rule and the discrete oscillator strengths obtained from published x-ray transition rates.

The experimental sensitivity was limited by the 180° Compton scattering of $K_{\alpha 2}$. With a revised geometry which completely eliminates Compton coincidences, we expect to increase the sensitivity by about a factor of 100 with a comparable number of singles events. If successful the energy distribution of Fig. 13.6-1 could be tested.

1. R. Marrus and R.W. Schmieder, Phys. Rev. A *5*, 1160 (1972).
2. I. Freund, Phys. Rev. A *7*, 1849 (1973).
3. J. Eichler, Phys. Rev. A *9*, 1762 (1974).
4. D. Burch, W.B. Ingalls, H. Wieman, and R. Vandenbosch, Phys. Rev. A *10*, 1245 (1974).

13.7 Auger-Electron and X-Ray Production in 50- to 2000-keV Ne + Ne Collisions

B. Aagrad*, E. Bøving*, D. Burch, B. Fastrup*, D. Schneider†, and N. Stolterfoht†

Electron and x-ray measurements carried out partially at the University of Washington Nuclear Physics Laboratory but primarily at the Hahn-Meitner-Institute in Berlin and the Institute of Physics of the University of Aarhus have been combined into a comprehensive study of inner and outer shell excitation in Ne + Ne collisions. This work is described in detail elsewhere.[1]

The production of vacancies in the inner and outer shells of the target and projectile have been studied in Ne^{i+} + Ne collisions in the incident energy range of 50 keV to 2 MeV through the observation of K x rays and Auger electrons. Data are compared for incident charge states i = 0, 1, and 2. Parameters necessary for the analysis of collision kinematics were extracted from previous data and used to investigate these effects on the observed Auger spectra. The centroid energies and average energy widths of the Auger groups from the target and projectile, together with absolute intensities, are reported as a function of the Ne^{+} energy and electron emission angle. After kinematic corrections, it is found that target and projectile Auger electron emission are isotropic to within ±10% and that the K vacancy created is equally shared (±10%) between the target and projectile when observed as an average over the various states of multiple L-shell ionization produced. For 500-keV Ne^{+}, the target Auger spectrum was measured with a resolution of 2.6 eV FWHM and compared to similar measurements for other projectiles and energies. The kinematic energy broadening in the Ne collisions is shown to obscure the peak structure characteristic of the multiple ionization states. The average number $\bar{n}$ of electrons removed from the L shell simultaneous with the K vacancy production is estimated from the centroid Auger electron energies and, independently, from previously measured probabilities for producing final charge states. It is found that $\bar{n}$ increases with Ne ion energy from ∿2.5 to 3.5 over the energy range studied. Absolute cross sections for x-ray and Auger electron production are reported with an accuracy of ±20% and mean fluorescence yields increase with incident Ne-ion energy and are consistent with the $\bar{n}$ data. Total K vacancy production cross sections agree well with available calculations below 200 keV, but the theoretical results underestimate the cross sections at higher energies. This reflects a breakdown of the two-state approximation and a neglect of vacancy sharing at higher velocities. Information regarding the vacancy sharing in the entrance channel is extracted from relative cross sections for projectiles with different incident charge states.

---

* Permanent address: University of Aarhus, Denmark.
† Permanent address: Hahn-Meitner-Institute, Berlin.

1. N. Stolterfoht, D. Schneider, D. Burch, B. Aagaard, E. Bøving, and B. Fastrup, Phys. Rev. A, to be published.

13.8 Applications of Inner-Shell Ionization by Heavy Ions to Other Areas of Physics and Technology

D. Burch

A technical report[1] is in preparation which outlines the applications of inner-shell ionization by heavy ions to other areas of physics and technology. The report is specifically limited to recent research carried out in nuclear physics laboratories.

The topics covered, in varying degrees of detail, include: multiple ionization as related to atomic structure calculations and ion source development, determination of charge states in solids, inner-shell transition rates for multiply ionized ions, nuclear reaction product identification by x rays, heavy-ion beam energy monitors from electron loss, radiative electron capture, or capture to the continuum, the relationship of fluorescence yields of multiply ionized atoms to x-ray lasers, heavy-ion induced optical emission or electron production as a time pick-off device, use of proton beams as a normalization for heavy ion measurements, applications of molecular-orbital x rays, ion-x-ray coincidence studies of metals diffusion, and the enhancement of chemical effects on x ray spectra produced by heavy ions.

---

1. To be submitted to the Ad Hoc Committee on Accelerator-related Atomic Physics Research, B. Crasemann, Chairman.

13.9 Excitation of Autoionization States in He by Energetic Heavy Ions

J. Bolger*, D. Burch, and C.F. Moore*

A high resolution measurement of the electron spectrum ejected at 90° from 30-MeV O^{5+} + He collisions has revealed that this collision is an efficient means of producing doubly excited states in He. Eleven states were observed, five of which are members of the (2p np) ^1D series not produced by previously used excitation methods, i.e., photoabsorption, electron or proton impact, or low-energy heavy ion impact. Doubly excited states of He are very important to atomic structure theory because of the strong influence of electron-electron correlation on the state description.

Results of this study are presented elsewhere.[1] The excitation was found to be nearly independent of the projectile charge state and energy. A two-step excitation mechanism was proposed to account for the oxygen excitation and also compared to the quite different results for 4-MeV proton excitation.

---

* Permanent address: University of Texas at Austin.

1. D. Burch, J. Bolger and C.F. Moore, Phys. Rev. Lett. *34*, 1067 (1975).

13.10 Search for Charge-Changing Electrons from Ag^{11+} + C (Foil)

J. Bolger*, D. Burch, B. Johnson*, and C.F. Moore*

It is well known that the average equilibrium charge state of a heavy ion after passage though a thin foil is much higher than that established after penetration through a gas. The effect can be quite large and is a major concern in heavy-ion accelerator design; in the case of 40 to 60-MeV Ag ions the difference is about 6 charge units.

Although it is a property difficult to specify precisely, it has been proposed that the equilibrium charge state inside a solid is, with regard to several types of atomic interactions, effectively the same as that created in a gas. It is argued that the difference between gas and solid penetration is the equilibrium excitation state of the remaining electrons and, more specifically, that the high frequency of close collisions in a solid results in an equilibrium presence of inner-shell vacancies which subsequently undergo the highly ionizing process of Auger cascade at the exit surface of the foil. There is a large amount of indirect experimental evidence supporting this model. A direct confirmation of this process, however, would be an observation of these "charge-changing" Auger electrons at the exit surface.

We have looked for these electrons in 40 to 60-MeV Ag^{11+} collisions with 10 $\mu g/cm^2$ carbon foils. The electron spectra were measured at 90° with the target at 45° in both a "transmission" and "reflection" mode. A typical spectrum is shown in Fig. 13.10-1. The apparent large peak is nearly identical to what one might expect from the process under investigation; we must however conclude that this is not the expected peak and, furthermore, that this type of measurement may not be possible for a large range of projectiles and energies. The apparent peak is artificial in that the spectrum shown is not corrected for the E^{-1} dependence of the analyzer transmission. After this correction is made, only a shoulder at ∿200 eV is observed, and from this electron energy, corresponding to an electron velocity equal to that of the projectile, this electron intensity can be identified as electron loss[1] from the incident Ag^{11+} ion as opposed to electron emission from an excited $(Ag^{n+})^*$ ion distribution.

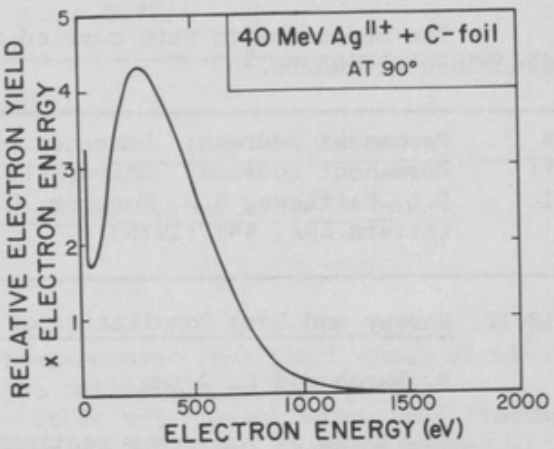

Fig. 13.10-1. Electron spectra at 90° from 40-MeV Ag^{11+} ions incident on a carbon foil. The yield shown is proportional to the cross section for electron production times the electron energy.

At 60 MeV the shoulder moves to higher energies supporting the electron-loss hypothesis, whereas electron emission would be kinematically shifted to lower energies. It was also found that the reflection-mode spectra has the

identical shape as in transmission and, further, that the reflection-mode intensity was consistently about a factor of 2 higher -- a result in the opposite direction expected for emission from excited states produced inside the foil.

It appears that the electron-loss process[1] will considerably hinder the observation of charge-changing electrons in nearly all tandem-energy heavy-ion interactions. Noting that the gas-target average equilibrium charge state of a 40-MeV Ag ion is, fortuitously, also equal to ~11+, together with the extremely high yield from electron loss reported here, it is tempting to speculate that electron loss from excited states may play a more important role than previously assumed in accounting for the gas-solid effects in charge-changing processes.

---

* Permanent address: University of Texas at Austin.

1. D. Burch, H. Wieman, and W.B. Ingalls, Phys. Rev. Lett. *30*, 823 (1973).

13.11 Charge State Distributions for 0.1-1.0 MeV Ne^+ + Ne Collisions Using K X-ray Measurements

D. Burch, R.J. Fortner*, B. Johnson†, D.L. Matthews*, and C.F. Moore†

High resolution measurements of K x-ray intensities are combined with total x-ray production cross sections and charge-state dependent fluorescence yields to obtain production cross sections for ions having one K and multiple L-shell vacancies. Deduced charge state distributions are compared with those determined from inelastic scattering studies and are used to set limits on the probability of having an electron in an excited state at the time of x-ray emission.

The measurements were carried out at the University of Texas and are described elsewhere.[1]

---

* Permanent address: Lawrence Livermore Laboratory, Livermore, California.

† Permanent address: University of Texas at Austin.

1. D.L. Matthews, R.J. Fortner, D. Burch, B. Johnson, and C.F. Moore, Phys. Letters *50A*, 441 (1975).

13.12 Survey and Data Compilation of Inner-Shell Ionization by Electrons

D. Burch and K. Green

Knowledge of the cross sections for inner shell-ionization by incident electrons is necessary for various applied areas of physics and for the interpretation of atomic collisions in solids. This source of inner-shell vacancy production may also be important in gas-target collisions of heavy ions possessing many electrons.

We have carried out a survey and compilation of data relating to inner-shell ionization by electrons and are working on a semi-empirical formula to

reproduce these data. Approximately 35 references have been located presenting K or L-shell data for over 50 elements. The data have been extracted and compiled according to element and incident energy relative to the binding energy. Corrections are being made for recent values of the fluorescence yields which, rather generally, are used inconsistently or inaccurately.

Approximately 10 semi-empirical formulas have appeared, most of which can be reduced to or rewritten in the Bethe form:

$$\sigma = 4N\ \pi a_o^2 \left(\frac{U_o}{U}\right)^2 \times b \times \frac{\ln K\varepsilon}{\varepsilon}\ , \qquad (1)$$

where N is the number of electrons in the shell being ionized which has a binding energy U, and ε is the incident electron energy relative to the binding energy, $\varepsilon = E_e/U$. a_o is the Bohr radius, 0.529 Å, and U_o is the Rydberg energy, 13.6 eV. b and K are empirical functions of the binding energy. Our preliminary results indicate

$$b \simeq 0.03\left(\frac{U}{U_o}\right)^{0.55}$$
$$K \simeq 5.0\left(\frac{U}{U_o}\right)^{-0.3}\ . \qquad (2)$$

Although Eqs. (1) and (2) are still preliminary and are not valid in the extreme relativistic region, they do provide a first estimate of the cross section which is more accurate and universal than previous formulas. The result will be improved as the data evaluation is completed. It is interesting to note that the non-relativistic binary encounter approximation result of Gryzinski[1] is very nearly equivalent to Eq. (1) with b = K = 0.77.

---

1. M. Gryzinski, Phys. Rev. *138A*, 336 (1965).

13.13 Excitation of Outer-Shell Electrons to Bound States in Ne^+ + Ne Collisions

D. Burch

The number and distribution of electrons removed from the L shell simultaneously with K vacancy production in Ne - Ne collisions is fairly well established now over a large energy range.[1] It is not however known what fraction of these are fully ionized as opposed to promoted or excited to bound states. This information could provide a sensitive test of the overall ion-atom interaction and is directly related to vacancy sharing in the exit channel of slow collisions. Excited electrons will also alter the K-shell fluorescence yield.

The purpose of this work is twofold: First, to relate the charge state distributions observed in x-ray spectra[1] to the final charge states produced after Auger decay using the fraction of L electrons in excited states as a

parameter. The final charge states have been measured by several groups. This analysis is straightforward in principle, but is tedious in practice. The result can be expressed in closed form depending upon an assumption about the fate of the promoted K electron, i.e., it goes to the incident ion which initially had one L vacancy, or to the initially neutral target atom, or to the continuum.

The results of this method, which are not completed, can be compared to a second determination which has been completed. In this approach, measured inelastic energy losses for specific final charge-state pairs are compared with Hartree-Fock calculations of the energy loss as a function of charge state. (Somewhat surprisingly this analysis has not been carried out in the past.) The energy loss for excitation to the M shell in Ne is approximately equal to the energy necessary for ionization, and therefore the difference in the observed charge states and the calculated ones is a measure of the excitation to bound states. It is important to note that the actual charge state measurements were made ∿20 ns after the collision, which is longer than typical radiative lifetimes for single electron excitation.

Some results are presented in Table 13.13-1. The results are found to be

Table 13.13-1. Comparison of present calculations with previous measurements of the inelastic energy losses in Ne^+ - Ne collisions. N is the number of electrons liberated per collision producing charge states m and n. The data are for three incident energies at fixed scattering angles and do not include K excitations.

N	(m,n)	$\bar{Q}_{m,n}$ [a)]	$\bar{Q}_{m,n} - Q_{HF}$	ΔN
		100 keV, 10°		
3	2,2	305 ± 25	203	2.8 ± 0.3
4	2,3	390 ± 25	222	2.7 ± 0.3
5	2,4	510 ± 40	249	2.7 ± 0.3
5	3,3	475 ± 25	242	2.4 ± 0.2
6	3,4	575 ± 25	249	2.3 ± 0.3
		150 keV, 10°		
5	3,3	510 ± 40	277	2.7 ± 0.3
6	3,4	610 ± 35	284	2.5 ± 0.3
7	4,4	770 ± 45	350	2.7 ± 0.3
		200 keV, 8°		
8	5,4	770 ± 100	227	1.7 ± 0.7
7	5,3	710 ± 80	260	2.3 ± 0.6
6	4,3	670 ± 50	344	3.0 ± 0.4

a) Q.C. Kessel, Case Studies in Atomic Physics *1*, 399 (1969).

consistent and indicate ∿1.3 electrons, $\Delta N/2$, as the average number excited to the M shell. Or, approximately 50% of the electrons removed from the L shell are left in excited states rather than ejected from the atom. Preliminary results show that the first method supports this conclusion, but in the present formulation of the first method the results are not unique.

---

1. See Secs. 13.7 and 13.11 of this report.

---

14. MEDIUM ENERGY PHYSICS

14.1 Pion-Nucleus Total Cross Section Measurements

M.D. Cooper, I. Halpern, L.D. Knutson, and R.E. Marrs*

During the past year, we had our first run at LAMPF on an experiment to measure pion-nucleus total cross sections. In this report we present some preliminary results which were obtained during this run.

Since the total elastic scattering cross section for charged particles is infinite, we must define more carefully the quantity which has been measured. We write the pion-nucleus scattering amplitude, $f(\theta)$, as a sum of Coulomb and nuclear terms:

$$f(\theta) = f_C(\theta) + f_N(\theta).$$

The total cross section is then defined to be

$$\sigma = \sigma_R + \int_{4\pi} |f_N|^2 \, d\Omega$$

where σ_R is the total reaction cross section. Since $|f|^2$ rather than $|f_N|^2$ is actually measured, one must rely on calculation to extract $|f_N|^2$. One tries to introduce the necessary calculation in a self consistent way.

Experimentally, the quantity

$$\sigma_R(\theta_i) + \int_{\theta>\theta_i} |f|^2 \, d\Omega$$

is determined for a series of angles θ_i. Here $\sigma_R(\theta_i)$ includes all reactions except those for which emitted charged particles emerge at angles smaller than θ_i. A schematic diagram of the experimental arrangement is shown in Fig. 14.1-1. The pion beam is defined geometrically by a pair of timing scintillators. Incident particles are identified as pions either by time of flight[1] or by the DISC, which measures the cone angle of Cerenkov radiation produced by a passing particle.

Pions which pass through the target without undergoing a nuclear interaction and those scattered through some small enough angle are detected in the concentric set of circular transmission counters which are coaxial with the beam. By comparing the number of pions which lead to outgoing charged particles to angles greater than θ_i with the number of incident pions, one determines a "partial total cross section", $\sigma(\theta_i)$. After correcting these cross sections for Coulomb scattering and for Coulomb-nuclear interference (both on the basis of some calculation), one extrapolates them to $\theta_i = 0$. This is the now standard[2] way to determine total cross sections as they have been defined above. For measurements presented in this report, the Coulomb-nuclear interference correction has not yet been made. It remains fairly small for light nuclei.

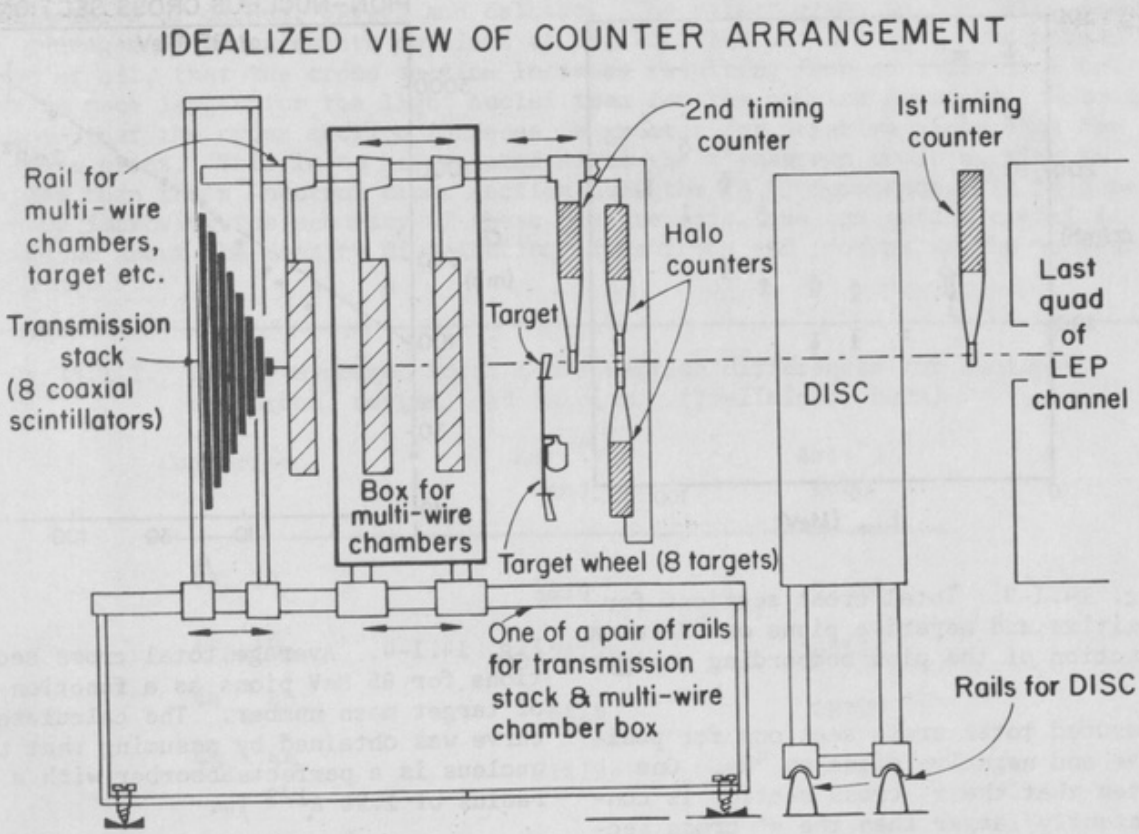

Fig. 14.1-1. Schematic diagram of the arrangement of apparatus in the pion total cross section experiment.

A typical extrapolation curve is shown in Fig. 14.1-2. The measurements are for negative pions on ^{12}C at 85 MeV. The extrapolation curve was obtained by fitting a quadratic polynomial to the measurements for the five largest counters.

In Figure 14.1-3 we present the

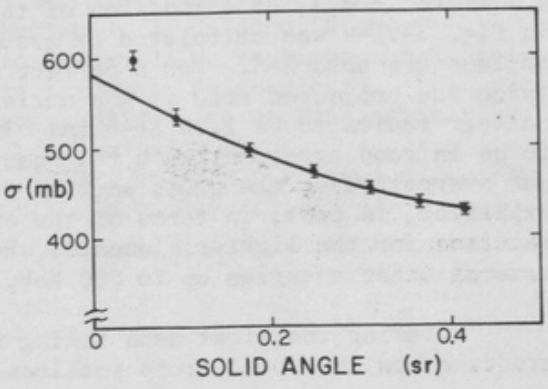

Fig. 14.1-2. A typical solid angle extrapolation curve. The measurements are for negative pions on ^{12}C at 85 MeV. The extrapolated total cross section is 580± 12 mb. The Coulomb-nuclear interference correction has not been included.

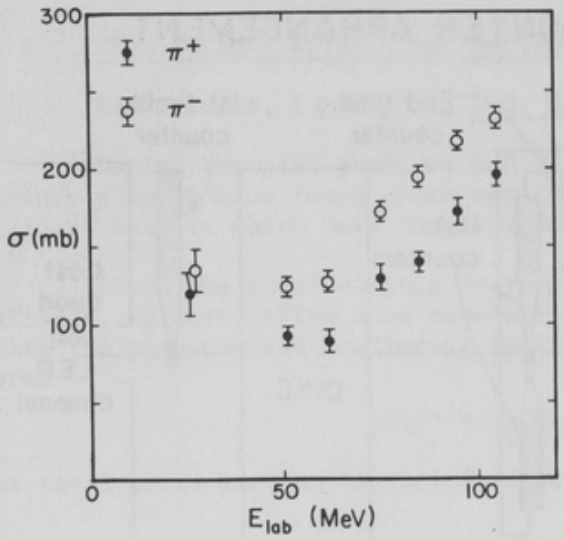

Fig. 14.1-3. Total cross sections for positive and negative pions on ^{4}He as a function of the pion bombarding energy.

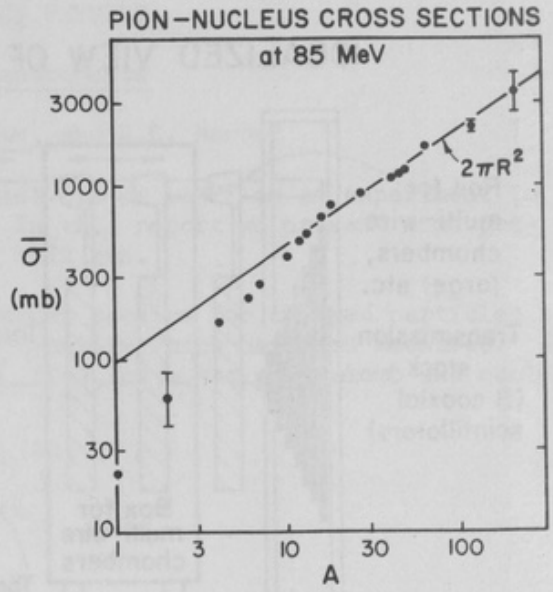

Fig. 14.1-4. Average total cross sections for 85 MeV pions as a function of target mass number. The calculated curve was obtained by assuming that the nucleus is a perfect absorber with a radius of 1.25 $A^{1/3}$ fm.

measured total cross sections for positive and negative pions on ^{4}He. One notes that the π^- cross section is consistently larger than the π^+ cross section. This difference results, in part, from the Coulomb-nuclear interference which increases the π^- cross section and decreases the π^+ cross section. Coulomb distortion of the incident pion wave function also contributes to the $\pi^+ - \pi^-$ difference. For negative pions the Coulomb force is attractive and tends to draw more pions into the nucleus, thus increasing the probability that a nuclear interaction will occur, whereas, for positive pions the effect of the Coulomb distortion is to decrease the cross section.

Figure 14.1-4 shows our measurements of the average total cross section, $\bar{\sigma} = 1/2(\sigma^+ + \sigma^-)$, as a function of target mass number for 85 MeV pions. The curve in Fig. 14.1-4 was calculated by assuming that all pions which penetrate into the nucleus are absorbed. For a perfect absorber, the total cross section is simply twice the projected area of the nucleus. The curve was obtained by taking the nuclear radius to be 1.25 $A^{1/3}$ fm. The prediction of this simple model is seen to be in good agreement with the measurements for intermediate and heavy nuclei, but overestimates the cross section for light nuclei. These deviations can be explained, in part, in terms of the effects of the (3,3) resonance on the cross sections for the lighter elements. We also have data for many of our targets at several other energies up to 200 MeV.

During the first data taking run, a special emphasis was placed on studying how the total cross sections increase when one adds a few neutrons to

any target. In Table 14.1-1 we present the measured cross section differences for isotopes of carbon, oxygen and calcium. The values given in the Table are the averages of measurements obtained at 85, 120, 145 and 170 MeV. One notes, first of all, that the cross section increase resulting from an individual neutron is much larger for the light nuclei than for the calcium isotopes. Second, we note that the cross section increase is greater for negative pions than for positive pions. This is to be expected since the π^+-neutron cross section is smaller than the π^--neutron cross section near the (3,3) resonance. It is hoped that by improving the accuracy of these measurements, one can obtain useful information about the density distribution of neutrons and protons at the nuclear surface.

Table 14.1-1. Energy-averaged total cross section differences for isotopes of carbon, oxygen, and calcium. (Preliminary Data)

Comparison	$\Delta\sigma(\pi^+)$ (mb)	$\Delta\sigma(\pi^-)$ (mb)
^{13}C-^{12}C	38±9	72±10
^{18}O-^{16}O	105±12	160±13
^{44}Ca-^{40}Ca	6±15	38±20
^{48}Ca-^{44}Ca	21±19	65±22

We are now getting ready for our second run. We hope in this run to remove some residual uncertainties in our earlier work. The main emphasis in the coming run (scheduled for Fall '75) will once again be isotope comparisons and also lower energy pion cross-sections. In the meantime we are continuing with the analysis and interpretation of our earlier data.

* R.E. Marrs is now at the California Institute of Technology, and M.D. Cooper is at LASL. Our other collaborators on this experiment include M. Jakobson and R. Jeppesen (U. of Montana), J. Calarco (Stanford), G. Burleson and K. Johnson (New Mexico State U), D. Hagerman and R. Redwine (LASL) and H.O. Meyer (University of Basel, Switzerland).

1. Nuclear Physics Laboratory Annual Report, University of Washington (1974), p. 175.
2. F. Binon *et al.*, Nucl. Phys. *17*, 168 (1970); C. Wilkin *et al.*, Nucl. Phys. *B62*, 61 (1973); A.S. Clough *et al.*, Nucl. Phys. *B76*, 15 (1974).

14.2 Excitation of Giant Resonances by Pion Inelastic Scattering

D. Chiang, I. Halpern, and L.D. Knutson*

Recently the subject of possible giant resonances in nuclei has received considerable attention.[1] A resonance-like structure which appears at an excitation energy of about 63 $A^{-1/3}$ MeV has been observed in variety of nuclei with $A \geq 40$ and has been studied extensively through the inelastic scattering of electrons, protons, deuterons, ^{3}He and alpha particles. It is generally believed that this structure is primarily a T=0 giant quadrupole resonance (GQR). During the past year we have undertaken an experiment to study excitation of the GQR by pion inelastic scattering.

Pions have some advantages over the heavier projectiles, because they interact with a relatively low orbital angular momentum. This means that the interesting features in the angular distributions (i.e., the first maximum and first minimum) occur at relatively large angles which are consequently easy to determine experimentally. In addition, the low pion angular momentum insures that nuclear excitations of high multipolarity will not readily occur in inelastic pion scattering. This fact may turn out to be important, since much of the "background" observed in the region of the GQR corresponds to excitation of these higher multipoles.[2]

The initial run on this experiment (which amounted to 24 hours of beam time) was designed as a feasibility study, during which we investigated counting rates and the properties of various spectra. A schematic diagram of the experimental setup is shown in Fig. 14.2-1. Positive pions with an energy of 60 MeV were incident on a natural Zr target. Scattered particles were counted by a pair of 1.5 cm thick intrinsic germanium detectors[3] which were used as a particle identification telescope. For each event observed, a particle identification value was calculated from the formula

$$PID = C[(E1 + E2)^{1.73} - (E2)^{1.73}]^{1/2}$$

where E1 and E2 are the energies deposited in the first and second detectors respectively. The germanium counters were surrounded by plastic scintillator veto detectors, which define the solid angle, reject particles which enter the telescope from the side, and reject particles which are sufficiently energetic

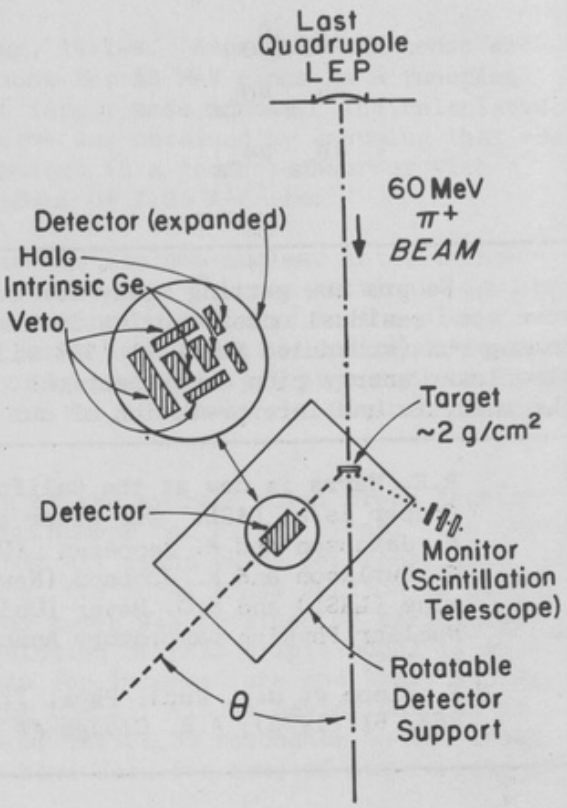

Fig. 14.2-1. Schematic diagram of the experimental arrangement.

to pass through both germanium counters.

In the following paragraphs, we will describe briefly what was learned during the feasibility study. In Fig. 14.2-2 we present a sample PID spectrum for pion scattering from Zr at an angle of 100°. We observe that the contamination of the inelastic pion spectrum by background events such as nuclear interactions in the detectors and events caused by protons, muons and electrons is insignificant. This conclusion is based on the assumption that contaminant events would produce a broad background in the PID spectrum. For the spectrum shown, elastically scattered pions were sufficiently energetic to pass through both germanium detectors and were rejected by the veto scintillator. Thus the peak in the PID spectrum arises entirely from inelastic pions. Note that in the region of the pion peak, the background from all contaminant events is less than 10%. In addition we have learned that the detector telescope effectively distinguishes pions from muons. At angles where the muon intensity was appreciable, a clean separation between the muon and pion peaks in the PID spectrum was obtained.

It was also determined that contaminant low energy pions in the primary beam are not plentiful enough to produce significant background in the spectrum. This conclusion was reached by means of a run in which the beam intensity was reduced to permit moving the germanium detector into the primary beam. The number of detected pions which had energies from 5 to 20 MeV below that of the nominal beam energy was found to be a small fraction (0.5%) of the total number of pions.

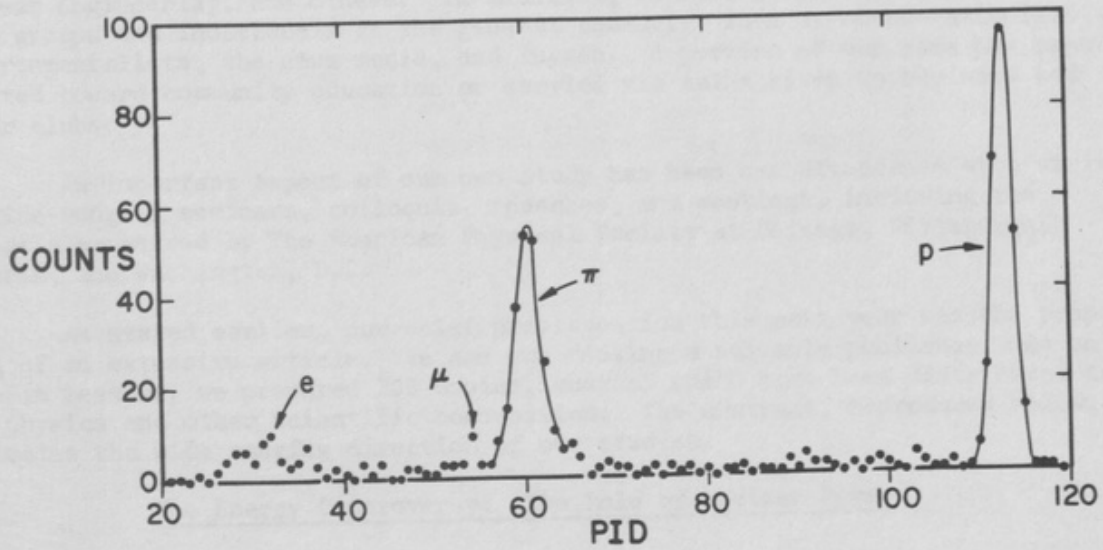

Fig. 14.2-2. Spectrum of PID values for inelastic scattering of 60 MeV positive pions from Zr at $\theta = 100°$. The peaks corresponding to electrons, muons, pions, and protons are identified.

The energy resolution obtained in the run was essentially that of the incident pion beam (∿2 MeV). This was confirmed by passing the scattered pions through an absorber to bring the elastic pions into the detector range. The width of this degraded elastic peak was about 2.5 MeV. By varying the absorber thickness, we confirmed that the detector resolution and efficiency are uniform throughout the energy region of interest.

Finally, we observed that the counting rate of inelastically scattered pions is sufficiently high that one should be able to see any significant structure in the region of the giant resonances. From the observed rate, it is calculated that with the expected ten-fold increase in beam intensity, we should collect 2-3 counts per minute per MeV of excitation energy. Beam time sufficient to carry out a meaningful inelastic scattering experiment has therefore been requested.

---

* Our collaborators in this work include: J. Amann, P. Barnes, S. Dytman, R. Eisenstein and J. Penkrot of Carnegie-Mellon University, A. Thompson of Lawrence Berkeley Laboratory, and M. Cooper, E. Flynn and J. Sherman of Los Alamos.

1. G.R. Satchler, Physics Reports *14C*, 98 (1974).
2. M.B. Lewis, Phys. Rev. C *9*, 1878 (1974).
3. The germanium detectors were provided by the Carnegie-Mellon group.

---

15. ENERGY STUDIES

15.1 Energy Studies

D. Bodansky and F.H. Schmidt

Our energy study program, which was begun in the spring of 1973, continued during the past year with the major emphasis directed toward preparation of an extensive article, or a small book. In order to devote our full attention to this project, we dropped the seminars which we had inaugurated the previous summer.

The early objectives of our studies were to gain overall views of the "Energy Crisis" via an understanding of the various resource issues, to be followed by technical assessments of the so-called alternatives to the presently deployed energy sources.

Although we did not initially believe that nuclear fission energy was of great importance in the "logical" equation, we now consider the probability that any other alternatives will prove feasible for major contributions to man's needs is remote. Thus, as our studies progressed, we found ourselves devoting more and more time to the technical and social aspects of fission energy, and especially to those issues generally surrounding the "Nuclear Controversy".

Our work has brought us into more and more contact with other disciplines on the University campus, such as Geology, Environmental Studies, Economics, Nuclear Engineering, and others. In addition, we have established communication with groups and individuals in the general community such as conservationists, environmentalists, the news media, and laymen. A portion of our time has been devoted toward community education or service via talks given to business and other clubs.

An important aspect of our own study has been our attendance at a variety of wide-ranging seminars, colloquia, speeches, and meetings, including the symposia sponsored by The American Physical Society at Chicago, Pittsburgh, Anaheim, and Washington, D.C.

As stated earlier, our chief preoccupation this past year was the preparation of an extensive article. We are now seeking a suitable publisher. As an interim measure, we prepared 300 copies, most of which have been distributed to the physics and other scientific communities. The abstract, reproduced below, indicates the wide ranging direction of our studies.

The Energy Controversy: The Role of Nuclear Power

Abstract

The objective of this paper is to show that nuclear fission power is the best, and may be the only, alternative source of energy. It is written for a wide range of readers, including non-scientists and scientists who are not particularly informed on the issues involved.

The first question concerns man's need for energy; it is concluded that conservation measures alone cannot suffice. Next, the earth's energy sources are examined, and the extent of each is estimated in the simple context of the length of time it could last at present use rates. Only nuclear fission, nuclear fusion, and solar energy can provide for future time scales commensurate with man's historic past, while avoiding the possibility of catastrophic social upheaval.

Fusion and solar energy are rejected on technological grounds because the world energy problem is so pressing that one cannot gamble on hopes for future technological breakthroughs. Thus, only nuclear fission meets the twin criteria of technological feasibility and adequate resource base.

Each of the controversial issues surrounding nuclear fission energy is examined in some detail. The conclusion is reached that none is serious, and that nuclear fission offers by far the best energy source from environmental, economic, longevity, and overall safety standpoints.

16. RESEARCH BY USERS AND VISITORS

16.1 Fast Neutron Beam Radiotherapy - Medical Radiation Physics*

J. Eenmaa†, H. Bichsel†, K. Weaver†, R. Seymour†, and P. Wootton†

The Division of Medical Radiation Physics has participated in and has supported essentially all facets of the fast neutron beam therapy program at the University of Washington 60-inch cyclotron during the past year. These activities have included the following: (1) Acquisition of basic neutron dosimetry data. (2) Dosimetry intercomparisons with other neutron therapy facilities. (3) Theoretical studies of neutron dosimetry. (4) Installation and development of computer-control and data acquisition systems. (5) Design and development of special patient handling devices and setup procedures. (6) Routine maintenance and continued development of the patient therapy facility. (7) Support of therapy operations, including actual patient therapy. (8) Support of radiobiological and experimental oncological studies and of other, non-clinical, outside users of the fast neutron beam. These activities are described in greater detail below.

(1) Acquisition of basic neutron dosimetry data. The physicists at the three centers in the United States engaged in fast neutron beam therapy have agreed to express depth-doses, for purposes of patient therapy, in tissue-equivalent (TE) liquid phantoms of density 1.07 g/cc, and of muscle-equivalent composition.[1] Tissue-equivalent liquid of this density and composition has been prepared and measurements of build-up curves, central-axis percentage depth dose distributions, transverse beam profiles, etc., for the range of field sizes and field configurations utilized in patient treatments, are under way. The effects of phantom density and phantom size on these quantities is being investigated.

Part of the dose delivered by a fast-neutron therapy beam is unavoidably due to photons. Most of the photon contamination is produced by neutron inelastic-scattering and absorption reactions in shields, collimators, and especially the patient's body. The photon dose fraction varies with field size, depth in tissue, and distance from the beam axis. A separation of the total dose into neutron and photon components is desirable for a number of reasons. Since the biological effectiveness of photons is much smaller (by about a factor of 3) than that of neutrons, the variance in the photon dose fraction with position in the irradiated volume should be known. In addition, some patients are treated with both the neutron beam and a pure photon beam; the need to sum neutron and photon dose fractions separately makes knowledge of the photon contamination of the neutron beam necessary. Finally, dosimetry data interchanged with other neutron therapy centers are often expressed as neutron doses rather than total doses. For these reasons a reliable technique for separating neutron and photon doses is needed.

Our technique for determining dose components involves the use of a tissue-equivalent proportional counter (TEPC). With this device, energy deposition by single ionizing particles travelling through small TE gas volumes can be recorded, and a distribution of dose as a function of energy absorbed per ionizing event, Fig. 16.1-1, can be determined. An integral over this distribution yields the total dose. On the average, neutron-induced events result in larger energy

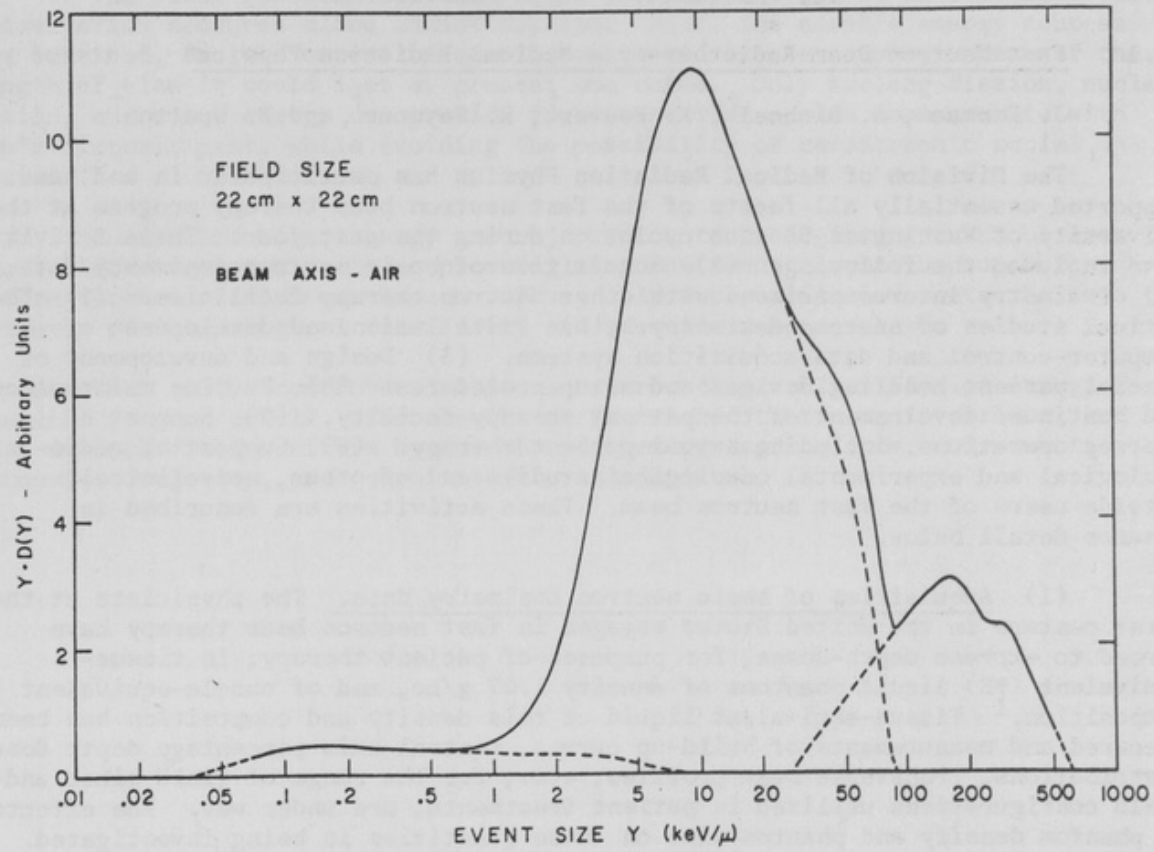

Fig. 16.1-1. A dose distribution measured in a neutron radiotherapy beam. The abscissa is the energy deposition in the counter divided by the effective sensitive-volume diameter (in this case, 2μ). The abscissa is plotted on a logarithmic scale to show detail over a large range of event sizes; to preserve the relationship of area to dose in this case, the product of dose and event size was plotted as the ordinate.

depositions than do photon-induced events; however, the portion of the dose distribution due to photons and the portion due to neutrons overlap. By separating and integrating individually the neutron and photon components of the total-dose distribution, we obtain dose fractions due to each type of radiation. The separation technique involves measuring dose distributions for pure photon sources and normalizing the spectral shapes so obtained to the neutron-plus-photon distribution at points where neutron events are negligible. Work is under way to measure the variation in photon dose fraction with field size and position inside and adjacent to an irradiated tissue-like volume. Preliminary results are shown in Table 16.1-1. This table also presents the relative fraction of the total dose that is due to recoil protons, and the part that is due to α's and heavy recoils.

(2) Dosimetry intercomparisons with other neutron therapy facilities. Dosimetry intercomparison measurements have taken place between physicists from

the M.D. Anderson Hospital -- TAMVEC, the Naval Research Laboratory, the MRC Cyclotron at Hammersmith Hospital in London, England, and the University of Washington. The parameters that are compared are: tissue kerma in air, build-up curves in phantom, tissue dose at depth of dose maximum, relative central axis depth dose, beam profiles, neutron/gamma ratios in air and in phantom, and photon calibrations of ionization chambers. Other parameters that are compared are values of W, stopping power ratios S_r, kerma corrections, and calculations that lead to the statement of tumor doses for patients.

The results of these intercomparisons to data show that the statement of the total (n + γ) dose agrees to three per cent among the United States institutions. However, it is recognized by all the fast neutron groups that the present dosimetry may eventually be modified by several per cent when accurate spectral and cross-section data have been obtained on all of the beams. Meanwhile, a comparison of the clinical results from each institution can be made with the knowledge of the agreements and disagreements of the dosimetry between the institutions.

(3) Theoretical aspects of neutron dosimetry with gas ionization chambers. The ionization in a TE ionization chamber is produced by a large number of species of charged particles (p, d, α, Be, B, C, N, O, etc.) with a wide range of energies. The relevant values of W (energy per ion pair) and stopping power ratios S_r, are particle and energy dependent. Calculations have been performed to obtain appropriate average values of W and S_r for a few particles so far. Since the input data are not well known, much further work remains to be done.

(4) Installation and development of computer-control and data acquisition systems. The Raytheon 704 computer system is being expanded to improve the patient treatment. The computer will aid in record keeping, machine settings, and treatment monitoring. The use of a dedicated computer will allow continuous surveillance of the treatment environment and quality, and data which might be lost or overlooked will be recorded automatically at all times. Programmed interaction with the operator will maintain full flexibility of operation with the additional safeguard of preplanned regimens of operation.

To organize and use the data being recorded during the therapy sessions, a small data bank system is being worked up for the computer. This will allow the physicians to review a patient's past treatments to aid in the planning of future therapy. Statistical data based on the entire patient population will also be available, although not as an on-line feature at first.

(5) Design and development of special patient handling devices and setup procedures. A motorized treatment couch has been designed and a contract let for its construction. This couch will have beam iso-centric positioning capability and can operate either as a chair, table, or stand-up support for various treatment configurations. Although its initial intent is to provide a method of better patient setup through metrification of position, it will also ease and speed up the setup operation for the clinicians. The couch will eventually be connected to the monitoring minicomputer, first to provide recording capability for the setup, and then to provide a means for external control, for the computer to bring the patient to his treatment position automatically. This

Table 16.1-1. Variation in the relative fraction of the total dose that is due to photons, recoil protons, and α's and heavy recoils with field size and position inside and adjacent to an irradiated tissue-like phantom.

Field Size at 150 cm SSD	Detector Position	% Contribution to Total Dose		
		γ	α & heavy recoil	protons
22 cm X 22 cm	beam axis - air	5	16	79
	2 cm deep in fluid	8.5	14.5	77
	10 cm deep in fluid	13	13	74
	edge of field - air	9	13	78
	shielded area - air	29	8	63
13 cm X 13 cm	beam axis - air	4	16	80
	2 cm deep in fluid	6	15	79
	10 cm deep in fluid	8	15	77
	20 cm deep in fluid	14	14	72
	10 cm in fluid - field edge	16	12.5	71.5
8.5 cm X 8.5 cm	beam axis - air	4	16	80
	2 cm deep in fluid	7	14	79
	10 cm deep in fluid	8	14	78
	edge of field - air	6	16	78

feature will allow utilization of the three-minute "cool-down" period following each exposure, when the residual background radiation levels in the treatment area keep the technicians from entering the treatment area to set up the patient's next field. By minimizing between-treatment time lag, a larger number of patients can be treated within a given time period.

(6) Routine maintenance and continued development of the patient therapy facility. Approximately thirty-five borated water-extended polyester resin (B-WEP) neutron beam collimators, in a range of circular, square and rectangular sizes, have been constructed for dosimetry measurements and patient treatment. These can be modified by B WEP inserts for specific field configurations. External blocking (20 cm steel) is utilized for treatment situations in which internal shimming of collimators is not feasible and for "on-the-spot" field modifications.

(7) Support of therapy operations. A physicist is on site and assists in routine therapy operations. These activities include personnel dosimetry monitoring, patient dosimetry calculations, setup of collimators, external blocks and wedges, and settings of dosimetry monitoring instrumentation.

(8) Support of non-clinical operations. These include support of radiobiological and experimental oncological studies, and of other, non-clinical outside users of the fast neutron beam: Dr. Rodney Withers and Dr. David Hussey from M.D. Anderson Hospital in Texas, Mr. Medhi Sohrabi from Georgia Institute of Technology and Dr. H.B. Knowles from Washington State University.

---

* Supported by the National Cancer Institute, Grant No. CA 12441.
† Division of Medical Ratiation Physics, Department of Radiology, University of Washington.
1. N.A. Frigerio *et al.*, Phys. Med. Biol. *17*, 792 (1972).

16.2 Fast Neutron Beam Radiotherapy -- Experimental Oncology*

Janet S.R. Nelson†

Research in the Division of Radiation Oncology is supportive of the neutron beam therapy program which is currently treating cancer patients with neutrons. This research program is concerned principally with the response of murine tumors *in vivo* and tumor cells *in vitro* to neutrons and to 250 kVp X-rays. The principal areas of investigation during the past year and at present are: (1) the response of C3HBA mammary tumors and mouse skin to fractionated neutrons or X-rays and to mixed neutron-photon fractionation schemes; (2) the mechanisms underlying reduced growth rate in C3HBA tumors recurring after X-rays or neutrons; (3) the effectiveness of neutrons compared to X-rays used as preoperative radiation of the C3HBA mammary tumor; (4) *in vitro* response of the EMT6 tumor cell line to neutron and X-irradiation; and (5) the response of the EMT6 mammary tumor *in vivo* to mixed neutron-photon fractionated irradiation.

Each project is described in more detail below.

1. The response of mouse foot skin and the C3HBA mammary adenocarcinoma of the C3H mouse to 250 kVp X-rays and cyclotron-produced neutrons (8 MeV mean energy) has been studied. Neutrons or X-rays were given in single fractions (fx): 2 fx 24 hours apart; 2 fx 96 hours apart; and 5 fx in 5 days. Two fx of neutrons + 3 fx of X-rays in 5 days also were given in the sequence n-n-x-x-x or n-x-x-x-n. When neutron-only schemes were compared to X-ray-only schemes, RBE's[1] for early skin damage and foot deformity at 6 months postirradiation increased with increasing number of fractions. The RBE for 2 fx of neutrons + 3 fx of X-rays (total dose of neutrons + X-rays) relative to 5 fx of X-rays was 1.3 for both mixed fraction sequences. Tumor growth delay following single and fractionated X-rays suggested an hypoxic fraction of cells which undergoes extensive and long-lasting reoxygenation, a situation in which fractionated neutrons might not be expected to show an advantage in terms of tumor damage relative to normal tissue injury. Therapeutic gain factors (TGF = tumor RBE/skin RBE) for single fractions ranged from 1.6 to 1.8 depending on dose level while TGF's for fractionated neutrons varied from 0.73 for 2 fx 24 hours apart to 0.96 for 5 fx in 5 days. For both the n-n-x-x-x and n-x-x-x-n fractionation schemes, a TGF of 1.1 suggests that the mixed fractionation schemes may be slightly better than neutron-only schemes in this tumor system.

2. C3HBA mammary tumors were irradiated with 3000 rads of 250 kVp X-rays or 1000 rads of 8 MeV neutrons, doses of radiation matched for producing equal growth delay. At 14 days postirradiation, tumors were regrowing at a reduced rate relative to controls. Cell kinetic parameters were examined using per cent labeled mitoses techniques, and blood vessel spacing and tumor architecture were examined histologically to determine if the mechanisms underlying growth rate changes were the same after neutrons as after photon irradiation.

The tumor volume doubling time (T_d) at 14 days posttreatment is similar in both irradiated groups (T_d = 117 hours for neutron irradiated tumors, 132.4 hours for X-irradiated tumors) and is approximately twice as long as the T_d of 61.4 hours in control tumors in the same size range. Both control and X-irradiated tumors have similar median cell cycle durations of 19.3 and 18.5 hours respectively; the more slowly growing X-irradiated tumors have a reduced growth fraction (GF) and increased cell loss factor (ϕ). Regrowing neutron irradiated tumors have a longer median of T_c of 27.2 hours, with GF and ϕ values intermediate between those for control and X-irradiated tumors.

The average distance from tumor parenchymal interphase cells to the nearest blood vessel is nearly identical in the two irradiated groups and for both groups is significantly greater than interphase to vessel distance in controls. This average distance in irradiated tumors approaches the maximum distance of O_2 diffusion in mouse adenocarcinomas of a corded structure surrounding a central blood vessel. Both neutron and X-irradiated tumors contain more necrosis and less viable-appearing parenchymal cell than do control tumors of the same size. The similar growth rate and growth delay in this tumor after 3000 rads of

1. RBE = relative biological effectiveness, = dose of X-rays necessary to produce a specified effect/dose of test irradiation necessary to produce same effect.

X-rays or 1000 rads of neutrons occurs in the face of different cell cycle durations and seems related to similar circulatory systems inadequacies which limit growth and are expressed as greater average cell to blood vessel distance and increased cell loss leading to necrosis, indicating oxygen or nutrient deprivation.

3. Experiments using single fractions of radiative are underway to determine the effects of preoperative X- or neutron irradiation on the recurrence of a primary C3HBA mammary tumor surgically excised after exposure. The number and size of lung metastases is also being studied and related to the response of the primary tumor. Determination of the 50% curative dose for this tumor with both types of radiation is being undertaken to establish a point of comparison between the curative dose and effective doses of preoperative neutrons and X-rays. The lung metastases study is of special interest due to the scatter and leakage radiation received by the animals when the primary tumor is locally irradiated with neutrons, a situation not encountered with the X-ray facilities. Several published reports show that X-irradiation to tumor-free organs can enhance their susceptability to metastatic tumor growth. (This study is being conducted by Tore Straume, a M.S. candidate in Radiological Sciences.)

4. EMT6 mouse mammary tumor cells have been irradiated *in vitro* with X-rays or neutrons to determine RBE's for cell killing and for mitotic delay. For 250 kVp X-rays, the D_o[1] = 165 rads; for cyclotron neutrons the D_o = 115 rads. The RBE for cell killing at different survival levels, is as follows:

Surviving Fraction	X-ray Dose, Rads	Equivalent Neutron Dose, Rads	RBE
0.5	350	180	1.9
0.1	625	415	1.5
0.01	1000	675	1.5
0.005	1115	755	1.5

Ratio of D_o values: $\frac{D_o \text{ X-rays}}{D_o \text{ neutrons}} = \frac{165}{115} = 1.43$

The RBE for mitotic delay also varies with dose.

Mitotic Delay, Hrs.	X-ray Dose, Rads	Equivalent Neutron Dose, Rads	Neutron RBE
6	330	50	6.6
8	625	250	2.5
10	900	450	2.0
12	1325	650	2.0

1. D_o = dose of radiation necessary to reduce cell survival by a factor of 0.37.

The RBE for mitotic delay is higher than the RBE for cell survival, a factor which must be considered in interpreting the results of experiments comparing the response of EMT6 solid tumors to X-rays and neutrons, particularly if one or two initial neutron fractions are used in a mixed fractionation scheme.

5. Experiments are now underway examining the response of EMT6 solid tumors to 1 fx, 2 fx or 5 fx of X-rays, given at 24 hour intervals, 1 or 5 fx of neutrons, and mixed neutron-photon fractionation schemes, in which 2 fx of neutrons + 3 fx of X-rays are given in 5 days, in the sequence n-n-x-x-x, or n-x-x-x-n. The results obtained with these treatment patterns will be compared to similar experiments done with the C3HBA tumors, described previously.

---

* Supported by the National Cancer Institute, Grant No. CA-12441.
† Division of Radiation Oncology, Department of Radiology, University of Washington.

16.3 Radiobiological Characterization of Radiotherapy Fast Neutron Beam*

J.P. Geraci†, K.L. Jackson†, and G.M. Christensen†

The major objective of this program is to obtain data which will permit safe and more effective application of fast neutrons in radiotherapy using the University of Washington cyclotron. For this purpose the RBE of cyclotron neutrons for esophagus and lung damage was measured. Mice die from esophagus damage between 10 and 50 days post-exposure. The $LD_{50/50\ day}$ with X-rays was 2840 (1955-3293) rad and the neutron RBE was 1.9. Death from lung damage occurred between two and six months post-exposure. The $LD_{50/6\ month}$ for lung damage with neutrons was 930 (755-1129) rad. The $LD_{50/6\ month}$ with X-rays was 1485 (1223-1802) rad, yielding an RBE of 1.6.

A study also was carried out to determine if there is a difference in the rate of cell repopulation and short term recovery in thymus, spleen, small intestine and testes following neutron as compared to X-irradiation. Based on changes in organ DNA content, no differences in rate of repopulation were observed in these tissues following single doses of X-rays or neutrons. The rate of short-term recovery following X-irradiation or neutron-irradiation did not differ in spleen, thymus or testes. However, in the small intestine there was a lag in the recovery process with neutrons, but equal recovery occurred with X-rays or neutrons by 16 hours.

Decrease in mouse testes DNA 28 days after exposure also was used to measure RBE at various positions in the fast neutron treatment facility. The neutron RBE for testes damage was found to be independent of depth in a tissue equivalent absorber along the central axis of the primary beam. However, the RBE increased with decreasing field size and was greater in the penumbra as compared to the central axis of the primary beam.

The rad dose in the shielded region of the facility was 2.8% of the primary beam central axis dose with a patient phantom in the primary beam. Under these conditions the average RBE for testes damage in the shielded area was 4.9 as

compared with 3.0 in the primary beam. Measurement of sodium activation at depth in an absorber indicated that the neutrons in the shielded region are fairly penetrating.

---

* Supported by the National Cancer Institute, Grant No. CA-12441.
† Division of Radiation Biology, Department of Radiology, University of Washington.

16.4 Fast Neutron Beam Radiotherapy-Clinical Program*

R.G. Parker†, A.J. Gerdes†, and H.C. Berry†

The ultimate objective of this project is the clinical evaluation of the treatment of human cancers with fast neutron beams. Theoretically, fast neutrons may be more effective than X-ray or gamma photons in killing cancer cells because of: less dependence on full physiologic oxygenation at the time or irradiation; less variations in responsiveness to radiation throughout the cell replication cycle; and less capacity for repair of cellular damage.

The first patient was treated on 10 September 1973. Since that time, 94 patients have been treated including: glioblastoma multiforme 27; carcinoma arising in the head and neck 49; metastatic adenopathy in the neck 12; epidermoid carcinoma of the thoracic esophagus 2; Pancoast tumor 4.

To date, the objectives of the study have been: (1) to develop treatment techniques; (2) to observe responses of selected tumors; and (3) to study normal tissue tolerances.

Techniques for the treatment of head and neck tumors have been developed. A versatile chair-couch for patients has been designed and is under construction. This device will facilitate the treatment of tumors in the chest, i.e., cancer of the esophagus and pelvis, i.e., cancer of the cervix.

Conclusions to date are: (1) short-term patient tolerance of fast neutron beam radiation therapy is comparable to that of conventional photon treatment; (2) nearly all cancers respond although the extent of those treated so far precludes a high rate of long-term control.

Within the next few months, patients with glioblastoma multiforme and certain head and neck cancers will be treated according to a protocol developed and shared with investigators at the M.D. Anderson Tumor Institute (Houston, Texas) -- TAMVEC -- and the MANTA (Washington, D.C.) program.

---

* Supported by the National Cancer Institute, Grant No. CA 12441.
† Division of Radiation Oncology, Department of Radiology, University of Washington.

16.5 Fast Neutron Production System at the University of Washington Van de Graaff for Delayed Neutron Studies*

G.W. Eccleston†, W.R. Sloan†, and G.L. Woodruff†

The energy spectra of delayed neutrons associated with the fast fission of ^{232}Th, ^{233}U, ^{235}U, ^{239}Pu isotopes is presently being measured.[1] The University of Washington Van de Graaff is used to produce the neutron source via the $^{9}Be(p,n)^{9}B$ reaction. This source is representative of a degraded fission spectrum.[2]

Delayed neutron measurements were initially being conducted at the University of Washington Cyclotron facility.[3] However, these studies were subjected to excessive gamma ray fluxes and were located in close proximity to a concrete wall backed by water which produced undesirable room return effects. Both of these difficulties were considerably reduced by moving the experiment to the Van de Graaff facility.

Measurements at the Van de Graaff were preceded by the design and construction of new beam control equipment, a target system, and an isotope-detector positioning mechanism.

This equipment was interfaced to a beam port at the analyzing magnet in Cave 3. At this position the beam passes straight through the tandem accelerator and onto the target without going through the corona regulator system. The advantage of this location is that electrostatic deflection of the proton beam can be accomplished at the low energy cup without interference from the corona regulator. Location of the experimental setup and the beam deflection module is shown in Fig. 16.5-1.

Delayed neutron measurements require sample irradiations followed by a counting cycle with the irradiation source removed. The neutron source is produced by impinging a 10 MeV proton beam onto a thick (80 mil) beryllium target.[4] Beam strengths from 1 μa to 10 μa are selected and occupy a somewhat circular area of 0.5 cm^2 at the center of the target. On-off beam control is accomplished using logic signals supplied from the experimental equipment. Beam deflection arises when a switched high voltage supply places 3000 volts onto the two chopper plates located near the low energy cup. On-off beam times less than 10 milliseconds are achieved.

---

* Work supported by U.S. Atomic Energy Commission, Contract No.

† Department of Nuclear Engineering, University of Washington.

1. See Sec. 16.7 of this report.
2. P. Porter, Masters Thesis, University of Washington, Department of Nuclear Engineering, Feb. 1975.
3. Nuclear Physics Laboratory Annual Report, University of Washington (1974), p. 194.
4. See Sec. 16.6 of this report.

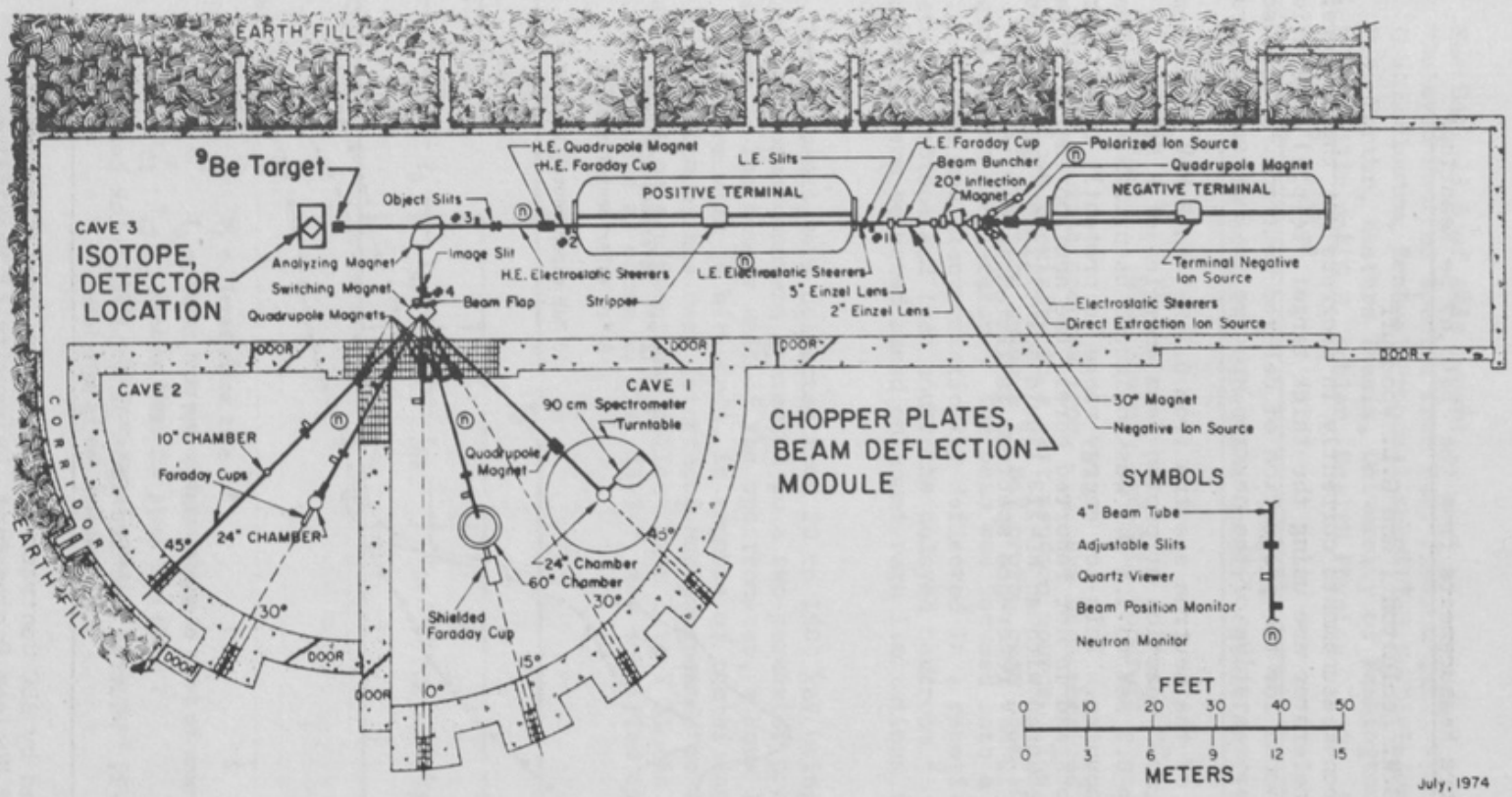

Fig. 16.5-1. Fast neutron production system for delayed neutron studies.

16.6 Neutron Spectra Measurements from the $^{9}Be(p,n)^{9}Be$ Reaction*

P. Porter†, G.W. Eccleston†, and G.L. Woodruff†

Delayed neutron measurements currently in progress[1] at the University of Washington Tandem Accelerator are using the thick target $^{9}Be(p,n)^{9}B$ reaction to generate a neutron source for the production of delayed neutrons.[2] This source is intended to be representative of the neutron spectra in fast reactor systems.[3]

Measurements of the neutron spectra from 0.3 MeV to 8 MeV have been collected for the $^{9}Be(p,n)^{9}B$ reaction at proton beam energies of 8 MeV and 10 MeV. The energy range from 0.3 MeV to 1.5 MeV was collected using a 5 atm methane filled proportional counter. This low energy range is presently being corrected for downscatter effects and is not reported here. The neutron energy range from 1 MeV to 8 MeV was measured with an NE-213 liquid scintillator[4] and is presented in Fig. 16.6-1. The 12 MeV reference spectrum is listed in Ref. 5.

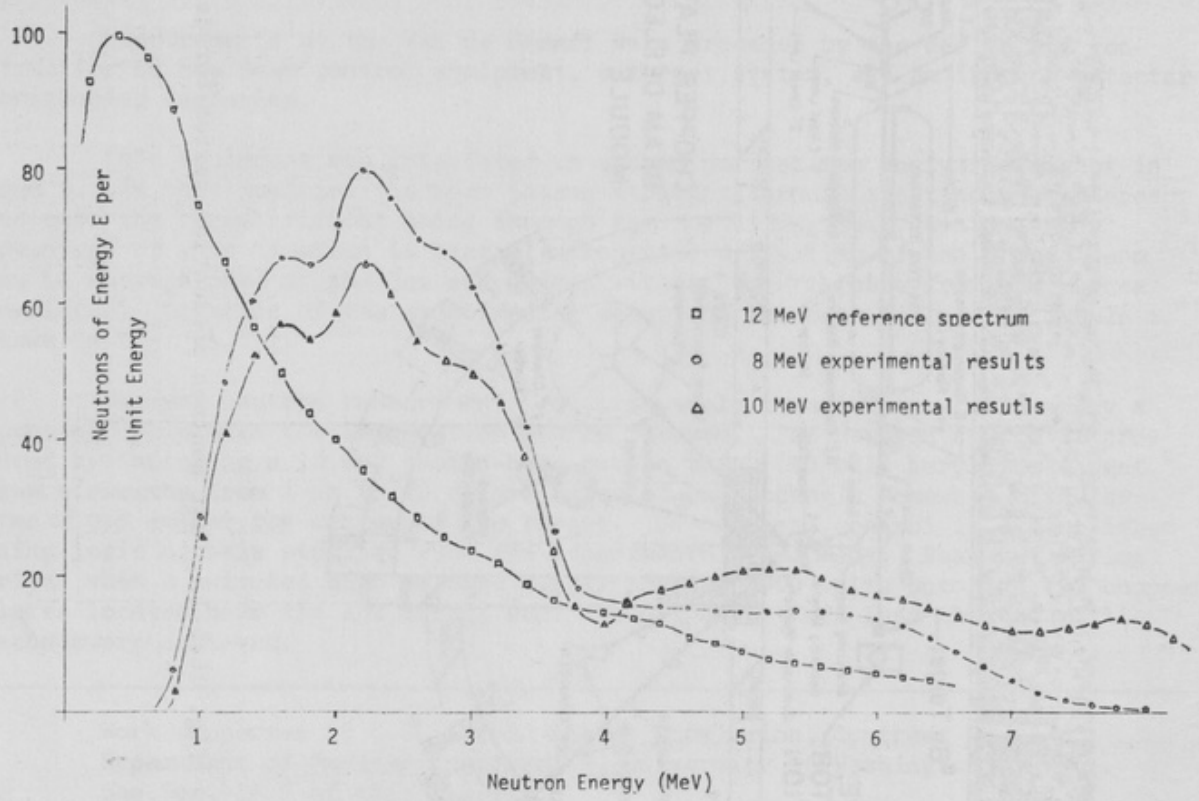

Fig. 16.6-1. Neutron spectra from protons on thick beryllium.

---

* Work supported by AEC Contract AT(45-1)-2225, Task Agreement 31.

† Department of Nuclear Engineering, University of Washington.

1. See Sec. 16.7 of this report.

2. See Sec. 16.5 of this report.
3. "Delayed Neutron Spectra from Fast Fission", G.L. Woodruff, W.R. Sloan, and G.W. Eccleston, Renewal Proposal submitted to Division of Research, USAEC.
4. P.H. Porter, Masters Thesis, University of Washington, 1975.
5. E. Tochilin and G.D. Kohler, Health Physics *1*, 332 (1958).

16.7 Measurements of Delayed Neutron Spectra Resulting from Fast Fission of ^{235}U*

G.W. Eccleston†, W.R. Sloan†, and G.L. Woodruff†

Delayed neutron spectra from ^{235}U have been obtained by placing the sample in close proximity to a fast neutron source. The source was produced by the $^{9}Be(p,n)^{9}B$ reaction using a 10 MeV proton beam from the University of Washington Tandem Accelerator.[1] The beam was focused onto a thick (80 mil) beryllium target and electrostatically deflected in a repetitive cycle to re-irradiate the isotope and then count the delayed neutrons.[2] Beam strengths from 1 μa to 10 μa were selected based on count rate limitations in the nuclear electronics.

Measurements were collected from 20 to 1500 keV using hydrogen and methane filled proportional counters connected to a two-parameter proton-recoil spectrometry system.[3] The memory unit of the spectrometer, a Nova 1220 computer consisting of a 32K core with 16 bit words, is capable of containing 7 full blocks of data. This equipment has been interfaced and programmed to automatically control the beam deflection equipment and collect from 1 to 7 blocks of data in a repetitive sequence, as shown in Fig. 16.7-1, for specified irradiation and

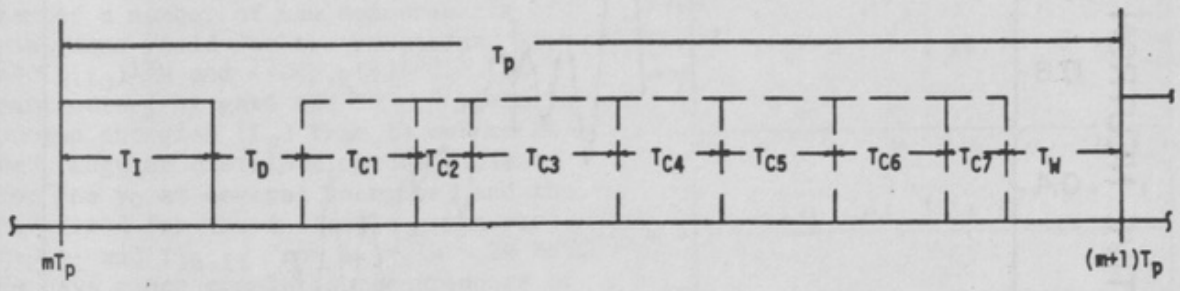

T_I = Irradiation time
T_D = Delay from end of irradiation to start of counting
$T_{C1} - T_{C7}$ = Counting times for block 1 to block 7
T_W = Wait time from end of counting to start of next cycle
T_p = Total time of one complete cycle

Fig. 16.7-1. The m^{th} irradiation-delay-count-wait cycle of a measurement using seven counting periods.

counting times. To date, measurements on the ^{235}U isotope have been completed for the two cycles of Table 16.7-1. The objective of measuring successive blocks in time is to permit an assignment of half-lives to the delayed neutron energy peaks.

Table 16.7-1. Cyclical irradiation and counting time for delayed neutron measurements from the short (<1 sec) and medium (1-3 sec) life precursors.

Cycle*	Times (Sec)								
	Irradiation	Delay	Count Block							Wait
			1	2	3	4	5	6	7	
Short	1.0	0.1	0.1	0.1	0.1	0.1	0.1	0.1	0.1	0.0
Medium	5.0	1.0	0.6	0.6	0.6	0.6	0.6	0.6	0.6	0.0

* Refer to Fig. 16.7-1 for general cycle diagram.

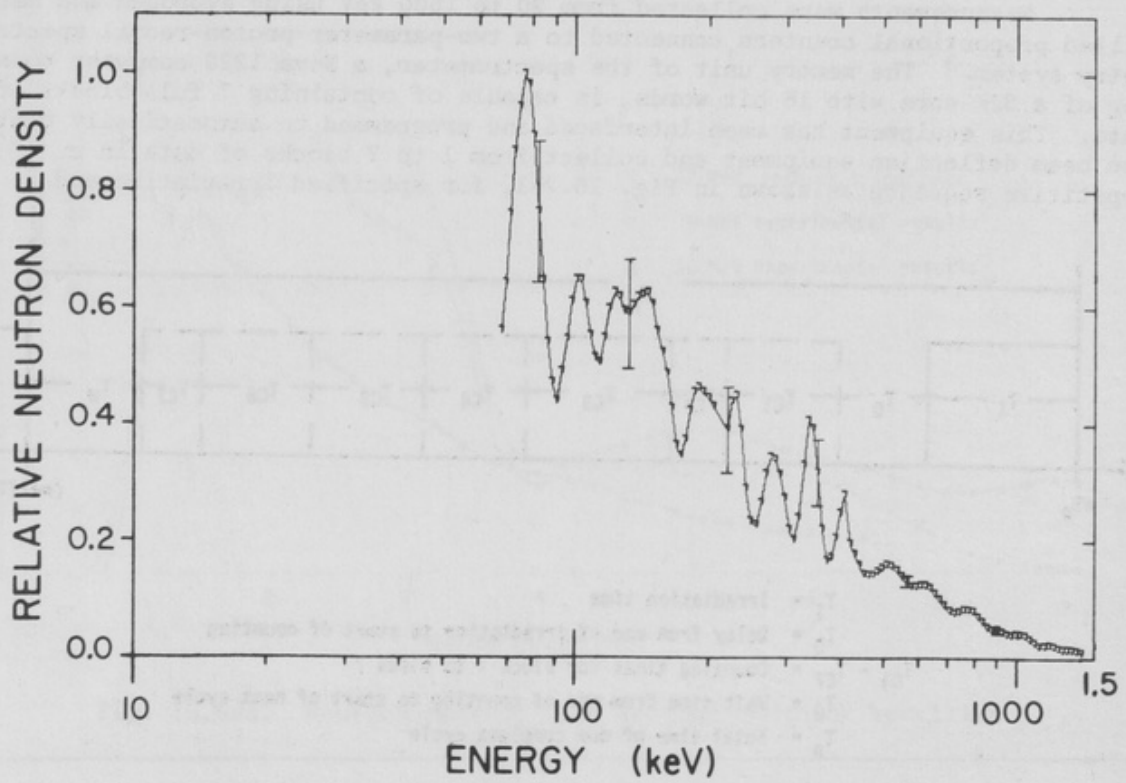

Fig. 16.7-2. ^{235}U delayed neutron data medium cycle -- 7th count block.

Delayed neutron spectra for the 7th counting block of the ^{235}U medium cycle is shown in Fig. 16.7-2. Approximately 48 hours were required to complete a full energy range measurement with 7 blocks of data. Presently, software programs to locate peaks in the spectra, integrate them and assign half-lives are in the developmental stage.

Recent arrival of a 2 curie Am-Li source has enabled the continuance of system diagnostics; such as, measurements of the Am-Li source, in the absence of a fissionable isotope, while cycling the Van de Graaff beam on and off. This information, although preliminary, indicates possible problems are occurring in the collection of pulsed source data. Until further measurements are completed and an in depth analysis performed, these results should be used with caution.

---

* Work supported by AEC Contract # A.T.(45-1)-2225.

† Department of Nuclear Engineering, University of Washington.

1. See Sec. 16.6 of this report.
2. See Sec. 16.5 of this report.
3. "Delayed Neutron Spectra from Fast Fission", G.L. Woodruff, W.R. Sloan, and G.W. Eccleston, Renewal Proposal submitted to Division of Research, USAEC.

16.8 Radiative Proton Capture by ^{12}C

D. Berghofer*, M.D. Hasinoff*, R. Helmer*, S.T. Lim*, and D.F. Measday

Last year in this report we presented a number of new measurements of the gamma yield for the reactions $^{12}C(p,\gamma_0)^{13}N$ and $^{12}C(p,p'\gamma)^{12}C$.[1] In particular, we gave the 90° γ_0 yield for proton energies (E_p) from 14 MeV to 24 MeV, angular distribution coefficients for the γ_0 at several energies, and the 90° yield for the inelastic gamma-rays $\gamma_{12.71}$ and $\gamma_{15.11}$ from E_p = 14 - 24 MeV. We have since completed measurements of the angular distributions in some detail throughout the region, and further measured the 90° yield to verify structure in certain regions.

Figure 16.8-1 give the angular distribution coefficients of the γ_0 according to the expansion

$$Y(\theta) = A_0(1 + \sum a_n P_n(\cos\theta)).$$

This figure includes the previously

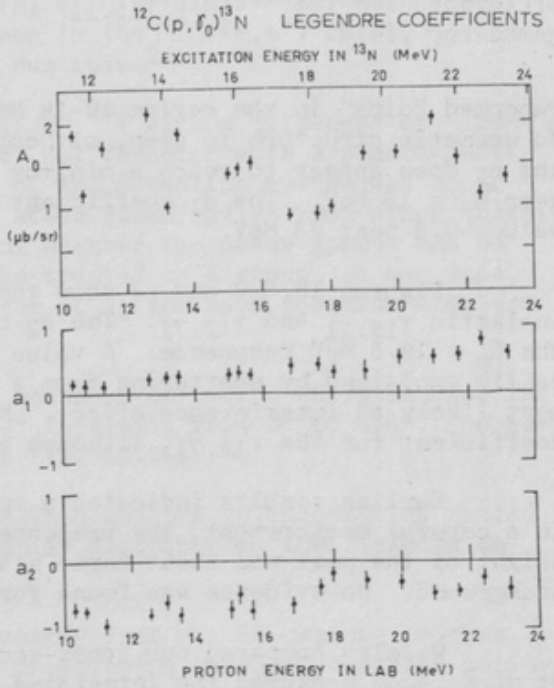

Fig. 16.8-1. Angular distribution coefficients for $^{12}C(p,\gamma_0)$.

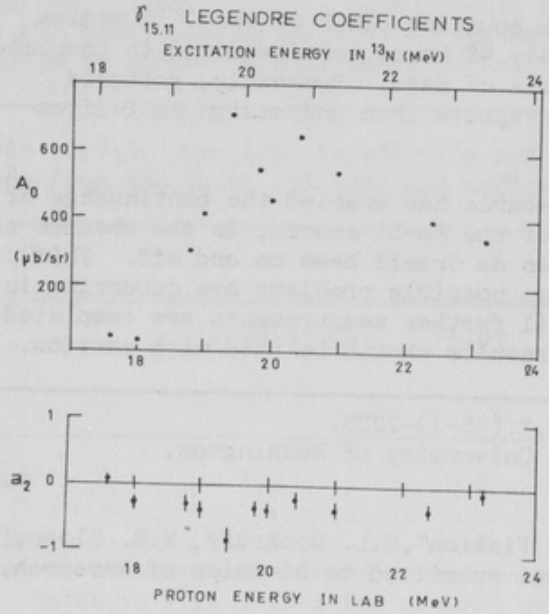

Fig. 16.8-2. Angular distribution coefficients for the $^{12}C(p,p'\gamma_{15.11})$ gamma-ray yield.

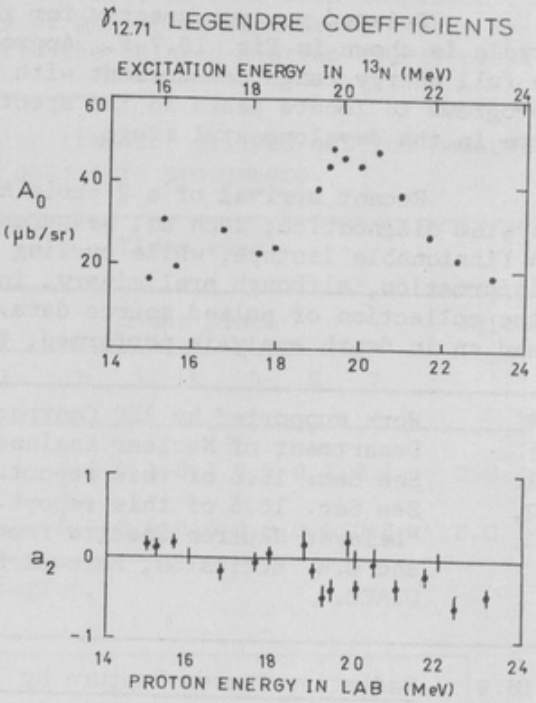

Fig. 16.8-3. Angular distribution coefficients for the $^{12}C(p,p'\gamma_{12.71})$ gamma-ray yield.

reported "dips" in the region 10-14 MeV. No dramatic structure is seen, although the a_2 does appear to reach a minimum near E_p = 18 MeV. The a_1 coefficient steadily rises, reaching the quite large value ~0.8 near 23 MeV.

Figures 16.8-2 and -3 show the angular distribution coefficients for the inelastic $\gamma_{15.11}$ and $\gamma_{12.71}$. The a_2 coefficient for the $\gamma_{15.11}$ is peaked near the E_p = 19.5 MeV resonance. A value of a_2 more negative than -0.5 is not easily explained by scattering from a single compound nuclear state, and thus is most likely an interference effect. No dramatic structure is seen in the a_2 coefficient for the $\gamma_{12.71}$, although a peak shape near 23 MeV seems well defined.

Earlier results indicated a small bump in the 90° γ_0 yield at E_p = 9.0 MeV. In a careful measurement, the presence of this slight peak was verified. The height of the peak was about three standard deviations above the broad resonant background. No evidence was found for structure near E_p = 14 MeV in the γ_0 yield.

We also compared our cross-section calibration to the results of Amos *et al.*[2] Amos measured the integrated proton cross-section for $^{12}C(p,p')^{12}C^*$ (12.71) at 22.3 MeV. Using a branching ratio Γ_γ/Γ = 0.025 for the 12.71 MeV state, our yield calibration was found to be in excellent agreement with Amos.

We further plan to study the $^{12}C(p,\gamma_0)^{13}N$ reaction using polarized protons in the region of the dips.

---

* Department of Physics, University of British Columbia, Vancouver, B.C., Canada.

1. Nuclear Physics Laboratory Annual Report, University of Washington (1974), p. 197.
2. K.A. Amos *et al.*, Phys. Lett. *52B*, 138 (1974).

16.9 The $^{89}Y(p,\gamma)^{90}Zr$ Reaction below the Giant Dipole Resonance

D. Berghofer*, M. Hasinoff*, R. Helmer*, B. Lim*, D. Measday*, and T. Trainor

Inelastic electron and proton scattering from many nuclei have shown the existence of strong states located below the Giant Dipole Resonance (GDR). Analysis of the electron data indicates an E0 or E2 assignment for these states, while the (p,p') results are interpreted as giant isoscalar E2 resonances.[1] In particular, a state has been excited below the GDR in ^{90}Zr by both inelastic electron[2] and inelastic proton[3] scattering.

Here we report the results of an investigation of the radiative capture of protons by ^{89}Y from E_p = 2.5 to 7.0 MeV (E_x = 10.8 - 15.3 MeV) which corresponds to the position of the broad state seen in the $^{90}Zr(e,e')$ reaction, which, if E2, exhausts ~56% of the energy weighted sum rule.[2]

The target was a self-supporting foil of ^{89}Y with a thickness of 4.2 mg/cm^2, and the gamma rays were detected in a 10"×10" NaI detector with a plastic anti-coincidence shield.[4] The resolution (FWHM) of the detection system was about 3.5%, which is ample to separate the ground state gamma ray γ_0 from other transitions seen in the spectra, but it is doubtful whether the other gammas can be analyzed separately; more likely, they can be treated as a group, as was done, for example, in Ref. 5. The statistical error of γ_0 for each spectrum was less than 2%.

Detailed angular distributions were measured at twelve energies over the region of interest, with spectra taken at 10° intervals from 0° to 130°. An example of an angular distribution is shown in Fig. 16.9-1.

To date, four energies have been analyzed and the γ_0 intensities fitted to a Legendre polynomial expansion. The angular distribution coefficients obtained are shown in Fig. 16.9-2.

The dominant A_2 coefficient arises mainly from the E1 capture process, while non-zero odd coefficients indicate an interfering level of opposite parity. The inclusion of an A_4 coefficient, while it would unambiguously define the presence of E2 capture, was not required to adequately fit the data.

On the basis of the present analysis, assuming the phases of the con-

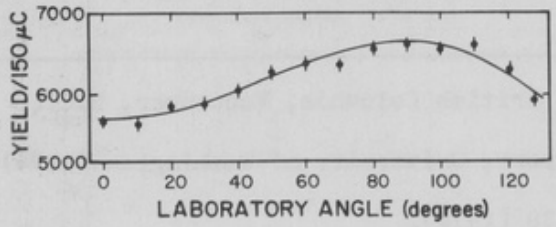

Fig. 16.9-1. The angular distribution for E_p = 4.2 MeV. The solid line is a fit to the Legendre polynomial expansion $\frac{d\sigma}{d\Omega} \propto \sum A_i P_i(\cos\theta)$ for i=0 to 3.

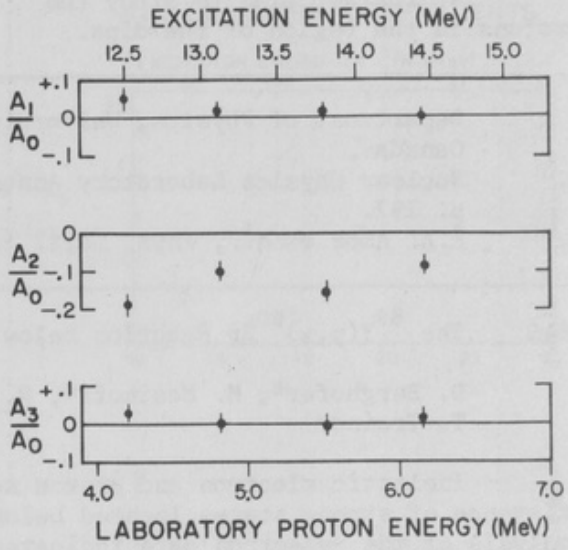

Fig. 16.9-2. Angular distribution coefficients normalized to A_0.

tributing partial waves (s, p, d, and f) are equal, we place an upper limit on the E2 strength of 2% of the E1 strength.

The assumption of equal phases can be removed by measuring the analyzing power of the reaction, since the information gained from such a study is physically imdependent of the information from the study of the unpolarized reaction. A measurement has been made elsewhere at E_p = 6.8 MeV, and the same upper limit to the E2 strength of about 2% of the E1 strength was obtained.[6] Measurements with a polarized proton beam are currently underway at this Laboratory at a few energies in the same region discussed above to remove the assumption about the phases, and to further restrict the estimate of the E2 strength.

---

* Department of Physics, University of British Columbia, Vancouver, B.C. Canada.

1. M.B. Lewis and F.E. Bertrand, Nucl. Phys. *A196*, 337 (1972).
2. S. Fukuda and Y. Torizuka, Phys. Rev. Letters *29*, 1109 (1972).
3. G.R. Satchler, Comm. Nucl. Part. Phys. *5*, 145 (1972).
4. Nuclear Physics Laboratory Annual Report, University of Washington (1973), p. 19.
5. Nuclear Physics Laboratory Annual Report, University of Washington (1974), p. 142.
6. S.S. Hanna, Int. Conf. on Photonuclear Reactions and Applications (March 1973), p. 429.

16.10 Radiative Proton Capture Into the Giant Dipole Resonance of ^{29}P

D. Berghofer*, K. Ebisawa, M. Hasinoff*, R. Helmer*, S.T. Lim*, and D. Measday*

Gamma yield measurements on the ^{28}Si(p,γ_0)^{29}P reaction[1] have been extended to a lower proton beam energy of 7.30 MeV. A strong resonance (Fig. 16.10-1) of width approximately 130 keV has been observed at E_p = 7.45 MeV by using a ^{28}Si

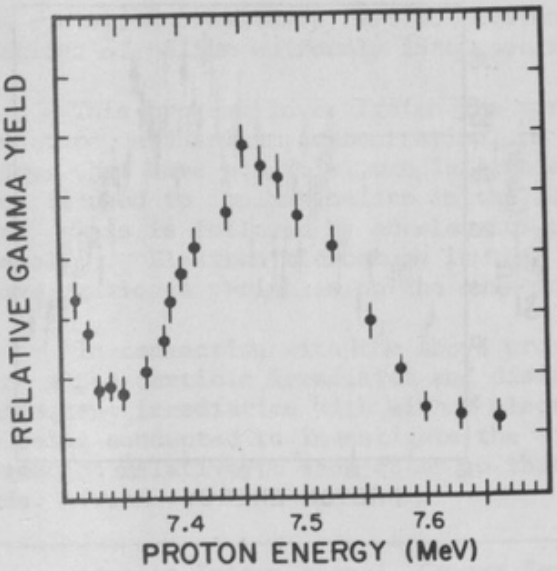

Fig. 16.10-1. Relative gamma yield in the vicinity of the 7.45 MeV resonance in $^{28}Si(p,\gamma_0)$.

target of thickness 400 μg/cm^2. The errors shown in Fig. 16.10-1 are uncertainties in unfolding the experimental gamma spectrum. The 90° differential cross section on the resonance is (13±4) μb/sr. Angular distribution measurements on and off the resonance (Fig. 16.10-2) strongly indicate a dipole gamma transition ($p_{3/2}$ to $s_{1/2}$).

It has been observed previously that the yield from the $^{28}Si(p,\gamma_5)^{29}P$ (3.45 MeV) reaction is significant for proton beam energies between 16.50 MeV and 24.0 MeV. Since the intrinsic resolution of the 10"×10" NaI spectrometer was not good enough to resolve γ_4 from γ_5 (Fig. 16.10-3), it was necessary to unfold the experimental gamma spectrum in terms of standard line-shapes keeping the separations between the line-shapes fixed throughout the least chi-square fitting process. These separations were based on the known excitations of the low-lying states in ^{29}P and careful energy calibration of

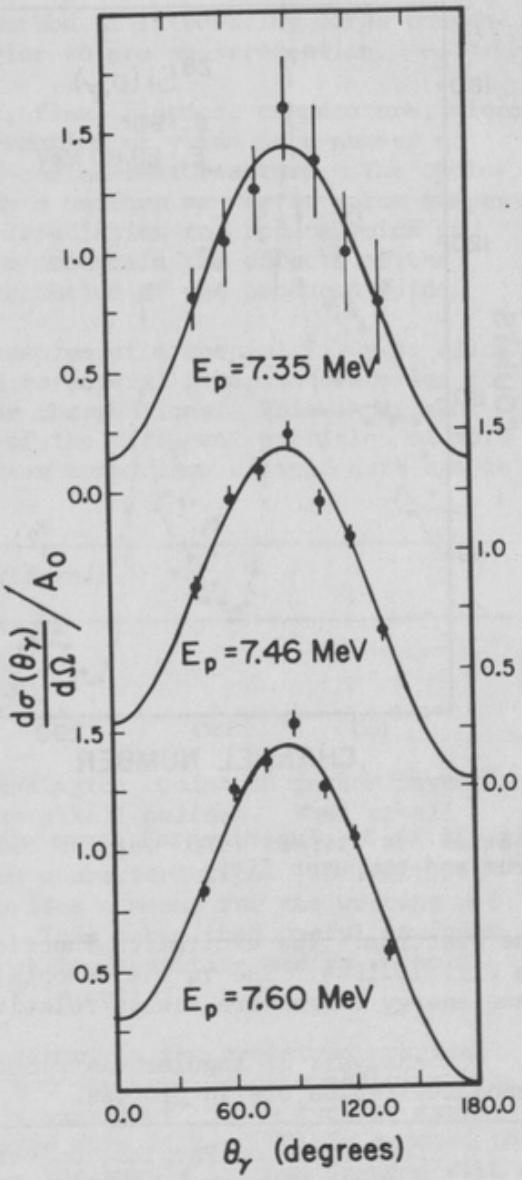

Fig. 16.10-2. Angular distribution measurements on and off the 7.45 MeV resonance in $^{28}Si(p,\gamma_0)$. Solid lines are $W(\theta)$, where

(i) E_p = 7.35 MeV, $W(\theta) = 1.0+0.1\ P_1(\theta) - 0.87\ P_2(\theta)$;

(ii) E_p = 7.46 MeV, $W(\theta) = 1.0+0.13\ P_1 - 0.84\ P_2$;

(iii) E_p = 7.60 MeV, $W(\theta) = 1.0+0.15\ P_1 - 0.85\ P_2$.

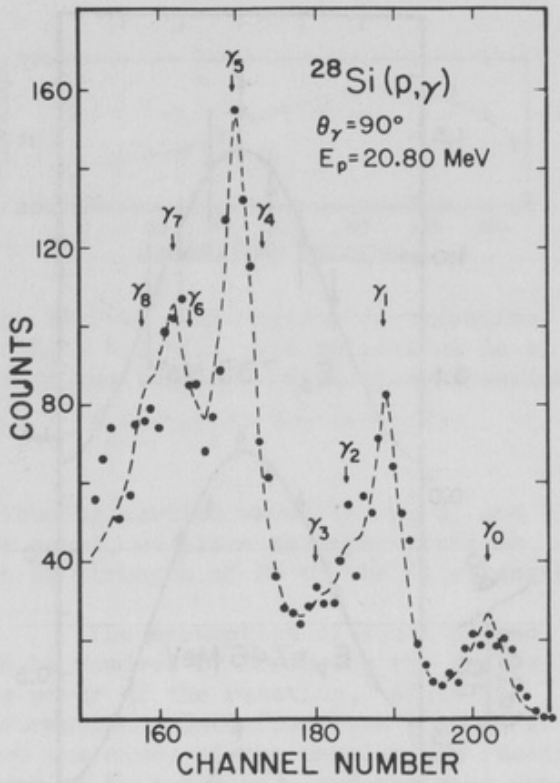

Fig. 16.10-3. Experimental gamma spectrum and computer fit.

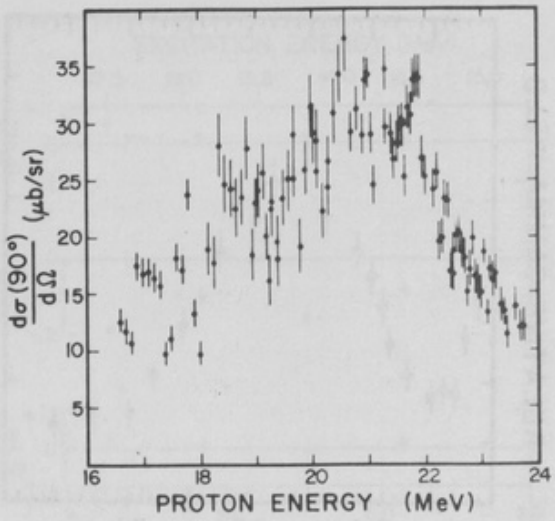

Fig. 16.10-4. 90° yield curve for the ^{28}Si(p,γ_5)^{29}P reaction. Errors are the uncertainties in unfolding the gamma spectrum.

the spectrum. The excitation function for the ^{28}Si(p,γ_5)^{29}P reaction is shown in Fig. 16.10-4. The γ_4 yields obtained from the fitting process throughout the same energy range were always relatively small (20% or less of γ_5).

Analysis of angular distribution measurements in the giant dipole resonance region are in process.

---

* Department of Physics, University of British Columbia, Vancouver, Canada.

1. Nuclear Physics Laboratory Annual Report, University of Washington (1974), p. 201.

16.11 Alpha Particle Injection into Reactor Materials

K.R. Garr*

Alpha-particle irradiations of fast-reactor cladding and structural material candidates are being carried out under a program at Atomics International sponsored by ERDA-RRD called "Proton-Bombardment-Alloy Development Program", Task 17, Contract A.T.(04-3)-824, using the University of Washington's cyclotron.

The cyclotron provides a fast and convenient method of introducing large concentrations of helium uniformly into specimens prior to proton irradiation.

This program investigates the variables, flux, fluence, temperature, microstructure, and helium concentration, on the formation of voids in a number of alloys that have potential use in liquid-metal-cooled-fast reactors. The cyclotron is used to implant helium in the alloys in a uniform manner at a low temperature. This is followed by accelerator proton irradiation to produce voids in the alloy. Electron microscopy is then used to ascertain the effects of the above mentioned variables on the size and distribution of the produced voids.

In connection with the above program, samples of a special Fe-Cr-Ni alloy were alpha-particle irradiated and distributed to several other laboratories for subsequent irradiation with either electrons or charged ions. This experiment is being conducted to investigate the effects of the different particles on void formation relative to each other so that a better comparison of void data can be made.

---

* Atomics International, Canoga Park, California.

16.12 Optical Properties of the Alkali Halides

M.J. Intlekofer*, and F.P. Carlson*

We have been using the University of Washington cyclotron in our investigation of some of the optical properties of the alkali halides. When alkali halide crystals are subjected to crystal lattice damage, color centers are formed which exhibit polarization sensitive absorption characteristics. In addition, the color centers are re-orientable, which provides a means for the writing and non-destructive reading of stored information. This makes them useful as input masks in coherent optical processing systems, as the sensitive medium in holography, and as the propagating medium in thin film optics.

We have found that alpha particle bombardment in the cyclotron provides the optical density and penetration necessary for our work, and in addition, the uniformity and persistence of the coloration is excellent. In a typical experimental session, a single crystal or an evaporated thin film of KCl is exposed to a diffuse beam of high energy alpha particles. The sample is then scanned with a spectrophotometer and reorientation and propagation studies are performed.

This work is being undertaken with the support of the U.S. Navy, under Contract #00014-67-A-0103-0024, Task Order NR 350-005.

---

* Department of Electrical Engineering, University of Washington.

16.13 Supporting Data for "^{18}F-21-Fluoropregnenolone-3-Acetate as an Adrenal Scanning Agent"

R. Eng,* G. Hinn,* and L. Spitznagle*

Recent work in this laboratory has been concerned with the development of methods for preparing ^{18}F-labeled steroids for use as adrenal scanning agents. Since our source of ^{18}F was a water target, we were limited in our choice of fluorinating agents. A review of the literature suggested the use of silver fluoride as an agent for fluorinating iodinated steroids. Tannhauser, et al.[1] reported 63% yields of 21-fluoropregnenolone-3-acetate when an aqueous solution of AgF was reacted with 21-iodopregnenolone-3-acetate. In our hands, the yields were not quite as good. However, we were successful in preparing 21-fluoropregnenolone-3-acetate in this manner.

Attempts to label $Ag^{18}F$ by exchange in the solution obtained from the cyclotron were unsuccessful. We were, however, able to synthesize $Ag^{18}F$ from Ag_2CO_3 by reacting Ag_2CO_3 with the $H^{18}F$ present in the water from the cyclotron.

Experiments in this laboratory show that the water from the cyclotron contains $H^{18}F$ accounting for from 5-10% of the ^{18}F activity. Attempts to increase the amount of $H^{18}F$ by exchange with HF were unsuccessful. Using the $Ag^{18}F$ prepared as described above, we were able to synthesize 21-^{18}F-fluoropregnenolone-3-acetate from 21-iodopregnenolone-3-acetate. The synthesis required four hours and resulted in about 700 microcuries of 21-^{18}F-fluoropregnenolone-3-acetate for an overall radiochemical yield of 1.6%. Efforts to improve the yield of this reaction require the development of a gas target to prepare $H^{18}F$ directly or $Ag^{18}F$ by exchange.

The commercial availability of 1,4,7,10,13,16-hexaoxacyclooctadecane (18-Crown-6)[2] and the report by Liotta and Harris[3] on the successful use of 18-Crown-6 and potassium fluoride as a fluorinating reagent prompted us to investigate the use of this technique for fluorinating steroids.

Carrier potassium fluoride was added to the water from the cyclotron and the solution evaporated to dryness. Acetonitrile and 18-Crown-6 were added to the flask to dissolve the $K^{18}F$. 21-Iodopregnenolone-3-Acetate was added to the solution and the reaction refluxed for 1.5 hr. The resulting 21-^{18}F-fluoropregnenolone-3-acetate (5 millicuries) represented an overall radiochemical yield of 15%. This reaction has been repeated twice with similar success.

Preliminary attempts to study the distribution of 21-^{18}F-fluoropregnenolone-3-acetate failed because the rats died from the i.v. injection of 0.5-1 ml of 95% ethanol in which the ^{18}F-labeled steroid was dissolved. A distribution study was made possible by dissolving the ^{18}F-labeled steroid in 1 ml of a solution of 95% ethanol, water and propylene glycol (1:1:2) and injecting the solution over a 1 min. period. Three animals were sacrificed at each of the time periods (1,5,10,15 and 30 min. after administration), the organs removed, and the ^{18}F activity determined by scintillation counting in a well counter. The results, corrected for decay and expressed as a percent dose per gram of tissue were averaged and are presented in Fig. 16.13-1. We believe that these

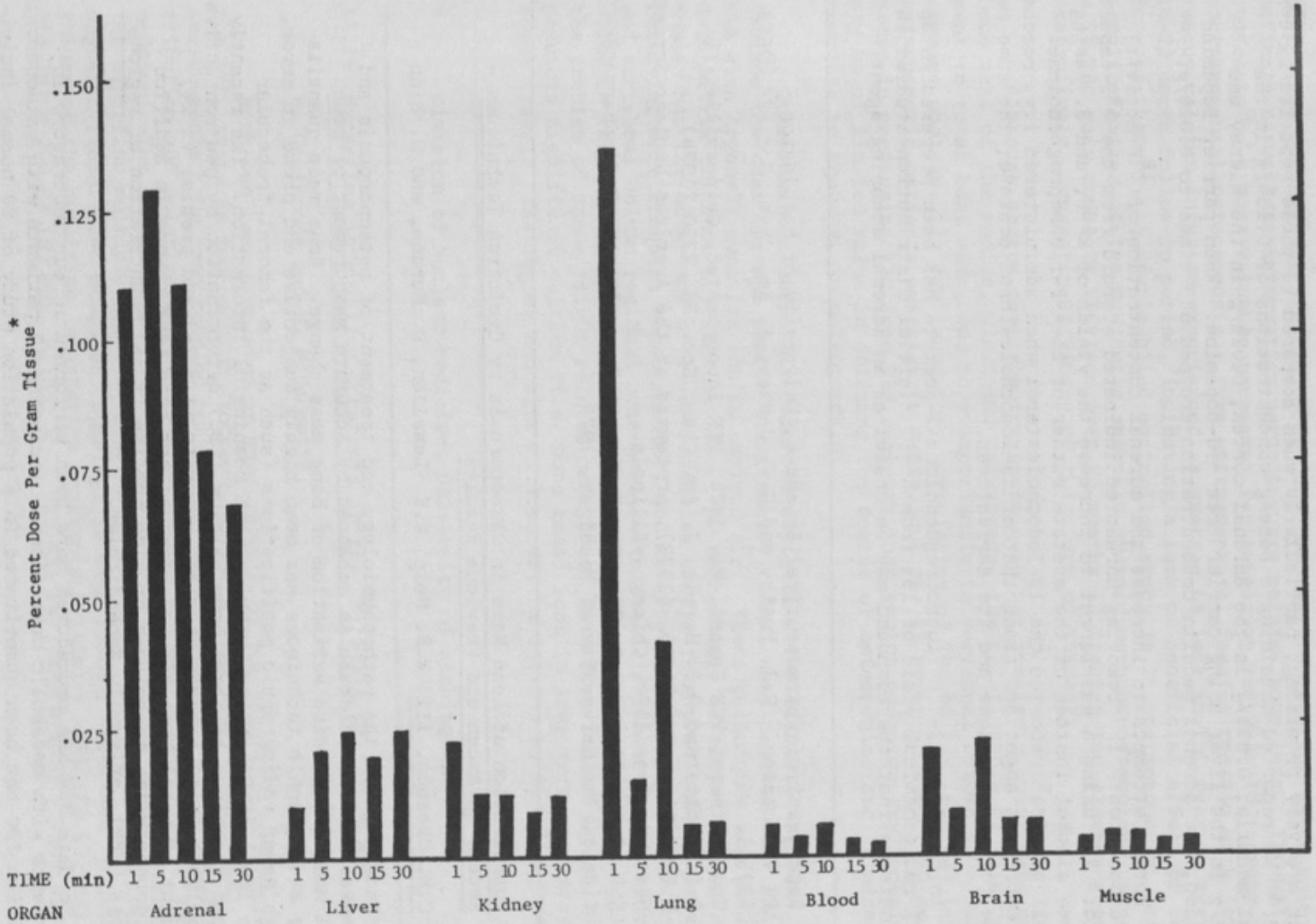

Fig. 16.13-1. Distribution of ^{18}F activity in rats at various times after IV 21-^{18}F-fluoropregnenolone-3-acetate. (* Mean from three animals at each time interval)

results are very promising, particularly when compared to those reported by Atkins.[4] He reported obtaining % Dose/g concentrations of 0.13%/g in the adrenal medulla, 0.03%/g in the adrenal cortex, 0.02%/g in the kidney and 0.015%/g in the liver using carrier free ^{11}C-Dopamine. When carrier Dopamine was added, the adrenal medulla concentration dropped 6.5 times to 0.02%/g.

Future attempts to increase the adrenal concentration of ^{18}F activity will be based on: 1. removing unreacted iodinated steroid from the ^{18}F-labeled steroid: 2. using a gas target to increase the yields of K^{18}F; and 3. using the free alcohol instead of the acetate esther of 21-^{18}F-fluoropregnenolone. Counsell and Ice[5] reported the 19-Iodocholesterol when administered i.v. reaches a concentration about 300 times that of 19-Iodocholesterol acetate; the same may be true for pregnenolone and its derivatives.

In summary, 21-^{18}F-fluoropregnenolone-3-acetate has been prepared in an overall radiochemical yield of 15% from K^{18}F. Initial distribution studies in rats indicate that the compound may be useful as an adrenal scanning agent.

---

* Department of Pharmaceutical Sciences, University of Washington.

1. P. Tannhauser, R.J. Pratt, and E.V. Jensen, J. Am. Chem. Soc. *78*, 2658 (1956).
2. Crown Ethers, PCR Report, May 1974, PCR Incorporated, Gainesville, FL.
3. C.L. Liotta and H.P. Harris, J. Am. Chem. Soc. *96*, 2250 (1974).
4. H.L. Atkins, BNL #18052 (1973), presented at the American Nuclear Society Meeting, June 1973, Chicago, Illinois.
5. R.E. Counsell and R.D. Ice, The Design of Organ Imaging Radiopharmaceuticals, The University of Michigan, 1973.

16.14 Quantitation of Bone Mass in Osteoporosis by Cyclotron Techniques - Recent Advances and Previous Results

C.H. Chesnut, III, W.B. Nelp, T.K. Lewellen, R. Murano, and G. Hinn

Knowledge of the pathophysiology and treatment of osteoporousis and other metabolic bone disease is enhanced by accurate measurement of bone mineral mass and precise estimation of bone mass change. Bone mass quantitation by radiographic techniques has been highly subjective and prone to error, although newer radiographic modifications (such as the femoral trabecular pattern index of Singh) may provide more meaningful information. The recently developed technique of total body calcium (TBC) determination by neutron activation analysis (NAA) however provides accurate (± 5.2%) and precise (± 2%) assessment of total bone mineral mass and net bone mass change in addition photon densitometry techniques provide precise (± 3%) quantitation of regional bone mass (RBM), primarily appendicular.

To date 364 NAA procedures have been performed in our laboratory in 134 patients with metabolic bone disease including 60 patients with osteoporosis. In addition TBC has been quantitated in a population study of 50 normal indivi-

duals (age and sex distributed) providing comparative data for osteopenic patients as well as information regarding age related bone loss. TBC-NAA has proven to be a most valuable parameter for assessing response to therapy in postmenopausal osteoporosis. Five postmenopausal females treated with intravenous calcium infusion experienced an average 6% loss in TBC over an average 14-22 month follow-up period, indicating a lack of beneficial effect of this form of therapy. A double-blind controlled study in 26 postmenopausal osteoporotic females of the synthetic anabolic steroid methandrostenolone revealed a 2% TBC gain and a 3% TBC loss over 26 months in treated and placebo groups respectively, suggesting efficacy of this form of therapy.

Although photon densitometry techniques may precisely quantitate regional bone mass of the radius, ulna, and calcaneous, the relationship of this measurement to total bone mass, and more importantly to vertebral column bone mass, remains unclear. In our laboratory correlation of TBC to RBM (radius) in 14 osteoporotic patients was high (r = .94) but the 8% error (S.E.E. ± 60 grams) noted in predicting TBC from RBM suggents that photon densitometry techniques may be of limited value in defining the degree of osteopenia, and in assessing response to therapy, in osteoporosis.

Other methods currently under investigation for quantitating bone mass include the dual isotope photon densitometry techniques, partial body NAA, and NAA with Argon-37 quantitation in expired air. These techniques have had to date little clinical application; the ^{37}Ar methodology developed in our laboratories has the advantage of lower radiation dosage than previous NAA procedures (allowing more frequent measurements), and may provide both total bone mass and vertebral column regional bone mass, with the latter measurement of obvious value in the assessment of osteoporosis. The ^{37}Ar technique will be applied to the problem of space flight related bone loss; data from recent Skylab missions predicts significant calcium (i.e. bone mass) loss in long term zero gravity space travel. The degree and site of loss may be defined by the ^{37}Ar technique.

---

* Division of Nuclear Medicine, University of Washington.

16.15 Hyperfine Interaction Constants in the $^3P_1$ State of $^{111}Cd^m$ and ^{105}Cd

B. Geelhood* and M. McDermott*

Work has been completed on measurements of the hyperfine structure of the 5^3P_1 state in two cadmium isotopes, 49-min $^{111}Cd^m$ and 55-min ^{105}Cd. The measurements have been carried out by detecting the change in the angular distribution and polarization of 326.1 nm photons scattered from a vapor sample of cadmium. The change occurs when two appropriately chosen Zeeman sublevels of the hyperfine multiplets are made to cross by the application of an external magnetic field. Two measured crossings in each isotope were used to extract values of the hyperfine interaction constants A(111m) = -696.888 (3) MHz, B(111m) = 202.94 (8) MHz, A(105) = -1,025.433 (4), and B(105) = -103.92 (8) MHz.

The precisely determined magnetic dipole interaction strengths can be used to determine features of the distribution of magnetism in the two nuclei if equally precise values of their magnetic dipole moments are available. In order to measure these moments further production of $^{111}Cd^{m}$ and ^{105}Cd is being carried out at the cyclotron by (α, xn) reactions on natural palladium targets. Once separated from the target the nuclei will be oriented by a circularly polarized photon beam and their nmr frequency measured in a known magnetic field. The narrow resonances which result from the small spin relaxation rate should lead to measured moments with a precision of a few parts per million.

---

* Department of Physics, University of Washington.

---

17. APPENDIX

17.1 Nuclear Physics Laboratory Personnel

Faculty

Eric G. Adelberger, Associate Professor[1]
John S. Blair, Professor[2]
David Bodansky, Professor[3]
John G. Cramer, Professor
Klaus A. Eberhard, Visiting Associate Professor
George W. Farwell, Professor; Vice President for Research[4]
I. Halpern, Professor
Fred H. Schmidt, Professor
Robert Vandenbosch, Professor
William G. Weitkamp, Research Associate Professor; Technical Director, Nuclear Physics Laboratory[5]

Research Staff

Robert Bangert, Research Associate
Holger Bohn, Research Associate
David F. Burch, Senior Research Associate
Martin D. Cooper, Research Associate[6]
Philip A. Dickey, Research Associate
Peggy L. Dyer, Research Associate
Lynn D. Knutson, Research Associate
Hans O. Meyer, Senior Research Associate[7]
Kurt A. Snover, Senior Research Associate
James W. Tape, Research Associate[8]
Thomas A. Trainor, Research Associate
Michael S. Zisman, Research Associate[9]

Laboratory Supervisory Personnel

Harold Fauska, Research Electronics Supervisor; Assistant Technical Director, Nuclear Physics Laboratory
John W. Orth, Accelerator Engineer; Assistant Technical Director, Nuclear Physics Laboratory

Predoctoral Research Associates

Chemistry

Michael P. Webb

Physics

Michael P. Baker[6]
Klaus G. Bernhardt
Hyoung C. Bhang
Douglas R. Brown[10]
John E. Bussoletti
Yuen-Dat Chan
David T.C. Chiang
Bernardo D. Cuengco
Katsuyaki Ebisawa
Kwok-Leung Liu
Roscoe E. Marrs[11]
H. Erik Swanson[12]
Howard Wieman[13]

Research Assistants

Chemistry

Man-Yee B. Tsang

Physics

Norman L. Back
Richard A. Clark[14]
Kelly C. Green
William G. Lynch
James C. Wiborg

Full-Time Technical Staff

Professional Staff

Noel R. Cheney, Computer Systems Engineer
William B. Ingalls, III, Research Scientist
Shirley Kellenbarger, Chemist, Detector Maker
Gary W. Roth, Physicist
Rod E. Stowell, Electronics Engineer

Accelerator Technicians

Carl E. Linder
Georgia J. Rohrbaugh
George E. Saling

Accelerator Operator

Barbara L. Lewellen

Design and Drafting

Peggy Douglass, Graphics Illustrator
Lewis E. Page, Designer

Instrument Makers

Louis L. Geissel
Norman E. Gilbertson
Charles E. Hart, Forman
Gustav E. Johnson
Byron A. Scott, Student Shop Leadman
Allen L. Willman, Leadman

Administrative Staff

Susan Lambert, Secretary
Helene Turner, Administrative Secretary

Part Time Technical Staff

Michael Anderson
Lawrence S. Baker
James E. Burger
David Chamberlin
Solomon W. Davis
Tim Denning[14]
Ronald Dickens
Jeffrey Dunham[14]
Lila Graham
Paul Hart[14]
Rochelle S. Kochin
San-Dah Lok[14]
Richard Methot, Jr.[14]
David D. Palmer[14]
Hung C. Pon[14]
Douglas W. Potter
M. Usman Qureshi[14]
Mojtaba Rezvani
Edwin Selker
Steven J. Stradley
Nicholas Suntzeff[14]
Gary Walters
Jennifer H. Wear

---

1. On leave at Princeton University and Caltech.
2. On leave Spring Quarter at Saclay.
3. On leave Nordita, Denmark and Oxford University, England.
4. On leave from the Department of Physics.
5. On leave at ETH, Zurich, Switzerland.
6. Now at Los Alamos Scientific Laboratory, Los Alamos, New Mexico.
7. Now at the University of Basel, Switzerland.
8. Now at Rutgers University, New Brunswick, New Jersey.
9. Now at Lawrence Berkeley, University of California, Berkeley, CA.
10. Now at Texas A & M University, College Station, Texas.
11. Now at Caltech, Pasadena, California.
12. Terminated in October.
13. Now at University of Colorado, Boulder, Colorado.
14. Terminated.

17.2 Advanced Degrees Granted, Academic Year 1974-1975

Michael P. Baker: Ph.D. "Depolarization in the Elastic Scattering of 17 MeV Polarized Protons from ^{9}Be"

Douglas R. Brown: Ph.D. "Neutron Pickup by Alpha Particles to Unbound States"

Roscoe E. Marrs: Ph.D. "Decays of T = 3/2 Levels in Mass 13 and T = 2 Levels in Mass 20"

William Q. Sumner: Ph.D. "Alpha Scattering and the Nuclear Surface"

Howard Wieman: Ph.D. "Highly Inelastic Scattering of Medium Energy Deuterons"

17.3 List of Publications

Publications Since the 1974 Report:

"Production of Li and B in Proton and Alpha-Particle Reactions on ^{14}N at Low Energies", W.W. Jacobs, D. Bodansky, D. Chamberlin, and D.L. Oberg, Phys. Rev. C *9*, 2134 (1974).

"Observations of an Anomalous Angular Distribution in the Single-Nucleon Transfer Reaction $^{12}C(^{14}N,^{13}N)^{13}C$ at 100 MeV", D.G. Kovar, R.M. Devries, M.S. Zisman, J.G. Cramer, K-L. Liu, F.D. Becchetti, B.G. Harvey, H. Homeyer, J. Mahoney, and W. von Oertzen, Phys. Rev. Lett. *32*, 680 (1974).

"Importance of Coulomb Interaction Potentials in Heavy-Ion Distorted-Wave Born-Approximation Calculations", R.M. DeVries, G.R. Satchler, and J.G. Cramer, Phys. Rev. Lett. *32*, 1377 (1974).

„$^{16,18}O$ Elastic Scattering from ^{58}Ni", M.S. Zisman, R.M. DeVries, J.G. Cramer, K-L. Liu, Y-d. Chan, and B. Cuengco, Phys. Rev. C *11*, 809 (1975).

"Upper Limit on the Radiative Width of the 9.64-MeV State of ^{12}C", D. Chamberlin, D. Bodansky, W.W. Jacobs, and D.L. Oberg, Phys. Rev. C *10*, 909 (1974).

"Projectile charge-state dependence of Ne K-shell ionization and fluorescence yield in 50-MeV Cl^{n+} + Ne collisions", D. Burch, N. Stolterfolt, D. Schneider, H. Wieman, and J.S. Risley, Phys. Rev. Lett. *32*, 1151 (1974).

"Effect of particle identity on the observed impact parameter dependence of inner-shell ionization in symmetric heavy-ion collisions", D. Burch, Phys. Lett. *47A*, 437 (1974).

"Mechanisms for electron production in 30-MeV O^{n+} + O_2 collisions", N. Stolterfoht, D. Schneider, D. Burch, H. Wieman, and J.S. Risley, Phys. Rev. Lett. *33*, 59 (1974).

"K-shell ionization of Pb at zero impact parameter in 50- to 100-MeV Cl + Pb", D. Burch, W.B. Ingalls, H. Wieman, and R. Vandenbosch, Phys. Rev. A *10*, 1245 (1974).

"Entrance-Channel Effects in the ^{32}S System: Comparison of ^{12}C + ^{20}Ne and ^{16}O + ^{16}O Elastic Scattering", R. Vandenbosch, M.P. Webb, and M.S. Zisman, Phys. Rev. Lett. *33*, 842 (1974).

"Isoscalar Electric Quadrupole Strength in ^{16}O", K.A. Snover, E.G. Adelberger, and D.R. Brown, Phys. Rev. Lett. *32*, 1061 (1974).

"Development of a Direct Extraction Ion Source for an FN Van de Graaff Terminal", G.W. Roth and W.G. Weitkamp, *Proc. of Second Symposium on Ion Sources and Formation of Ion Beams*, Lawrence Berkeley Laboratory Report 3399 (1974).

"Production of ^{6}Li, ^{9}Be, and ^{10}B in p + ^{13}C Reactions at Low Energies", D.L. Oberg, D. Bodansky, D. Chamberlin, and W.W. Jacobs, Phys. Rev. C *11*, 410 (1975).

"Recoil Corrections in DWBA Calculations of Heavy Ion Transfer Reactions", J.S. Blair, R.M. DeVries, and K.G. Nair, A.J. Baltz, and W. Reisdorf, Phys. Rev. C *10*, 1856 (1974).

"Elastic and inelastic scattering of ^{18}O by ^{18}O and ^{16}O", R. Vandenbosch, W.N. Reisdorf, and P.H. Lau, Nucl. Phys. *A230*, 59 (1974).

"Gamma decay of the ^{238}U shape isomer", P.A. Russo, J. Pedersen, and R. Vandenbosch, Nucl. Phys. *A240*, 13 (1975).

"The University of Washington Three-Stage Tanden Van de Graaff Accelerator", W.G. Weitkamp and F.H. Schmidt, Nucl. Instrum. Methods *122*, 65 (1974).

"Parity Mixing in ^{19}F", E.G. Adelberger, H.F. Swanson, M.D. Cooper, J.W. Tape, and T.A. Trainor, Phys. Rev. Lett. *34*, 402 (1975).

"Charge Dependent Mixing", E.G. Adelberger, *Proc. Int. Conf. Nucl. Structure and Spectroscopy, Vol. II*, ed. by H.P. Blok and A.E.L. Dieperink,(Scholars Press, Amsterdam, 1974).

"Angular Distributions in the Radiative Capture of 14-MeV Neutrons", D.M. Drake, E.D. Arthur, and I. Halpern, *Proc. of Int. Symposium on Neutron Capture Gamma Ray Spectroscopy,* Petten, The Netherlands (1974).

"Correlation between α-Particle Scattering and Other Reaction Channels", K.A. Eberhard, in *Proc. of Louvain-Cracow Conf. on "Alpha Particle Scattering"*, Cracow, Poland (1974), p. 103.

"^{1}D Autoionization Series in He", D. Burch, J. Bolger, and C.F. Moore, Phys. Rev. Lett. *34*, 1067 (1975).

Other Publications by Members of the Laboratory:

"The Heavy Ion Reaction Channels of the System ^{16}O + ^{16}O", H.H. Robner, G. Hinderer, A. Weidinger, and K.A. Eberhard, Nucl. Phys. *A218*, 606 (1974).

"High-Lying Neutron-Hole States Populated in the Reaction $^{13}C(p,d)^{12}C$ at 62 MeV", L.J. Parish, R.A. Brown, K.A. Eberhard, A. Richter, and W. von Witsch, Phys. Rev. C *9*, 876 (1974).

"Back-Angle Elastic and Inelastic Scattering of α-Particles from the Even Ni-Isotopes", W. Trombik, K.A. Eberhard, G. Hinderer, H.H. Rossner, A. Weidinger, and J.S. Eck, Phys. Rev. C *9*, 1813 (1974).

"On the Anomalies of Back-Angle Alpha Scattering: Inelastic Scattering from the Calcium Isotopes", W. Trombik, J.S. Eck, and K.A. Eberhard, Phys. Rev. C *11*, 685 (1975).

"Auger-electron and X-ray production in 50- to 2000-keV Ne^{i+} + Ne collisions", N. Stolterfoht, D. Schneider, D. Burch, B. Aagaard, E. Bøving, and B. Fastrup, Phys. Rev. A, to be published.

"Charge state distributions for 0.1 to 1 MeV Ne^{+} + Ne collisions from K x-ray measurements", D. Matthews, R.J. Fortner, D. Burch, B. Johnson, and C.F. Moore, Phys. Lett. *50A*, 441 (1975).

"Vector Analyzing Powers of $^{58}Ni(\vec{d},n)^{59}Cu$", B.P. Hichwa, L.D. Knutson, P.A. Quin, J.A. Thomson, and W.H. Wong, Bull. Am. Phys. Soc. *19*, 91 (1974).

"Deuteron D-State Effects for $^{117,119}Sn(\vec{d},p)$", L.D. Knutson, J.A. Thomson, and H.O. Meyer, Bull. Am. Phys. Soc. *19*, 478 (1974).

"Tensor Analyzing Powers and D-State Effects for (d,t) Reactions", B.P. Hichwa and L.D. Knutson, Bull. Am. Phys. Soc. *19*, 1019 (1974).

"El transitions in ^{17}F. I. The low-lying T = 3/2 states", M.N. Harakeh, P. Paul, and K.A. Snover, Phys. Rev. C *11*, 998 (1975).

"Recoil-Distance Lifetime Measurements of ^{48}V Levels", B.A. Brown, D.B. Flossan, J.M. McDonald, and K.A. Snover, Phys. Rev. C, to be published.

"Observation of resonances in ^{24}Mg at 32-40 MeV excitation energy via the $^{12}C(^{12}C,^{8}Be)^{16}O$ reaction", K.A. Eberhard, E. Mathiak, J. Stettmeier, W. Trombik, A. Weidinger, L.N. Wüstefeld, and K.G. Bernhardt, Phys. Lett. (to be published).

"The $^{12}C(\alpha,\gamma)^{16}O$ Reaction and Stellar Helium Burning", P. Dyer and C.A. Barnes, Nucl. Phys. *A233*, 495 (1974).

"A Lamb-shift Polarized Ion Source for the TUNL Tandem Accelerator", T.B. Clegg, G.A. Bissinger, and T.A. Trainor, Nucl. Instrum. Methods *120*, 445 (1974).

"Isospin-forbidden Proton Partial Width in ^{41}Sc and Similar A = 4n + 1 Nuclei", T.A. Trainor, T.B. Clegg, and W.J. Thompson, Phys. Rev. Lett. *33*, 229 (1974).

"A Comparison of High-intensity Multiaperture and Single-aperture Duoplasmatrons for a Lamb-shift Polarized Ion Source", T.A. Trainor and T.B. Clegg, Symposium: *Ion sources and the formation of ion beams*, Lawrence Berkeley Laboratory Report LBL-3399 (1974), p. IV-5-1.

Papers Submitted or in Press:

"Recoil effects on the impact parameter dependence of inner-shell ionization", D. Burch and Knud Taulbjerg Phys. Rev. A, to be published.

"K-shell ionization of carbon by 1 to 18 MeV protons", D. Burch (submitted to Phys. Rev. A).

"Deuteron D-State Effects for the Reactions $^{117}Sn(d,p)^{118}Sn$ and $^{119}Sn(d,p)^{120}Sn$", L.D. Knutson, J.A. Thomson, and H.O. Meyer (submitted to Nucl. Phys.).

"Mirror Gamma Decays in ^{13}C and ^{13}N", R.E. Marrs, E.G. Adelberger, K.A. Snover, and M.D. Cooper (submitted to Phys. Rev. Lett.).

"On the Production of Li, Be, and B at Low Energies", D. Bodansky, W.W. Jacobs, and D.L. Oberg (submitted to Astrophysical Journal).

"The Energy Controversy: The Role of Nuclear Power", Fred H. Schmidt and David Bodansky.

"Fore-Aft Anisotropy in the Radiative Capture of 14 MeV Neutrons", E.D. Arthur, D.M. Drake, and I. Halpern (submitted to Phys. Rev. Lett).

"Substate excitation of the 3.73 MeV 3^- state of ^{40}Ca produced by the inelastic scattering of 20.3 MeV protons", Tom K. Lewellen (submitted to Nucl. Phys.).

"One-neutron and two-neutron transfer in the scattering of ^{18}O by ^{16}O", W.N. Reisdorf, P.H. Lau, and R. Vandenbosch (submitted to Nucl. Phys.).

Abstracts, Talks and Short Conference Papers:

"Optical Potentials for Heavy Ion Scattering and Reactions", R.M. DeVries, J.G. Cramer, M.S. Zisman, Y.D. Chan, and K.-L. Liu, *Proc. of Int. Conf. on Reactions between Complex Nuclei,* R.L. Robinson, F.K. McGowan, J.B. Ball, and J.H. Hamilton, eds., North Holland, Amsterdam (1974), p. 16.

"Phase Shift Analysis of p + ^{12}C Elastic Scattering", H.O. Meyer and W.G. Weitkamp, presented at the April 11, 1975 meeting of the Schweizerischen Physikalischen Gesellschaft, Zurich.

"Isospin Forbidden β, γ and Particle Transitions", E.G. Adelberger, Invited paper presented at Symposium on Interaction Studies in Nuclei, Mainz, Germany, February 1975.

"Parity Mixing in ^{19}F Studied with Polarized Protons", E.G. Adelberger, Paper presented at Symposium on Interaction Studies in Nuclei, Mainz, Germany, February 1975.

"The Nuclear Power Controversy: Some Misconceptions", F.H. Schmidt, Bull. Am. Phys. Soc. *19*, 1027 (1974).

"Some Views from the Positive Side", David Bodansky and Fred Schmidt. Guest Editorial, Seattle Times, May 29, 1974.

Letter concerning resources. F.H. Schmidt et al., Physics Today, p. 9, June 1974.

"The Need for Accelerating our Nuclear Power Program", David Bodansky and Fred Schmidt. Testimony submitted to Project Independence Hearings, Seattle, Aug. 29, 1974 (Subsequently published in record of these hearings).

Letter commenting on an editorial concerning Reactor Safety; "Defends Reactor Study", F.H. Schmidt, Bulletin of the Atomic Scientists, p. 3, January 1975.

"$\pi^{\pm}$ - ^{4}He Total Cross-Sections from 50 to 100 MeV", M.D. Cooper, D.C. Hagerman, H.O. Meyer, R.P. Redwine, M.J. Jakobson, R.H. Jepesson, G.R. Burleson, K.F. Johnson, J.R. Calarco, I. Halpern, L.D. Knutson, and R.E. Marrs Bull. Am. Phys. Soc. *20*, 663 (1975.

"K Shell Ionization Cross-Sections as a Function of Charge State in 100-1000 keV Ne^{+} - Ne Collisions", D. Matthews, R.J. Fortner, D. Burch, B. Johnson, and C.F. Moore, Bull. Am. Phys. Soc. *19*,1181 (1974).

"A Unique Energy-Independent Optical Potential for ^{16}O + ^{28}Si Elastic Scattering", J.G. Cramer, M.S. Zisman, R.M. DeVries, Y.D. Chan, K.L. Liu, B. Cuengco, and J. Wiborg, Symposium on Classical and Quantum Mechanical Aspects of Heavy Ion Collisions, Heidelberg 1974.

"Are Heavy Ion Optical Potentials Non-Local?" J.G. Cramer, Y.D. Chan, and W. Lynch, Symposium on Classical and Quantum Mechanical Aspects of Heavy Ion Collisions, Heidelberg 1974.

"Elastic and Deeply Inelastic Scattering of Kr by ^{208}Pb and ^{194}Pt", R. Vandenbosch, M.P. Webb, and T.D. Thomas, Symposium on Classical and Quantum Mechanical Aspects of Heavy Ion Collisions, Heidelberg 1974.

"The Importance of Coulomb Interaction Potentials in Heavy Ion DWBA Calculations", R.M. DeVries, G.R. Satchler, and J.G. Cramer, *Proc. of the Int. Conf. on Reactions between Complex Nuclei,* R.L. Robinson, F.K. McGowan, J.B. Ball, and J.H. Hamilton, eds., North Holland, Amsterdam (1974), p. 61.

"On Reaction Mechanism of α-Transfer Reactions: A Study of ^{24,26}Mg(^{12}C,^{8}Be)^{28,30}Si", E. Mathiak, J.G. Cramer, K.A. Eberhard, J. Stettmeier, and L.N. Wustefeld, *Proc. of Int. Conf. on Reactions between Complex Nuclei,* R.L. Robinson, F.K. McGowan, J.B. Ball, and J.H. Hamilton, eds., North Holland, Amsterdam (1974), p. 95.

"^{16,18}O Elastic Scattering on ^{58}Ni", M.S. Zisman, R.M. DeVries, J.G. Cramer, K-L. Liu, Y-d. Chan, and B. Cuengco, Bull. Am. Phys. Soc. *19*, 503 (1974).

"Elastic Scattering of Polarized Protons from ^{206}Pb", M.P. Baker, J.S. Blair, J.G. Cramer, T.A. Trainor, and W.G. Weitkamp, Bull. Am. Phys. Soc. *19*, 478 (1974).

"Applications of Non-Local Optical Potentials to the Analysis of Heavy Ion Scattering", John G. Cramer and Yuen-dat Chan, Bull. Am. Phys. Soc. *19*, 1015 (1974).

"A Comparison between ^{16}O Scattering and ^{15}N, ^{17}O Scattering from ^{28}Si", M.S. Zisman, J.G. Cramer, R.M. DeVries, K-L. Liu, Y-d. Chan, B. Cuengco, and J. Wiborg, Bull. Am. Phys. Soc. *19*, 1015 (1974).

"Scattering of ^{16}O Ions from ^{28}Si, ^{59}Co, and ^{60}Ni at 142 MeV", E.E. Gross, N.M. Clarke, C.B. Fulmer, M.L. Halbert, D.C. Hensley, C.A. Ludemann, D. Martin, A. Scott, J.G. Cramer, and M. Zisman, Bull. Am. Phys. Soc. *19*, 1015 (1974).

"(^{12}C,^{8}Be): A New Alpha Transfer Reaction?", K.A. Eberhard, E. Mathiak, L.N. Wusterfeld, J.G. Cramer, A. Weidinger, and R.M. DeVries, Bull. Am. Phys. Soc. *19*, 989 (1974).

"^{238}U and ^{232}Th Photofission and Photoneutron Emission near Threshold", P.A. Dickey and P. Axel Bull. Am. Phys. Soc. *20*,582 (1975).

"Electron Production in Energetic Heavy-Ion Collisions", D.Burch, Invited Talk, Bull. Am. Phys. Soc. *20*,608 (1975).

"^{16}O + ^{20}Ne Elastic Scattering", M.S. Zisman, R. Vandenbosch, and M.P. Webb, Bull. Am. Phys. Soc. *20*, 718 (1975).

"Back-Angle Excitation Functions of α + ^{39}K and α + $^{40,44}Ca$ Scattering between 20 and 27 MeV", K.A. Eberhard, T.H. Braid, T. Renner, J.P. Schiffer, and S. Vigdor, Bull. Am. Phys. Soc. *20*, 627 (1975).

"Direct and Semi-Direct Radiative Proton Capture into ^{16}O", K.A. Snover and K. Ebisawa, Bull. Am. Phys. Soc. *20*, 629 (1975).

"Depolarization of Elastically Scattered Protons and the Quadrupole Spin Flip Effect", J.S. Blair, Bull. Am. Phys. Soc. *19*, 1010(1974).

"Role of the Nuclear Potential in Elastic and Deeply Inelastic Scattering of Kr", R. Vandenbosch, Stony Brook Workshop, April 1975.

"On the Reaction Mechanism of α-Transfer Reactions: A Study of $^{24,26}Mg(^{12}C,^{8}Be)^{28,30}Si$", E. Mathiak, J.G. Cramer, K.A. Eberhard, J. Stettmeier, and L.N. Wüstefeld, *Proc. of Int. Conf. on "Reactions between Complex Nuclei"*, Nashville, Tenn. 1974, p. 95.

"Angular Distributions and Excitation Functions for the "α-Transfer" Reaction $^{12}C(^{12}C,^{8}Be)^{16}O$", J. Stettmeier, K.A. Eberhard, E. Mathiak, H.H. Rossner, A. Weidinger, and L.N. Wüstefeld, *Proc. of Int. Conf. on "Reactions between Complex Nuclei"*, Nashville, Tenn. 1974, p. 94.

"Back-Angle Anomalies in α-Scattering and a Possible Connection to Multinucleon Removal Pion Experiments", J. Schiele, K.A. Eberhard, and J.P. Schiffer, in *Nuclear Structure and Spectroscopy*, Vol. 1, eds. H.P. Blok and A.E.L. Dieperink (Scholar's Press, Amsterdam, 1974) p. 168.

"Korrelationen zwischen elastischer Streuung und anderen Reaktionskanälen im Hinblick auf Anomalien in der Alpha- und Schwerionen Streuung", K.A. Eberhard, J.S. Eck, J. Schiele, W. Trombik, und A. Weidinger, Verhandl. DPG(VI)*9*, 120 (1974).

"Anregungsfunctionen und Winkelverteilungen der Kernreaktion $^{12}C(^{12}C,^{8}Be)^{16}O$", K.A. Eberhard, E. Mathiak, H.H. Rossner, J. Stettmeier, A. Weidinger, and L.N. Wüstefeld, Verhandl. DPG(VI)*9*, 58 (1974).

"$(^{12}C,^{8}Be)$-Reaktionen an ^{24}Mg und ^{26}Mg", E. Mathiak, J.G. Cramer, K.A. Eberhard, H.H. Rossner, J. Stettmeier, und L.N. Wüstefeld, Verhandl. DPG(VI)*9*, 87 (1974).

"Fluktuationsanalyse der Reaktion $^{12}C(^{12}C,^{8}Be)^{16}O$", W. Trombik, K.A. Eberhard, E. Mathiak, J. Stettmeier, A. Weidinger, und L.N. Wüstefeld, Verhandl. DPG(VI) *10*, 767 (1975).

"Systematische Untersuchung der α-Streuung unter Rückwärtswinkeln im Massenbereich A=20 bis 208", K.A. Eberhard, J. Schiele, J.P. Schiffer, M. Wit, W. Trombik, und E. Mathiak, Verhandl. DPG(VI) *10*, 786 (1975).

"DWBA-Analyse der $(^{12}C,^{8}Be_{g.s.})$-Reaktion an leichten und mittelschweren Kernen", E. Mathiak, R.M. DeVries, K.A. Eberhard, J. Stettmeier, A. Weidinger, und L.N. Wüstefeld, Verhandl. DPG(VI) *10*, 802 (1975).

"Parity Mixing in ^{19}F", E.G. Adelberger, Bull. Am. Phys. Soc. *20*, 36 (1975).

"Spin assignment of $J^{\pi} = 12^{+}$ for the $^{12}C + ^{12}C$ resonance at $E_{^{12}C}$(c.m.) = 18.5 MeV", K.G. Bernhardt, K.A. Eberhard, and A. Weidinger, contributed paper to 2nd Conference "Clustering Phenomena in Nuclei", April 1975, Maryland.

"Experimental Study of Nuclear Structure Effects in Backward-Angle Alpha Scattering", J.P. Schiffer, K.A. Eberhard, J. Schiele, and M. Wit, contributed paper to 2nd Conference "Clustering Phenomena in Nuclei", April 1975, Maryland.

"Recent Developments in Nuclear Astrophysics", D. Bodansky, Israel Physical Society Annual Meeting, Tel Aviv, 2-13-75.

"Light Element Production Rates", D. Bodansky, Workshop on the Abundances of the Light Elements, Tel Aviv 2-21-75.

"The Production of the Light Elements", D. Bodansky, Europhysics Conference on Nuclear Interactions at Medium and Low Energies, Harwell 3-24-75.

"The Abundance and Generation of the Light Elements", D. Bodansky, Cosmology Conference, Oxford 4-8-75.

"^1D autoionization series in He", C.F. Moore, J. Bolger and D. Burch, Bull. Am. Phys. Soc. *20*, 678 (1975).